UNIVERSITY OF OKLAHOMA

GRADUATE COLLEGE

ZEOLITE-CATALYZED SURFACE CHEMISTRY IN ALKANE ISOMERIZATION AND METHANOL-TO-HYDROCARBONS CATALYSIS

A DISSERTATION

SUBMITTED TO THE GRADUATE FACULTY

in partial fulfillment of the requirements for the

Degree of

DOCTOR OF PHILOSOPHY

By

MATTHEW J. WULFERS
Norman, Oklahoma
2013

Downloaded from SHAREOK. Persistent Handle URL: https://hdl.handle.net/11244/318868

ZEOLITE-CATALYZED SURFACE CHEMISTRY IN ALKANE ISOMERIZATION AND METHANOL-TO-HYDROCARBONS CATALYSIS

A DISSERTATION APPROVED FOR THE
SCHOOL OF CHEMICAL, BIOLOGICAL AND MATERIALS ENGINEERING

BY

_____
Dr. Friederike C. Jentoft, Chair

_____
Dr. Rolf E. Jentoft

_____
Dr. Lance L. Lobban

_____
Dr. Daniel E. Resasco

_____
Dr. Kenneth M. Nicholas

© Copyright by MATTHEW J. WULFERS 2013
All Rights Reserved.

Acknowledgements

First and foremost, I would like to express the most sincere gratitude to my thesis advisor, Dr. Friederike Jentoft. She has selflessly given her time, thoughts, and resources to this project, all of which contributed to my learning the correct way to do rigorous scientific research. Her abundance of patience and a cheerful disposition have made her a pleasure to work with, and being her first PhD student at the University of Oklahoma has truly been a wonderful experience.

The other members of my committee, including Dr. Rolf Jentoft, Dr. Lance Lobban, Dr. Kenneth Nicholas, and Dr. Daniel Resasco, are also acknowledged, as are other faculty members and research scientists who provided input, namely Dr. Richard Mallinson, Dr. Steven Crossley, Dr. Roberto Galliasso, and Dr. Tawan Sooknoi. Many hours have been spent with Dr. Rolf Jentoft, either setting up for or planning experiments, or in discussion of interesting scientific, or non-scientific, topics. Dr. Resasco provided extremely valuable criticisms of my work during Friday group meetings, all of which pushed me to improve and polish my work.

When you work at a research institution for five years, many non-faculty also impact your work and your life. It has been a great pleasure to work with the graduate students and postdocs of the Jentoft group over the years, including Kassie Ngo, Chandramouli Vaddepalli, Dr. Zhimin Liu, Ali Mehdad, Kelsey Potter, and Alana Denning. Additionally, I appreciated the opportunity to work with two undergraduate students, Blake Myrick and Lauren Gilbert, on their honors research projects. The members of the larger “Biofuels” group are too numerous to name, but my development as a scientist benefitted greatly through my interactions with them. I was able to gain a

broader perspective of the heterogeneous catalysis scientific field than I otherwise might have through close observation of their research projects.

While doing science is interesting and fun, it can become quite cumbersome without having some fun outside the lab. Jimmy Brown was a fantastic companion in school-related, but more importantly in non school-related, matters. John Krais was a cohort in some of my fondest Oklahoma memories, those being our tornado-chasing escapades. Others who have had a particularly positive impact on my life outside the lab in Oklahoma include Amalia Botero, Cristina Caamaño, Jesús Campagna, Kyle Elam, Brandon Engebretson, Jeffrey Fontenot, and Joe Uzarski.

I would also like to acknowledge my parents, who have provided me with an excellent example of how to live a happy, meaningful, purpose-driven life, and have always provided me with exactly what I needed (or didn't need) to be successful. Finally, to my fiancé, Lacy, who has contributed as much as anybody to this project by keeping me emotionally stable, and whose meeting was reason enough to spend almost five years in Oklahoma.

Table of Contents

Acknowledgements ..... **iv**

Table of Contents ..... **vi**

List of Tables ..... **xi**

List of Figures ..... **xii**

Abstract ..... **xxi**

1 Introduction **1**

1.1 Outline 1
1.2 Alkane skeletal isomerization 1
1.2.1 Motivation 1
1.2.2 Industrial processes 4
1.2.3 Catalysts 7
1.2.3.1 H-mordenite 7
1.2.4 Skeletal isomerization chemistry 11
1.2.4.1 In mineral acids 13
1.2.4.2 On solid acids 15
1.2.4.3 Effect of olefins on butane isomerization 17
1.2.5 Formation of carbonaceous deposits 19

2 Scientific Problem and Strategy **26**

2.1 Scientific problem 26
2.2 Strategy – Analysis of *n*-butane reaction pathways 27
2.2.1 Kinetics 27
2.2.2 Carbon-13 labeled *n*-butane 29
2.3 Strategy – Identification of carbonaceous deposits 30
2.3.1 In situ spectroscopy 30
2.3.2 Solvent extraction 31

3 Materials and Methods **34**

3.1 Materials 34
3.2 Packed bed reactor 35
3.2.1 Apparatus 35
3.2.2 Catalytic measurements 37
3.2.3 Treatment of GC data 39
3.3 In situ spectroscopy 40
3.3.1 Spectrometers 40
3.3.2 Diffuse reflectance and in situ spectroscopic equipment 42
3.3.3 The Kubelka-Munk function 44

3.3.4 Photophysics of electronic spectra of unsaturated hydrocarbons 46

4 The Effect of Olefins or Co-adsorbates on Reaction Pathways of *n*-Butane on H-mordenite and Pt/H-mordenite 54

4.1 Introduction 54
4.2 Experimental 56
4.2.1 Experiments with an impure feed 56
4.2.1.1 Conversion of *n*-butane using a separate reactor to control the concentration of *n*-butenes in the feed 56
4.2.1.2 Conversion of *n*-butane while administering pulses of olefin or other co-adsorptives 57
4.2.2 Experiments with a pure feed 58
4.2.2.1 Measurement of product formation rates over a range of temperatures, *n*-butane partial pressures, and H_2 partial pressures 58
4.2.2.2 Measurement of product formation rates on Pt/H-mordenite using different space times 59
4.3 Results 60
4.3.1 Conversion of *n*-butane with olefins or co-adsorptives in the feed 60
4.3.1.1 Conversion of *n*-butane while co-feeding *n*-butene 60
4.3.1.2 Conversion of *n*-butane while administering pulses of propene, 1-butene, or 1-hexene 61
4.3.1.3 Conversion of *n*-butane while administering pulses of nitrobenzene or 1,3-bis(trifluoromethyl)benzene 63
4.3.2 Conversion of a pure *n*-butane feed 64
4.3.2.1 Catalyst stability 64
4.3.2.2 Product formation rates and selectivities over a range of reaction conditions 65
4.3.2.3 Evidence for equilibration of *n*-butane, *n*-butenes, and H_2 67
4.3.2.4 Conversion of *n*-butane over a range of space times 70
4.4 Discussion 71
4.4.1 Experiments with olefins or co-adsorptives in the feed 71
4.4.1.1 Effect of co-feeding *n*-butenes on product formation rates 71
4.4.1.2 Effect of olefin pulses on product formation rates 73
4.4.1.3 Effect of aromatic co-adsorbates on product formation rates 74
4.4.2 Experiments without olefin or co-adsorptives in the feed 75
4.4.2.1 Assessment of possible mass transport corruptions 75
4.4.2.2 Equilibration of *n*-butane, *n*-butenes, and H_2 on Pt/H-mordenite 77
4.4.2.3 Possible reaction pathways of *n*-butane and *n*-butene 79
4.4.2.4 Dependence of isomerization and disproportionation pathways on the olefin partial pressure 81
4.4.2.5 The apparent activation energy of isobutane formation 83
4.4.3 Linking experimental results with proposed reaction pathways 86

5 Conversion of 1,4-$^{13}C_2$-*n*-butane on H-mordenite and Pt/H-mordenite 98

5.1 Introduction 98
5.2 Experimental 99
5.2.1 Materials 99
5.2.2 Apparatus 100
5.2.3 Collection of data 100
5.2.4 Analysis of fragmentation patterns measured with online GC-MS 101
5.3 Results 104
5.3.1 Product formation rates and isotope distributions from conversion of a non-purified feed 104
5.3.2 Product formation rates and isotope distributions from conversion of a purified feed 108
5.4 Discussion 110
5.4.1 Isotope distribution in products formed from 1,4-$^{13}C_2$-*n*-butane 110
5.4.2 The effect of olefins on reaction pathways and isotope distributions 113
5.4.3 Implications for the skeletal isomerization mechanism 116
5.4.4 A unified model for interpreting the results from carbon-13 labeled butane conversion 118

6 Identification of Low Temperature Carbonaceous Deposits and Their Impact on Alkane Conversion 124

6.1 Introduction 124
6.2 Experimental 126
6.2.1 Materials 126
6.2.2 *n*-Butane and *n*-pentane conversion with in situ spectroscopic analysis 127
6.2.3 In situ spectroscopic analysis of adsorption and reaction of olefins 127
6.2.4 Adsorption of olefins with subsequent digestion and extraction 128
6.3 Results 129
6.3.1 In situ investigations of H-mordenite during alkane conversion 129
6.3.1.1 Catalyst activation 129
6.3.2 *n*-Butane conversion on H-mordenite: Catalytic performance and spectra collected in situ 130
6.3.3 *n*-Pentane conversion on H-mordenite: Catalytic performance and spectra collected in situ 133
6.3.4 Adsorption of reference compounds 135
6.3.4.1 Spectra collected in situ at temperatures below ≈ 550 K after adsorption of 1-butene, 1-pentene, or 1-hexene 135
6.3.5 In situ infrared spectra after adsorption of 1-pentene 137
6.3.6 Neutralization of cationic species 138
6.3.7 Extraction of deposits formed on H-mordenite 140
6.4 Discussion 141
6.4.1 Catalytic performance of H-mordenite in *n*-butane and *n*-pentane conversion 141

6.4.2 Interpretation of spectra and identification of deactivation-causing species 142

7 Identification of high temperature carbonaceous deposits formed on H-mordenite and Pt/H-mordenite and their impact on *n*-Butane Conversion 153

7.1 Experimental..... 153
7.1.1 Materials..... 153
7.1.2 N_2 physisorption..... 153
7.1.3 CO chemisorption 154
7.1.4 Temperature-programmed oxidation (TPO) 154
7.1.5 *n*-Butane conversion with in situ spectroscopic analysis: switching experiments 154
7.1.6 In situ spectroscopic analysis of adsorption and reaction of olefins 155
7.1.7 Adsorption of olefins with subsequent digestion and extraction 155
7.2 Results 156
7.2.1 Catalytic performance and spectra collected with H_2 in the feed 156
7.2.2 Catalytic performance and spectra collected when H_2 in the feed is replaced with helium 160
7.2.3 Catalytic performance and spectra collected after reintroducing H_2 to the feed 161
7.2.4 Diffuse reflectance infrared spectra recorded in situ during conversion of *n*-butane 164
7.2.5 Adsorption of reference compounds: 1-Butene and 1-pentene 165
7.2.6 Evolution of UV-vis spectra upon exposure to water vapor or ammonia 166
7.2.7 Extraction of carbonaceous deposits formed from 1-butene and 1-pentene 168
7.3 Discussion..... 170
7.3.1 H-mordenite: Impact of deposits on reaction pathways..... 170
7.3.2 Pt/H-mordenite: Impact of deposits on reaction pathways 173
7.3.3 Interpretation of UV-vis absorption bands..... 176
7.3.4 Surface species evolution and catalyst performance..... 181

8 Connecting gas phase product formation with growth of the hydrocarbon pool on H-ZSM-5 and H-beta during methanol conversion 187

8.1 Introduction 187
8.2 Experimental..... 193
8.2.1 Materials..... 193
8.2.2 Equipment 193
8.2.3 Reaction conditions for switching experiments using continuous flow of methanol 193
8.2.4 Reaction conditions for a methanol pulse 194

8.2.5 Adsorption and spectroscopic analysis of hexamethylbenzene and 1,2,3,4,5-pentamethylcyclopentadiene 194
8.3 Results 195
8.3.1 Products formed on H-ZSM-5 in continuous methanol flow 195
8.3.2 Diffuse reflectance UV-vis spectra recorded in situ during continuous flow of methanol on H-ZSM-5 196
8.3.3 Spectra collected and hydrocarbons detected while flushing H-ZSM-5 with inert gas after methanol conversion 198
8.3.4 Spectra collected and products formed while administering methanol pulses 200
8.3.5 Products formed during methanol conversion on H-beta 201
8.3.6 Diffuse reflectance UV-vis spectra recorded in situ during conversion of methanol on H-beta 203
8.3.7 Spectra collected and hydrocarbon products detected while flushing H-beta with inert gas after methanol conversion 204
8.3.8 Adsorption of hexamethylbenzene and 1,2,3,4,5-pentamethylcyclopentadiene 206
8.4 Discussion 208
8.4.1 Gas phase product formation 208
8.4.2 Background information for identification of electronic bands 211
8.4.3 Interpretation of UV-vis-NIR spectra taken during conversion of methanol on H-ZSM-5 215
8.4.4 Interpretation of UV-vis-NIR spectra taken during conversion of methanol on H-beta 218
8.4.5 Connecting spectroscopic and catalytic data 220

9 Recommendations 229

10 Appendix A: Diffuse reflectance UV-vis spectra of additional adsorbed reference compounds 231

List of Tables

Table 3.1: Properties of the H-mordenite and Pt/H-mordenite samples 34

Table 3.2: List of events that occur in the Lambda 950 UV-vis-NIR spectrometer during a scan 42

Table 4.1: Rates (μmol g^{-1} h^{-1}, top) and selectivities (mol %, in parentheses, bottom) of products formed at a temperature of 573 K on Pt/H-mordenite and H-mordenite with an *n*-butane partial pressure of 10 kPa and a H_2 partial pressure of 30-90 kPa. 66

Table 4.2: Value of Eqn. 6 over a range of reaction conditions 69

Table 4.3: Apparent reaction parameters for production of *n*-butenes on Pt/H-mordenite 70

Table 4.4: Apparent reaction orders with respect to *n*-butene on Pt/H-mordenite 83

Table 4.5: Apparent activation energies (kJ mol^{-1}) for isobutane formation on Pt/H-mordenite. The change in *n*-butene concentration with temperature was accounted for by using Eqn. 16. 84

Table 5.1: Normalized intensity of fragments measured in the GC-MS for propane, isobutane, *n*-pentane, and isopentane at natural isotopic abundance of carbon 102

Table 5.2: Contributions of isobutane species (at natural abundance of carbon) with zero and one carbon-13 isotope to the GC-MS signal..... 104

Table 5.3: Ratios of the molecular ion (M^+) signal to the signals at lower masses for propane, isobutane, *n*-pentane, and isopentane..... 104

Table 5.4: Product formation rates (μmol g^{-1} h^{-1}) from conversion of 1,4-$^{13}C_2$-*n*-butane on H-mordenite (M1) and Pt/H-mordenite (Pt/M-C1)..... 105

Table 5.5: Product selectivities (mol %) from conversion of 1,4-$^{13}C_2$-*n*-butane on H-mordenite (M1) and Pt/H-mordenite (Pt/M-C1). 105

Table 5.6: Percent of 1,4-$^{13}C_2$-*n*-butane with internally scrambled carbon-13 atoms after conversion on H-mordenite or Pt/H-mordenite. 105

Table 5.7: Isotope distributions in products produced from 1,4-$^{13}C_2$-*n*-butane. 108

Table 7.1: Properties of Pt/H-mordenite measured before and after 20 h reaction with *n*-butane 174

List of Figures

Figure 1.1: Thermodynamic gas phase equilibrium composition of *n*-butane and isobutane (left), and *n*-pentane and 2-methylbutane (right), as a function of temperature. The temperature dependence of the enthalpy of reaction was neglected. Thermodynamic data is from [12]..... 4

Figure 1.2: The "plumbing system" of mordenite [29]. 8MRb: 8-membered ring parallel to b direction; 8MRc: 8-membered ring parallel to c direction; 12MRc: 12 membered ring parallel to c direction..... 9

Figure 1.3: The intramolecular acid-catalyzed skeletal isomerization pathway of *n*-pentane. 12

Figure 1.4: Rearrangements of cationic species relevant to conversion of: a) *n*-pentane to isopentane, b) 1-^{13}C-*n*-butane to 2-^{13}C-*n*-butane, and c) 1-^{13}C-*n*-butane to 1-^{13}C-isobutane..... 13

Figure 1.5: Intramolecular reaction pathway proposed by Boronat et al. for butene skeletal isomerization on a zeolite. Adapted from [62]. 17

Figure 2.1: Basic intramolecular rate equation for A → B with the surface reaction as the rate-limiting step..... 28

Figure 2.2: Rate equation for an intermolecular 2A → C + D reaction involving Langmuir adsorption, Eley-Rideal bond formation, and bond breaking as the rate-limiting step..... 28

Figure 2.3: Expected number of isotopes and their distribution in isobutane produced via intramolecular and intermolecular skeletal isomerization pathways of 1,4-$^{13}C_2$-*n*-butane. 30

Figure 3.1: A schematic of the gas manifold..... 36

Figure 3.2: A picture of the furnace used to heat the packed bed apparatus. 38

Figure 3.3: Temperature profile of furnace shown in Fig. 3.2, with a set point of 673 K, as measured from the top (black) or bottom (red) of the furnace. 38

Figure 3.4: A picture of the HVC-VUV environmental chamber hooked up to gas lines and placed in the DRP-P72 Praying Mantis accessory (left), and a zoomed-in picture of the HVC-VUV environmental chamber (right). 43

Figure 3.5: Diffuse reflectance UV-vis spectra of $CuSO_4 \cdot 5H_2O$, Na-mordenite, and mixtures thereof. Blue line: ground $CuSO_4 \cdot 5H_2O$; black line: Na-mordenite powder; red line: ground $CuSO_4 \cdot 5H_2O$ covered by Na-mordenite powder (situation 1); green line: ground $CuSO_4 \cdot 5H_2O$ on top of Na-mordenite powder (situation 2)..... 45

Figure 3.6: Representation of the π molecular orbitals of benzene. 49

Figure 3.7: Ultraviolet-visible spectrum of anthracene in hexane 50

Figure 4.1: The concentration of gas phase products resulting from conversion of *n*-butane (10 kPa partial pressure) on H-mordenite (M1) at a temperature of 473 K using 50 kPa H_2 and 40 kPa helium as diluents. The concentration of *n*-butenes in the feed was 0 ppm during the first 75 minutes on stream and 18 ppm after 75 minutes on stream. 60

Figure 4.2: Concentration of gas phase products produced from conversion of *n*-butane (10 kPa partial pressure) on H-mordenite (M1) at a temperature of 473 K with 30 µL gas pulses of 1-butene and propene, and a 0.5 µL liquid pulse of 1,3-bis(trifluoromethyl)benzene. 62

Figure 4.3: Concentration of gas phase products produced from conversion of *n*-butane (10 kPa partial pressure) on H-mordenite (M2) at a temperature of 473 K with three consecutive 1 µL liquid injections of 1-hexene. 62

Figure 4.4: Concentration of gas phase products produced from conversion of *n*-butane (10 kPa partial pressure) on H-mordenite (M2) at a temperature of 473 K before (first 50 min) and after (after the first 50 min) a 1 µL injection of nitrobenzene (m/z = 123). 63

Figure 4.5: Rates of formation of the main gas phase products produced during conversion of *n*-butane (10 kPa partial pressure) on Pt/H-mordenite (Pt/M-C1, W/F = 0.17 h) as a function of time on stream. Other conditions: 30 ml min^{-1} total flow rate, 50 kPa H_2 partial pressure, and 40 kPa helium partial pressure. The temperature was increased from 543 K to 583 K in 10 K increments and then lowered to 543 K. 65

Figure 4.6: Selectivities of isobutane (upper part of graph) or pentanes (lower part of graph) on Pt/H-mordenite with respect to conversion. Changes in conversion were caused by changes in reaction parameters. An increase in conversion resulted from increasing the temperature (blue squares: Pt/M-C1, 543-583 K, 10 kPa *n*-butane, 50 kPa H_2, W/F = 0.17 h), increasing the *n*-butane partial pressure (purple diamonds: Pt/M-C1, 573 K, 3.3-13.3 kPa *n*-butane, 50 kPa H_2, W/F = 0.13-0.51 h), decreasing the H_2 partial pressure (red circles: Pt/M-C1, 573 K, 10 kPa *n*-butane, 30-90 kPa H_2, W/F = 0.17 h), or increasing the space time (green triangles: Pt/M-C2, 573 K, 10 kPa *n*-butane, 50 kPa H_2, W/F = 0.13-1.29 h). The dotted lines are intended to show trends and are not the result of a fit. 67

Figure 4.7: Measured concentrations and calculated equilibrium concentrations of *trans*-2-butene at a temperature of 563 K over the range of *n*-butane and H_2 partial pressures. Solid circles: measured on Pt/H-mordenite. Open squares: measured on H-mordenite. Lines: calculated equilibrium concentrations using the software package Thermosolver (v. 1.0). 69

Figure 4.8: Concentration of the main gas phase products produced from conversion of *n*-butane on Pt/H-mordenite (Pt/M-C2) at a temperature of 573 K. Other conditions: 50 ml min^{-1} total flow, 50 kPa H_2, 40 kPa helium, W/F = 0.13-1.29. 71

Figure 4.9: Possible reaction pathways of *n*-butane on H-mordenite. Yellow highlights indicate possible areas for participation of olefins. 80

Figure 4.10: The rates of isobutane (a) and pentanes (b) formation at a temperature of 563 K on Pt/H-mordenite (Pt/M-C1) are plotted as a function of the butene concentration measured in the reactor effluent. The dotted lines are not the result of a fit and are intended to guide the reader's eye. 82

Figure 4.11: The catalytic cycle for intramolecular skeletal isomerization of *n*-butane. 88

Figure 4.12: A kinetic description of the intermolecular skeletal isomerization pathway assuming that beta-scission (Step 5) is the rate-limiting step. 89

Figure 4.13: Dimerization products formed by reaction of a *sec*-butyl carbenium ion with a gas phase *n*-butene molecule. 91

Figure 4.14: Beta-scission reactions of C8 skeletal isomers that produce either propene, isobutene, or a C5 olefin as a gas phase product. 93

Figure 5.1: The mass spectrum of isobutane, at natural abundance of carbon, from m/z = 45 to m/z = 60. 102

Figure 5.2: Isotope distributions in products produced from 1,4-$^{13}C_2$-*n*-butane on H-mordenite with (HM-T) and without (HM) an olefin trap. 107

Figure 6.1: Diffuse reflectance NIR spectra of H-mordenite (M1) recorded during activation. Initial spectrum: black line, during heating to 673 K in a flow of synthetic air: blue lines, and after further treatment in N_2 and H_2 at 673 K and cooling to 623 K: red line. 129

Figure 6.2: Rates of formation of gas phase products during conversion of *n*-butane (10 kPa partial pressure) on H-mordenite (M1, W/F = 0.16 h) at a reaction temperature of 563 K using either H_2 (first 1.5 h) or helium (after 1.5 h) as the diluent. The Kubelka-Munk value at 292 nm is plotted on the right axis. The corresponding UV–vis spectra are shown in Fig. 6.3. 131

Figure 6.3: Evolution of diffuse reflectance UV–vis spectra recorded in situ during conversion of *n*-butane (10 kPa partial pressure) on H-mordenite (M1, W/F = 0.16 h) at a reaction temperature of 563 K. The corresponding gas phase products are shown in Fig. 6.2. Black line: pretreated catalyst; red line (superimposed on black line): last spectrum in *n*-butane/H_2; blue lines: in *n*-butane/helium. 132

Figure 6.4: DRIFT spectra recorded during in situ conversion of *n*-butane (10 kPa partial pressure) on H-mordenite (M1) in helium (90 kPa partial pressure) at a reaction temperature of 563 K. Black line: pretreated catalyst. Red line: spectrum taken 20 min after admission of *n*-butane. Blue line: subtraction of the red line from the black line. 133

Figure 6.5: Rates of formation of the gas phase products during conversion of *n*-pentane (13 kPa partial pressure) on H-mordenite (M1, W/F = 0.08 h) at 453 K using helium as the diluent. The Kubelka-Munk value at 295 nm is plotted on the right axis. The corresponding UV–vis spectra are shown in Fig. 6.6. 134

Figure 6.6: Evolution of diffuse reflectance UV–vis spectra recorded in situ during conversion of *n*-pentane (13 kPa partial pressure) on H-mordenite (M1, W/F = 0.08 h) at a reaction temperature of 453 K using helium as the diluent. Black line: pretreated catalyst; blue lines: in *n*-pentane/helium. 134

Figure 6.7: Diffuse reflectance UV-vis spectra of H-mordenite (M1) recorded in situ during exposure to a 30 µL gas pulse of 1-butene at 303 K (red line). The in situ cell was held at 303 K for 5 h (blue lines) and then heated at 2 K min^{-1} to 483 K in 30 ml min^{-1} N_2 (green lines). Pretreatment was at 673 K with subsequent treatments of synthetic air, N_2, and H_2. 135

Figure 6.8: Diffuse reflectance UV–vis spectra of H-mordenite (M1) recorded in situ during exposure to 1-pentene at a temperature of 303 K. Five µL of 1-pentene vapor was taken from the headspace above 1-pentene liquid and then injected. The in situ cell was held at 303 K for 2 h (blue lines) and then heated at 2 K min^{-1} to 523 K (green lines). Spectra were collected in 10 minute intervals. Pretreatment was at 673 K in N_2. 136

Figure 6.9: Diffuse reflectance UV–vis spectra of H-mordenite (M1) recorded in situ during exposure to 1 µL of 1-hexene liquid at a temperature of 303 K (red line). The cell was held at 303 K for 30 minutes (blue lines) and then heated at 10 K min^{-1} to 573 K (green lines). Pretreatment was performed at 673 K with sequential 30 minute treatments in synthetic air, N_2, and H_2. 137

Figure 6.10: Diffuse reflectance infrared spectra of a physical mixture of H-mordenite (M1) and KBr (1:2 mass ratio) recorded in situ before (pretreated, black line) and after (red line) introduction of 0.2 µL 1-pentene (injected as liquid) with the chamber at a temperature of 453 K. The blue line is a subtraction of the black line from the red line. The resolution is 2 cm^{-1}. The zeolite was pretreated at 573 K in N_2. 138

Figure 6.11: Diffuse reflectance UV–vis spectra of H-mordenite (M2) recorded in situ after exposure to 0.1 µL of 1-pentene (injected as liquid) at a temperature of 373 K (blue line) and after application of water vapor at 303 K (purple lines). Spectra were taken in 10 minute intervals. Pretreatment was performed at 673 K in 30 ml min^{-1} N_2. 139

Figure 6.12: Diffuse reflectance UV–vis spectra of H-mordenite (M2) recorded in situ during exposure to 3 µL 1-pentene (injected as liquid) at a sample temperature of 373 K (red line) and subsequent application of ammonia at 303 K (blue line). Pretreatment was at 673 K in N_2. 139

Figure 6.13: GC-MS chromatogram of the dichloromethane extract collected from H-mordenite (M2) after exposure to 1-butene at a temperature of 323 K and digestion in hydrofluoric acid. The retention times of several reference compounds are provided. The UV–vis spectrum of the dichloromethane extract is shown in Fig. 6.14. The red X indicates known *cis*- and *trans*- decalin impurities leached from the polyethylene vials. 140

Figure 6.14: Diffuse reflectance UV–vis spectrum of H-mordenite (M2) after exposure to 1-butene at a temperature 323 K and transfer under ambient conditions (blue line) and transmission UV–vis spectrum the dichloromethane extract (red line) collected after digestion of the zeolite in hydrofluoric acid. The GC-MS chromatogram of the dichloromethane extract is shown in Fig. 6.13. 141

Figure 7.1: Rates of formation of various products of *n*-butane conversion on H-mordenite, (a) major products and (b) minor products. Pressure 101 kPa; total feed flow 30 ml min^{-1}; 10% *n*-butane mixed with 90% H_2 or helium (from 3 to 6 h on stream); temperature of in situ cell ≈623 K. 157

Figure 7.2: Rates of formation of various products of *n*-butane conversion on Pt/H-mordenite, (a) major products and (b) minor products. Pressure 101 kPa; total feed flow 30 ml min^{-1}; 10% *n*-butane mixed with 90% H_2 or helium (from 3 to 6 h on stream); temperature of in situ cell ≈623 K. 158

Figure 7.3: Diffuse reflectance UV–vis spectra of (a) H-mordenite and (b) Pt/H-mordenite recorded during *n*-butane conversion. Pressure 101 kPa; total feed flow 30 ml min^{-1}; 10% *n*-butane mixed with 90% H_2 or helium; temperature of in situ cell ≈623 K. Spectra originate from the same experiments as catalytic data in Figs. 7.1 and 7.2. Black line: activated catalyst; red line: last spectrum in *n*-butane/H_2 (3 h on stream); blue lines: in *n*-butane/He. Numbers indicate wavelength positions of vertical lines. 159

Figure 7.4: Diffuse reflectance UV–vis spectra of (a) H-mordenite and (b) Pt/H-mordenite recorded during *n*-butane conversion. Pressure 0.1 MPa; total feed flow 30 ml/min; 10% *n*-butane mixed with 90% H_2 or helium; temperature of in situ cell ≈623 K. Spectra originate from the same experiments as catalytic data in Figs. 7.1 and 7.2. Black dashed line: activated catalyst; red line: last spectrum in *n*-butane/He (3 h on stream); blue lines: in *n*-butane/H_2. Numbers indicate wavelength positions of vertical lines. 162

Figure 7.5: Evolution of various bands in the UV–vis spectra shown in Figs. 7.3 and 7.4 with time on stream. (a) H-mordenite and (b) Pt/H-mordenite. 163

Figure 7.6: Evolution of diffuse reflectance infrared spectra recorded in situ during conversion of *n*-butane (10 kPa partial pressure) on H-mordenite (M1, W/F = 0.13 h) at a reaction temperature of 633 K using helium as the diluent. Black line: pretreated catalyst; green lines: during conversion of *n*-butane. The time interval between spectra is 20 minutes. The resolution is 4 cm^{-1}. 164

Figure 7.7: Diffuse reflectance UV–vis spectra of H-mordenite after exposure to a pulse of 1-butene at 303 K and subsequent heating to 673 K. The spectra below a temperature of 483 K are the same as those reported in Fig. 6.7. Numbers indicate wavelength positions of vertical lines. Inset shows a zoom. 165

Figure 7.8: Diffuse reflectance UV–vis spectra of H-mordenite after exposure to a pulse of 1-pentene at 303 K and subsequent heating to 673 K. The spectra at and below a temperature of 523 K are the same as those reported in Fig. 6.8. Numbers indicate wavelength positions of vertical lines. Inset shows a zoom. 166

Figure 7.9: Diffuse reflectance UV–vis spectra of pretreated, spent, humidified, and re-heated catalyst. *n*-Butane (10 kPa partial pressure) conversion was performed on H-mordenite (M1) for 2 h at a reaction temperature of 636 K using helium as the diluent. The *n*-butane was then removed from the gas stream and the chamber was cooled to 303 K. The gas flow was then switched to 5 ml min^{-1} N_2 saturated with water vapor. After exposure to water vapor for 2.5 h, the catalyst was re-heated to 573 K in a stream of pure N_2. Black line: pretreated catalyst; red line: last spectrum during conversion of *n*-butane; blue line: after 2.5 h exposure to water vapor; purple line: re-heated after exposure to water vapor. 167

Figure 7.10: Diffuse reflectance UV–vis spectra of H-mordenite (M1) after exposure to a pulse of 1-pentene at 303 K and subsequent heating to 673 K. After heating to 673 K, the cell was cooled to 303 K and ammonia was admitted. The spectra have been normalized to account for reflectance values higher than the reflectance standard. Black line: pretreated zeolite; maroon line: cooled to 303 K after heating to 673 K; turquoise line: exposed to ammonia. 168

Figure 7.11: GC-MS chromatogram of the dichloromethane extract collected from H-mordenite (M2) after exposure to 1-butene at a temperature of 573 K and digestion in hydrofluoric acid. The UV-vis spectrum of the dichloromethane extract is shown in Fig. 7.12. The red X indicate known *cis*- and *trans*- decalin impurities leached from the polyethylene vials. 169

Figure 7.12: UV–vis spectra of spent catalyst and extract. H-mordenite (M2) was activated in an isothermal reactor, exposed to 1-butene at a temperature of 323 K, heated to 573 K, and held for 1 h. The two spectra represent the solid, ambient-exposed H-mordenite before digestion (blue line, Kubelka–Munk scale) and the dichloromethane extract obtained after digestion (red line, absorbance scale). 170

Figure 7.13: Gas phase equilibrium constants for the hydrogenation of ethene, propene and trans-2-butene, to their respective alkanes, as calculated by the software package Thermosolver v. 1.0. 171

Figure 8.1: A proposed reaction pathway in methanol-to-hydrocarbons catalysis involving cleavage of alkyl side-chains by the paring mechanism. Stars (*) denote carbon-13 labels. Reprinted from Journal of Catalysis, 221, M. Bjørgen, U. Olsbye, D. Petersen, S. Kolboe, The methanol-to-hydrocarbons reaction: insight into the reaction mechanism from [^{12}C]benzene and [^{13}C]methanol coreactions over zeolite H-beta, 1-10, Copyright (2004), with permission from Elsevier [27]. 191

Figure 8.2: Rates of formation of the main gas phase products formed during conversion of methanol (10 kPa partial pressure) on H-ZSM-5 (W/F = 0.14 h) at a reaction temperature 573 K. The corresponding UV-vis spectra during the first 3 h are shown in Fig. 8.3. 196

Figure 8.3: Evolution of diffuse reflectance UV-vis spectra recorded in situ during conversion of methanol (10 kPa partial pressure) on H-ZSM-5 (W/F = 0.14 h) at a reaction temperature of 573 K. The corresponding gas phase products are shown in Fig. 8.2. Purple line: pretreated catalyst; black lines: in methanol flow; blue line: after 63 min in methanol flow; green line: after 3 h in methanol flow. 197

Figure 8.4: Evolution of diffuse reflectance UV-vis spectra recorded in situ after conversion of methanol on H-ZSM-5. The temperature remained at 573 K and the flow rate of N_2 was 30 ml min^{-1}. The spectra correspond to the period of 3-6 h on stream in Figs. 8.2 and 8.15. Purple line: pretreated catalyst; green line: last spectrum in methanol flow (same as in Fig. 8.3); orange line: first spectrum during flush; black lines: during flush; red line: after 1 h of flushing; pink line: after 3 h of flushing. 198

Figure 8.5: Evolution of selected products (determined by the m/z ratio) while flushing H-ZSM-5 with N_2 after conversion of methanol (10 kPa partial pressure) at 573 K. 199

Figure 8.6: Evolution of gas phase products produced on H-ZSM-5 after a 0.5 µl pulse of methanol was administered at a temperature of 623 K. The corresponding UV-vis spectra are shown in Fig. 8.7. 200

Figure 8.7: Diffuse reflectance UV-vis spectra of H-ZSM-5 taken after administering a 1 µl pulse of methanol at a temperature of 623 K. Gas phase products produced from the pulse are shown in Fig. 8.6. 201

Figure 8.8: Rates of formation of the main gas phase products formed during conversion of methanol (10 kPa partial pressure) on H-beta (W/F = 0.14 h) at a reaction temperature of 548 K. The corresponding UV-vis spectra during the first 2 h are shown in Fig. 8.9. 202

Figure 8.9: Evolution of diffuse reflectance UV-vis spectra recorded in situ during conversion of methanol (10 kPa partial pressure) on H-beta (W/F = 0.14 h) at a reaction temperature of 548 K. The corresponding gas phase products are shown in Fig. 8.8. Purple line: pretreated catalyst; blue line: after 7 min in methanol flow; black lines: in methanol flow; green line: after 2 h in methanol flow. 204

Figure 8.10: Evolution of diffuse reflectance UV-vis spectra recorded in situ after conversion of methanol on H-beta. The temperature remained at 548 K and the flow rate of N_2 was 30 ml min^{-1}. The spectra correspond to the period of 2-4 h on stream in Figs. 8.8 and 8.16. Purple line: pretreated catalyst; green line: last spectrum in methanol flow (same as in Fig. 8.9); orange line: first spectrum during purge; black lines: during purge; pink line: after 2 h purge. 205

Figure 8.11: Evolution of selected products (determined by the m/z ratio) while flushing H-beta with N_2 after conversion of methanol (10 kPa partial pressure) at a temperature of 548 K. 206

Figure 8.12: UV-vis spectra of hexamethylbenzene adsorbed on H-beta (top) and in sulfuric acid (bottom). Green line: on H-beta at room temperature; blue line: on H-beta at 473 K; purple line: in cyclohexane; orange line: in sulfuric acid. 207

Figure 8.13: UV-vis spectra of 1,2,3,4,5-pentamethylcyclopentadiene on H-mordenite at 323 K (blue line) or in cyclohexane (purple line) or sulfuric acid (orange line)..... 208

Figure 8.14: Reported wavelengths of absorption for protonated single ring methylated aromatic species in mineral acids [38,55,59-61] or on solid acids [39,62]. 214

Figure 8.15: Evolution of various bands in the UV-vis spectra of H-ZSM-5 shown in Figs. 8.3 and 8.4, and the ion current at selected m/z ratios monitored with an online MS. 221

Figure 8.16: Evolution of various bands in the UV-vis spectra of H-beta shown in Figs. 8.9 and 8.10, and the ion current at selected m/z ratios monitored with an online MS..... 221

Figure 10.1: Adsorption of 1,4-pentadiene (Aldrich, 99%) on H-mordenite (M2). Pretreatment was at 673 K in 40 ml min^{-1} N_2. The cell was cooled to 303 K and 5 µL of headspace above 1,4-pentadiene liquid was injected. After 30 min, the cell was heated at 5 K min^{-1}. 231

Figure 10.2: Adsorption of 1-methylcyclopentene on H-mordenite (M2). Pretreatment was at a temperature of 573 K in a flow of 30 ml min^{-1} N_2 (black line). Initial adsorption of 0.2 µl 1-methylcyclopentene occurred at 303 K (red line). After 80 min, the chamber was heated at 2 K min^{-1} to 673 K (green line).

The chamber was then cooled to 303 K and water vapor was admitted (blue line). 232

Figure 10.3: Adsorption of 1-methylnaphthalene on H-mordenite (M2). Pretreatment was at a temperature of 673 K in synthetic air. The chamber was then cooled to 303 K in N_2 (black line) and 1 µl of 1-methylnaphthalene was admitted to the chamber (red line). The chamber was then heated at 5 K min^{-1} to 673 K (green line). 233

Figure 10.4: Adsorption of biphenyl on H-mordenite (M1) was performed by placing both on separate watchglasses in an evacuated desiccator. The biphenyl-containing H-mordenite was then placed in the chamber and heated at 5 K min^{-1} in a 30 ml min^{-1} flow of N_2. The temperature range over which a scan was taken during heating is given in the legend. 234

Figure 10.5: Adsorption of cyclohexene on H-mordenite (M2). Pretreatment was at 673 K in 30 ml min^{-1} N_2. The cell was then cooled to 303 K (black line) and 1 µl of cyclohexene liquid was injected. After 60 min at 303 K (red line), the chamber was heated at 5 K min^{-1} to 673 K. Blue line: taken between 250 K and 300 K; green line: taken after 2 h at 673 K. 235

Abstract

Zeolite catalysts are eminently vital to production of liquid transportation fuels and commodity chemicals. In each particular application, the surface reactions catalyzed by the zeolite determine its productivity. It is a fundamental understanding of these surface reactions that are the main focus of this thesis.

In the case of butane isomerization, the zeolite H-mordenite has been at the center of much controversy. Heavily debated are the relative contributions of intramolecular and intermolecular skeletal isomerization reaction pathways. In this thesis, it is shown that butenes facilitate both pathways, but that intermolecular pathways have a greater dependence on the butene partial pressure. Thus, when the butene partial pressure is kept low an intramolecular skeletal isomerization pathway dominates. When the butene partial pressure is high, either through in situ formation of butenes or through addition of butenes to the feed, an intermolecular skeletal isomerization pathway dominates.

Solid acids, in general, are plagued by a tendency to form carbonaceous deposits during alkane conversion. Platinum and H_2 are effective at preventing formation of the deposits, but the deposits themselves are usually not well characterized. In this thesis, diffuse reflectance UV-vis-NIR (Ultraviolet-visible-near infrared) spectroscopy and Diffuse Reflectance Infrared Fourier Transform Spectroscopy (DRIFTS) performed in situ are used to show that alkyl-substituted cyclopentenyl cations are formed during conversion of *n*-butane or *n*-pentane at industrially relevant reaction temperatures (453-563 K). The corresponding olefins are shown to be precursors of the carbonaceous deposits. At higher reaction temperatures (563-653 K), methyl-substituted acenes are

formed. An effective strategy combining in situ spectroscopy and extractions of spent catalysts to identify the deposits is demonstrated.

Finally, diffuse reflectance UV-vis-NIR spectroscopy performed in situ is used to characterize the "hydrocarbon pool" on working methanol-to-hydrocarbons (MTH) catalysts. Alkyl-substituted cyclopentenyl cations are again detected, but this time are found to be important reaction intermediates. While the hydrocarbon pool on zeolites such as H-ZSM-5 and H-beta is generally thought of as being aromatic in nature, our analysis indicates that cyclopentenyl species also play a critical role in the reaction chemistry.

1 Introduction

1.1 Outline

The thesis is structured as follows: various aspects of alkane skeletal isomerization are the topics of Chapters 1, 2, and 4-7, while conversion of methanol to hydrocarbons is the topic of Chapter 8. Chapter 1 delivers background information about acid-catalyzed skeletal isomerization of alkanes. Chapter 2 describes the open scientific questions relating to alkane skeletal isomerization and the strategy used to perform the investigation. Chapter 3 describes the catalysts and the main pieces of equipment. Chapters 4 and 5 cover mechanistic information that was gathered while operating the alkane isomerization catalysts under non-deactivating conditions. Chapters 6 and 7 cover information about the carbonaceous deposits formed during deactivation. Chapter 8 provides a brief introduction to methanol-to-hydrocarbons catalysis and reports complementary spectroscopic and kinetic data connecting the chemical composition of the "hydrocarbon pool" to gas phase product formation.

1.2 Alkane skeletal isomerization

1.2.1 Motivation

Branched alkanes are used to make a variety of important consumer products. Isobutane is used in production of gasoline [1] and has other niche uses as a propellant and as a chlorine-free refrigerant [2]. Isobutene, which can be produced easily from isobutane, is used in production of methyl and ethyl *tert*-butyl ethers (MTBE and ETBE) [3] and synthetic rubber [4]. MTBE is used worldwide, with the exception of the

United States, as a high-octane gasoline additive. The branched isomers of pentane and hexane are used as high-octane blending components for gasoline [5].

Transportation fuels require the largest quantities of branched alkanes and are, therefore, worthy of further discussion. As of 2012, refineries in the United States had an isobutane production capacity of 191,467 barrels per stream day (BPSD) [6]. In the United States, the main use of isobutane is for alkylation. Refineries require a unit devoted to transformation of *n*-butane to isobutane only if the supply of isobutane from other sources does not satisfy the requirements of the alkylation plant. This can happen in refineries that have an alkylation plant and a fluidized catalytic cracker (FCC), but usually not in those that have a hydrocracker [7]. Outside of the United States, refineries also use isobutane for synthesis of MTBE via isobutene and methanol. The global demand for MTBE in 2011 was 12.1 million tons [8].

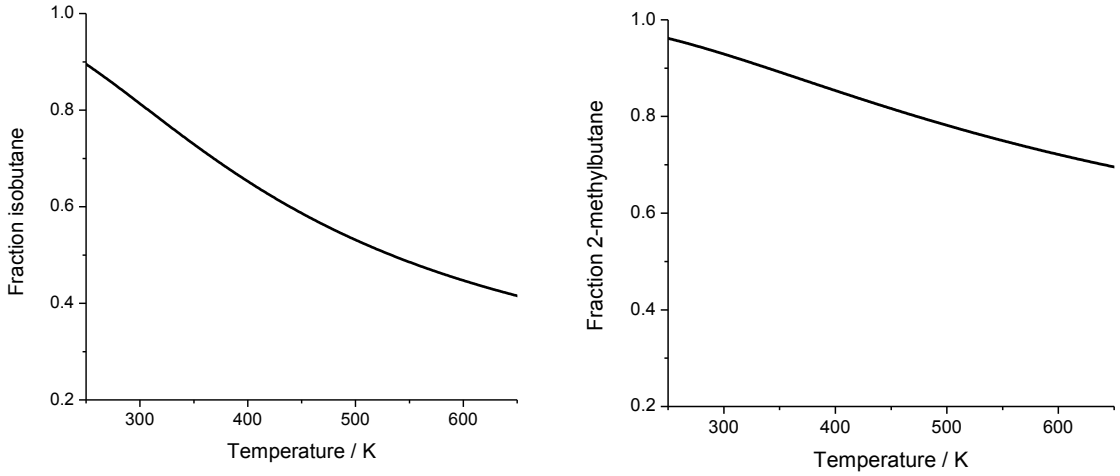
Although pure *n*-pentane and *n*-hexane have unimpressive motor octane numbers (MON) of 62 and 26 [9], respectively, their favorable response to lead allowed them to be blended into gasoline for many years. However, as the United States Environmental Protection Agency (EPA) has incrementally lowered the allowed concentration of lead in gasoline over the past 40 years, it has gradually been removed. Consequently, conversion of *n*-pentane and *n*-hexane to their higher octane, branched skeletal isomers has become imperative. To illustrate, the isopentane/isohexane production capacity of United States refineries was only 145,200 BPSD in 1985 [6]. On January 1, 1986, EPA regulations were implemented that lowered the maximum allowed lead in gasoline from 1.10 g to 0.10 g per leaded gallon [10] and, as a result, the

isopentane/isohexane production capacity of United States refineries increased to 397,415 BPSD by 1988 [6].

The current refining infrastructure allows for large quantities of *n*-alkanes to be transformed to isoalkanes. Solid acids are used to catalyze the transformation. Although they have been widely implemented, the solid acids also catalyze reactions that lead to formation of carbonaceous deposits on the catalyst surface that cause deactivation. Addition of platinum to the catalyst and H_2 to the feed has been found to effectively slow formation of the deposits, but requires an expensive noble metal and valuable H_2 to be used [1]. Some catalysts require an organic chloride to be co-fed, which necessitates pretreatment of feed streams and cleanup of product streams [11]. The additional catalyst and process requirements have provided motivation for development of a replacement catalyst for many years. However, the replacement candidates have proven to be inferior to the currently used catalysts for a number of reasons, including i) low selectivity to the desired products, ii) rapid deactivation, iii) or high temperature requirements.

Formation of branched isomers is thermodynamically favored at low temperatures. Thus, a strong acid must be used. The thermodynamic equilibrium between *n*-butane and isobutane, and between *n*-pentane and 2-methylbutane, is shown in Fig. 1.1 over a range of temperatures. Addition of a noble metal active for hydrogenation/dehydrogenation to the catalyst can enable a classical dual-functional reaction pathway in which the alkane is dehydrogenated on a metal, the olefin is isomerized on an acid site, and the olefin product is re-hydrogenated on a metal. The catalysts are called dual-functional because they contain two types of active sites, in this

case Brønsted acid and metal sites, with only one being implicated in the rate-limiting step. The presence of olefins can also cause undesired reactions such as oligomerization and disproportionation to occur.



$\Delta_r G° = -3.7$ kJ mol^{-1}
$\Delta_r H° = -8.4$ kJ mol^{-1}

$\Delta_r G° = -6.4$ kJ mol^{-1}
$\Delta_r H° = -8.1$ kJ mol^{-1}

Figure 1.1: Thermodynamic gas phase equilibrium composition of *n*-butane and isobutane (left), and *n*-pentane and 2-methylbutane (right), as a function of temperature. The temperature dependence of the enthalpy of reaction was neglected. Thermodynamic data is from [12].

Considering the abundance of reports in the literature, it is obvious that a suitable replacement catalyst will not be discovered serendipitously and must instead be rationally designed. Such design requires an intimate knowledge of the surface reactions leading to formation of both gas phase products and deactivation-causing surface species. An understanding of the relevant chemistry is at the heart of this thesis.

1.2.2 Industrial processes

Although the first scientific paper on skeletal isomerization of individual paraffinic hydrocarbons was published in the scientific literature in 1933 [9], the

reaction was not performed industrially until 1941 [13]. At that time the technology was still in its infancy, but had been developed to the point where it could be "quickly brought to full scale operation when the situation warranted" [9]. The situation presented itself during World War II, when the United States and other allied countries used the alkylation process to produce aviation fuel. Production was limited by the supply of isobutane and, at the end of the War, 38 *n*-butane isomerization units were operating in the United States and 5 were operating in other allied countries [11].

The first butane isomerization unit began production at one of Shell's Houston area refineries in November 1941 using Shell's Isocel technology [9]. The essential features are that it was a vapor phase, fixed bed process that used $AlCl_3$ on bauxite as the catalyst. Dried butane was mixed with anhydrous hydrochloric acid at the top of the reactor and passed through the catalyst bed at a temperature of 362-422 K and a total pressure of 1.4 MPa. A guard column of bauxite was used to recover $AlCl_3$ that eluted from the reactor with the hydrocarbon, and the hydrochloric acid was removed by passing the product stream through both a stripper tower and caustic wash. Because water was rigorously removed from the feed streams, corrosion was only a minor problem, and cheaper carbon steel could be used as the reactor material [9].

Three liquid phase isomerization processes were also developed and used during the War. Molten $HCl/AlCl_3$ was used as the catalyst, and in some cases $SbCl_3$ was added. In the liquid phase units, corrosion was a problem, and corrosion-resistant materials had to be used in the reactor lining and other pieces of equipment [9]. In general, both vapor and liquid phase units were marred by serious problems such as

plugging of catalyst beds and equipment, high catalyst consumption, and corrosion, and were very costly to operate [11]. Most units were shut down after the War [9].

A paradigm shift in isomerization technology occurred with the introduction of heterogeneous, dual-functional catalysts. UOP's Butamer process is one of the most successful isomerization technologies that uses a dual-functional catalyst. First implemented in a refinery on the United States' West Coast in 1959 [11], the Butamer process operates using a fixed bed, vapor phase reactor with a Pt/chlorided alumina catalyst. The catalyst is very sensitive to common contaminants such as water and sulfur [1]. As a consequence, both hydrocarbon and H_2 streams must be rigorously dried before entering the reactor. The hydrocarbon feed must also be put through a hydrodesulfurization (HDS) unit, and an additional sulfur guard is necessary [1]. To maintain the acidity, an organic chloride source must be co-fed, requiring that the product stream be scrubbed with caustic solution to remove HCl produced in the reactor [13]. H_2 is also co-fed and works in conjunction with platinum to prevent deactivation. In earlier units, high H_2 pressures were used and the processes required a recycle stream for the excess H_2. However, current units can operate using once-through hydrogen at a H_2 to hydrocarbon molar ratio of 0.03 [11].

Isomerization of light straight-run (LSR) naphtha, consisting of pentanes and hexanes, was also first performed industrially during World War II, but was only performed in two plants [9]. In practice, isomerization of C5/C6 and butane streams is performed separately, but the technology used for conversion of each was (and still is) similar. Thus, dual-functional heterogeneous catalysts are also used today for C5/C6 isomerization. Some currently used technology, such as UOP's Penex process [11], also

uses a Pt/chlorided alumina catalyst. The process suffers from the same problems as those described for the Butamer process.

Zeolite catalysts, specifically Pt/H-mordenite, are also used commercially for C5/C6 isomerization. Shell's Hysomer process [14] uses a Pt/H-mordenite catalyst but operates at a relatively high temperature of about 523 K. The zeolite-based catalysts offer the significant advantage that they are more tolerant than chlorided alumina to common contaminants such as water and sulfur and, because a chloride source is not necessary, less process equipment is required [1].

1.2.3 Catalysts

Numerous materials are capable of catalyzing alkane skeletal isomerization. These include some Friedel-Crafts catalysts, such as $HCl/AlCl_3$, chlorided alumina, some H-form zeolites, sulfated zirconia, WO_3/ZrO_2, some heteropoly acids, molybdenum or tungsten oxycarbide, partially reduced MoO_3 [15], and even platinum in the metallic state [16]. Commercial processes are available that use Brønsted acidic solid acids: chlorided alumina, sulfated zirconia, and H-mordenite. In all cases, the industrially applied catalyst consists of both the acidic component and a small amount of platinum.

1.2.3.1 H-mordenite

Of particular importance in the alkane skeletal isomerization literature is the catalyst used in this study, the zeolite H-mordenite. In 1965, H-mordenite emerged as a potentially useful catalyst when it was found to convert *n*-butane and cyclohexane to isobutane and methylcyclopentane, respectively, at 473 K [17]. It was commercialized shortly thereafter by Shell for alkane isomerization in the Hysomer process [18]. While

its main industrial use is for isomerization of C5/C6 alkanes, mordenite can also be applied for hydrocracking, dewaxing, NO_x reduction, cumene synthesis, transalkylation of aromatics, and as an adsorbent [19].

By some measures, H-mordenite has the most acidic Brønsted acid sites of the H-form zeolites. It has been reported that the Sanderson electronegativity of H-mordenite is higher than that of other common zeolites [20]. Other indicators of zeolite acidity, such as the heat of adsorption of nitrogen-containing bases [21] or the position of ^{1}H NMR shifts of bridging hydroxyl groups [22], also indicate that the Brønsted acid sites in H-mordenite are at least equal in strength, if not stronger than, sites found in other commonly used H-form zeolites. It is noted that certain variables affecting the intrinsic strength of Brønsted acid sites in zeolites are still being debated. For example, coordinatively unsaturated extraframework aluminum ions have long been suspected of enhancing the strength of Brønsted acid sites in their vicinity [23]. The Next Nearest Neighbor (NNN) theory has been used to help explain differences in acid strength with varying Si/Al ratio [24,25].

H-mordenite is considered to be a one-dimensional, "large pore" zeolite because of its 12-membered ring channel (aperture 7.0 x 6.5 Å) [19] parallel to the lattice plane (001) [26]. A highly compressed, ellipsoidal 8-membered ring channel (aperture 5.7 x 2.6 Å) parallel to the lattice plane (001) also exists [27], but the narrow pore diameter almost certainly prohibits access to most adsorptives. Within the 12-membered ring channel there are 8-membered ring "side pockets" (aperture 3.4 x 4.8 Å) [28] that have a depth of almost 8 Å [**Error! Bookmark not defined.**]. The "plumbing system" of the mordenite framework is shown in Fig. 1.2.

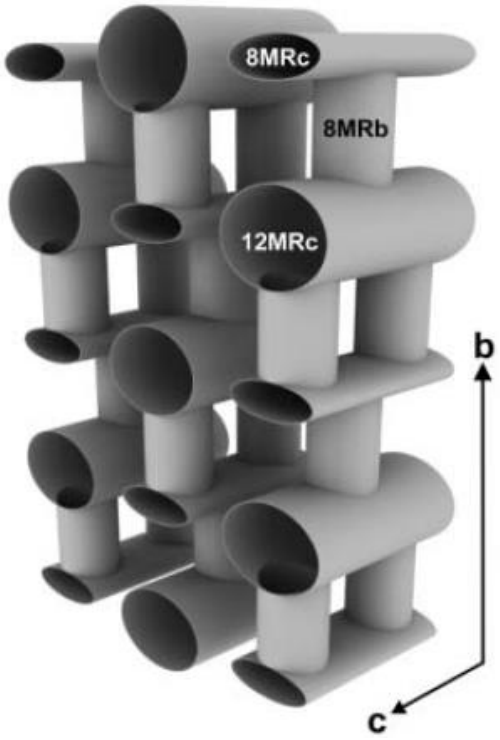


Figure 1.2: The “plumbing system” of mordenite [29]. 8MRb: 8-membered ring parallel to b direction; 8MRc: 8-membered ring parallel to c direction; 12MRc: 12 membered ring parallel to c direction.

Although pristine mordenite has a well-defined crystal structure, in practice, all mordenites are not equal. In fact, the terms “large-port” and “small-port” have been coined to describe mordenites that differ in their adsorption properties for molecules of a certain size. Large-port mordenite is hydrothermally synthesized in the Na-form between 348 and 533 K and accepts some molecules with a diameter larger than 4.5 Å [**Error! Bookmark not defined.**]. Small-port mordenite is synthesized between 548 and 573 K and does not accept molecules with a diameter larger than 4.2 Å [**Error! Bookmark not defined.**]. Chemical recipes exist for transforming small-port to large-port mordenite [29], and vice versa [**Error! Bookmark not defined.**]. The reasons for the different adsorption behavior are not clear, and several hypotheses have been made.

They include i) partial blocking of the pores by cations, ii) amorphous material that plugs structural windows, and iii) the presence of stacking faults [**Error! Bookmark not defined.**], which can be seen using transmission electron microscopy (TEM) [30].

An interesting catalytic feature of H-mordenite that has received much recent attention is the behavior of Brønsted acid sites residing at different locations of the framework. Brønsted acid sites located in 12-membered ring channels and 8-membered ring side pockets have been found to vary in the rates at which they catalyze dimethyl ether carbonylation [31], dehydrogenation and cracking of propane and *n*-butane [32], dehydrogenation and cracking of isobutane [33], and skeletal isomerization of *n*-hexane [34]. Assigning catalytic activity to acid sites in separate locations requires that i) the concentration of sites in separate locations must be able to be controlled synthetically, and ii) the site distribution must be convincingly characterized. Sodium has been found to preferentially ion-exchange with protons in 8-membered ring side pockets [31], and is usually used in lieu of protons to balance the negatively charged lattice in this location. Thus, it is possible to synthesize Na,H-mordenite with protons residing only in 12-membered ring channels.

Infrared spectroscopy has emerged as the method of choice by which the location of Brønsted acid sites in H-mordenite can be determined. In general, a high frequency band is assigned to bridging OH groups in 12-membered ring channels, and a low frequency band is assigned to bridging OH groups in 8-membered ring side pockets. Wakabayashi et al. [35] fit the OH region with Gaussian curves and reported the high and low frequency absorptions to occur at wavenumbers of 3616 and 3590 cm^{-1}, respectively. A third location for a Brønsted acid site has also been suggested.

Using CO and pyridine as probes on a series of Na,H-mordenites, Marie et al. [36] assigned infrared bands at 3610, 3605, and 3585 cm^{-1} to bridging OH groups located in the main channel, at the opening window between main channel and side pockets, and at the end of the side pocket, respectively. Bevilacqua et al. [37] used a series of variously sized nitrile probe molecules to assign infrared bands at 3609, 3605, and 3588 cm^{-1} to bridging OH groups located at the opening window between main channel and side pockets, in the main channels, and inside the side pockets. Thus, there is some variability in the band assignments. In general, one can say that the more easily accessible OH groups absorb infrared radiation at higher frequencies than those that are less accessible.

As inferred by the use of variously sized probe molecules to ascertain the location of Brønsted acid sites, the accessibility of sites located in side pockets to certain reactants has been questioned. For example, alkanes such as *n*-butane [38], *n*-pentane [39], and *n*-hexane [28] have all been shown to not perturb OH groups absorbing at low frequency. Wakabayashi et al. [35] found that even N_2 did not perturb OH groups in the side pockets. Maache et al. [40] found that OH groups in the side pockets became accessible to pyridine only after dealumination.

To summarize, H-mordenite is a highly acidic zeolite that is currently used in some industrial applications. It is a zeolite with interesting catalytic and structural properties, some of which are not fully understood.

1.2.4 Skeletal isomerization chemistry

The general reaction chemistry of alkane skeletal isomerization can be described using classical carbenium ion chemistry. The acid-catalyzed skeletal isomerization of *n*-

pentane is used as an example in Fig. 1.3. Activation of the alkane can occur by i) protonation to form an alkanium ion, which quickly decomposes to a carbenium ion with loss of H_2, ii) abstraction of a hydride ion by a Lewis acid to form a carbenium ion, or iii) protonation of the corresponding alkene, which can be formed by dehydrogenation on a noble metal (or on sulfated zirconia via oxidative dehydrogenation). Once formed, rearrangement to a branched carbenium ion proceeds through a species containing a cyclopropane ring. The branched carbenium ion forms upon opening of the cyclopropane ring, and can further react to form a branched alkane either through hydride transfer or by undergoing deprotonation to form a branched olefin with subsequent hydrogenation.

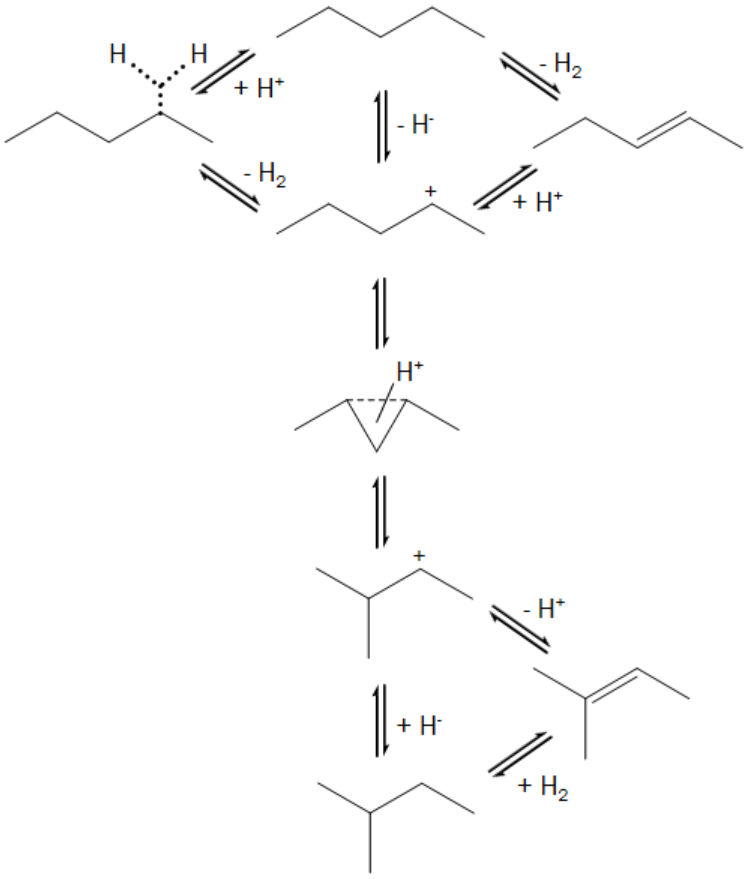


Figure 1.3: The intramolecular acid-catalyzed skeletal isomerization pathway of *n*-pentane.

1.2.4.1 In mineral acids

There have been conflicting reports about the rate at which *n*-butane is converted to its skeletal isomer in mineral acids. An early report from Heldman [41] indicated that the reaction could proceed in aluminum bromide with various promoters already at 298 K. It was later claimed by Pines and Wackher [42] that a tiny amount of butene impurity was responsible for the catalytic activity reported by Heldman. The effect of olefins is very important, and will be the topic of Section 1.2.4.3.

The most widely known report is that of Brouwer [43], who observed that although 1-^{13}C-*n*-butane was converted to 2-^{13}C-*n*-butane in HF-SbF_5 at a rate only

slightly lower than the rate at which *n*-pentane was converted to 2-methylbutane, no isobutane was formed. The difference in product formation rates could be explained by

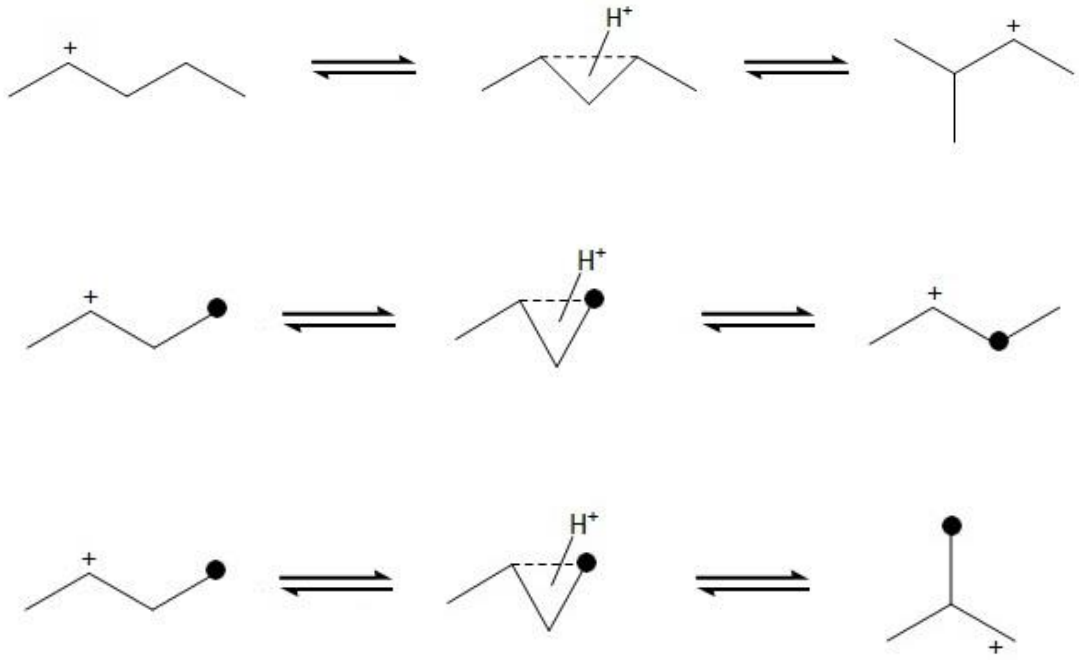


Figure 1.4: Rearrangements of cationic species relevant to conversion of: a) *n*-pentane to isopentane, b) 1-^{13}C-*n*-butane to 2-^{13}C-*n*-butane, and c) 1-^{13}C-*n*-butane to 1-^{13}C-isobutane

the types of carbenium ion that are formed during the rearrangement, assuming the reaction coordinate involves a cyclopropane ring intermediate. Reaction pathways from 4-^{13}C-butan-2-ylium to 3-^{13}C-butan-2-ylium and from pentan-2-ylium to 2-methylbutan-3-ylium require formation of only secondary carbenium ions, as shown in Fig. 1.4. The reaction pathway from 4-^{13}C-butan-2-ylium to 3-^{13}C-2-methylpropan-1-ylium requires formation of a primary carbenium ion.

Carbocations are stabilized by i) an inductive effect, and ii) partial overlap of filled orbitals with empty ones. Polarizable alkyl groups allow an electron-deficient carbon atom to withdraw electron density through sigma bonds; thus, more alkyl groups result in a more stable carbocation [44]. The difference in carbocation stability has an

effect on the activation energy when they are formed in a transition state. For internal carbon scrambling of a *sec*-butyl cation, formed by addition of *sec*-butyl chloride to SbF_5/SO_2ClF, Saunders et al. [45] measured an activation energy of 31 kJ mol^{-1}. The activation energy for formation of a *tert*-butyl cation from a *sec*-butyl cation was 75 kJ mol^{-1} [45]. Although the activation energy was high, Brouwer [46] found it to be "too low to be reconcilable with the occurrence of the primary isobutyl ion" and said the mechanism must be somehow concerted. Saunders et al. [47] claimed that the activation energy was evidence of a transition state with "structures close to primary ions". Ab initio calculations later showed that a primary carbenium is indeed formed in the transition state [48]. Thus, as suggested by the difference in reaction rates at room temperature, and by the measured activation energies, the intramolecular skeletal rearrangement of an *n*-butyl species in mineral acid is much slower than the intramolecular skeletal rearrangement of species with longer carbon chains due to the types of carbenium ion that form during the rearrangement.

1.2.4.2 On solid acids

Until recently, reaction mechanisms in mineral acids and on solid acids were considered to be analogous. This changed, however, in the mid 1980's and early 1990's when calculations performed by Kazanzky and co-workers revealed that the mechanism of olefin protonation on zeolites involves both a proton and a neighboring oxygen atom, and that alkoxides are formed as intermediates instead of carbenium ions [49,50]. Because of these differences, Kazansky suggested that a variety of concerted reaction pathways would be possible on zeolites that may be prohibited in mineral acids [51]. It should be noted that alkoxide formation is energetically favored only if the steric

constraints of C-O bond formation are not pronounced; in some cases, as with aromatic hydrocarbons containing larger π systems, formation of a true cation is energetically favored over formation of an alkoxide [52].

Reaction chemistry known to occur in mineral acids has long been used to explain aspects of alkane skeletal isomerization on solid acids. For example, it is widely accepted that skeletal isomerization of *n*-pentane on a solid acid occurs by an energetically facile intramolecular pathway [13]. To the contrary, it has been claimed that intramolecular skeletal isomerization of butane does not occur [53,54], or occurs very slowly [55] and with great difficulty [56], or is not the main isomerization pathway [57,58] due to the energetically prohibitive formation of a primary carbenium ion. However, numerous solid acids catalyze butane skeletal isomerization, meaning that pathways allowing for the reaction to occur must exist. Much evidence has indicated that intermolecular reaction pathways are responsible. Such pathways involve formation of a C8 intermediate from two C4 entities, rearrangement of the C8 species, and further cracking, hydride transfer, or hydrogenation to form isobutane [57]. Undesired side products such as propane and pentanes can also form through the intermolecular pathway, in which case the term "disproportionation" is used.

A concerted intramolecular skeletal isomerization pathway has been proposed to explain experimental results obtained from conversion of *n*-butene on 10-membered ring zeolites. Discussion of these results is also relevant to discussion about the skeletal isomerization mechanism of *n*-butane. De Jong and co-workers found that on H-ferrierite, after an initial period of deactivation, isobutene was formed from *n*-butene at a steady rate with almost 90% selectivity [59]. Experiments with carbon-13 labeled

n-butene revealed that after the initial deactivation, 100% of the isobutene product retained the same number of carbon-13 isotopes as the feed [60], suggesting an intramolecular pathway of formation. Boronat and co-workers [61] used density functional theory (DFT) calculations to determine the lowest energy intramolecular skeletal isomerization pathway. They found that (referring to the transition state), "unlike in superacid media, neither the optimized geometry nor the net atomic charges of this structure correspond to a primary isobutyl cation." A representation of Boronat's proposed reaction pathway is shown in Fig. 1.5. Unlike in a mineral acid, DFT calculations show that the transition state on a solid acid is the cyclopropane ring itself. In mineral acids the transition state is formed upon opening of the cyclopropane ring. On solid acids, this step results in formation of a (stable) primary alkoxide.

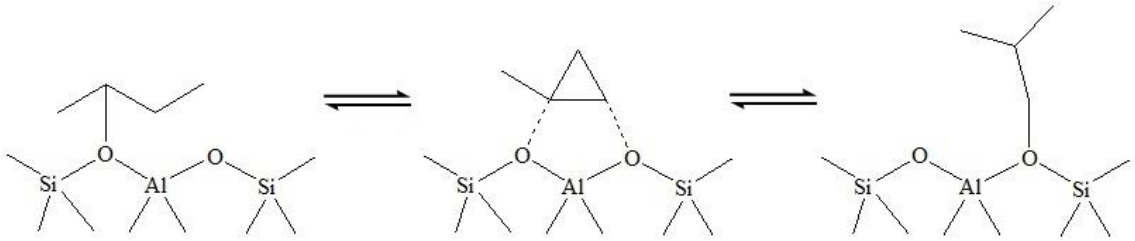


Figure 1.5: Intramolecular reaction pathway proposed by Boronat et al. for butene skeletal isomerization on a zeolite. Adapted from [61].

The current view on skeletal isomerization mechanisms of relevant species on solid acids can be summarized as follows: *n*-alkanes with at least five carbon atoms are believed to form their skeletal isomer through an intramolecular pathway. Convincing evidence has been presented supporting both intra- and intermolecular rearrangement pathways of *n*-butane and will be discussed in Chapters 4 and 5 in further detail.

1.2.4.3 Effect of olefins on butane isomerization

With respect to butane isomerization, three principle effects of olefins can be discerned from the literature. Olefin addition to a butane feed has been found to i) cause an increase in product formation rates, ii) cause products to form at temperatures they otherwise would not have, and iii) promote deactivation. The latter effect will be discussed in Section 1.2.5, and the former two effects will be discussed here.

The important role that olefins can play in butane isomerization was identified at least as early as 1946. Pines and Wackher [42] found that addition of as little as 0.01% of *n*-butene to *n*-butane was sufficient to cause conversion of *n*-butane to skeletal isomerization and disproportionation products at 373 K in $HCl/AlCl_3$, with disproportionation products being favored by higher *n*-butene concentrations. Their findings about the lack of conversion of pure *n*-butane were in direct contradiction to those of Heldman [41], who they suggested did not use a pure *n*-butane source. The butenes were claimed to be the source of initial carbonium (now carbenium) ions [42].

On solid acids, similar experimental results have been reported. The most dramatic examples are those reported by Dumesic and co-workers, who found H-mordenite to be completely inactive at 473 K for *n*-butane [62] or isobutane [63] conversion in the absence of olefins in the feed. However, when as little as 55 ppm of butene was added, product formation rates were significant. Engelhardt [64] found that the rate of *n*-butane conversion could be significantly enhanced by addition of ethene, propene, or isobutene to the feed. Thus, the promoting effect of olefins is not limited to butenes.

Olefins have also been found to promote conversion of butane on other, non-zeolitic, solid acids. A famous example is that of sulfated zirconia. After initial reports from Hino and Arata [65,66] showed that sulfated zirconia was active for butane isomerization at room temperature, there was great interest in its catalytic abilities and its material properties. Several investigations found that although sulfated zirconia is a strong acid, the acidity does not exceed that of sulfuric acid, H-ZSM-5, or H-mordenite [67-69], and it is not a superacid as first reported. A revealing report was that of Jatia et al. [70], who found that CO_2 was produced on sulfated zirconia and promoted sulfated zirconias during temperature-programmed desorption (TPD) of benzene. Thus, oxidation is also a possible reaction on sulfated zirconia, whereas it is not on a zeolite.

Tabora et al. [71] observed that after butene impurities were removed from the feed, sulfated zirconia was much less active for *n*-butane conversion. It was later proposed that butenes are formed in situ via oxidative dehydrogenation and initiate conversion of *n*-butane. Evidence was collected by Li et al. [72], who measured the butene formed during TPD of *n*-butane, and measured water formation with in situ infrared spectroscopy during conversion of *n*-butane. They also observed a rate enhancement when impure *n*-butane was used, and claimed that a chain-type mechanism converts 500 butane molecules for every butene molecule [72]. Goodwin and co-workers [73-75] have coined the phrase “olefin-modified site” to describe the additional carbenium ions formed as a result of olefin addition. Thus, olefins are also known to significantly enhance rates of butane conversion on sulfated zirconia.

1.2.5 Formation of carbonaceous deposits

Solid acids used for alkane isomerization are plagued by a tendency to deactivate. Chlorided alumina will deactivate if a source of chloride is not continuously provided [1]. Sulfated zirconia may deactivate by i) surface reduction ($Zr^{4+} \rightarrow Zr^{3+}$), ii) reduction of the surface sulfate groups and H_2S formation, iii) a change of phase from tetragonal to monoclinic, and iv) surface poisoning by water [76]. A major problem common to both catalysts, and also zeolites, is that carbonaceous deposits accumulate on the catalyst surface unless platinum (typically less than 1 wt%) is added to the catalyst and H_2 is added to the feed. It should be noted that the joint function of platinum and H_2 on the catalytic isomerization process is debated in the literature and is not thought to be solely limiting deactivation. Three principal ideas can be distinguished: i) coke prevention by hydrogenation of unsaturated species [57] ii) facilitation of a classical dual-functional reaction pathway [77], and iii) formation of additional acid sites through spillover of hydrogen [78].

Several reports exist about the carbonaceous deposits formed during alkane isomerization. Some implicate alkenes, which are suspected as precursors [62,63]. Stepanov et al. [79] found that in addition to oligomers, methyl-substituted cyclopentenyl species formed from 1-butene at low temperatures on H-ferrierite. Cycloalkenyl cations were also named by Knözinger [80] as a possible assignment for an electronic band at 292 nm that formed during *n*-butane conversion on sulfated zirconia. Thus, the deposits may persist as cations, suggesting that the mechanism by which they cause deactivation is to block acid sites.

On H-mordenite, the catalyst used in this study, coke has been found after *n*-butane conversion in the absence of H_2 [58,81,82] in amounts of a few weight percent. In some instances, a decrease in surface area and pore volume was explained by coke filling the pores [83] or blocking pore entrances. Coke formation has again been associated with alkenes; for example H-mordenite deactivates more rapidly during butane isomerization with increasing amounts (ppm levels) of alkenes in the feed [62,63]. It was thus proposed that the combination of platinum and H_2 regulates the alkene concentration through hydrogenation, thus suppressing coke formation [57].

Whereas some general trends relating catalyst deactivation to reaction conditions have been reported, the link to carbonaceous surface deposits is lacking. Little information is available regarding the nature of the coke; the only detail was provided by Villegas et al. [84], who analyzed a variety of acidic zeolites (excluding mordenite) after use for *n*-butane isomerization at 623 K and detected linear alkenes and polycyclic aromatic compounds. No analytical detail is available concerning the nature of coke precursors or their evolution with time on stream.

References

[1] H. Weyda, E. Köhler, Catal. Today 81 (2003) 51.

[2] Y.S. Lee, C.C. Su, Appl. Therm. Eng. 22 (2002) 507.

[3] M.A. Asensi, A. Corma, A. Martínez, J. Catal. 158 (1996) 561.

[4] N.N. Krupina, A.Z. Dorogochinskii, N.F. Meged, V.I. Shmailova, React. Kinet. Catal. Lett. 23 (1983) 273.

[5] C.-L. Li, L. Shi, G.-X. Huang, R.-Y. Wang, Chem. Eng. Comm. 121 (1993) 1.

[6] United States Energy Information Administration, Production Capacity of Operable Petroleum Refineries <http://www.eia.gov/dnav/pet/pet_pnp_capprod_dcu_nus_a.htm>, accessed February 6, 2013.

[7] W.L. Leffler, Petroleum Refining in Non-Technical Language, PennWell Books, Tulsa, 2008, p. 107.

[8] Energy Global, Rising Gasoline Consumption in Developing Countries, <http://www.energyglobal.com/news/processing/articles/Developing_economies_and_MTBE.aspx>, accessed February 6, 2013.

[9] R.C. Gunness, Progress in Petroleum Technology, American Chemical Society, 1951, p. 109-119.

[10] United States Environmental Protection Agency, <http://www.epa.gov/aboutepa/history/topics/lead/01.html>, accessed February 6, 2013.

[11] N.A. Cusher, in: R.A. Meyers (Ed.), Handbook of Petroleum Refining Processes, ed. 3, McGraw-Hill, New York, 2004, Ch. 9.2-9.3.

[12] D.R. Stull, E.F. Westrum, G.C. Sinke, The Chemical Thermodynamics of Organic Compounds, Wiley, New York, 1969.

[13] S.T. Sie, in: G. Ertl, H. Knözinger, F. Schüth, J. Weitkamp (Eds.), Handbook of Heterogeneous Catalysis, ed. 2, John Wiley and Sons, Inc., 2008, p. 2809-2830.

[14] P.M.M. Blauwhoff, J.W. Gosselink, E.P. Kieffer, S.T. Sie, W.H.J. Stork, in: J. Weitkamp, L. Puppe (Eds.), Catalysis and Zeolites: Fundamentals and Applications, Springer-Verlag, Berlin, 1999, p. 491.

[15] Y. Ono, Catal. Today 81 (2003) 3.

[16] G.A. Somorjai, Introduction to Surface Chemistry and Catalysis, Wiley, New York, 1994.

[17] V.J. Frilette, M.K. Rubin, J. Catal. 4 (1965) 310.

[18] T.F. Degnan Jr., Top. Catal. 13 (2000) 349.

[19] M. Stöcker, Microporous Mesoporous Mater. 82 (2005) 257.

[20] J. Dwyer, Chem. Ind. (London) 7 (1984) 258.

[21] D.J. Parrillo, R.J. Gorte, J. Phys. Chem. 97 (1993) 8786.

[22] M. Hunger, Catal. Rev.-Sci. Eng. 39 (1997) 345.

[23] M.A. Makarova, S.P. Bates, J. Dwyer, J. Am. Chem. Soc. 117 (1995) 11309.

[24] L.A. Pine, P.J. Maher, W.A.J. Wachter, J. Catal. 85 (1984) 2887.

[25] D. Barthomeuf, Mater. Chem. Phys. 17 (1987) 49.

[26] W.M. Meier, Z. Kristallogr. 115 (1961) 439.

[27] Ch. Baerlocher and L.B. McCusker, Database of Zeolite Structures: <http://www.iza-structure.org/databases/>, accessed February 6, 2013.

[28] M. Bevilacqua, A.G. Alejandre, C. Resini, M. Casagrande, J. Ramirez, G. Busca, Phys. Chem. Chem. Phys. 4 (2002) 4575.

[29] P.C. van Geem, K.F.M.G.J. Scholle, G.P.M. van der Velden, J. Phys. Chem. 92 (1988) 1585.

[30] S.G. Song, J. Mater. Res. 14 (1999) 2616.

[31] A. Bhan, E. Iglesia, Acc. Chem. Res. 41 (2008) 559.

[32] R. Gounder, E. Iglesia, J. Am. Chem. Soc. 131 (2009) 1958.

[33] R. Gounder, E. Iglesia, Angew. Chem., Intl. Ed. 49 (2010) 808.

[34] H. Chiang, A. Bhan, J. Catal. 283 (2011) 98.

[35] F. Wakabayashi, J. Kondo, A. Wada, K. Domen, C. Hirose, J. Phys. Chem. 97 (1993) 10761.

[36] O. Marie, P. Massiani, F. Thibault-Starzyk, J. Phys. Chem. B 108 (2004) 5073.

[37] M. Bevilacqua, G. Busca, Catal. Comm. 3 (2002) 497.

[38] J.A. van Bokhoven, M. Tromp, D.C. Koningsberger, J.T. Miller, J.A.Z. Pieterse, J.A. Lercher, B.A. Williams, H.H. Kung, J. Catal. 202 (2001) 129.

[39] V.I. Bogdan, A.E. Koklin, V.B. Kazanskii, Kinet. Catal. 51 (2010) 736.

[40] M. Maache, A. Janin, J.C. Lavalley, E. Benazzi, Zeolites 15 (1995) 507.

[41] J.D. Heldman, J. Am. Chem. Soc. 66 (1944) 1786.

[42] H. Pines, R.C. Wackher, J. Am. Chem. Soc. 68 (1946) 595.

[43] D.M. Brouwer, Recl. Trav. Chim. Pay.-B. 87 (1968) 1435.

[44] L.G. Wade, Jr., Organic Chemistry, 6th Ed., Pearson Prentice-Hall, Upper Saddle River, NJ, 2006, p. 156.

[45] M. Saunders, E.L. Hagen, J. Rosenfeld, J. Am. Chem. Soc. 90 (1968) 6882.

[46] D.M. Brouwer, H. Hogeveen, in A. Streitwieser, Jr., R.W. Taft (Eds.), Progress in Physical Organic Chemistry, vol. 9, Wiley-Interscience, New York, 1972, p. 224-225.

[47] M. Saunders, P. Vogel, E.L. Hagen, J. Rosenfeld, Acc. Chem. Res. 6 (1973) 53.

[48] M. Boronat, P. Viruela, A. Corma, J. Phys. Chem. 100 (1996) 633.

[49] I.N. Senchenya, N.D. Chuvilkin, V.B. Kazansky, Kinet. Catal. 26 (1985) 1073.

[50] R.A. Van Santen, X. Rozanska, Adv. Chem. Eng. 28 (2001) 399.

[51] V.B. Kazansky, Acc. Chem. Res. 24 (1991) 379.

[52] H. Fang, A. Zheng, J. Xu, S. Li, Y. Chu, L. Chen, F. Deng, J. Phys. Chem. C 115 (2011) 7429.

[53] C. Bearez, F. Chevalier, M. Guisnet, React. Kinet. Catal. Lett. 22 (1983) 405.

[54] M. Guisnet, N.S. Gnep, Appl. Catal., A 146 (1996) 33.

[55] C. Bearez, F. Avendano, F. Chevalier, M. Guisnet, Bull. Soc. Chim. Fr. 3 (1985) 346.

[56] M.T. Tran, N.S. Gnep, G. Szabo, M. Guisnet, Appl. Catal., A 170 (1998) 49.

[57] R.A. Asuquo, G. Eder-Mirth, K. Seshan, J.A.Z. Pieterse, J.A. Lercher, J. Catal. 168 (1997) 292.

[58] R.A. Asuquo, G. Eder-Mirth, J.A. Lercher, J. Catal. 155 (1995) 376.

[59] S. Van Donk, E. Bus, A. Broersma, J.H. Bitter, K.P. de Jong, Appl. Catal., A 237 (2002) 149.

[60] K.P. de Jong, H.H. Mooiweer, J.G. Buglass, P.K. Maarsen, Stud. Surf. Sci. Catal. 111 (1997) 127.

[61] M. Boronat, P. Viruela, A. Corma, J. Phys. Chem. A 102 (1998) 982.

[62] K.B. Fogash, Z. Hong, J.M. Kobe, J.A. Dumesic, Appl. Catal., A 172 (1998) 107.

[63] K.B. Fogash, Z. Hong, J.A. Dumesic, J. Catal. 173 (1998) 519.

[64] J. Engelhardt, J. Catal. 164 (1996) 449.

[65] M. Hino, S. Kobayashi, K. Arata, J. Am. Chem. Soc. 101 (1979) 6439.

[66] M. Hino, K. Arata, J.C.S. Chem. Comm. 18 (1980) 851.

[67] V. Adeeva, J.W. de Haan, J. Jänchen, G.D. Lei, V. Schünemann, L.J.M. van de Ven, W.M.H. Sachtler, R.A. van Santen, J. Catal. 151 (1995) 364.

[68] F. Babou, G. Coudurier, J. Vedrine, J. Catal. 152 (1995) 341.

[69] F. Haase, J. Sauer, J. Am. Chem. Soc. 120 (1998) 13503.

[70] A. Jatia, C. Chang, J.D. MacLeod, T. Okubo, M.E. Davis, Catal. Lett. 25 (1994) 21.

[71] J.E. Tabora, R.E. Davis, J. Am. Chem. Soc. 118 (1996) 12240.

[72] X. Li, K. Nagaoka, L.J. Simon, R. Olindo, J.A. Lercher, A. Hofmann, J. Sauer, J. Am. Chem. Soc. 127 (2005) 16159.

[73] N. Lohitharn, J.G. Goodwin Jr., E. Lotero, J. Catal. 234 (2005) 199.

[74] N. Lohitharn, E. Lotero, J.G. Goodwin Jr., J. Catal. 241 (2006) 328.

[75] N. Lohitharn, J.G. Goodwin Jr., J. Catal. 245 (2007) 198.

[76] R. Ahmad, J. Melsheimer, F.C. Jentoft, R. Schlögl, J. Catal. 218 (2003) 365.

[77] H. Liu, V. Adeeva, G.D. Lei, W.M.H. Sachtler, J. Mol. Catal. A: Chem. 100 (1995) 35.

[78] H. Hattori, T. Shishido, Catal. Surveys Japan 1 (1997) 205.

[79] A.G. Stepanov, M.V. Luzgin, S.S. Arzumanov, H. Ernst, D. Freude, J. Catal. 211 (2002) 165.

[80] H. Knözinger, Top. Catal. 6 (1998) 107.

[81] J.C. Yori, M.A. D'Amato, G. Costa, J.M. Parera, React. Kinet. Catal. Lett. 56 (1995) 129.

[82] J.C. Yori, J.C. Luy, J.M. Parera, Appl. Catal. 46 (1989) 103.

[83] J.I. Villegas, N. Kumar, T. Heikkilä, A. Smiešková, P. Hudec, T. Salmi, D.Yu. Murzin, Appl. Catal., A 284 (2005) 223.

[84] J.I. Villegas, N. Kumar, T. Heikkilä, V.–P. Lehto, T. Salmi, D.Yu. Murzin, Chem. Eng. J. 120 (2006) 83.

2 Scientific Problem and Strategy

2.1 Scientific problem

Heterogeneous catalysts used for skeletal isomerization of alkanes are suboptimal in several ways. One is that platinum on the catalyst and H_2 in the feed are necessary to prevent deactivation. As platinum is an expensive noble metal and H_2 is a valuable refining commodity, eliminating these material requirements would be of significant benefit. Obtaining knowledge of the surface chemistry involved in formation of deactivation-causing carbonaceous deposits would represent a significant intellectual step forward to achieving this ambitious goal. A speciation of the deposits may aid in developing this fundamental understanding. Similarly, the composition of the deposits that form has not been well characterized, nor has the evolution of such deposits been characterized with time on stream.

In the case of *n*-butane, the mechanistic aspects of the skeletal rearrangement on solid acids are poorly understood. Because a major downfall of catalysts with the potential to replace Pt/chlorided alumina is a low selectivity to isobutane, a detailed and careful analysis of all reaction pathways leading to formation of gas phase products could be beneficial. Of particular interest is the kinetic relevance of an intramolecular skeletal isomerization pathway that would produce isobutane with 100% selectivity. Elucidating the variables that allow for the pathway to operate, or the variables that favor formation of side products, is important.

To conduct a fundamental investigation, the catalyst should be well defined, and the scenario should be kept as simple as possible. Chlorided alumina is sensitive to many contaminants, including traces of water, and requires an organic chloride co-feed.

Sulfated zirconia is not only acidic but also redox-active, complicating the collection and interpretation of data. Zeolite catalysts appear most suitable because they are structurally uniform and less prone to be involved in side reactions. We chose to use H-mordenite, the zeolite used in some commercial processes for pentane and hexane isomerization, to conduct the investigation.

2.2 Strategy – Analysis of *n*-butane reaction pathways

2.2.1 Kinetics

Analysis of reaction kinetics is commonly used to gather mechanistic information about a particular reaction. In the case of *n*-butane isomerization, it may be possible to differentiate intramolecular and intermolecular pathways by studying the reaction kinetics. If both isobutane and disproportionation products, such as propane and pentanes, are produced exclusively through intermolecular pathways, they *may* have similar kinetic parameters such as activation energy, reaction order with respect to *n*-butane, and reaction order with respect to H_2. If isobutane is produced mainly through an intramolecular pathway, the kinetic parameters may be significantly different than those for the disproportionation products. The rate equation for an intramolecular reaction pathway, assuming Langmuir adsorption, a rate-limiting surface reaction, and not considering the particular chemistry of a Brønsted acid site on a zeolite, is shown in Fig. 2.1; r_B is the rate of formation of product B, A is the reactant, s is the active site, C_T is the total concentration of active sites, K is an equilibrium constant, k_2 is the rate constant for the forward reaction, k_{-2} is the rate constant for the reverse reaction, and P indicates a partial pressure. The rate equation for an intermolecular pathway involving

1. $A + s \rightleftharpoons A \cdot s$
2. $A \cdot s \longrightarrow B \cdot s$
3. $B \cdot s \rightleftharpoons B + s$

Complete rate equation:

$$r_B = \frac{k_2 K_1 C_T P_A}{1 + K_1 P_A + \frac{P_B}{K_3}} - \frac{k_{-2} C_T P_B}{K_3 \left(1 + K_1 P_A + \frac{P_B}{K_3}\right)}$$

At differential conversion with low coverage:

$$r_B = k P_A$$

Figure 2.1: Basic intramolecular rate equation for A → B with the surface reaction as the rate-limiting step.

1. $A + s \rightleftharpoons A \cdot s$
2. $A \cdot s + A \rightleftharpoons B \cdot s$
3. $B \cdot s \rightleftharpoons C \cdot s$
4. $C \cdot s \longrightarrow D \cdot s + E$
5. $D \cdot s \rightleftharpoons D + s$

Complete rate equation:

$$r_E = \frac{k_4 K_1 K_2 K_3 C_T P_A^2}{\left(1 + K_1 P_A + K_1 K_2 P_A^2 + K_1 K_2 K_3 P_A^2 + \frac{P_D}{K_5}\right)} - \frac{k_{-4} C_T P_D P_E}{K_5 \left(1 + K_1 P_A + K_1 K_2 P_A^2 + K_1 K_2 K_3 P_A^2 + \frac{P_D}{K_5}\right)}$$

At differential conversion with low coverage:

$$r_E = k P_A^2$$

Figure 2.2: Rate equation for an intermolecular 2A → C + D reaction involving Langmuir adsorption, Eley-Rideal bond formation, and bond breaking as the rate-limiting step.

Langmuir adsorption, Eley-Rideal bond formation, bond breaking (Step 4) as the rate-limiting step, and again not considering the particular chemistry of a Brønsted acid site on a zeolite, is shown in Fig. 2.2. The symbols can be thought of as representing: *A*, *n*-butane; *B*, the initial dimerization product; *C*, the isomerized dimerization product; *D*,

pentane or butane; and *E*, propane or butane. Thus, there may at least be measurable differences in the dependence on the reactant partial pressure, as the intramolecular pathway is first order with respect to the reactant and the intermolecular pathway may be second order with respect to the reactant, depending on the rate-limiting step. More detailed rate equations, considering production of butenes and the particular chemistry associated with Brønsted acid sites on a zeolite, are discussed in Chapter 4.

2.2.2 Carbon-13 labeled *n*-butane

Carbon-13 labeled butane has previously been used to investigate reaction pathways on solid acids that lead to formation of gas phase products. The *general* interpretation of the data is as follows: if carbon-13 labeled *n*-butane is transformed to isobutane through an intramolecular pathway, the isobutane will contain the same number of carbon-13 isotopes as the *n*-butane feed. If isobutane is formed through intermolecular pathways, significant isotope scrambling will occur. If carbon-13 isotopes in the C8 intermediates are scrambled to a statistical degree, the isobutane will contain a binomial distribution of carbon-13 isotopes. Both product distributions are depicted in Fig. 2.3 for the case in which a 1,4-^{13}C-*n*-butane feed is used.

One variable that received close attention in this work, which has not been carefully accounted for in the past, is the concentration of olefins. As discussed in Section 1.2.4.3, there are some indications that olefins play a dominant role in determining reaction pathways of butane, thus potentially altering isotope distributions in products. The 1,4-$^{13}C_2$-*n*-butane used in this work was purchased from Isotec, Inc., and came with 1,200 ppm of 1-butene as an impurity. Consequently, we were able to

vary the olefin concentration in the feed. The results and discussion are presented in Chapter 5.

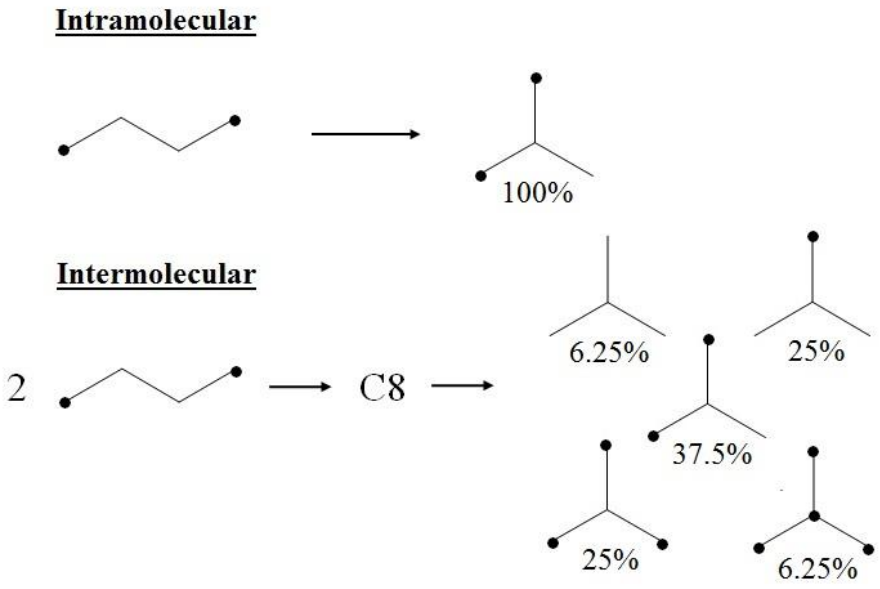


Figure 2.3: Expected number of isotopes and their distribution in isobutane produced via intramolecular and intermolecular skeletal isomerization pathways of 1,4-$^{13}C_2$-*n*-butane.

2.3 Strategy – Identification of carbonaceous deposits

2.3.1 In situ spectroscopy

Of the many methods used to analyze carbonaceous deposits, in situ techniques are the only ones capable of delivering information about the deposits as they exist on the working catalyst. As stated by Gabor Somorjai, using conventional ex situ techniques is "like studying a life with access only to the prenatal and postmortem states" [1]. To properly characterize the deposits as they exist during catalysis, in situ techniques are necessary.

Diffuse reflectance UV-vis-NIR spectroscopy performed in situ is one such technique used in this work. With only zeolite and hydrocarbon in the in situ cell, the main absorptions expected to be seen are those of π* ← π transitions in unsaturated hydrocarbons. These transitions are quite intense; the absorption coefficients for electronic transitions are usually orders of magnitude larger than those for vibrational transitions [2]. Because the technique was found to provide valuable information about the deposits, and was used frequently, the photophysics of the electronic transitions in unsaturated hydrocarbons are discussed in Section 3.3.4. DRIFTS was also performed in situ and was used to complement the information gathered by UV-vis spectroscopy.

2.3.2 Solvent extraction

While spectroscopic methods are a useful tool by which to gather information about carbonaceous deposits, individual species are usually not identifiable. The deposits can consist of tens, or hundreds, of individual species. To identify individual components of such a mixture with UV-vis or infrared spectroscopy is impossible. To perform a speciation, a different analytical technique such as GC-MS must be used, requiring the deposits to be extracted from the solid catalyst.

There are a wide variety of solvent extraction techniques. In some cases, simply placing a spent catalyst in a solvent can be effective. In other cases, extraction can be executed more rapidly by using a Soxhlet device or an accelerated solvent extraction (ASE) device that operates at high temperatures and pressures. Various solvents, such as *n*-heptane, toluene, tetrahydrofuran, or carbon disulfide, can be used.

With zeolites, dispersion in a solvent is, in general, not an effective means of extraction. Because extracting carbonaceous deposits from zeolites can be difficult,

Guisnet and co-workers [3] developed a new solvent extraction procedure, published in 1987, involving digestion of the zeolite in hydrofluoric acid and subsequent liquid-liquid extraction with dichloromethane. This method has since become the "gold standard" for extraction of hydrocarbon species from zeolites.

The main goal of using the Guisnet technique to extract hydrocarbon species from our spent zeolites was to help assign the bands observed with in situ UV-vis and infrared spectroscopies during conversion of *n*-butane or *n*-pentane. We found previous assignments in the literature to be, in many ways, unsatisfying. For example, as will be discussed in Chapter 6, when an olefin such as 1-butene is adsorbed on a zeolite, electronic bands immediately form that cannot be attributed to 1-butene. In previous reports, the bands have largely been assigned only to a general class of species, monoenylic cations, based only on a comparison with spectra of monoenylic cations that have been formed and characterized in mineral acid. The band assignment would be much more convincing if the specific monoenylic cation could be extracted from the solid acid, probably as a neutral species. Recovery of such species is common practice after characterization in mineral acid. However, no papers have been published that unify spectroscopic band assignments of adsorbed species on solid acids with extracted species from the same solid acids.

References

[1] B.M. Weckhuysen, Chem. Commun. 2 (2002) 97.

[2] W. Schmidt, Optical Spectroscopy in Chemistry and Life Sciences, Wiley-VCH, Weinheim (Germany), 2005.

[3] P. Magnoux, P. Roger, C. Canaff, V. Fouche, N.S. Gnep, M. Guisnet, in: Studies in Surface Science and Catalysis – Catalyst Deactivation, Proceedings of the 4th International Symposium, vol. 34, Elsevier B.V., 1987, p. 317-330.

3 Materials and Methods

3.1 Materials

Several H-mordenite and Pt/H-mordenite samples were used in this work. All of them were supplied by UOP. Details of individual samples are shown in Table 3.1, as well as the designation that will be used to refer to each sample. The silicon to aluminum ratio and platinum contents were measured with ICP-AES. Lot 32125-99 was received as NH_4-mordenite and was calcined to make H-mordenite. The designation M1 refers to the calcined sample. AS33805-74B was received as Na-mordenite and was ion exchanged with 1 M NH_4NO_3 for 6 h at 333 K to make NH_4-mordenite, which was calcined to make H-mordenite. The designation M2 refers to the calcined sample. All calcinations were performed at 623-673 K; further details are provided in individual sections. Gases used in experiments throughout the thesis were: N_2 (Airgas, UHP 99.99%), O_2 (Airgas, UHP 99.994%), H_2 (Airgas, UHP 99.999%), and helium (Airgas, UHP 99.999%). N_2, O_2, H_2, and helium were passed through moisture traps (Agilent, MT400-2 for N_2, O_2, and H_2; Restek for helium), and N_2 was additionally passed through an O_2 trap (Chromres, Model 1000).

Table 3.1: Properties of the H-mordenite and Pt/H-mordenite samples

Catalyst	Designation	Si/Al	Pt wt %	Pt precursor	Other
H-mordenite	M1	9.1	-	-	Received as NH_4-MOR, Lot 32125-99
H-mordenite	M2	5.4	-	-	Received as Na-MOR, Lot AS33805-74B
Pt/H-mordenite	Pt/M-T	9.1	0.358	Tetraammineplatinum chloride	Lot 32125-100
Pt/H-mordenite	Pt/M-C1	9.1	0.328	Hexachloroplatinic acid	Lot 33407-1
Pt/H-mordenite	Pt/M-C2	9.1	0.328	Hexachloroplatinic acid	Reduced by supplier. Lot 33436-24

3.2 Packed bed reactor

3.2.1 Apparatus

An isothermal, downflow, packed bed reactor was used in some cases to perform catalytic experiments. The apparatus consisted of three main components: i) a gas flow control system, ii) furnace, and iii) equipment for online gas analysis.

The flow rate of individual gases was controlled using mass flow controllers (Bronkhorst). Flow rates are referenced to normal (NTP) conditions. Swagelok tube fittings and 1/8 inch stainless steel or copper tubing were used throughout the gas distribution system. A general schematic of the system is shown in Fig. 3.1. Some experiments required modification of the distribution system; as such, the figure should be interpreted as being representative of the general state of the gas distribution system and not specific to any particular experiment. Specific modifications will be explained in the experimental section of individual chapters. The use of two 4-way valves (VICI, Valco Instruments) allowed a catalyst to be pretreated in the furnace under gas flow while taking bypass measurements of the reactant gas stream with online gas analysis equipment.

Reactors were either made of borosilicate glass (5.5 mm ID) or quartz (12 mm ID) tubing. The catalyst powder was held between two plugs of quartz wool in the borosilicate tubing and was supported by a quartz frit in the quartz tubing. The furnace was made from a stainless steel tube measuring 32 cm in length with an 18 mm ID and was heated by a Thermocoax heating element. The apparatus was wrapped with insulation and is shown in Fig. 3.2. In early experiments, a Novocontrol Micro 96 controller was used in conjunction with a K-type thermocouple placed in a well at the

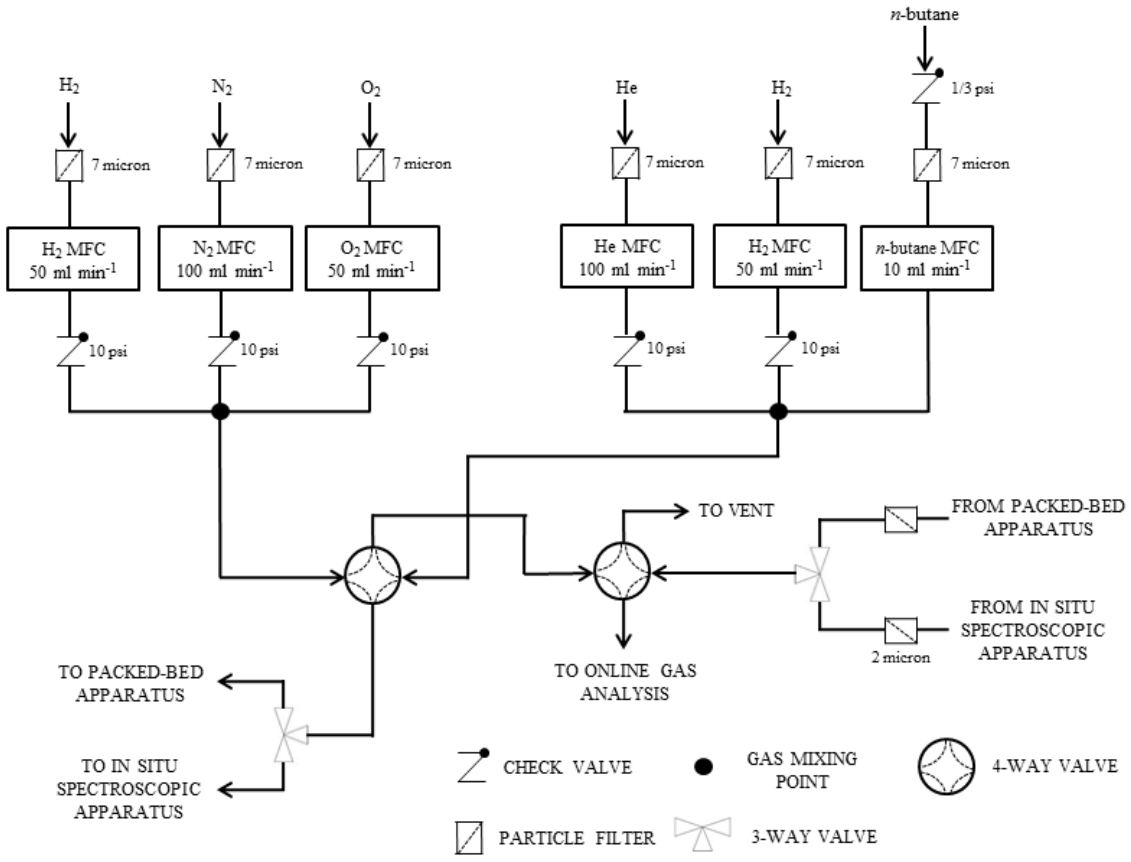


Figure 3.1: A schematic of the gas manifold.

center of the furnace's isothermal zone to control the temperature. In later experiments, the Micro 96 controller was replaced by an Omega CN3251 controller.

The length and location of the isothermal zone in the furnace was determined experimentally using a rod-like, K-type thermocouple inserted through the top, and then the bottom, of the furnace. Both the top and bottom openings (at the ends of the furnace) were covered with glass wool during the measurements. The temperature setting of the furnace was 673 K, and the measured temperature profiles are shown in Fig. 3.3. A discrepancy between measurements taken from the top and bottom of the reactor is caused by heat conducted down the rod of the thermocouple. After the tip is extended through the center of the isothermal zone (the point with the highest

temperature), heat conducted down the rod causes a temperature reading that is higher than the true temperature. The intersection of the two temperature profiles shown in Fig. 3.3 reveals the true center of the isothermal zone, which was estimated to be about 4 cm long. Thus, catalyst powder in all experiments was placed in the center of the experimentally determined isothermal zone.

Online gas analysis was performed using any combination of a gas chromatograph with a flame ionization detector (GC-FID), gas chromatograph with a mass spectrometer (GC-MS), or mass spectrometer (MS). The GC-MS was only used for online gas analysis in experiments involving carbon-13 labeled butane. The GC-FID (Varian, 3800 GC) and was equipped with a Fused Silica PLOT (Chrompack, 0.32 mm ID x 60 m) column for separation. The gas sample was injected using a sample loop connected to a 6-way valve with a split ratio of 6. The column pressure was held constant at 14 psi with N_2 as the carrier gas. After each injection, the column oven was held at a temperature of 353 K for 3 min and then heated at 20 K min^{-1} to 468 K. The temperature was held at 468 K for a period of time varying from 3.25 to 11.25 min. Online analysis was also performed in some cases with a Pfeiffer OmniStar GSD 320 MS. The equipment used electron impact ionization at 70 eV to cause fragmentation, and a C-SEM (Channeltron) and Faraday Cup for ion detection.

3.2.2 Catalytic measurements

A typical catalytic experiment began by pretreating the catalyst inside the reactor with one gas stream while taking bypass measurements of the reactant concentration in the other gas stream. Pretreatment of platinum-free samples involved



Figure 3.2: A picture of the furnace used to heat the packed bed apparatus.

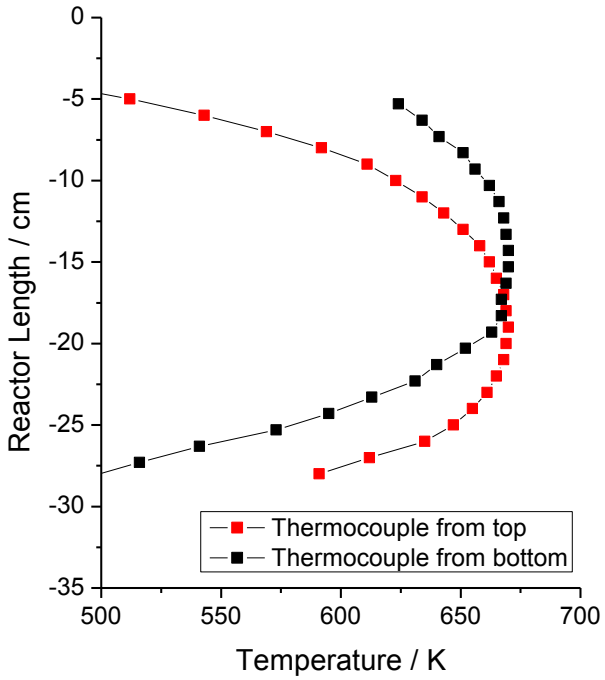


Figure 3.3: Temperature profile of furnace shown in Fig. 3.2, with a set point of 673 K, as measured from the top (black) or bottom (red) of the furnace.

heating the sample in a gas flow to remove adsorbed water. Details of the pretreatment are provided in individual chapters. Pretreatment of the platinum-containing samples involved a step to first remove adsorbed water and a subsequent step to reduce platinum to the metallic state.

The actual process parameters used during conversion of reactants varied widely. They included continuous flow of the reactant, pulses of the reactant, continuous flow of the reactant with pulses of a co-reactant, periodic changes in temperature, and other variations. Because of the wide variety, further experimental details have been placed in the Experimental section of individual chapters.

3.2.3 Treatment of GC data

Calibration of the online GC-FID was performed for acyclic alkanes and alkenes with up to six carbon atoms using gas mixtures from Matheson (GMT10416TC, GMT10450TC, GMT10407TC, and GMT10411TC). Product peak areas were converted to concentrations using response factors measured with the calibration gases, and then to formation rates using Eqn. 1:

$$r_A = \frac{\left(\frac{C_A}{1{,}000{,}000}\right) v_0 \left(\frac{F_T}{F_{T0}}\right)}{R \times T \times W \times 1E-6} \quad (1)$$

r_A is the product formation rate of species A (μmol g^{-1} h^{-1}), C_A is the concentration of species A in the effluent (ppm), v_0 is the total volumetric inlet flow rate (L h^{-1}, NTP), F_T is the flow rate of effluent stream (mol h^{-1}), F_{T0} is the flow rate of inlet stream (mol h^{-1}), R is the universal gas constant (mol K atm^{-1} L^{-1}), T is the temperature at normal conditions (273.15 K), and W is the catalyst mass (g). Selectivities are also reported in some cases, and are always molar selectivities (%) calculated using Eqn. 2:

$$\%S_A = \frac{C_A}{C_T} \times 100 \quad (2)$$

S_A is the molar selectivity of species A, C_A is the concentration of species A in the effluent (ppm), and C_T is the sum of all product concentrations (ppm).

3.3 In situ spectroscopy

3.3.1 Spectrometers

UV-vis-NIR spectroscopy was performed using a PerkinElmer Lambda 950 spectrometer. The spectrometer is a double beam instrument and was used to take both solution and diffuse reflectance spectra. The main components are i) the radiation source, ii) the wavelength selection and beam shaping elements, and iii) the detectors. Both D_2 and tungsten halogen lamps are necessary to provide acceptable radiation throughput over the wavelength region of interest (200-2500 nm). The D_2 lamp is used to provide radiation at shorter wavelengths in the ultraviolet region. The tungsten halogen lamp is used to provide radiation at longer wavelengths in the ultraviolet region, in the visible region, and in the near infrared region. The wavelength at which the instrument switches between the two radiation sources can be controlled by the operator.

The beam is first collimated, and then passes through an optical filter on its way to a holographic grating monochromator. The grating is used to separate the different wavelengths of radiation. In the Lambda 950 spectrometer, the grating is double sided and consists of 1440 lines/mm UV-vis blazed at 240 nm and 360 lines/mm NIR blazed at 1100 nm [1]. A slit, common beam mask (CBM), and attenuators are used to shape the beam and, if necessary, moderate its intensity. For diffuse reflectance experiments, a

CBM setting of 90% was used, and the slit was set at 2 nm in the UV-vis region and was controlled by a servo motor operating on a feedback loop in the NIR region. A photomultiplier is used as the detector in the UV-vis region and a PbS detector is used in the NIR region. The wavelength at which the detector switch occurs is also controlled by the operator.

A common problem when using optical accessories with a UV-vis-NIR spectrometer is the appearance of artifacts in the spectra when one of several changes occur in the spectrometer. For example, artificial jumps in the spectra are sometimes seen when the monochromator flips, the detector changes, the filter wheel rotates, or the lamp changes. The jumps are caused by large differences in throughput between sample and reference beams, and can consequently be lessened in severity if the throughput is balanced. With a Harrick Praying Mantis diffuse reflectance accessory, even when using a highly reflecting sample such as Spectralon, the radiation throughput in the sample beam is only about 4% of the throughput in the reference beam [2]. Throughout much of the work, the 10% attenuator installed in the spectrometer was used in the reference beam to help balance the throughput. More recently, we found that placing an external 4% attenuator in the reference beam (using a magnet) and foregoing use of the 10% attenuator in the spectrometer was even more effective. Because artifacts sometimes appear in the spectra, it is important to have a list of changes that occur in the spectrometer during a scan. The wavelength at which each event occurs can be controlled in the software; the wavelengths that were used in this work are provided in Table 3.2.

Table 3.2: List of events that occur in the Lambda 950 UV-vis-NIR spectrometer during a scan

Wavelength / nm	Spectrometer event
3350	Filter T-LPG-2.5
2681	Filter T-LPG-1.5
1670	Filter T-LPG-1.0
1190	Filter RG780
860.8	Monochromator flip
860.8	Detector switch
810	Filter RG665
690	Filter OG550
562	Filter BG38
379	Filter UG11
319	Lamp change (and filters removed)
150	Glass filter

A PerkinElmer Spectrum 100 FTIR spectrometer was used in conjunction with an optical accessory to collect diffuse reflectance infrared spectra. A mercury cadmium telluride (MCT) detector was used in all experiments and the J-stop iris was set at 8.94 mm. The resolution is specified in individual figures.

3.3.2 Diffuse reflectance and in situ spectroscopic equipment

A Praying Mantis diffuse reflectance accessory (Harrick Scientific, DRP-P72 for UV-vis-NIR, DRP-P11 for FTIR) was used to collect diffuse reflectance spectra. The accessories use two off-axis ellipsoidal mirrors, arranged with a common focal point, to both direct radiation onto the sample and collect the diffusely reflected radiation from the sample. A review of both the theory, and practical application, of such optical accessories has been provided by Jentoft [2]. A picture of the DRP-P72 is shown in Fig. 3.4. Fluorilon-99 (Avian Technologies) was used as a reflectance standard in UV-vis-NIR experiments. KBr (Sigma, FT-IR grade) was dried in situ and used as a reflectance standard in FTIR experiments.

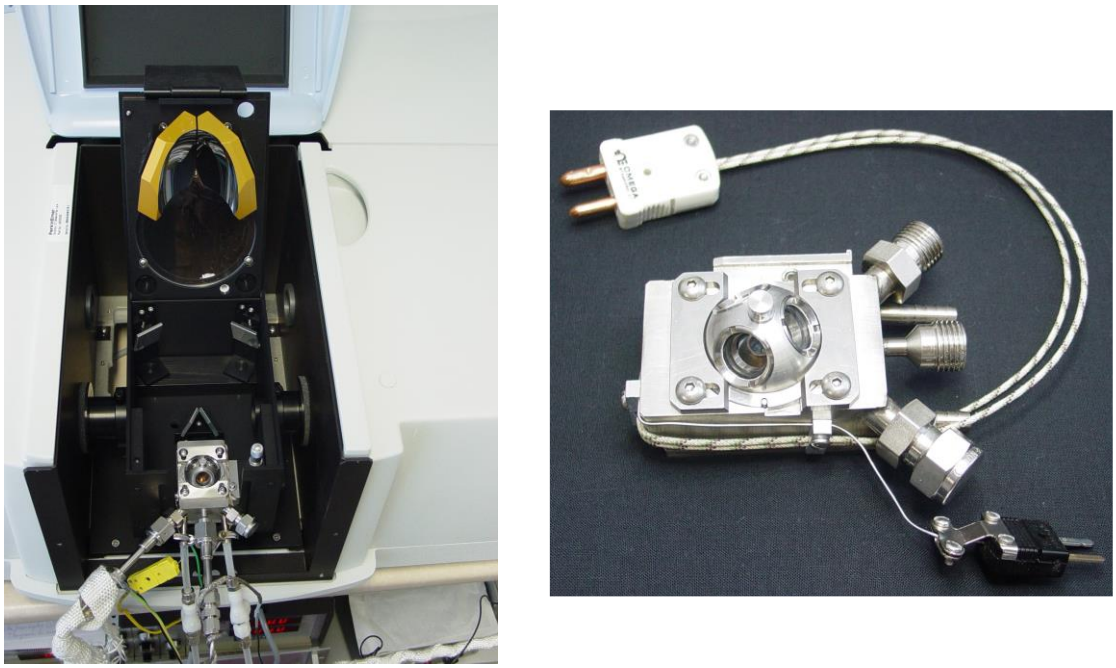


Figure 3.4: A picture of the HVC-VUV environmental chamber hooked up to gas lines and placed in the DRP-P72 Praying Mantis accessory (left), and a zoomed-in picture of the HVC-VUV environmental chamber (right).

In situ experiments were performed in environmental chambers (Harrick Scientific, HVC-VUV for UV-vis-NIR, CHC-CHA-3 for FTIR). The chambers are made of 316 stainless steel, which is supposed to be inert under the temperatures applied, but for unknown reasons became catalytically active for methanation in early stages of the work. Both chambers have since been coated with a layer of silicon (Silcotek, Silcolloy 1000 coating) that eliminated the methanation activity. A picture of the HVC-VUV chamber (before coating) is shown in Fig. 3.4.

Several important features of the environmental chambers are the i) sample stage, ii) three gas ports, iii) removable dome, and iv) heating element. The chambers can be operated at elevated temperatures under flow-through conditions, allowing for "operando" experiments to be performed. Catalyst powder is placed in the sample cup

on top of a holder; if higher catalyst loadings are desired, a wire screen can be used as the holder. If lower catalyst loadings are desired, a stainless steel frit can be used to occupy some of the sample cup volume but still permit downflow. One point of contention with similar chambers has been the actual temperature in the sample bed. Because the chamber is heated with a cartridge placed below the sample cup, it has been argued that the temperature in the catalyst bed, specifically at the top, is significantly lower than the setting of the control thermocouple placed next to the heating cartridge. For example, Gao et al. [3] reported a temperature discrepancy between the setpoint of the chamber and the temperature in the powder at the top of the sample cup, as measured with an additional thermocouple, of as much as 125 K. Several other examples are given in the review by Jentoft [2]. Because a thermocouple cannot be in intimate contact with a powder, it is possible that the measured temperatures overestimate the true temperature gradient. In any case, in all sections of this work, the reported temperature is the setpoint of the thermocouple integrated in the body of the chamber below the sample cup.

3.3.3 The Kubelka-Munk function

In diffuse reflectance spectroscopy, the Kubelka-Munk function is often used in an attempt to relate spectroscopic information to the concentration of an absorbing species. A derivation of the Kubelka-Munk function, and a review of the theory behind it, has been provided by Jentoft [2]. The mathematical relation is shown in Eqn. 3:

$$\frac{K}{S} = \frac{(1 - R_\infty)^2}{2R_\infty} = F(R_\infty) \tag{3}$$

K is the absorption coefficient, S is the scattering coefficient, R_∞ is the reflectance, and $F(R_\infty)$ is the Kubelka-Munk value. The function is only proportional to the

concentration over a limited range of reflectance; the range may vary from sample to sample, but the preferred working range is 20% to 60% reflectance (corresponding to Kubelka-Munk values of 0.13 and 1.6) [2]. In theory, the function requires the sample to be "infinitely thick" so that no light is transmitted. In practice, the depth at which spectroscopic information is gathered has been debated, and almost certainly varies from sample to sample. Simmons claimed that most powdered samples could be considered infinitely thick at 1 mm [4]. Others have concluded that a deeper sample is required [5]. To gauge the depth at which spectroscopic information was gathered in our mordenite samples, a series of experiments was performed in the HVC-VUV environmental chamber with mixtures of Na-mordenite powder, which is white in appearance, and copper sulfate powder, which is blue in appearance. The depth of the

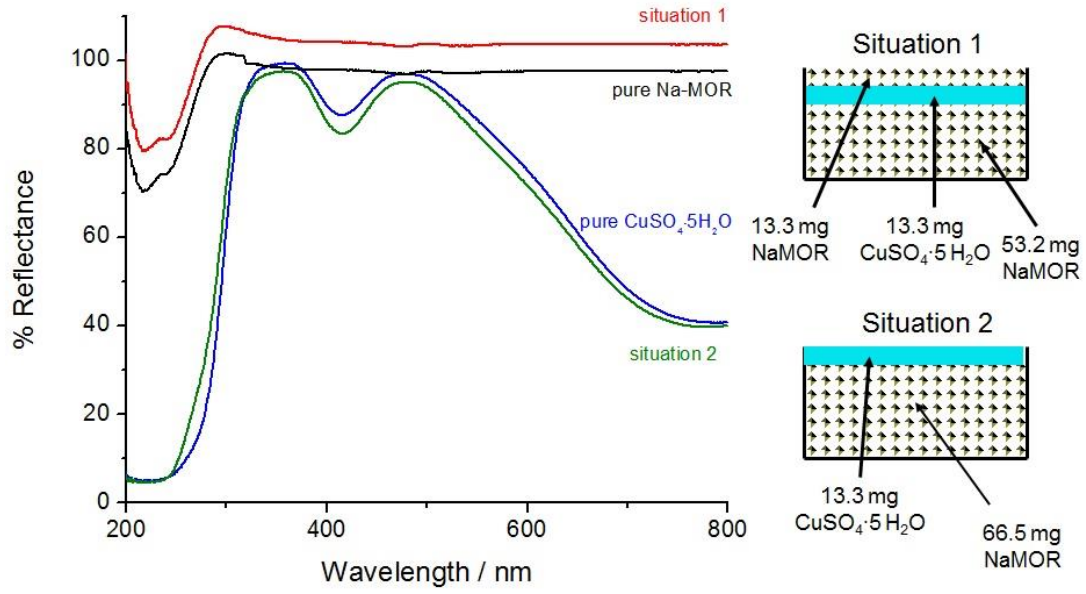


Figure 3.5: Diffuse reflectance UV-vis spectra of $CuSO_4 \cdot 5H_2O$, Na-mordenite, and mixtures thereof. Blue line: ground $CuSO_4 \cdot 5H_2O$; black line: Na-mordenite powder; red line: ground $CuSO_4 \cdot 5H_2O$ covered by Na-mordenite powder (situation 1); green line: ground $CuSO_4 \cdot 5H_2O$ on top of Na-mordenite powder (situation 2).

sample cup in the environmental chamber is 3.15 mm. As shown in Fig. 3.5, when copper sulfate was covered by only 13.3 mg of Na-mordenite (corresponding to an estimated depth of 0.5 mm) the spectroscopic features of the copper sulfate were completely eliminated. Thus, it is likely that much of the spectroscopic information was gathered from the catalyst powder in the top of the sample cup.

3.3.4 Photophysics of electronic spectra of unsaturated hydrocarbons

Electronic spectroscopy is used throughout Chapters 6-8 to analyze unsaturated hydrocarbons. In this section, the necessary background information about absorption of UV-vis radiation by unsaturated hydrocarbons will be provided. Special attention is given to some of the species that will be of interest in later chapters.

Absorption of UV-vis radiation by any species corresponds to a quantized transition of an electron. In terms of molecular orbital (MO) theory, this involves exciting an electron from a molecular orbital that is lower in energy to a molecular orbital that is higher in energy. In unsaturated hydrocarbons, this mostly involves excitation from a π bonding molecular orbital to a π anti-bonding (π^*) molecular orbital. Other transitions, such as $\sigma^* \leftarrow \sigma$ transitions are also possible, but occur at energies that are too high to be measured with standard UV-vis equipment. Although the transitions are quantized, the absorptions appear in spectra as broad bands. Various vibrational and rotational energy levels higher in energy than the fundamental $\pi^* \leftarrow \pi$ transition are also involved as excited states and are responsible for radiation being absorbed over a wider range of energy. Vibrational and rotational features can sometimes be resolved in low temperature, gas phase spectra. The energy (wavelength) at which the absorption occurs depends on the particular molecular orbitals involved in

the transition. More specifically, the probability that a transition will be induced by the oscillating electric field in an electromagnetic wave depends on the square of the transition moment integral [6]. A simplified transition moment integral expression is shown in Eqn. 4:

$$M = \int \psi'^{*} \hat{\mu} \psi d\tau \tag{4}$$

M is the transition moment integral, ψ is the time independent wavefunction, $\hat{\mu}$ is the dipole moment operator, * denotes a complex conjugate, and *prime* denotes an excited state [7]. Because the wavefunction contains vibrational, electronic, and spin components, and because the dipole moment operator depends on both nuclear and electron coordinates, the transition moment integral may be re-written as Eqn. 5:

$$M = \int \psi_{v'}^{*} \psi_{v} d\tau_{n} \int \psi_{e'}^{*} \widehat{\mu_{e}} \psi_{e} d\tau_{e} \int \psi_{s'}^{*} \psi_{s} d\tau_{s} \tag{5}$$

ψ_v is the vibrational wavefunction, ψ_e is the electronic orbital wave function, and ψ_s is the electron spin wave function [7]. The equation is important because it is the basis for several selection rules, some of which are obeyed more rigorously than others.

The first term in Eqn. 5 is known as the Franck-Condon factor and represents the overlap of vibrational wavefunctions in the ground and excited states [6]. If the wave functions are in phase the transition is reinforced, and if the wavefunctions are orthogonal the transition moment integral drops to zero and the transition is said to be "forbidden". The Franck-Condon factor also plays a role in determining the band shape [6]. The second term in Eqn. 5 is the basis for the symmetry selection rules, which can be understood using group theory. The transition is orbitally allowed if the triple product of the irreducible representations of the point group for the ground state ψ_e,

transition moment integral $\hat{\mu}$, and excited state $\psi_{e'}$ contains the totally symmetric irreducible representation of the molecule [7]. The third term in Eqn. 5 shows that the transition is forbidden if the spins in ground and excited states are different. That is, singlet ← singlet and triplet ← triplet transitions are spin allowed, whereas singlet ← triplet and triplet ← singlet transitions are spin forbidden [7].

Two general statements can be made about trends in absorption of UV-vis radiation within series of unsaturated hydrocarbons. Both the wavelength of maximum absorption and the absorption coefficient generally increase with the size of the conjugated π system. For example, the position of the LUMO ← HOMO (lowest unoccupied and highest occupied molecular orbitals, respectively) transitions of naphthalene, anthracene, and tetracene occur at approximately 280, 370, and 475 nm, respectively, and the absorption coefficients increase with the size of the molecule [6]. The same trends have been shown to be true for series of aliphatic polyenes [8].

An individual species can have multiple electronic transitions, and there are many systems of notation for labeling such transitions. Some of the most popular include: enumerative, group theory, Kasha, Platt, Mulliken, and Clar [6]. Additionally, rules exist that correlate molecular structure and the energy of the LUMO ← HOMO transition. For example, the Woodward-Fieser rules use the wavelength of maximum absorption of the chromophore and adjust for the number and type of auxochromes in dienes, polyenes, and conjugated ketones and aldehydes [9].

The electronic absorptions of benzene can be used to illustrate some of the aforementioned points, and to introduce some new ones. The benzene molecule belongs to the point group D_{6h} and has π molecular orbitals as shown in Fig. 3.6. The ground

state corresponds to an electron configuration of $a_{2u}(2)\ e_{1g}(4)$ and has $^1A_{1g}$ symmetry. Exciting an electron from the HOMO to the LUMO causes the electron configuration to change to $a_{2u}(2)\ e_{1g}(3)\ e_{2u}(1)$ and, because the HOMO and the LUMO molecular orbitals are both degenerate, there are three spin-allowed transitions. They are: $^1E_{1u} \leftarrow {}^1A_{1g}$, $^1B_{1u} \leftarrow {}^1A_{1g}$, and $^1B_{2u} \leftarrow {}^1A_{1g}$ [7]. Only the $^1E_{1u} \leftarrow {}^1A_{1g}$ transition is orbitally allowed, but the other two transitions can be intensified by coupling with vibrations of a particular symmetry. For example, the $^1B_{2u} \leftarrow {}^1A_{1g}$ transition can couple with vibrations of b_{1g} or e_{2g} symmetry to become vibronically allowed [6].

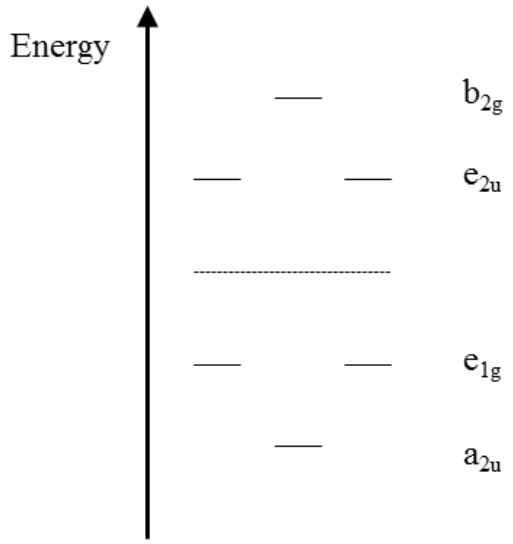


Figure 3.6: Representation of the π molecular orbitals of benzene.

Some bands, especially in symmetric, planar molecules, show vibrational fine structure. In the acene family, the band characterized by the most well resolved vibrational structure is known as the benzenoid band. The benzenoid band of anthracene is shown as an example in Fig. 3.7. The spacing between the individual components of the benzenoid band provides information about the spacing between vibrational levels

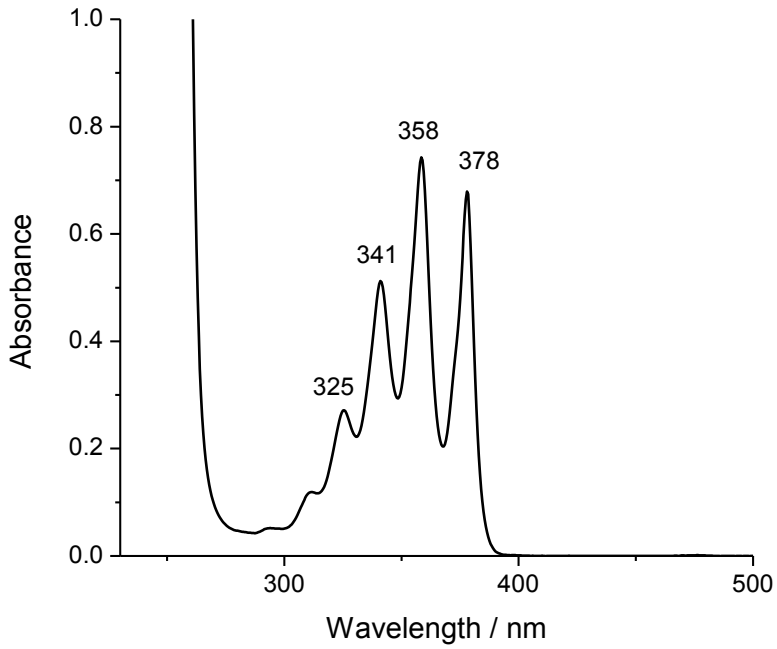


Figure 3.7: Ultraviolet-visible spectrum of anthracene in hexane

in the excited state. The lowest energy transition in benzene ($^1B_{2u} \leftarrow {}^1A_{1g}$) shows vibrational structure but is orbitally forbidden. However, if the symmetry of the molecule is lowered, for example by adsorption on a surface, the absorption becomes more intense [10]. Additionally, the wavelength at which the neutral species absorbs is altered very little by adsorption on a surface [10,11].

One final point is about the change in electronic structure upon protonation. Although it was written in 1968, a noteworthy review of the topic is provided by Olah and co-workers [12]. Upon protonation of an aromatic hydrocarbon or a polyene in a mineral acid, a new electronic band appears at longer wavelengths. For example, a band forms at 325 nm after protonation of benzene [13]. Protonation of 2,4-dimethyl-1,3-pentadiene (absorbing as a neutral species at 217 + 3x5 = 232 nm by the Woodward-Fieser rules) forms the 2,4-dimethylpentenyl cation, which absorbs at 305 nm [8]. The

absorption positions of protonated aromatic species have been shown, in multiple cases [11,14], to not differ significantly in mineral acid versus on a solid acid. Additionally, DFT calculations have shown the aromatic cations to be stable within the framework of a zeolite [15].

Surprisingly, knowledge about the electronic structure of protonated hydrocarbons is limited [16]. Further, simulation of electronic spectra, even of neutral species, is still rather inaccurate. Currently, the most popular means by which to calculate electronic spectra in a DFT framework is time-dependent density functional theory (TDDFT). The excited states are solutions of the time-independent stationary Schrödinger equation, and thus are not time-dependent. However, time dependent response is necessary to capture the perturbation by an electronic field oscillating at a particular frequency [17]. Rode et al. [16] recently calculated the electronic absorption spectrum of protonated benzene using TDDFT and found the calculated absorption bands to be within 30 nm of those measured by experiment. Calculations have also been performed on polyenes and cations of polyenes, and were found to more accurately represent the spectra of the cations [18].

References

[1] Perkin Elmer, Technical Specifications for the LAMBDA 1050 UV/Vis/NIR and LAMBDA 950 UV/Vis/NIR Spectrophotometers <http://www.perkinelmer.com/CMSResources/Images/44-74789SPC_LAMBDA1050LAMBDA950.pdf>, accessed February 15, 2013.

[2] F.C. Jentoft, Adv. Catal. 52 (2009) 129.

[3] X. Gao, J.-M. Jehng, I.E. Wachs, J. Catal. 209 (2002) 43.

[4] E.L. Simmons, Appl. Optics 14 (1975) 1380.

[5] Z. Sojka, F. Bozon-Verduraz, M. Che, in G. Ertl, H. Knözinger, J. Weitkamp, Eds., Handbook of Heterogeneous Catalysis, ed. 2, Verlag Chemie, Weinheim, 2008.

[6] M. Klessinger, J. Michel, Excited States and Photochemistry of Organic Molecules, New York, VCH, 1995.

[7] D.C. Harris, M.D. Bertolucci, Symmetry and Spectroscopy: An Introduction to Vibrational and Electronic Spectroscopy, Dover Publications, New York, 1989.

[8] T.S. Sorensen, J. Am. Chem. Soc. 87 (1965) 5075.

[9] L.G. Wade, Jr., Organic Chemistry, 6th Ed., Pearson Prentice-Hall, Upper Saddle River, NJ, 2006.

[10] F.C. Jentoft, in M. Che, J.C. Védrine (Eds.), Characterization of Solid Materials and Heterogeneous Catalysts: From Structure to Surface Reactivity, Wiley-VCH, Weinheim, Germany, 2012.

[11] M. Bjørgen, F. Bonino, S. Kolboe, K.P. Lillerud, A. Zecchina, S. Bordiga, J. Am. Chem. Soc. 125 (2003) 125.

[12] G.A. Olah, C.U. Pittman, M.C.R. Symons, in G.A. Olah, R.v.R. Schleyer (Eds.), Carbonium Ions, vol. 1, Interscience, New York, 1968, p. 153-222.

[13] H.-H. Perkampus, E. Baumgarten, Angew. Chem. Intl. Ed. 3 (1964) 776.

[14] H.P. Leftin, M.C. Hobson, Adv. Catal. 14 (1963) 115.

[15] H. Fang, A. Zheng, J. Xu, S. Li. Y. Chu, L. Chen, F. Deng, J. Phys. Chem. C 115 (2011) 7429.

[16] M.F. Rode, A.L. Sobolewski, C. Dedonder, C. Jouvet, O. Dopfer, J. Phys. Chem. A 113 (2009) 5865.

[17] F. Furche, D. Rappoport, in M. Olivucci (Ed.), Computational Photochemistry, Elsevier, Amsterdam, 2005.

[18] U. Salzner, J. Chem. Theory Comput. 3 (2007) 219.

4 The Effect of Olefins or Co-adsorbates on Reaction Pathways of *n*-Butane on H-mordenite and Pt/H-mordenite

4.1 Introduction

As discussed in Section 1.2.2, the Pt/chlorided alumina catalysts currently used to perform skeletal isomerization of *n*-butane are suboptimal for a number of reasons. The zeolite H-mordenite, already used industrially to perform skeletal isomerization of C5/C6 alkanes, is a natural replacement candidate and has received much attention. Two glaring problems with its implementation are the low selectivity to isobutane, at the expense of formation of side products such as propane and pentanes, and high temperature requirements. Each is related to the mechanism by which gas phase products are formed. A review of the isomerization reaction chemistry is provided in Section 1.2.4.

Thus far, there has been no consensus about the relative contributions of intra- and intermolecular skeletal isomerization pathways of *n*-butane on solid acids. On H-mordenite, experimental evidence suggesting dominance of intermolecular pathways has included: intermolecular carbon-13 scrambling from 1-^{13}C-*n*-butane [1] and 1-^{13}C-isobutane [2], production of propane and pentane side products [3,4], isobutane reaction orders with respect to *n*-butane of close to 2 [4,5], and a product distribution similar to that from isooctane [6]. Some investigators claim the participation of each pathway can be tuned by varying process conditions such as temperature [3], concentration of acid sites [3,7], conversion [3], reactant partial pressure [3,8], presence of H_2 [4], and presence of platinum for the production of olefins [9]. Evidence of a significant contribution from an intramolecular isomerization pathway includes: isobutane reaction

orders with respect to *n*-butane of 1.17 [7] and 1 [4], differences in selectivity to isobutane with varying reaction conditions [4], and the inability to model isobutane formation using only a second order kinetic model [8].

One important variable, which has been investigated to some extent but not linked to specific isomerization pathways, is the concentration of gas phase olefins. Fogash et al. found H-mordenite to be completely inactive at 473 K for *n*-butane [10] or isobutane [11] conversion in the absence of olefins in the feed, but to catalyze product formation when as little as 55 ppm of butene was added. Engelhardt [12] found that the rate of *n*-butane conversion could be significantly enhanced by addition of ethene, propene, or isobutene to the feed. Similar observations regarding the effect of olefins have been made with sulfated zirconia; olefins have been found to promote both conversion of *n*-butane [13-17] and deactivation [14,62]. Okuhara and co-workers [18,19] found that carbon-13 scrambling in products produced from 1,4-$^{13}C_2$-*n*-butane on sulfated zirconia could be greatly suppressed by inclusion of platinum on the catalyst and H_2 in the feed. They hypothesized that platinum and H_2 were unfavorable to the intermolecular pathway because they control the butene concentration, but did not show any data relating to the butene concentration to prove the point. The promoting effect of olefins on butane isomerization is certainly not a new revelation; the observation can be traced back at least to 1946 and the work of Pines and Wackher [20].

The original goal of this work was to determine the amount of isobutane formed by intramolecular and intermolecular pathways using a rigorous kinetic analysis. In theory, the two pathways should be distinguishable by kinetic parameters such as reaction order and activation energy. If propane, pentanes, and isobutane are all

produced through similar intermolecular pathways, their kinetic parameters may be similar. However, a rigorous kinetic analysis proved to be elusive because olefins, specifically *n*-butenes, were found to play a critical role in the reaction chemistry. Instead of the originally intended kinetic model, we report here on the dependence of isomerization and disproportionation pathways on the *n*-butene partial pressure and discuss the implications for the skeletal isomerization mechanism.

4.2 Experimental

4.2.1 Experiments with an impure feed

4.2.1.1 Conversion of *n*-butane using a separate reactor to control the concentration of *n*-butenes in the feed

An experiment was performed using two reactors placed in series, one of which was used to control the concentration of *n*-butenes in the feed. The first reactor was the HVC-VUV environmental chamber described in Section 3.3.2. It contained a 1 wt% Pt/SiO_2 catalyst, which was reduced in the chamber at 548 K in a flow of 30 ml min^{-1} H_2 for 1.5 h and then cooled to the desired operating temperature. The second reactor was the packed bed apparatus described in Section 3.2.1 which contained 87 mg of H-mordenite (M1) in a 5.5 mm ID borosilicate glass tube. The mordenite had been calcined in a horizontal muffle furnace under an air (Airgas, zero grade) flow rate of 100 ml min^{-1} at a temperature of 873 K for 2 h. Before reaction, the H-mordenite was pretreated by raising the temperature at 5 K min^{-1} to 673 K in a 30 ml min^{-1} (NTP) flow of synthetic air and given sequential 0.5 h treatments in synthetic air, N_2, and H_2, and then cooled to the reaction temperature of 473 K. During reaction, the flow to the first

reactor consisted of 3 ml min^{-1} *n*-butane and 12 ml min^{-1} helium and was mixed with 15 ml min^{-1} of H_2 after exiting the chamber. A temperature of 323 K was used to keep the concentration of butenes at 0 ppm and a temperature of 433 K was used to control the butene concentration at 18 ppm.

4.2.1.2 Conversion of *n*-butane while administering pulses of olefin or other co-adsorptives

Conversion of *n*-butane while administering pulses of propene, 1-butene, and 1,3-bis(trifluoromethyl)benzene was performed in the packed bed apparatus described in Section 3.2.1. A 5.5 mm ID borosilicate glass tube was used as the reactor. Conversion of *n*-butane while administering pulses of 1-hexene or nitrobenzene was performed in the environmental chamber described in Section 3.3.2.

H-mordenite (M1) was used for experiments with pulses of propene, 1-butene, and 1,3-bis(trifluoromethyl)benzene. Calcination was performed in a horizontal muffle furnace at a temperature of 873 K for 2 h in a 100 ml min^{-1} flow of air (Airgas, zero grade). H-mordenite (M2) was used for experiments with 1-hexene and nitrobenzene. Calcination was performed in a 12 mm ID quartz tube at a temperature of 823 K for 3 h under synthetic air flowing at 100 ml min^{-1} using the apparatus described in Section 3.2.1. M1 was pretreated before reaction using the procedure described in Section 4.2.1.1. M2 was pretreated by heating to a temperature of 673 K at 5 K min^{-1} in a flow of 30 ml min^{-1} N_2 and holding for 1 h. Other materials were: propene (Matheson, 99.97%), 1-butene (Sigma, ≥ 99%), 1-hexene (Fluka, 99.8%), 1,3-bis(trifluoromethyl)benzene (Sigma, 99%), and nitrobenzene (Sigma, 99+%).

Reactions were performed at 473 K using a total flow rate of 30 ml min^{-1} with a 10 kPa *n*-butane partial pressure and 90 kPa helium partial pressure. 1-Butene and propene pulses were added to the gas stream using a 6-way valve with a 30 µL sample loop. 1-Hexene, 1,3-bis(trifluoromethyl)benzene, and nitrobenzene pulses were admitted to the gas stream via a septum in the inlet gas line using a 10 µl Hamilton GASTIGHT syringe.

4.2.2 Experiments with a pure feed

4.2.2.1 Measurement of product formation rates over a range of temperatures, *n*-butane partial pressures, and H_2 partial pressures

The catalysts used were H-mordenite (M1) and Pt/H-mordenite (Pt/M-C1). Calcination to make M1 was performed in a horizontal muffle furnace. A quartz boat containing a catalyst mass of 1.5 g was placed inside a 2.3 cm ID quartz tube, which was placed inside the furnace. The air (Airgas, zero grade) flow rate was 100 ml min^{-1}. The temperature was first increased at 2 K min^{-1} to 423 K, held for 1 h, and then increased at 5 K min^{-1} to 873 K and held for 2 h.

The packed bed apparatus described in Section 3.2.1 was used with a 5.5 mm ID borosilicate glass tube as the reactor. Pretreatment of the H-mordenite was performed as described in Section 4.2.1.1. Pretreatment of Pt/H-mordenite began by raising the temperature at 5 K min^{-1} to 403 K in N_2 flowing at 30 ml min^{-1} and was held isothermal for 4 h. The temperature was then increased at 5 K min^{-1} to 560 K in H_2 flowing at 30 ml min^{-1} and was held for 4 h. The reactant gas mixture was composed of *n*-butane (Matheson, Research Grade 99.99%, 14 ppm isobutane, < 1 ppm propylene impurities measured in-house), helium, and H_2.

Product formation rates were measured over a range of temperatures (543-583 K, 10 K increments), *n*-butane partial pressures (3.3-13.3 kPa, 3.3 kPa increments), and H_2 partial pressures (30-90 kPa, 20 kPa increments). The total conversion was in the range of what is considered to be differential, not exceeding 1.7% on H-mordenite or 2.6% on Pt/H-mordenite. The catalyst loading was 82 mg for H-mordenite and 80 mg for Pt/H-mordenite.

Conversion of *n*-butane on both catalysts began at conditions of 543 K, 3.3 kPa *n*-butane, and 90 kPa H_2. Helium was used as the balance gas. After taking four GC measurements over a duration of about 1 h, the temperature was increased by 10 K and four measurements were taken again. This procedure was repeated until measurements had been taken over the specified range of temperatures. The temperature was then lowered to 543 K and four measurements were taken at the initial set of conditions to determine if deactivation had occurred. The partial pressure of *n*-butane was then increased by 3.3 kPa while holding the partial pressure of H_2 constant, and the process was repeated. After taking measurements at the four *n*-butane partial pressures of interest, the partial pressure of H_2 was lowered by 20 kPa and the process was repeated. This procedure was used to measure product formation rates under all conditions of interest or until deactivation was apparent from time-on-stream data.

4.2.2.2 Measurement of product formation rates on Pt/H-mordenite using different space times

Experiments were performed using the apparatus described in Section 3.2.1 using a 12 mm ID quartz tube as the reactor. The catalyst was Pt/M-C2 and was mixed with 1.0 mm diameter quartz beads in a 3:2 mass ratio. Four catalyst loadings between

0.10 g and 1.00 g were used. Pretreatment began by raising the temperature at 5 K min^{-1} to 403 K under N_2 flowing at 50 ml min^{-1} and was held isothermal for 4 h. The temperature was then increased at 5 K min^{-1} to 573 K under flowing H_2 and held for 4 h. Reactions were performed at 573 K using a total gas flowrate of 50 ml min^{-1}, with *n*-butane, helium, and H_2 partial pressures of 10, 40, and 50 kPa, respectively.

4.3 Results

4.3.1 Conversion of *n*-butane with olefins or co-adsorptives in the feed

4.3.1.1 Conversion of *n*-butane while co-feeding *n*-butene

Figure 4.1 illustrates the dramatic impact of *n*-butenes on the rate of *n*-butane conversion. An olefin-free feed was used in the first 75 minutes on stream, and there

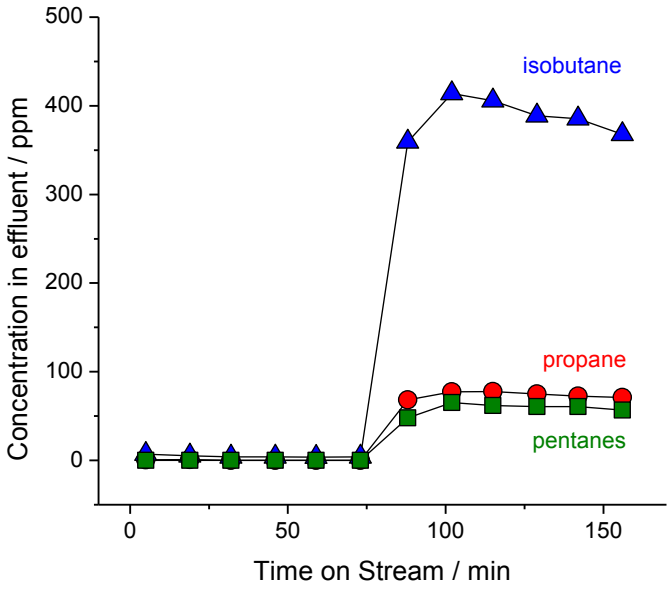


Figure 4.1: The concentration of gas phase products resulting from conversion of *n*-butane (10 kPa partial pressure) on H-mordenite (M1) at a temperature of 473 K using 50 kPa H_2 and 40 kPa helium as diluents. The concentration of *n*-butenes in the feed was 0 ppm during the first 75 minutes on stream and 18 ppm after 75 minutes on stream.

was almost no conversion of *n*-butane to any gas phase products. After 75 minutes on stream, 18 ppm of *n*-butenes were added to the feed and significant conversion of *n*-butane was observed. The concentration of products in the reactor effluent is shown in parts per million (ppm) in Fig. 4.1 in lieu of the rate to help illustrate the magnitude of the effect of *n*-butenes on gas phase product formation. The isobutane concentration reached 415 ppm and the concentration of propane and pentanes (*n*-pentane and 2-methylbutane) was between 60 and 80 ppm. The concentration of *n*-butenes in the effluent stream was 1-3 ppm indicating that, to some extent, they were consumed. A small decrease in product concentration was observed with time on stream during the period in which gas phase products were formed.

4.3.1.2 Conversion of *n*-butane while administering pulses of propene, 1-butene, or 1-hexene

Pulses of olefin also had an effect on *n*-butane conversion. Propene and 1-butene pulses caused products to form above the base rate for about 5 min, even though the residence time in the catalyst bed was only about 0.2 s (Fig. 4.2). Isobutane was produced with the highest selectivity in both cases, and propane and pentanes were the main side products. Pulses of 1-hexene also caused gas phase products to form (Fig. 4.3). In this case, a measureable amount of hexanes were also formed. For example, the GC injection immediately following the first pulse of 1-hexene measured 34 ppm of hexanes. From the signal at m/z = 96, it is apparent that the concentration of hexanes in the effluent increased quickly and then declined over the next 2-3 min. The diffuse reflectance UV-vis spectra collected in situ (not shown) revealed an intense band at 294 nm. This band is known to be formed from olefins and will be discussed in Chapter 6.

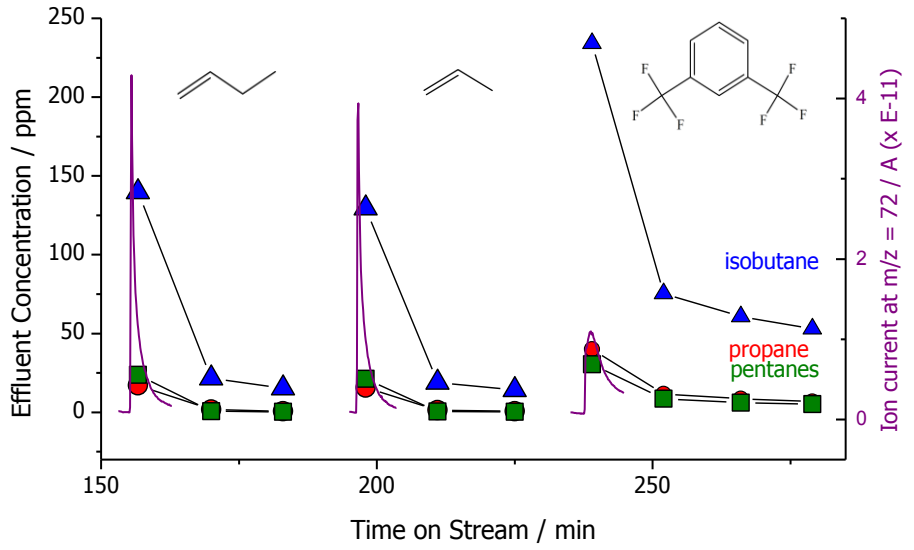


Figure 4.2: Concentration of gas phase products produced from conversion of *n*-butane (10 kPa partial pressure) on H-mordenite (M1) at a temperature of 473 K with 30 µL gas pulses of 1-butene and propene, and a 0.5 µL liquid pulse of 1,3-bis(trifluoromethyl)benzene.

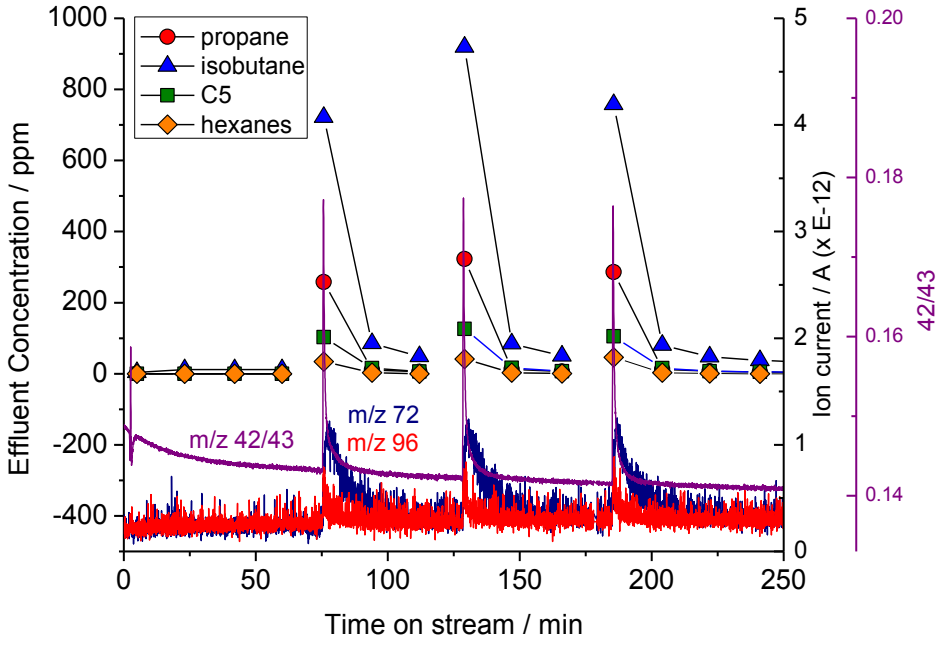


Figure 4.3: Concentration of gas phase products produced from conversion of *n*-butane (10 kPa partial pressure) on H-mordenite (M2) at a temperature of 473 K with three consecutive 1 µL liquid injections of 1-hexene.

4.3.1.3 Conversion of *n*-butane while administering pulses of nitrobenzene or 1,3-bis(trifluoromethyl)benzene

Two aromatic species were also found to promote *n*-butane conversion. A pulse of 1,3-bis(trifluoromethyl)benzene caused a longer period of *n*-butane conversion than pulses of either propene, 1-butene, or 1-hexene (Fig. 4.2). While the initial burst of activity was not as intense as observed with pulses of aliphatic olefins, the conversion did not return to the base level within 1 h after the pulse.

A somewhat similar effect was observed with pulses of nitrobenzene (Fig. 4.4). A nitrobenzene pulse caused the rate of *n*-butane conversion to double. Because nitrobenzene has a boiling point of 484 K, and because both the inlet line and reaction chamber were only heated to 473 K, the flow of nitrobenzene into the reaction chamber

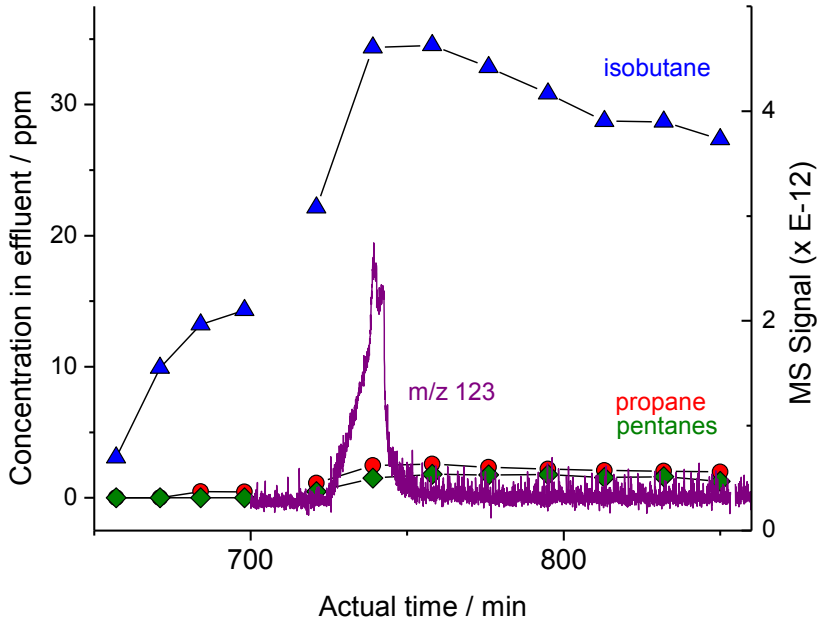


Figure 4.4: Concentration of gas phase products produced from conversion of *n*-butane (10 kPa partial pressure) on H-mordenite (M2) at a temperature of 473 K before (first 50 min) and after (after the first 50 min) a 1 µL injection of nitrobenzene (m/z = 123).

relied on vapor pressure. Thus, the MS trace of the selected nitrobenzene fragment (m/z = 123) showed that nitrobenzene eluted from the cell for about 20 min. Diffuse reflectance UV-vis spectra recorded in situ (not shown) revealed a strong band at 285 nm, indicating that nitrobenzene remained on the catalyst throughout the duration of the experiment.

4.3.2 Conversion of a pure *n*-butane feed

4.3.2.1 Catalyst stability

To ensure that measurements taken over the duration of the experiments described in Section 4.2.2.1 were not corrupted by deactivation, rate measurements were periodically repeated under conditions that had already been tested. An example of the data collected using the procedure is shown in Fig. 4.5. An obvious decrease in the rate of product formation was not observed, either in time on stream data or by re-measuring rates at previously used conditions, using H_2 partial pressures of 50, 70, or 90 kPa. On Pt/H-mordenite, the onset of deactivation was observed in time on stream data at conditions of 583 K, 10 kPa *n*-butane, and 30 kPa H_2. This set of conditions was not used in reporting rates and selectivities or in calculation of apparent kinetic parameters.

The final measurement was performed under a set of conditions used within the first five hours on stream (3.3 kPa *n*-butane, 90 kPa H_2, 583 K), allowing a direct comparison of catalyst performance at the beginning and end of the five day measurement period. Comparing the initial to the final rates, the overall conversion decreased by 15% on Pt/H-mordenite and 16% on H-mordenite. Approximately 6% of the decrease on Pt/H-mordenite occurred under conditions at which deactivation was

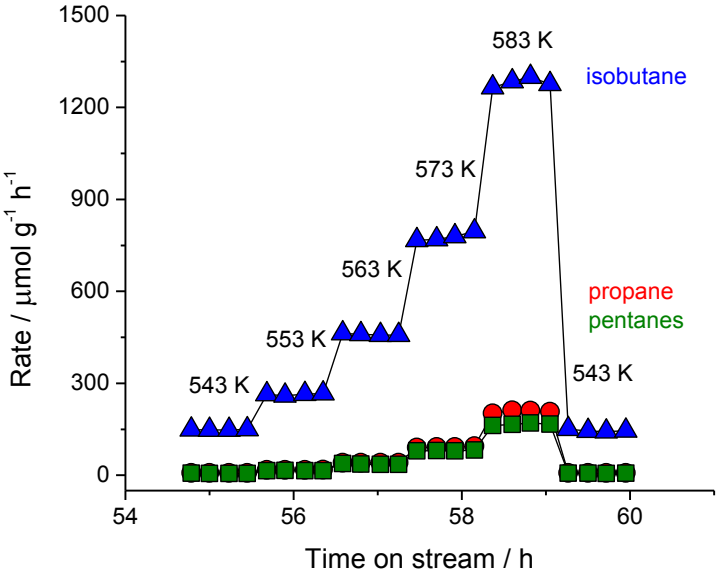


Figure 4.5: Rates of formation of the main gas phase products produced during conversion of *n*-butane (10 kPa partial pressure) on Pt/H-mordenite (Pt/M-C1, W/F = 0.17 h) as a function of time on stream. Other conditions: 30 ml min^{-1} total flow rate, 50 kPa H_2 partial pressure, and 40 kPa helium partial pressure. The temperature was increased from 543 K to 583 K in 10 K increments and then lowered to 543 K.

observed in time on stream data (*vide supra*). The rates of methane and ethane formation on Pt/H-mordenite were lower at the final set of conditions, but the rate of formation of butenes was unaffected. The same deactivation of hydrogenolysis pathways was observed in experiments used to measure yields at varying space times.

4.3.2.2 Product formation rates and selectivities over a range of reaction conditions

The product produced with the highest rate and highest selectivity under all reaction conditions was isobutane. Propane and pentanes were the most significant side products, with the propane/pentanes ratio being always larger than 1. Methane, ethane, ethene, propene, and hexanes (*n*-hexane, 2-methylpentane, and 3-methylpentane) were

minor products. Butenes (including some isobutene at higher conversions) were also produced. The rates and selectivities of all products are shown in Table 4.1 at the specified conditions.

Table 4.1: Rates (μmol g^{-1} h^{-1}, top) and selectivities (mol %, in parentheses, bottom) of products formed at a temperature of 573 K on Pt/H-mordenite and H-mordenite with an *n*-butane partial pressure of 10 kPa and a H_2 partial pressure of 30-90 kPa.

	Pt/H-mordenite				H-mordenite			
P_{H2} (kPa)	30	50	70	90	30	50	70	90
Methane	5 (0.2)	6 (0.6)	7 (1.1)	10 (2.1)	8 (0.8)	8 (0.9)	8 (1.1)	8 (1.3)
Ethane	10 (0.6)	8 (0.8)	8 (1.3)	11 (2.3)	7 (0.7)	8 (0.9)	9 (1.2)	10 (1.6)
Ethene	0	0	0	0	4 (0.4)	3 (0.4)	2 (0.3)	1 (0.2)
Propane	281 (15.4)	93 (9.4)	40 (6.3)	24 (4.9)	94 (9.8)	77 (9.1)	55 (8.0)	45 (7.3)
Propene	2 (0.1)	0 (0.1)	0	0	1 (0.1)	1 (0.1)	0	0
Isobutane	1286 (70.2)	782 (78.8)	537 (83.8)	422 (85.6)	748 (78.1)	674 (79.4)	555 (81.0)	498 (82.1)
1-Butene	5 (0.3)	3 (0.3)	2 (0.4)	2 (0.4)	3 (0.3)	3 (0.3)	2 (0.3)	2 (0.3)
trans-2-Butene	14 (0.8)	10 (1.0)	7 (1.1)	6 (1.1)	9 (0.9)	8 (0.9)	6 (0.9)	5 (0.9)
cis-2-Butene	9 (0.5)	6 (0.6)	4 (0.7)	4 (0.7)	5 (0.6)	5 (0.6)	4 (0.6)	3 (0.6)
Isobutene	6 (0.3)	3 (0.3)	2 (0.3)	0	3 (0.3)	2 (0.3)	2 (0.3)	1 (0.2)
n-Pentane	78 (4.2)	31 (3.1)	12 (1.9)	5 (1.0)	22 (2.3)	18 (2.1)	13 (1.9)	10 (1.6)
2-Methylbutane	128 (7.0)	49 (5.0)	21 (3.2)	9 (1.9)	52 (5.4)	42 (5.0)	30 (4.4)	23 (3.8)
n-Hexane	3 (0.2)	0	0	0	1 (0.1)	0	0	0
2-Methylpentane	4 (0.2)	0	0	0	1 (0.1)	0	0	0
3-Methylpentane	2 (0.1)	0	0	0	0	0	0	0

The rate of product formation increased with increasing temperature, increasing *n*-butane partial pressure, and decreasing H_2 partial pressure. Concurrent with the

increase in product formation rates was a decrease in selectivity to isobutane and an increase in selectivity to side products, represented by pentanes in Fig. 4.6.

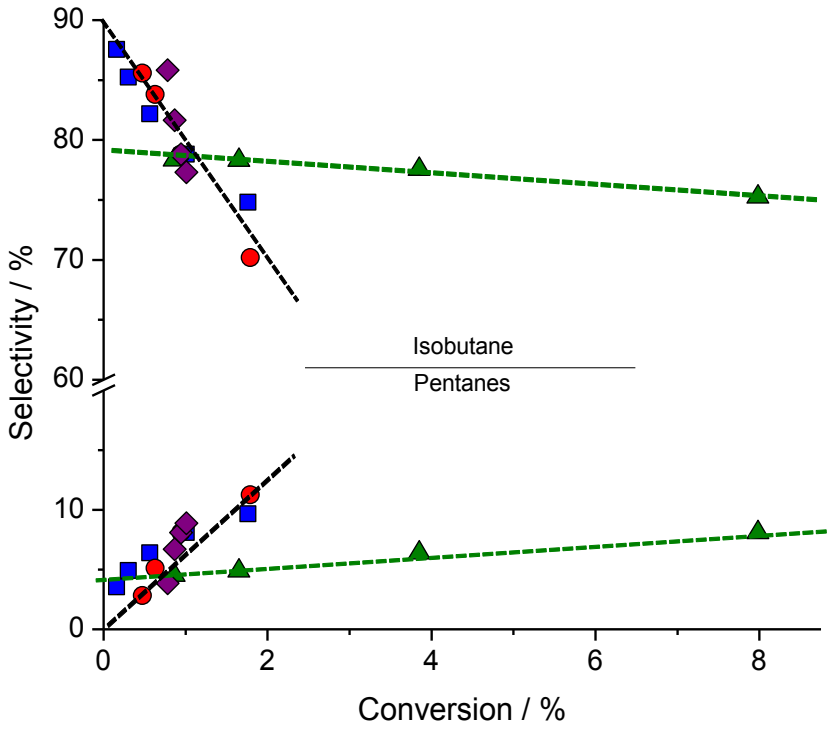


Figure 4.6: Selectivities of isobutane (upper part of graph) or pentanes (lower part of graph) on Pt/H-mordenite with respect to conversion. Changes in conversion were caused by changes in reaction parameters. An increase in conversion resulted from increasing the temperature (blue squares: Pt/M-C1, 543-583 K, 10 kPa *n*-butane, 50 kPa H_2, W/F = 0.17 h), increasing the *n*-butane partial pressure (purple diamonds: Pt/M-C1, 573 K, 3.3-13.3 kPa *n*-butane, 50 kPa H_2, W/F = 0.13-0.51 h), decreasing the H_2 partial pressure (red circles: Pt/M-C1, 573 K, 10 kPa *n*-butane, 30-90 kPa H_2, W/F = 0.17 h), or increasing the space time (green triangles: Pt/M-C2, 573 K, 10 kPa *n*-butane, 50 kPa H_2, W/F = 0.13-1.29 h). The dotted lines are intended to show trends and are not the result of a fit.

4.3.2.3 Evidence for equilibration of *n*-butane, *n*-butenes, and H_2

The measured concentrations of *n*-butene (1-butene, *trans*-2-butene, and *cis*-2-butene) in the reactor effluent were within parts per million of the calculated equilibrium concentrations over the entire range of conditions on Pt/H-mordenite and

at high H_2 partial pressures on H-mordenite. The three *n*-butene species were always present in their thermodynamically expected ratios. The measured concentration and calculated equilibrium concentration of *trans*-2-butene at 563 K are plotted in Fig. 4.7 as a function of the H_2 partial pressure with the *n*-butane partial pressure as a parameter. The proximity of the measured concentration to the equilibrium concentration can be described over a more extended range of conditions with Eqn. 6:

$$P = \frac{C_{eq} - C_{meas}}{C_{eq}} \tag{6}$$

C_{eq} is the equilibrium concentration of *n*-butenes calculated using the software program Thermosolver (v. 1.0), and C_{meas} is the concentration of *n*-butenes measured in the effluent stream. A value of zero indicates that the calculated and measured concentrations were the same, while a value of 1 means that no butenes were measured. The result of Eqn. 6 at various reaction conditions is reported in Table 4.2. The values indicate a similar proximity to equilibrium on Pt/H-mordenite at H_2 partial pressures of 50, 70, and 90 kPa. On H-mordenite, the concentration of *n*-butenes deviated significantly from the calculated equilibrium concentration at low H_2 partial pressures, but was equal to the concentration produced on Pt/H-mordenite with a H_2 partial pressure of 90 kPa. Also relevant to the discussion of attaining chemical equilibrium between *n*-butane, *n*-butenes, and H_2 are the apparent kinetic parameters measured for production of *n*-butenes. The reaction order with respect to *n*-butane, the reaction order with respect to H_2, and the apparent activation energy for *n*-butene formation on Pt/H-mordenite are reported in Table 4.3. The reader should note that

changing any reaction parameter causing there to be a higher concentration of *n*-butenes also caused a decrease in selectivity to isobutane (see Fig. 4.6).

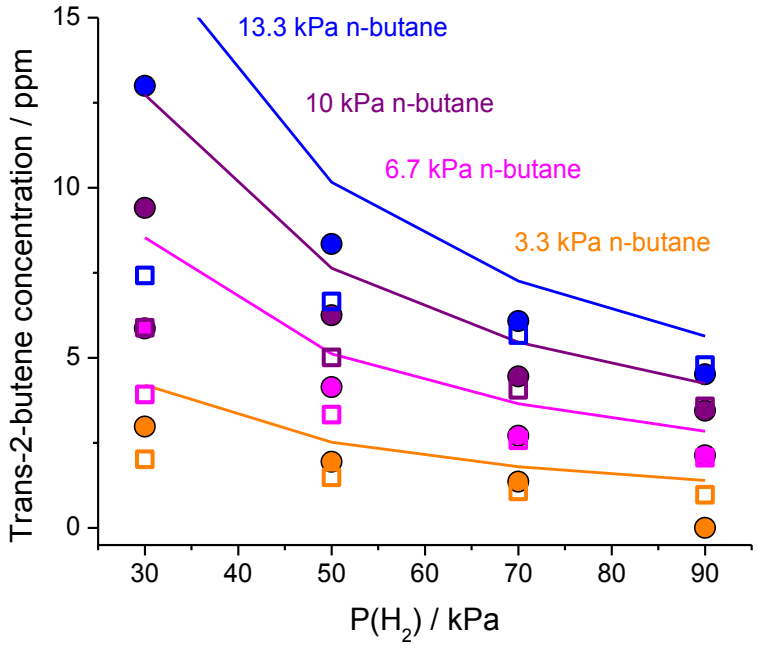


Figure 4.7: Measured concentrations and calculated equilibrium concentrations of *trans*-2-butene at a temperature of 563 K over the range of *n*-butane and H_2 partial pressures. Solid circles: measured on Pt/H-mordenite. Open squares: measured on H-mordenite. Lines: calculated equilibrium concentrations using the software package Thermosolver (v. 1.0).

Table 4.2: Value of Eqn. 6 over a range of reaction conditions

	Pt/H-mordenite		H-mordenite	
P_{nC4H10}, P_{H2} / kPa (down) Temperature / K (right)	563	583	563	583
6.6, 90	0.17	0.14	0.23	0.28
6.6, 70	0.19	0.17	0.28	0.31
6.6, 50	0.15	0.18	0.36	0.39
6.6, 30	0.27	0.34	0.53	0.55
13.3, 87.7	0.15	0.10	0.12	0.18
13.3, 70	0.12	0.14	0.20	0.24
13.3, 50	0.15	0.19	0.33	0.34
13.3, 30	0.21	-	0.55	0.55

Table 4.3: Apparent reaction parameters for production of *n*-butenes on Pt/H-mordenite

Reaction order with respect to *n*-butane					
P_{H2} (down) Temp (right)	543	553	563	573	583
30	1.1	1.1	1.0	1.0	1.0
50	-	1.1	1.0	1.0	1.0
70	-	1.1	1.0	1.0	1.0
90	-	-	1.0	1.2	1.0
Reaction order with respect to H_2					
P_{nC4} (down) Temp (right)	543	553	563	573	583
3.3	-	-	-	-0.8	-0.8
6.7	-	-1.0	-0.9	-0.8	-0.8
10	-1.0	-1.0	-0.9	-0.8	-0.8
13.3	-1.0	-0.9	-0.9	-0.8	-0.9
Apparent activation energy (E_{app})					
P_{nC4} (down) P_{H2} (right)	30	50	70	90	
3.3	122	114	-	-	
6.7	113	122	130	126	
10	109	123	126	129	
13.3	116	130	126	130	

4.3.2.4 Conversion of *n*-butane over a range of space times

Product concentrations measured at different space times are reported in Fig. 4.8. The space time was adjusted by changing the amount of catalyst. Reported concentrations are those measured between 80 and 130 minutes on stream. During the first hour on stream, products were formed at a steady rate with the exception of methane and ethane. After the first hour, methane and ethane were also produced at a steady rate. The measured concentrations of *n*-butenes did not change with increasing space time, suggesting that equilibration with *n*-butane and H_2 does occur, and occurs rapidly. As shown in Fig. 4.6, increasing the space time had little effect on the selectivity to isobutane and pentanes.

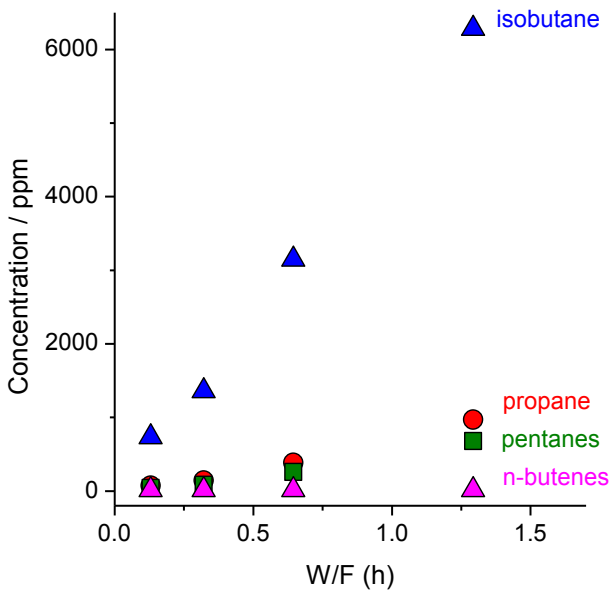


Figure 4.8: Concentration of the main gas phase products produced from conversion of *n*-butane on Pt/H-mordenite (Pt/M-C2) at a temperature of 573 K. Other conditions: 50 ml min^{-1} total flow, 50 kPa H_2, 40 kPa helium, W/F = 0.13-1.29.

4.4 Discussion

4.4.1 Experiments with olefins or co-adsorptives in the feed

4.4.1.1 Effect of co-feeding *n*-butenes on product formation rates

The importance of olefins on the rate of *n*-butane conversion is illustrated, quite dramatically, in Fig. 4.1. H-mordenite was inactive for *n*-butane conversion at 473 K in the absence of feed olefins, in agreement with the results of Fogash et al. [10]. When only 18 ppm of *n*-butenes were added to the feed, gas phase products were formed and minimal deactivation was observed with time on stream. The *n*-butene concentration in the effluent stream was 1-3 ppm, indicating that there was a chemical transformation of the species. Likely products are carbonaceous deposits, which are known to be formed in "high" concentrations of butene [21], or *n*-butane, which can be formed in the

presence of H_2 on Brønsted acid sites [22]. The deactivation with time on stream suggests that some of the butenes may have been consumed by formation of carbonaceous deposits, although deactivation of the Pt/SiO_2 catalyst used to produce the butenes can not be ruled out. The *n*-butene concentration in the feed of 18 ppm was much higher than the equilibrium concentration of 0.1 ppm, so consumption of *n*-butenes by hydrogenation may be more likely.

The stability of our H-mordenite is different than the stability reported by Fogash et al. [10], who found H-mordenite to deactivate almost completely after 100 minutes on stream with 59-237 ppm of *n*-butene in the feed. Three parameters that could contribute to the difference are i) the catalyst, ii) the *n*-butene concentration, and iii) the partial pressure of H_2. As discussed by Engelhardt et al. [23] and Cortright et al. [24], there can be dramatic differences between mordenite samples in terms of catalytic activity. One of the differences may be the propensity to form carbonaceous deposits. Additionally, the higher *n*-butene partial pressure (59-237 ppm) and lower H_2 partial pressure (10 kPa) used by Fogash et al. [10] are two parameters that would promote formation of carbonaceous deposits. In our work, the highest concentration of *n*-butene was only 18 ppm and was undoubtedly lower towards the end of the catalyst bed. As the olefin concentration in the effluent was only 1-3 ppm, it can be inferred that there was an olefin gradient through the bed. Because the olefin concentration is apparently vital to product formation rates, and there was an olefin gradient through the bed, one must view the reactor as an *integral reactor* even though the total conversion was less than 1%.

4.4.1.2 Effect of olefin pulses on product formation rates

Pulses of propene, 1-butene, and 1-hexene also promoted conversion of *n*-butane. The most likely explanation is that the olefins are easily protonated and allow *n*-butane to enter catalytic cycles through hydride transfer. Once formed, the *sec*-butyl surface species can i) engage in hydride transfer with gas phase molecules, ii) desorb as an olefin, iii) form a dimer with a gas phase olefin, or iv) transform to the skeletal isomer. The probability that the *sec*-butyl species will desorb as an olefin explains why the response to the olefin pulse is transient.

If hydride transfer is the mechanism by which the olefin allows *n*-butane to enter reaction cycles, then the hydrogenated version of the olefin should be found in the gas phase if the surface species is not cracked. This was the case when hexanes were formed after pulses of 1-hexene. For example, in the GC injection taken just after the first pulse of 1-hexene, the measured concentrations of 1-hexene and hexanes (2,2-dimethylbutane, 2-methylpentane, 3-methylpentane, and *n*-hexane) were 1980 and 35 ppm, respectively. The measured hexane impurities in the 1-hexene were about 0.02 mol%, and are thus insufficient to account for the measured concentration in the effluent. The mass spectrometer signal for hexanes at m/z = 96 was about 2-3 minutes wide, whereas the signal at m/z = 72 for pentanes was about 15 minutes wide. In a reactor with less dead volume the hexane signal may have been only seconds wide, but because the environmental chamber was used, gas mixing in the cell must be taken into consideration. In the exact cell that was used, it takes about 1.25 min with a flow rate of 30 ml min^{-1} to exchange 90% of the gas in the chamber [21].

4.4.1.3 Effect of aromatic co-adsorbates on product formation rates

The promoting effect of aromatic co-adsorbates is not completely understood. The effect is currently being investigated in further detail by another member of the group. The use of co-adsorbates in heterogeneous catalysis is a novel idea and its current practice is, at the very least, limited.

One possible explanation for the promoting effect of the aromatic co-adsorbates comes from Haw and co-workers [25]. Motivated by the hypothesis that the dielectric constant in a zeolite pore is low [26], and that charge separation consequently has a high energy cost, co-adsorbates were used in conjunction with acetone on H-ZSM-5 in an effort to induce solution-like proton transfer. Using ^{13}C NMR, Haw [25] was able to show a correlation between the dielectric constant of several co-adsorbates and the chemical shift of the carbonyl carbon of acetone adsorbed on H-ZSM-5. The co-adsorbate that caused the largest chemical shift was nitromethane (dielectric constant = 34.8 at 298 K [27]). Isopropanol dehydration and methanol conversion were used as test reactions, and cofeeding nitromethane was found to increase the rate of conversion for both [25]. Theoretical calculations indicated that the rate enhancement could be explained by an increase in the basicity of the reactant caused by interactions with the co-adsorbate [28].

The co-adsorbates used in this work that had a promoting effect on *n*-butane conversion, 1,3-bis(trifluoromethyl)benzene and nitrobenzene, have dielectric constants of 6.0 and 34.8, respectively [27]. We note that toluene and trichloroethylene (dielectric constants of 2.4 and 3.4, respectively [27]) did not have a promoting effect. Nitrobenzene was also found to have a promoting effect at temperatures of both 473 and

573 K [29]. As the dielectric constant of nitrobenzene is the same as nitromethane, it is possible that the effect we observed is the same effect as that observed by Haw. However, the dielectric constant of 1,3-bis(trifluoromethyl)benzene is low by comparison, and the reason for increased conversion after application of this species may not be linked to a more facile charge separation.

Introducing co-adsorbates significantly increases the complexity of the reaction chemistry. It is possible that after adsorbing aromatic species in the pores of a one-dimensional zeolite such as H-mordenite, mass transport effects become dominant. Nitro compounds are also oxidizing agents, so dehydrogenation of butane is a possible reaction with nitrobenzene. A thorough investigation of the reason for increased conversion in the presence of these aromatic co-adsorbates is currently in progress.

4.4.2 Experiments without olefin or co-adsorptives in the feed

4.4.2.1 Assessment of possible mass transport corruptions

The possibility of external mass transfer limitations was evaluated using the Mears criterion [30], which uses the measured rate of reaction to determine if mass transfer from the bulk gas to the catalyst surface can be neglected. The criterion is satisfied if Inequality 7 is true:

$$\frac{r_A \rho_b R n}{k_c C_{Ab}} < 0.15 \qquad (7)$$

r_A is the measured rate of butane disappearance (kmol kg_{cat}^{-1} s^{-1}), ρ_b is the bulk density of the catalyst bed (kg_{cat} m^{-3}), R is the catalyst particle radius (m), n is the reaction order, k_c is the mass transfer coefficient (m s^{-1}), and C_{Ab} is the bulk gas concentration (kmol m^{-3}). An example calculation will be explained using the rate of disappearance of

n-butane on Pt/H-mordenite in the experiment described in Section 4.2.2.1 at a temperature of 573 K with *n*-butane and H_2 partial pressures of 10 kPa and 90 kPa, respectively. The rate of *n*-butane disappearance was 1.2 x 10^{-4} mol kg^{-1} s^{-1}. The bulk density of the catalyst bed, measured by dividing the catalyst mass by the volume it occupied in the reactor, was 100 kg m^{-3}. The radius of the particles was estimated from SEM images (not shown). Most particles were between 1 and 3 microns in the longest dimension, with a few as large as 6 microns. A conservative estimate of 10 microns was used in the calculations. The reaction order was 1 (*vide infra*, Section 4.4.2.4). The bulk density of *n*-butane was 2.1 mol m^{-3}. The mass transfer coefficient was estimated, assuming spherical particles, for a mixture of 10% *n*-butane and 90% H_2 using Eqn. 8:

$$k_c = \frac{D_{AB}}{d_p}\left(2 + 0.552 Re^{1/2} Sc^{1/3}\right) \tag{8}$$

D_{AB} is the gas diffusivity for *n*-butane in H_2, d_p is the particle diameter, *Re* is the Reynolds number, and *Sc* is the Schmidt number [31]. The gas diffusivity was estimated to be 1.34 x 10^{-4} m^2 s^{-1} using the equation of Hirschfelder [32]. Thus, the mass transfer coefficient k_c was 26.9 m s^{-1}, and the Mears criterion was satisfied by the value of 2.1 x 10^{-9} for Inequality 7.

The possibility of internal mass transfer limitations was evaluated using the Weisz-Prater parameter given by Eqn. 9:

$$C_{WP} = \frac{r_A \rho_C R^2}{D_e C_{As}} \tag{9}$$

C_{WP} is the Weisz-Prater parameter, r_A is the rate of butane disappearance (mol kg^{-1} s^{-1}), ρ_C is the catalyst density (kg_{cat} m^{-3}), *R* is the radius of the catalyst particle (m), D_e is the effective diffusivity (m^2 s^{-1}), and C_{As} is the concentration of A at the catalyst surface

(mol m^{-3}) [33]. An example calculation will be described using the isobutane formation rate measured under the same reaction conditions used in determining the Mears criterion. A catalyst density of 2,150 kg m^{-3} [34] was used. *n*-Butane was assumed to be the reactant. The effective diffusivity was calculated to be 1 x 10^{-7} m^2 s^{-1} assuming Knudsen diffusion and a pore diameter of 6.7 Å. The resulting value for Eqn. 9 was 1.2 x 10^{-4}. A value below 1 means there are no internal diffusion limitations [33].

4.4.2.2 Equilibration of *n*-butane, *n*-butenes, and H_2 on Pt/H-mordenite

Performing a reaction at differential conversions is useful for measuring kinetic parameters. Under differential conditions, conversion remains low so a constant concentration of the reactant along the length of the reactor can be assumed. In the case of *n*-butane, it is clear that *n*-butenes play a critical role in the reaction chemistry. Thus, it is also necessary to hold the concentration of *n*-butenes constant along the length of the reactor for the reactor to be considered differential. This can be done by utilizing a noble metal that rapidly facilitates equilibration of *n*-butane, *n*-butenes, and H_2. In our case, platinum was used as the noble metal, which is known to be an effective alkane dehydrogenation catalyst [35].

On Pt/H-mordenite there are three pieces of evidence indicating that equilibration does occur: i) the close proximity of the measured *n*-butene concentration to the calculated equilibrium *n*-butene concentration, ii) measured apparent kinetic parameters that are consistent with equilibration, and iii) a non-changing *n*-butene concentration with increasing space time. The first point is illustrated in Fig. 4.7 and Table 4.2. The measured concentration of *trans*-2-butene over the range of *n*-butane and H_2 partial pressures was within a few parts per million of the calculated equilibrium

concentration. The comparison depends on both the accuracy of the measurement and the accuracy of the thermodynamic data. Changes in the measured concentration closely mirror changes in the calculated equilibrium concentration over the range of conditions. The similarity of the measured *n*-butene concentration and the calculated equilibrium *n*-butene concentration is one piece of evidence suggesting equilibration.

Apparent kinetic parameters for *n*-butene formation, reported in Table 4.3, are used in discussion of the second point. When equilibrium has been reached, the apparent kinetic parameters should reflect the appropriate thermodynamic equation. The relevant equation for equilibrium between *n*-butane, *n*-butenes, and H_2 is shown in Eqn. 11:

$$nC_4H_{10} \rightleftharpoons nC_4H_8 + H_2 \tag{10}$$

$$[nC_4H_8] = \frac{K[nC_4H_{10}]}{[H_2]} = \frac{e^{-\frac{\Delta g_{rxn}}{RT}}[nC_4H_{10}]}{[H_2]} \tag{11}$$

K is the equilibrium constant, Δg_{rxn} is the Gibbs free energy of reaction, *R* is the universal gas constant, and *T* is the temperature. The van't Hoff equation is used to correct for changes in temperature when the enthalpy of reaction is constant:

$$\frac{\mathrm{d}\ln K}{\mathrm{d}T} = \frac{\Delta h_{rxn}}{RT^2} \tag{12}$$

Δh_{rxn} is the enthalpy of reaction. At equilibrium, the concentration of *n*-butenes should have a first order dependence on the partial pressure of *n*-butane and a negative first order dependence on the partial pressure of H_2. The temperature dependence lies in the enthalpy of reaction. Indeed, the measured parameters on Pt/H-mordenite are close to those expected at equilibrium. Over the range of reaction conditions, the mean of the reaction order with respect to *n*-butane was 1.0, the mean of the reaction order with

respect to H_2 was -0.9, and the mean of the apparent activation energy was 122 kJ mol^{-1}. The enthalpy of reaction at 543-583 K is 121 kJ mol^{-1}. Thus, the apparent reaction parameters are consistent with equilibration of *n*-butane, *n*-butenes, and H_2.

The final point to address is the rate at which equilibration is achieved in the catalyst bed. That is, is there an *n*-butene gradient through the bed? Experiments at varying W/F showed a non-changing concentration of *n*-butenes, indicating rapid equilibration. Thus, the olefin gradient on Pt/H-mordenite is, at the very least, minimal. The same can not be said for H-mordenite, as the equilibrium concentration is not even achieved at a H_2 partial pressure of 30-70 kPa. Thus, there must be an *n*-butene gradient through the catalyst bed, making the reactor an *integral reactor* and extraction of meaningful kinetic parameters much more difficult.

4.4.2.3 Possible reaction pathways of *n*-butane and *n*-butene

For the sake of brevity, the discussion of reaction pathways will be limited to those that form the isomerization product, isobutane, and the main disproportionation products, propane and pentanes. The main parts of the reaction scheme are shown in Fig. 4.9. The first step is formation of a *sec*-butyl alkoxide, which can occur by, i) protonation of *n*-butane on a Brønsted acid site to form an alkanium ion, which decomposes to a *sec*-butyl alkoxide and H_2, ii) abstraction of a hydride ion from *n*-butane by a Lewis acid, or iii) protonation of *n*-butene. Protonation of *n*-butene is necessary to form the first alkoxide, as no gas phase products were formed at 473 K in the absence of olefins, but were formed when 18 ppm of *n*-butenes were added to the feed. Product species on the surface can act as Lewis acids to activate additional feed alkanes, thus creating a catalytic cycle.

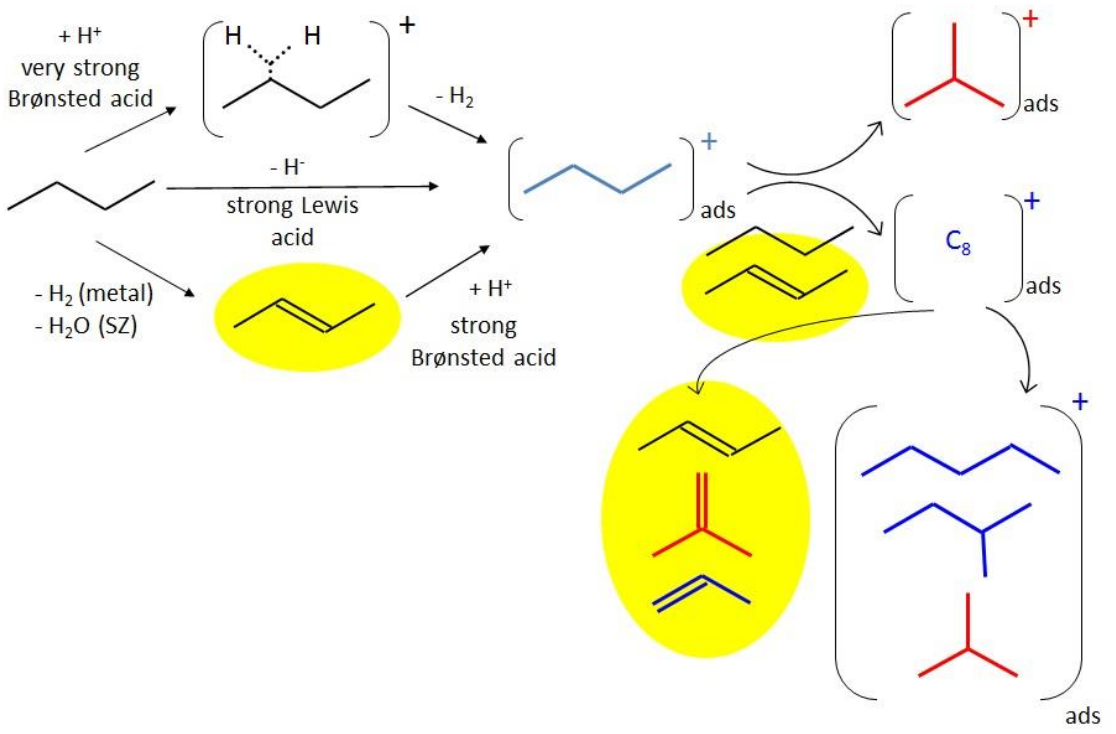


Figure 4.9: Possible reaction pathways of *n*-butane on H-mordenite. Yellow highlights indicate possible areas for participation of olefins.

Once a *sec*-butyl alkoxide is formed, there are two pathways that can lead to formation of isobutane. The first is an intramolecular pathway, the kinetic relevance of which has previously been doubted. In this pathway, the *sec*-butyl alkoxide must rearrange to form a branched alkoxide, which can undergo hydride transfer with a gas phase alkane or desorb as isobutene and become hydrogenated on a metal or on a Brønsted acid site (via an alkanium ion). That very few olefins are produced, even on H-mordenite without platinum, is evidence that hydride transfer is facile.

It is also possible to form isobutane through an intermolecular pathway that proceeds through a C8 intermediate. Formation of the C8 species has been proposed to proceed both via dimerization with butene and alkylation with butane [3]. If butenes are available, the former is likely to be the dominant pathway. The original C8 species that

is formed and the subsequent rearrangements are very important and will be discussed in Section 4.4.3. For now, it will suffice to say that both isomerization and disproportionation products can be formed through the intermolecular pathway, whereas only isobutane can be formed through the intramolecular pathway. Additionally, there are two possible roles for olefins in the intermolecular pathway, whereas there is only one role in the intramolecular pathway. Thus, the two pathways may differ in their dependence on the olefin partial pressure.

4.4.2.4 Dependence of isomerization and disproportionation pathways on the olefin partial pressure

The butene partial pressure had a large impact on the selectivity to either isomerization or disproportionation products. When examining Fig. 4.6, the reader must keep in mind the equilibration of *n*-butane, *n*-butenes, and H_2 on Pt/H-mordenite. Any change that caused an increase in the concentration of *n*-butenes also resulted in decreased selectivity to isobutane and increased selectivity to disproportionation products. The result indicates that isomerization and disproportionation pathways have a different dependence on the butene partial pressure.

The butene partial pressure dependence of each pathway is clarified in Fig. 4.10, which shows the rates of isobutane and pentanes formation on Pt/H-mordenite as a function of the butene partial pressure. Isobutane had a linear dependence on the butene partial pressure, whereas pentanes had an exponential dependence on the butene partial pressure. The first order relationship between *n*-butane and *n*-butene allows the apparent reaction orders for each product with respect to *n*-butene to be extracted from the data, which are shown in Table 4.4. The apparent reaction orders with respect to *n*-butene

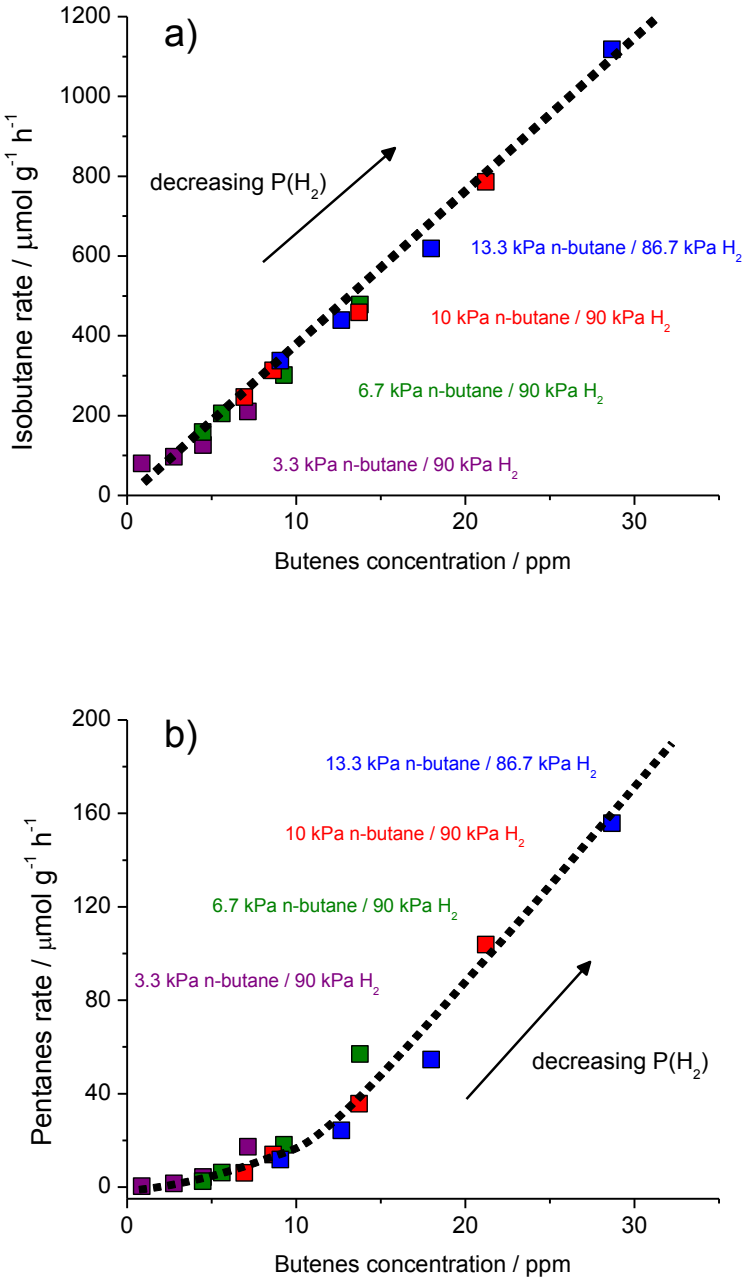


Figure 4.10: The rates of isobutane (a) and pentanes (b) formation at a temperature of 563 K on Pt/H-mordenite (Pt/M-C1) are plotted as a function of the butene concentration measured in the reactor effluent. The dotted lines are not the result of a fit and are intended to guide the reader's eye.

Table 4.4: Apparent reaction orders with respect to *n*-butene on Pt/H-mordenite

P_{H2} (down) Temp (right)	543	553	563	573	583
Isobutane					
30	1.1	1.1	1.2	1.2	1.2
50	1.0	1.0	1.1	1.1	1.1
70	1.0	1.0	1.0	1.0	1.0
90	0.9	0.9	1.0	1.0	1.0
Pentanes					
30	1.5	1.5	1.5	1.5	1.4
50	-	1.7	1.7	1.7	1.7
70	-	-	1.9	2.0	2.0
90	-	-	-	2.2	2.2

over the range of reaction conditions were 0.9-1.2 for isobutane and 1.4-2.2 for pentanes. For isobutane, apparent orders with respect to *n*-butane of 1 [4] and 1.17 [7] have previously been attributed to an intramolecular route of formation, while an apparent order of 2 has been attributed to intermolecular formation [4]. For pentanes, apparent orders with respect to *n*-butane of 1.9 [7] and 2 [5] have been reported. Thus, our results are consistent with some previous reports, and seem to indicate a primarily intramolecular route of isobutane formation and an intermolecular route of pentanes formation.

4.4.2.5 The apparent activation energy of isobutane formation

Because product formation rates depend on the butene partial pressure, extraction of apparent activation energies is not a straightforward procedure. A standard Arrhenius plot assumes that the reactant concentration remains constant over the range of temperatures used to collect the data. The appropriate equations for the standard method are shown in Eqns. 13 and 14:

$$r = Ae^{-\frac{E_a}{RT}}[nC_4H_{10}]^{\propto} \quad (13)$$

$$\ln r = \ln(A[nC_4H_{10}]^{\propto}) - \left(\frac{1}{T}\right)\left(\frac{E_a}{R}\right) \quad (14)$$

r is the rate of product formation, A is the pre-exponential factor, E_a is the activation energy, R is the universal gas constant, T is the temperature, and α is the reaction order. In our case, the equilibration of *n*-butane, *n*-butene, and H_2, causes the concentration of *n*-butene to increase with temperature. This is important because product formation rates are linked to the butene partial pressure, and must be accounted for. Eqns. 13 and 14 can be modified to account for the equilibration of *n*-butenes as shown in Eqns. 15 and 16 and a meaningful apparent activation energy can be extracted. Because the

$$r = Ae^{-\frac{E_a}{RT}}[nC_4H_8]^1 \quad (15)$$

$$\ln\frac{r}{[nC_4H_8]^1} = \ln A - \left(\frac{1}{T}\right)\left(\frac{E_a}{R}\right) \quad (16)$$

isobutane formation rate has a linear dependence on the butene concentration, an order of 1 was used for *n*-butene. The concentration used in the calculations can be either the measured or calculated equilibrium concentration; we used the calculated concentration to reduce the uncertainty inherent in the measurement. The resulting apparent activation energies for isobutane, calculated using Eqn. 16, are shown in Table 4.5. The correlation coefficient was 0.993 or greater in all Arrhenius plots.

Table 4.5: Apparent activation energies (kJ mol^{-1}) for isobutane formation on Pt/H-mordenite. The change in *n*-butene concentration with temperature was accounted for by using Eqn. 16.

P_{nC4H10} (down) P_{H2} (right)	50	70	90
6.7	-	20	23
10	21	23	24
13.3	23	24	23

The extracted apparent activation energy for isobutane formation was 20-24 kJ mol^{-1}. There is precedent in the literature for such a low value. The apparent activation energy is related to the true activation energy and the enthalpy of adsorption by Eqn. 17, which is a modification of the Temkin equation:

$$E_a = E_{app} - \Delta H_{ads} \tag{17}$$

E_a is the true activation energy, E_{app} is the apparent activation energy, and ΔH_{ads} is the enthalpy of adsorption. Under conditions of "high" coverage the measured activation energy will be equal to the true activation energy, whereas under conditions of "low" coverage the measured activation energy will be equal to the apparent activation energy. Because only parts per million of butene was measured in the effluent, it is reasonable to infer conditions of low coverage. Thus, the measured energy should be the apparent activation energy, and the true activation energy can be determined if the enthalpy of adsorption is known.

Fogash et al. [11] estimated the enthalpy of adsorption for butene on H-mordenite to be -100 kJ mol^{-1} using a correlation between the enthalpy of adsorption and the gas phase proton affinity. Bell [36] recently reported an experimentally determined enthalpy of adsorption for 1-butene on H-MFI of -110 kJ mol^{-1} that closely matched the enthalpy of adsorption predicted by DFT of -114 to -121 kJ mol^{-1}. Using these experimentally determined enthalpies of adsorption from the literature and our experimentally determined apparent activation energy, the true activation energy should be 120-138 kJ mol^{-1}.

Using DFT calculations, Boronat et al. [37] predicted the true activation of the rearrangement step of *n*-butene skeletal isomerization on the 10-membered ring zeolite

Theta-1 to be 110-145 kJ mol^{-1}, depending on the basis set that was used. More recently, Wattanakit et al. [38] predicted the true activation energy of the same step to be 87 kJ mol^{-1} on H-ferrierite. Gleeson [39] predicted the true activation energy of carbenium ion and alkoxide based mechanisms to be 103 and 143 kJ mol^{-1}, respectively, on H-ferrierite. Domokos et al. [40] measured the apparent activation energy of isobutene and isobutane formation from *n*-butene on H-ferrierite and found them to be 59 and 28 kJ mol^{-1}, respectively. They hypothesized that desorption is the rate-limiting step for isobutene, but did not comment on the rate-limiting step for isobutane. However if the rearrangement is the rate-limiting step for isobutane, it could explain the difference. Villegas et al. [41] used a kinetic model to determine the true activation energy for isobutene formation from *n*-butene and found it to be 136 kJ mol^{-1} on H-ZSM-22, albeit with a low heat of adsorption. Previously reported apparent activation energies for isobutane formation on Pt/H-mordenite were between 44 and 71 kJ mol^{-1} and were found to depend on the H_2 to hydrocarbon ratio [8]. The values were "to be taken with care in mechanistic considerations". Overall, we find the extracted apparent activation energies for isobutane shown in Table 4.5 to be both reasonable and consistent with a significant contribution from an intramolecular route of formation.

4.4.3 Linking experimental results with proposed reaction pathways

It is clear from the literature, and from the data presented in this chapter, that reaction conditions can be chosen to favor selectivity to the desired product, isobutane. Asuquo et al. [3] found isobutane selectivity to be highest at low *n*-butane partial pressures, low temperatures, and with high Si/Al ratios. Tran et al. [4] found the isobutane selectivity to be highest when H_2 was used as the feed diluent instead of N_2.

The results of our study corroborate some of these findings, and also answer the question as to *why* these parameters impact the selectivity in the way they do. Asuquo et al. [42] proposed that alkene formation is suppressed by H_2, but did not show any data to prove the point. The data presented in this thesis (Fig. 4.6 in particular) clarifies that the gas phase concentration of butenes is the missing link; the butene partial pressure dependence is different for isomerization and disproportionation pathways.

The kinetic parameters presented here focus on the role of *n*-butenes, but this has not been the case in previous reports. Our analysis reveals that the reaction order for isobutane is close to first order with respect to *n*-butenes, and the reaction order for pentanes is 1.5 or greater. Similar reaction orders with respect to *n*-butane have previously been used as evidence of specific reaction pathways, but did not include information about the concentration of butenes. The reason for the first order dependence of isobutane on the *n*-butene partial pressure is control of the surface concentration of *sec*-butyl alkoxides. A purely intramolecular reaction scheme is outlined in Fig. 4.11, in which both *n*-butene and *n*-butane are in equilibrium with the C4 surface species. At least at a temperature of 473 K, this surface species is not able to form in the absence of *n*-butene. Once formed from *n*-butene, a hydride transfer pathway becomes available and *n*-butane is able to enter catalytic cycles.

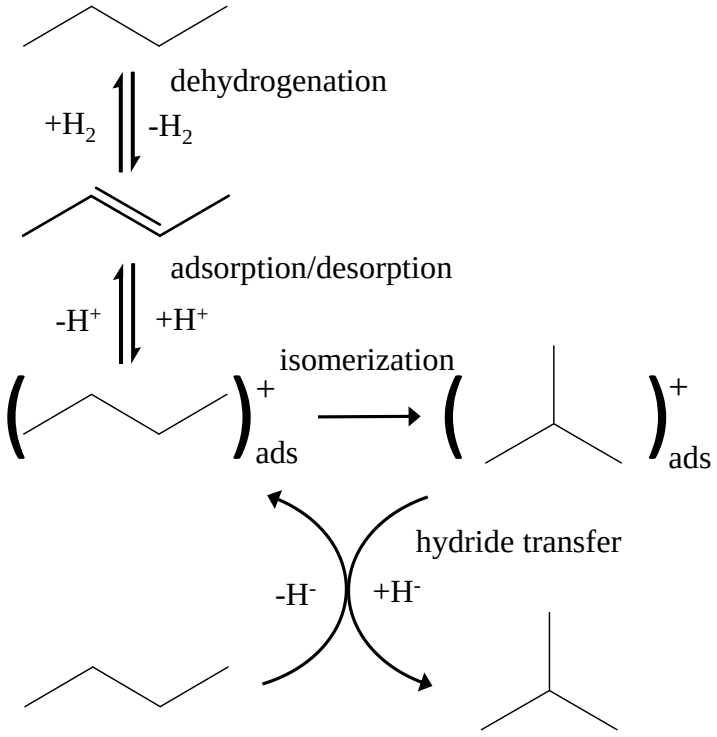


Figure 4.11: The catalytic cycle for intramolecular skeletal isomerization of *n*-butane.

The higher order with respect to *n*-butene for pentanes indicates an additional role of butenes in their formation. When the kinetic description of the intermolecular pathway includes beta-scission as the rate-limiting step, an order with respect to *n*-butene of 2 would be expected, as shown in Fig. 4.12. In the figure, *r* is the reaction rate, *k* is a rate constant, *K* is an equilibrium constant, *P* indicates a partial pressure, subscripts indicate the corresponding reaction step, Z^- is the negatively charged zeolite lattice, and H^+ is a charge balancing proton. One step in the pathway is formation of a C8 intermediate on an acid site, which requires an additional butene, giving the second order dependence on butene or butane (if they are in equilibrium).

1. $nC_4H_{10}\,(g) \rightleftharpoons nC_4H_8 + H_2\,(g)$
2. $nC_4H_8\,(g) + H^+Z^- \rightleftharpoons nC_4H_9^+ \cdot Z^-$
3. $nC_4H_9^+ \cdot Z^- + nC_4H_8\,(g) \rightleftharpoons C_8H_{17}^+ \cdot Z^-$
4. $C_8H_{17}^+ \cdot Z^- \rightleftharpoons iC_8H_{17} \cdot Z^-$
5. $iC_8H_{17}^+ \cdot Z^- \longrightarrow iC_4H_8\,(g) + iC_4H_9^+ \cdot Z^-$
6. $iC_4H_8\,(g) + H_2\,(g) \rightleftharpoons iC_4H_{10}\,(g)$

$$r_5 = k_5 C_{iC_8H_{17}^+ \cdot Z^-} - k_{-5} P_{iC_4H_8} C_{C_4H_9^+ \cdot Z^-}$$

At differential conversion:

$$r_5 = k_5 C_{iC_8H_{17}^+ \cdot Z^-}$$

$$r_5 = k_5 K_4 K_3 C_{nC_4H_9^+ \cdot Z^-} P_{nC_4H_8}$$

$$r_5 = k_5 K_4 K_3 K_2 P_{nC_4H_8}^2 C_{H^+Z^-}$$

$$r_5 = k_5 K_4 K_3 K_2 K_1 \left(\frac{P_{nC_4H_{10}}}{P_{H_2}}\right)^2 C_{H^+Z^-}$$

Final equation, at low coverage:

$$r_5 = k_5 K \left(\frac{P_{nC_4H_{10}}}{P_{H_2}}\right)^2$$

Figure 4.12: A kinetic description of the intermolecular skeletal isomerization pathway assuming that beta-scission (Step 5) is the rate-limiting step.

Because a dimerization-cracking pathway is clearly active on both catalysts, as evident by the formation of propane and pentane side products, a discussion of the selectivity of this pathway is prudent. Such a discussion should begin with formation of the initial C8 species. At the low conversions used in this work, this step probably involves dimerization of a *sec*-butyl alkoxide with *n*-butene. The possible C8 species formed in the dimerization are shown in Fig. 4.13. The C8 species will subsequently rearrange and eventually undergo beta-scission to form a gas phase olefin and another surface alkoxide. Both the thermodynamics and kinetics of the rearrangement are important, and will be addressed. Olefins are required to form the C8 species and are also cracking products of the C8 species; thus the intermolecular pathway does not result in a net production of olefins.

The extent of the rearrangement of the surface C8 species can be probed with isotope labeling. Guisnet et al. [2] converted 1-^{13}C-*n*-butane on H-mordenite and found a binomial distribution of isotopes in pentanes over a wide range of conversions, suggesting that at least for C8 species that produce disproportionation products, the rearrangement occurs rapidly in comparison to the rate at which cracking occurs.

If the surface concentration of C8 species resembles that of the gas phase equilibrium concentration, then the initially formed surface species should not preferentially rearrange to form isomers with more methyl branches. de Lucas et al. [43] converted *n*-octane on Pt/H-mordenite at 603 K and already at 50% conversion found the isomer distribution to consist entirely of species with only one or two methyl branches. At 600 K, the equilibrium composition of C8 isomers with 0, 1, 2, and 3 methyl branches is 3.4, 37, 43, and 10 mol%, respectively [44]. That species with three

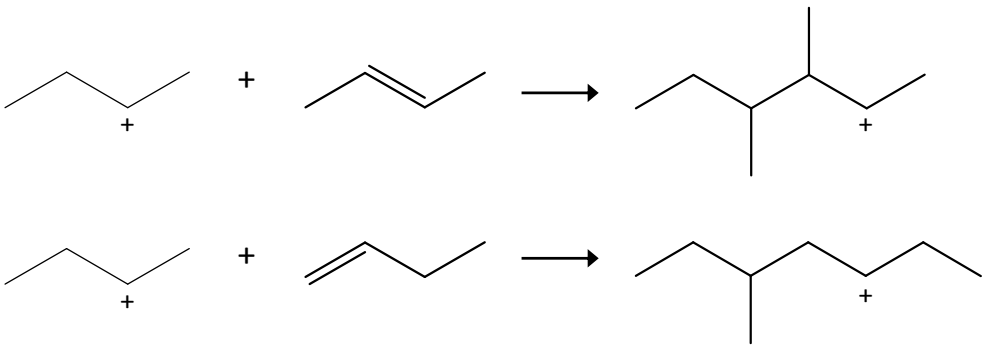


Figure 4.13: Dimerization products formed by reaction of a *sec*-butyl carbenium ion with a gas phase *n*-butene molecule.

methyl branches were not detected suggests that there is not a transition state selectivity favoring formation of these species. Thus, it is conceivable that the distribution of C8 surface species closely resembles that of the gas phase equilibrium. An argument has been put forth that 2,2,4-trimethylpentane is selectively formed from *n*-butane and cracks to eventually make two isobutane molecules [45]; however, the equilibrium composition of 2,2,4-trimethylpentane at 600 K is only 1.5 mol% [44].

The extent of branching in the surface C8 species greatly impacts the cracking products and kinetics. It is true that 2,2,4-trimethylpentane produces isobutane with high selectivity; Lugstein et al. [46] hydrocracked the species on Ni/H-mordenite and found an isobutane to (propane + pentanes) ratio of 21. A ratio of only 1.4 was found when 2,5-dimethylhexane was hydrocracked [46]. *n*-Octane has been hydrocracked on various mordenites and ratios of 1.1 [43,46] and 0.5 [47] have been found. Lugstein et al. [46] found the ratio between turnover frequencies of *n*-octane, 2,5-dimethylheptane, and 2,2,4-trimethylpentane hydrocracking at 533 K on the same Ni/H-mordenite catalyst to be 1: 3.3: 1.6. Thus, whereas cracking of triply branched species may selectively produce isobutane, hydrocracking of less branched species is not highly

selective to isobutane, and is not significantly slower than cracking of species with more methyl branches.

The final step in the intermolecular reaction pathway is beta-scission, which is probably the rate-limiting step. Cracking of 2,2,4-trimethylpentane is predicted to have a lower activation energy than cracking reactions that form C3 and C5 species because it is possible to have a tertiary carbenium ion both before and after liberation of the olefin. However, as stated previously, the equilibrium composition of this isomer is very low. All other reactions that form isobutane require a secondary or primary carbenium ion either before or after liberation of the olefin, which is the same case as cracking to form C3 and C5 species. An inclusive list of the beta-scission reactions of C8 isomers that produce isobutene, propene, or a C5 olefin is shown in Fig. 4.14.

If it is true that *n*-butane skeletal isomerization can occur via an intramolecular pathway, one must ask why so much data in the literature has pointed towards an intermolecular route. An intermolecular pathway to isobutane almost surely exists, and probably even has a lower activation energy than an intramolecular pathway. However, the intermolecular pathway has a near second order dependence on the olefin partial pressure. Thus, conditions that favor olefin formation will also favor intermolecular reaction pathways. However, as we have shown, the intermolecular pathways are not highly selective to isobutane formation.

It is puzzling that although copious amounts of evidence implicate dominance of the intramolecular skeletal isomerization pathway of *n*-butenes on 10-membered ring zeolites, in some cases after an initial induction period, it is often written that its hydrogenated counterpart isomerizes through a completely different pathway [48].

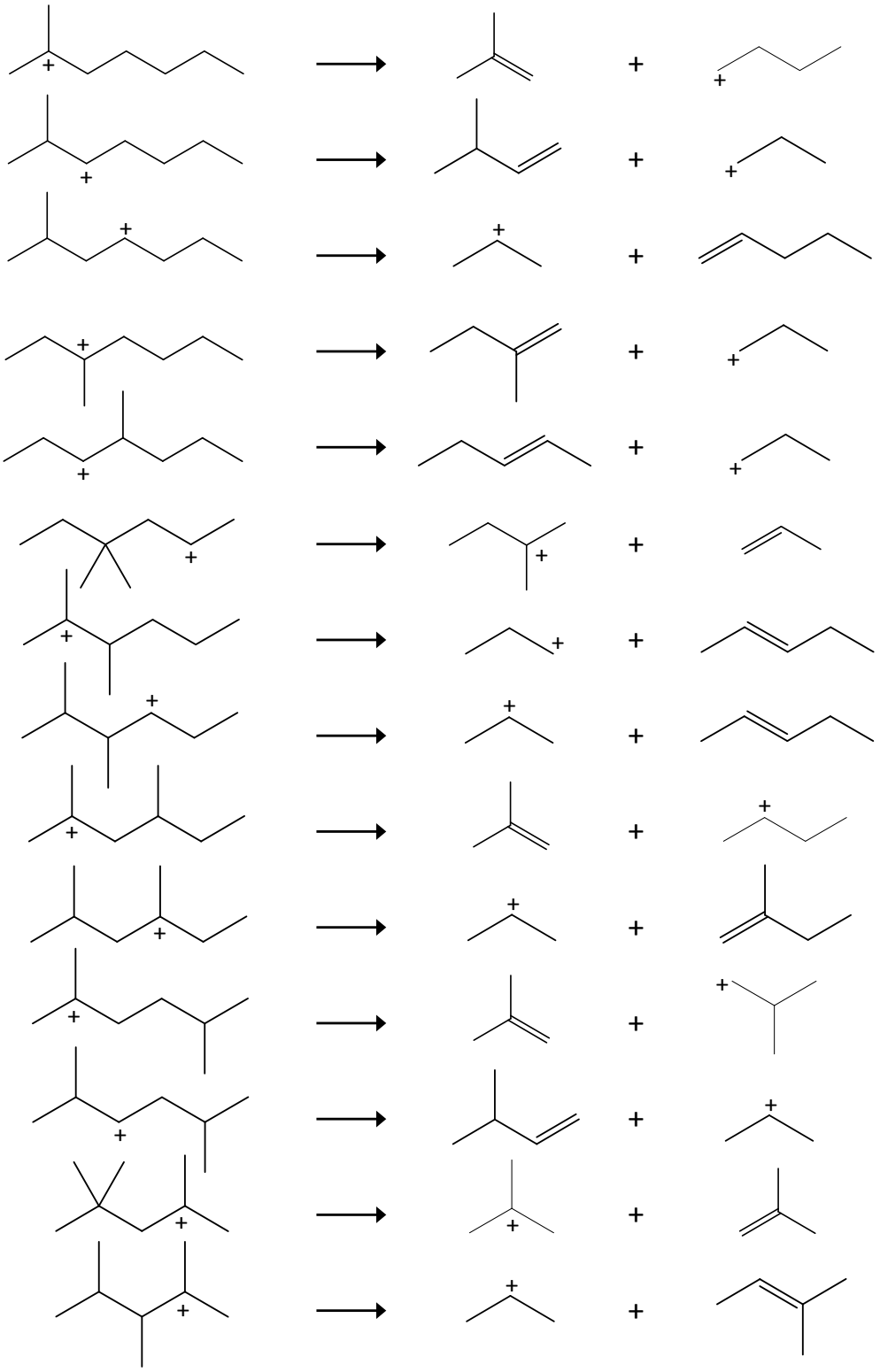


Figure 4.14: Beta-scission reactions of C8 skeletal isomers that produce either propene, isobutene, or a C5 olefin as a gas phase product.

In principle, the two reactions differ only by the mechanisms of activation and termination, those being the facile protonation of an olefin and termination by loss of a proton to the zeolite or the more difficult protonation of a paraffin (or hydride transfer) and termination by hydride transfer from a neighboring molecule. In both cases the actual skeletal rearrangement of the *sec*-butyl alkoxide should occur by the same mechanism. A theoretical investigation by Boronat et al. [49] concerning the skeletal isomerization of linear butenes on a zeolite determined that the cyclopropane ring maintains elongated C-O bonds with the zeolite lattice in the transition state and thus does not resemble a primary carbenium ion. Upon opening of the cyclopropane ring a primary alkoxide is formed, which some reports indicate are more energetically favorable than secondary and tertiary alkoxides [50]. The transition state in the skeletal isomerization pathway catalyzed by liquid superacids is distinctly different; in this case, the transition state is the species formed upon opening of the cyclopropane ring, which must result in formation of a primary carbenium ion [51].

We conclude that on Pt/H-mordenite, equilibration of *n*-butane, *n*-butenes, and H_2 occurs rapidly. Conditions that result in "high" butene concentrations enable intermolecular skeletal isomerization and disproportionation pathways because of their near second order dependence on the butene partial pressure. However, an intramolecular skeletal isomerization pathway also operates at a kinetically relevant rate. Conditions that result in "low" butene concentrations are more selective to this pathway because of its near first order dependence on the butene partial pressure.

References

[1] M. Guisnet, N.S. Gnep, Appl. Catal., A 146 (1996) 33.

[2] C. Bearez, F. Avendano, F. Chevalier, M. Guisnet, Bull. Soc. Chim. Fr. 3 (1985) 346.

[3] R.A. Asuquo, G. Eder-Mirth, J.A. Lercher, J. Catal. 155 (1995) 376.

[4] M.T. Tran, N.S. Gnep, G. Szabo, M. Guisnet, J. Catal. 174 (1998) 185.

[5] C. Bearez, F. Chevalier, M. Guisnet, React. Kinet. Catal. Lett. 22 (1983) 405.

[6] N.N. Krupina, A.L. Proskurnin, A.Z. Dorogochinskii, React. Kinet. Catal. Lett. 32 (1986) 135.

[7] P. Cañizares, A. de Lucas, F. Dorado, Appl. Catal., A 196 (2000) 225.

[8] V. Nieminen, M. Kangas, T. Salmi, D.Yu. Murzin, Ind. Eng. Chem. Res. 44 (2005) 471.

[9] J.C. Yori, M.A. D'Amato, G. Costa, J.M. Parera, React. Kinet. Catal. Lett. 56 (1995) 129.

[10] K.B. Fogash, Z. Hong, J.M. Kobe, J.A. Dumesic, Appl. Catal., A 172 (1998) 107.

[11] K.B. Fogash, Z. Hong, J.A. Dumesic, J. Catal. 173 (1998) 519.

[12] J. Engelhardt, J. Catal. 164 (1996) 449.

[13] H. Liu, V. Adeeva, G.D. Lei, W.M.H. Sachtler, J. Mol. Catal. A: Chem. 100 (1995) 35.

[14] J.E. Tabora, R.J. Davis, J. Am. Chem. Soc. 118 (1996) 12240.

[15] N. Lohitharn, J.G. Goodwin, E. Lotero, J. Catal. 234 (2005) 199.

[16] N. Lohitharn, E. Lotero, J.G. Goodwin, J. Catal. 241 (2006) 328.

[17] N. Lohitharn, J.G. Goodwin, J. Catal. 245 (2007) 198.

[18] T. Suzuki, T. Okuhara, Catal. Lett. 72 (2001) 111.

[19] T. Echizen, T. Suzuki, Y. Kamiya, T. Okuhara, J. Mol. Catal. A: Chem. 209 (2004) 145.

[20] H. Pines, R.C. Wackher, J. Am. Chem. Soc. 68 (1946) 595.

[21] M.J. Wulfers, G. Tzolova-Müller, J.I. Villegas, D.Yu. Murzin, F.C. Jentoft, J. Catal. 296 (2012) 132.

[22] R. Gounder, E. Iglesia, J. Catal. 277 (2011) 36.

[23] J. Engelhardt, J. Valyon, J. Catal. 181 (1999) 294.

[24] R.D. Cortright, K.B. Fogash, J.A. Dumesic, J. Catal. 181 (1999) 299.

[25] J.F. Haw, T. Xu, J.B. Nicholas, P.W. Goguen, Nature 389 (1997) 832.

[26] R.A. Van Santen, X. Rozanska, Adv. Chem. Eng. 28 (2001) 399.

[27] A.A. Maryott, E.R. Smith, National Bureau of Standards Circular 514, 1951, <http://www.dtic.mil/cgi-bin/GetTRDoc?AD=ADA278956> accessed February 12, 2013.

[28] J.B. Nicholas, Top. Catal. 9 (1999) 181.

[29] M.J. Wulfers, L.C. Gilbert, F.C. Jentoft, unpublished data, University of Oklahoma, 2012.

[30] M. Mohagheghi, G. Bakeri, M. Saeedizad, Chem. Eng. Technol. 30 (2007) 1721.

[31] J.R. Welty, C.E. Wicks, R.E. Wilson, G.L. Rorrer, Fundamentals of Momentum, Heat, and Mass Transfer, 5th Ed., John Wiley & Sons, Inc., 2008.

[32] J.O. Hirschfelder, R.B. Bird, E.L. Sporz, Chem. Rev. 44 (1949) 205.

[33] H.S. Fogler, Elements of Chemical Reaction Engineering, 4th Ed., Prentice Hall, 2006.

[34] International Zeolite Association, <http://www.iza- online.org/natural/Datasheets/Mordenite/mordenite.htm>, accessed January 28, 2013.

[35] D.E. Resasco, in I.T. Horvath (Ed.), Encyclopedia of Catalysis, vol. 3, John Wiley & Sons, Hoboken, NJ, 2002.

[36] A.T. Bell, "Applications of Quantum Theory and Molecular Dynamics to the Analysis of Zeolite-Catalyzed Reactions", Spring 2012 American Chemical Society National Meeting, San Diego, CA, March 25-29, 2012, <http://presentations.acs.org/common/presentation-detail.aspx/Spring2012/CATL/CATL004a/16-01-0019>, accessed February 11, 2013.

[37] M. Boronat, P. Viruela, A. Corma, Phys. Chem. Chem. Phys. 3 (2001) 3235.

[38] C. Wattanakit, S. Nokbin, B. Boekfa, P. Pantu, J. Limtrakul, J. Phys. Chem. C 116 (2012) 5654.

[39] D. Gleeson, J. Phys. Chem. A 115 (2011) 14629.

[40] L. Domokos, L. Lefferts, K. Seshan, J.A. Lercher, J. Catal. 197 (2001) 68.

[41] J.I. Villegas, M. Kangas, R. Byggningsbacka, N. Kumar, T. Salmi, D.Yu. Murzin, Catal. Today 133-135 (2008) 762.

[42] R.A. Asuquo, G. Eder-Mirth, K. Seshan, J.A.Z. Pieterse, J.A. Lercher, J. Catal. 168 (1997) 292.

[43] A. de Lucas, J.L. Valverde, P. Sanchez, F. Dorado, M.J. Ramos, Appl. Catal., A 282 (2005) 15.

[44] R.A. Alberty, E. Burmenko, J. Phys. Chem. Ref. Data 13 (1986) 1173.

[45] V. Adeeva, W.M.H. Sachtler, Appl. Catal., A 163 (1997) 237.

[46] A. Lugstein, A. Jentys, H. Vinek, Appl. Catal., A 176 (1999) 119.

[47] J.M. Grau, J.M. Parera, Appl. Catal., A 162 (1997) 17.

[48] J. Houzvicka, V. Ponec, Ind. Eng. Chem. Res. 36 (1997) 1424.

[49] M. Boronat, P. Viruela, A. Corma, J. Phys. Chem. A 102 (1998) 982.

[50] Y.V. Joshi, A. Bhan, K.T. Thomson, J. Phys. Chem. B 108 (2004) 971.

[51] M. Boronat, P. Viruela, A. Corma, J. Phys. Chem. 100 (1996) 633.

5 Conversion of 1,4-$^{13}C_2$-*n*-butane on H-mordenite and Pt/H-mordenite

5.1 Introduction

In addition to kinetics, carbon-13 labeled reagents have historically been an effective means by which to analyze reaction pathways. When applied to butane isomerization on solid acids, the results have been controversial. For the catalyst used in this investigation, the zeolite H-mordenite, the results from conversion of carbon-13 labeled butane have been reported only twice (by the same group) and significant carbon-13 scrambling in products was observed [1,2]. Carbon-13 scrambling is typically explained by participation of intermolecular reaction pathways.

Isotope scrambling in products produced from conversion of carbon-13 labeled butane has also been observed using sulfated zirconia [3,4], promoted sulfated zirconia [3,5], and industrial chlorided alumina catalysts [6]. In these cases, it was concluded that the isobutane was produced predominately through intermolecular reaction pathways. However, conversion of carbon-13 labeled butane has also led to different results and conclusions. Very little isotope scrambling was observed by Garin et al. [7], who concluded that the intramolecular skeletal isomerization pathway was most active on sulfated zirconia. Okuhara and co-workers [8,9] found the mechanism to depend on the presence of platinum and H_2 on sulfated zirconia, WO_3/ZrO_2, and the heteropolyacid $Cs_{2.5}H_{0.5}PW_{12}O_{40}$. These contradictory reports suggest that there are important variables affecting the extent of isotope scrambling, and thus the extracted mechanistic information, that have not been identified.

In experiments using carbon-13 labeled butane as the reactant, a binomial distribution of isotopes will be found in any product produced through intermolecular pathways in which the carbon atoms in C8 intermediates are scrambled to a statistical degree. Any intramolecular pathway would not cause intermolecular scrambling of the isotopes, and all C4 products would retain the same number of carbon-13 labels as the feed. Adeeva et al. [6] argued that a non-binomial distribution of carbon-13 isotopes in isobutane does not definitively prove the existence of an intramolecular pathway, as specific intermolecular pathways that selectively produce isobutane but do not result in carbon scrambling can operate. The isotope distribution in side products that can only be produced through intermolecular pathways, such as pentane, also provide information about the extent of isotope scrambling in C8 intermediates, but is rarely reported.

In this contribution, isotopic data in products produced from conversion of 1,4-$^{13}C_2$-*n*-butane on H-mordenite and Pt/H-mordenite is used to address the skeletal isomerization mechanism of *n*-butane. The effect of olefin concentration, shown in both Chapter 4 and in the literature [10-12] to be an important variable, is addressed.

5.2 Experimental

5.2.1 Materials

The catalysts used were H-mordenite (M1) and Pt/H-mordenite (Pt/M-C1). Calcination of the NH_4-mordenite was performed in the apparatus described in Section 3.2.1 using a 12 mm ID quartz reactor, supporting 2.0 g on a quartz frit in a synthetic air flow of 100 ml min^{-1} (NTP). The furnace was heated at 2 K min^{-1} to 423 K, held for 1 h,

and then heated at 5 K min^{-1} to 823 K and held for 2 h. 1,4-$^{13}C_2$-*n*-Butane (Isotec Inc., specified as 99.7% gas purity and 99% isotope purity) contained 5200 ppm ethane and 1200 ppm 1-butene as impurities, as measured by in-house GC analysis.

5.2.2 Apparatus

Catalytic experiments were performed using the apparatus described in Section 3.2.1. A 5.5 mm ID piece of borosilicate glass tubing was used as the reactor. The mass of H-mordenite or Pt/H-mordenite used in each experiment was 81-87 mg. HY zeolite (Zeolyst, Si/Al 2.5) was used as an olefin trap in specified experiments.

Product analysis was performed online with GC-MS (Agilent 5975E), MS (Pfeiffer OmniStar GSD 320), and GC-FID (Varian 3800 GC) placed in series. Reaction products were separated using a GS-Gaspro PLOT column (Agilent, 0.32 mm ID x 60 m) in the GC-MS. Splitless injections were performed on the GC-MS in all cases except when Pt/H-mordenite was used without an olefin trap, in which case a split ratio of 5:1 was used. Gas transfer lines were heated to 343 K.

5.2.3 Collection of data

Pretreatment of the H-mordenite sample began by heating at 5 K min^{-1} to 673 K in a synthetic air flow rate of 30 ml min^{-1} and was continued with sequential 0.5 h treatments in synthetic air, N_2, and H_2. Pretreatment of Pt/H-mordenite began by heating at 5 K min^{-1} to 403 K in N_2 at a flow rate of 30 ml min^{-1} and holding for 4 h. The temperature was then increased at 5 K min^{-1} to 560 K in H_2 at a flow rate of 30 ml min^{-1} flow of H_2 and held for 4 h. In experiments that used an olefin trap, 190-200 mg of HY zeolite was placed in a separate borosilicate glass tube through which the gas stream passed before reaching the reactor containing the H-mordenite. Before heat was applied

for the mordenite pretreatment, the trap was heated with heating tape to 473 K in the starting gas flow (either synthetic air for H-mordenite or N_2 for Pt/H-mordenite) and held at this temperature for 1 h. At the end of the mordenite pretreatment, the trap was cooled to ambient temperature and the temperature of the reactor containing the mordenite was set at 573 K. The reactant gas mixture was composed of H_2, helium, and 1,4-$^{13}C_2$-*n*-butane flowing at rates of 21, 6, and 3 ml min^{-1}, respectively, for all experiments except when Pt/H-mordenite was used without an olefin trap, in which case the gas mixture consisted of H_2 and 1,4-$^{13}C_2$-*n*-butane flowing at rates of 27 and 3 ml min^{-1}, respectively. For experiments in which an olefin trap was not used, online GC and GC-MS injections were taken 3 minutes after hydrocarbon flow to the reactor had started. For experiments in which an olefin trap was used, injections were taken 6.5 minutes after hydrocarbon flow to the reactor had started. GC-MS data was used to determine isotope distributions and GC-FID data was used to report rates and selectivities, except where noted. Conversion of *n*-butane to gas phase products other than isotopomers of the feed was less than 5 % in all cases.

5.2.4 Analysis of fragmentation patterns measured with online GC-MS

Because an electron impact ionization source was used in the GC-MS, fragmentation of product species produced a signal at many m/z ratios other than that of the molecular ion (M^+). The fragmentation must be accounted for to properly determine the isotope distribution for a mixture of chemically identical species (for example, 100% isobutane) differing only in their isotopic composition (various amounts of carbon-13 atoms).

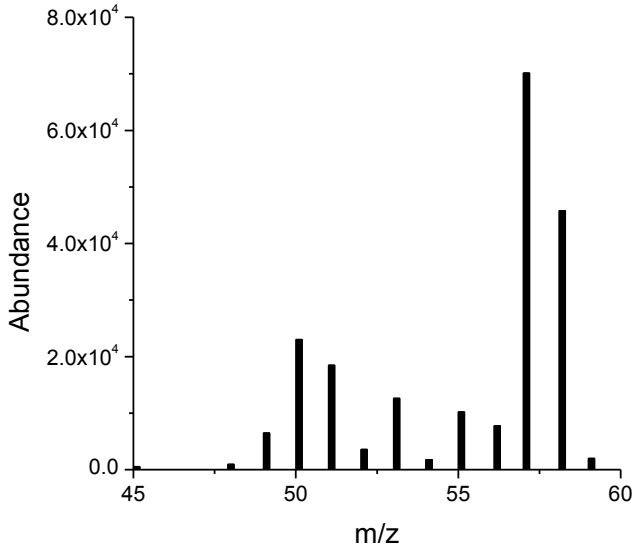


Figure 5.1: The mass spectrum of isobutane, at natural abundance of carbon, from m/z = 45 to m/z = 60.

In separate experiments, the fragmentation patterns of the main gas phase products (propane, isobutane, *n*-pentane, and 2-methylbutane) were measured at a natural abundance of carbon. From this data, the ratio between the M^+ fragment and fragments at sequentially lower masses (i.e. M^+-1, M^+-2, etc.) was determined. A portion of the mass spectrum of isobutane at natural abundance of carbon is shown in Fig. 5.1. The intensity of fragments in the region of interest, normalized to a sum of 100, are shown in Table 5.1.

Table 5.1: Normalized intensity of fragments measured in the GC-MS for propane, isobutane, *n*-pentane, and isopentane at natural isotopic abundance of carbon

Propane		**Isobutane**		***n*-Pentane**		**Isopentane**	
m/z	**Normalized Intensity**	**m/z**	**Normalized Intensity**	**m/z**	**Normalized Intensity**	**m/z**	**Normalized Intensity**
45	1.1	59	1.4	73	4.6	73	3.8
44	32.0	58	33.3	72	80.5	72	69.6
43	35.1	57	50.9	71	8.0	71	24.2
42	6.7	56	5.6	70	1.9	70	1.4
41	20.0	55	7.4	69	2.2	69	1.0
40	5.2	54	1.3	68	0.4		
				67	2.0		

Because 1.1% of carbon atoms at natural abundance are carbon-13, the ratios in Table 5.1 must be corrected. Species containing a carbon-13 atom undergo fragmentation with the same pattern as species containing only carbon-12 atoms, but produce a signal at different m/z ratios. The signal for isobutane at m/z = 58 is used as an example in Eqn. 18:

$$S_{58} = S_{MW=58} + S_{MW=59} \tag{18}$$

S_{58} is the signal at m/z = 58 measured by the mass spectrometer, $S_{MW=58}$ is the signal from isobutane species with four carbon-12 atoms (this is the M^+ peak), and $S_{MW=59}$ is the signal from isobutane species with three carbon-12 atoms and one carbon-13 atom (this is the M^+-1 peak). Thus, the intensity of the signal at m/z = 58 is a combination of the signal from the M^+ peak of species with four carbon-12 atoms and the signal from the M^+-1 peak of species with three carbon-12 atoms and one carbon-13 atom. The desired information is the true peak ratios, for example between the M^+ peak and the M^+-1 peak of an isotopically pure species. This can be extracted by solving a system of linear algebraic equations that keeps the M^+/M^+-n ratios of species with and without carbon-13 constant. The signal at M^++1, (for example, m/z = 59 for isobutane) can only come from species with one carbon-13 atom, and this is used as a basis to determine the contribution from species containing one carbon-13 atom. An example of the contribution from carbon-13 atoms to the total signal is shown in Table 5.2 for isobutane. Note that the peak ratios for species with and without a carbon-13 atom are the same. For example, in both columns the M^+/M^+-1 ratio is 0.6. The peak ratios determined using this method were used to extract the isotope distributions in gas phase products from 1,4-$^{13}C_2$-*n*-butane and are shown in Table 5.3.

Table 5.2: Contributions of isobutane species (at natural abundance of carbon) with zero and one carbon-13 isotope to the GC-MS signal

m/z	Normalized Intensity	Contribution from carbon-13 containing species	Contribution from species with only carbon-12
59	1.4	1.4	0
58	33.3	2.4	30.9
57	50.9	0.2	50.7
56	5.6	0.3	5.3
55	7.4	0	7.4
54	1.3	0.4	0.9

Table 5.3: Ratios of the molecular ion (M^+) signal to the signals at lower masses for propane, isobutane, *n*-pentane, and isopentane.

Ratio	Propane	Isobutane	*n*-Pentane	Isopentane
M^+/M^+-1	0.87	0.61	10.14	2.83
M^+/M^+-2	4.99	5.85	44.67	52.45
M^+/M^+-3	1.51	4.19	37.30	65.95
M^+/M^+-4		34.39	246.59	
M^+/M^+-5			39.71	

5.3 Results

5.3.1 Product formation rates and isotope distributions from conversion of a non-purified feed

The rate of product formation on H-mordenite using a non-purified 1,4-$^{13}C_2$-*n*-butane feed is shown in Table 5.4. The rates were significantly higher than at any other set of conditions, and the selectivity to isobutane of 60%, reported in Table 5.5, was the lowest of those measured. The concentration of *n*-butenes was 32 ppm, which is higher than the calculated equilibrium concentration of 16 ppm. Traces of ethene and propene, which were not detected in other cases, were measured. Internal scrambling of carbon-13 atoms in *n*-butane, estimated from the ratio of m/z = 45 to m/z = 44, was 11.0% (Table 5.6). The overall conversion to gas phase products other than *n*-butane with internally scrambled carbon-13 atoms was 3.8%.

Table 5.4: Product formation rates (µmol g^{-1} h^{-1}) from conversion of 1,4-$^{13}C_2$-*n*-butane on H-mordenite (M1) and Pt/H-mordenite (Pt/M-C1).

Catalyst	H-mordenite[a]	Pt/H-mordenite[b]	H-mordenite[a]	Pt/H-mordenite[a]
$P(H_2)$ / kPa	70	90	70	70
Purified feed	No	No	Yes	Yes
Methane	9	n.q.	8	9
Ethene	37	n.q.	0	0
Propane	755	62	110	46
Propene	7	n.q.	1	0
Isobutane	1770	370	765	495
C4 olefins	39	13	18	13
Pentanes	330	37	75	30
Hexanes	23	n.q.	1	0

[a] measured with GC-FID
[b] measured with GC-MS
n.q. means not quantified

Table 5.5: Product selectivities (mol %) from conversion of 1,4-$^{13}C_2$-*n*-butane on H-mordenite (M1) and Pt/H-mordenite (Pt/M-C1).

Catalyst	H-mordenite[a]	Pt/H-mordenite[b]	H-mordenite[a]	Pt/H-mordenite[a]
$P(H_2)$ / kPa	70	90	70	70
Purified feed	No	No	Yes	Yes
Methane	0	n.q.	1	2
Ethene	1	n.q.	0	0
Propane	25	13	11	8
Propene	0	n.q.	0	0
Isobutane	60	77	78	83
Butenes	1	3	2	2
Pentanes	11	8	8	5
Hexanes	1	n.q.	0	0

[a] measured with GC-FID
[b] measured with GC-MS
n.q. means not quantified

Table 5.6: Percent of 1,4-$^{13}C_2$-*n*-butane with internally scrambled carbon-13 atoms after conversion on H-mordenite or Pt/H-mordenite.

Catalyst	**Trap**	**Internal scrambling**
H-mordenite	No	11.0 %
H-mordenite	Yes	10.1 %
Pt/H-mordenite	No	9.7 %
Pt/H-mordenite	Yes	10.9 %

Significant carbon-13 scrambling was seen in all products. Isobutane molecules with two carbon-13 atoms accounted for 49% of the total product, whereas 37.5% would be expected in a binomial distribution (Fig. 5.2 and Table 5.7). The carbon-13 isotopes in propane and pentanes were almost scrambled to a statistical degree. Propane species with 1 and 2 carbon-13 isotopes accounted for 41% and 39% of the total product, respectively, whereas 37.5% would be expected in a binomial distribution. Isotopes were also extensively scrambled in pentanes, with 34% to 36% of both *n*-pentane and 2-methylbutane having 2 or 3 carbon-13 atoms, whereas 31.25% is expected in a binomial distribution.

Conversion of non-purified 1,4-$^{13}C_2$-*n*-butane on Pt/H-mordenite resulted in product formation rates, selectivities, and isotope distributions, that differed considerably from those produced on H-mordenite. The rates of formation (Table 5.4) of all products were lower; for example, the rate of isobutane formation was 75% lower. The selectivity to isobutane was 77% on Pt/H-mordenite, which is 17% higher than on H-mordenite. The isobutane composition with two carbon-13 isotopes was 72% (Table 5.7). The concentration of propane and pentane was too low to measure a reliable mass spectrum in the GC-MS, and the isotope distributions are, consequently, not reported. The concentration of *n*-butenes in the effluent was 12 ppm. It should be noted that the partial pressure of H_2 was different in both experiments, but in both cases a large excess of H_2 was used relative to *n*-butane.

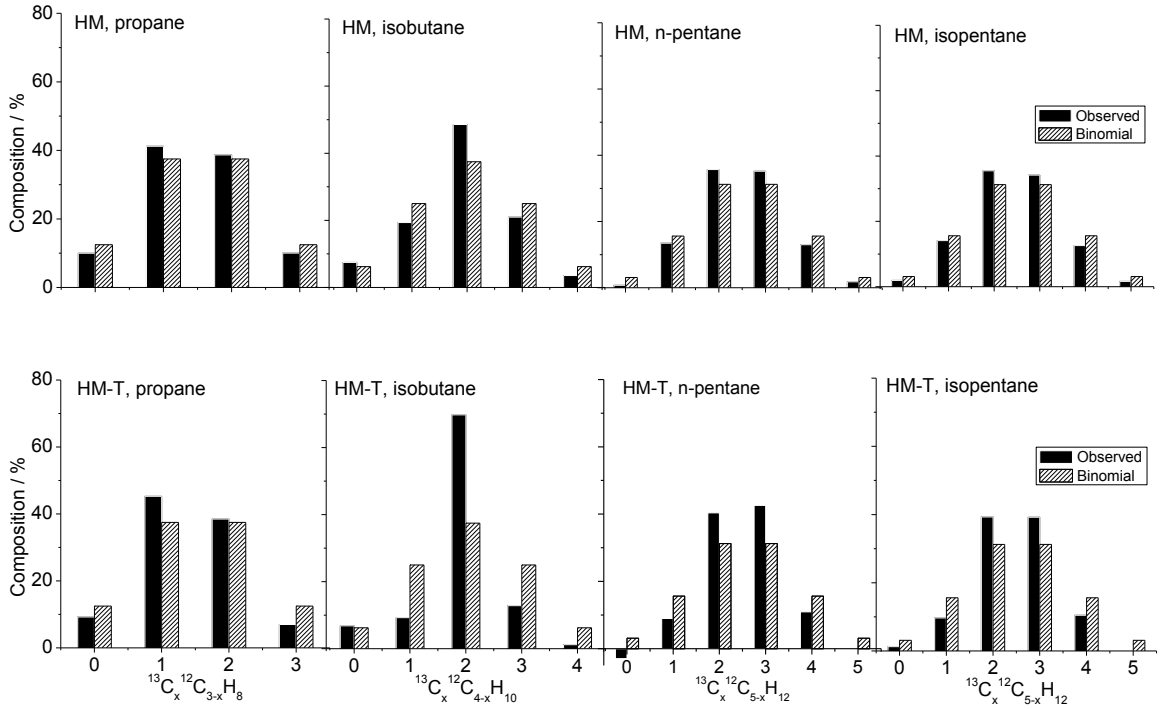


Figure 5.2: Isotope distributions in products produced from 1,4-$^{13}C_2$-*n*-butane on H-mordenite with (HM-T) and without (HM) an olefin trap.

Table 5.7: Isotope distributions in products produced from 1,4-$^{13}C_2$-*n*-butane.

Catalyst	Trap	% ^{13}C isotopes					
		0	**1**	**2**	**3**	**4**	**5**
Propane							
H-mordenite	No	10	41	39	10		
H-mordenite	Yes	9	45	38	7		
Binomial		*12.5*	*37.5*	*37.5*	*12.5*		
Isobutane							
H-mordenite	No	8	19	49	21	4	
Pt/H-mordenite	No	3	14	72	10	0	
H-mordenite	Yes	7	9	70	13	1	
Pt/H-mordenite	Yes	9	3	81	7	0	
Binomial		*6.2*	*25*	*37.5*	*25*	*6.2*	
2-Methylbutane							
H-mordenite	No	2	14	36	34	13	2
H-mordenite	Yes	1	10	39	39	10	0
Binomial		*3.1*	*15.6*	*31.2*	*31.2*	*15.6*	*3.1*
***n*-Pentane**							
H-mordenite	No	1	14	36	35	13	2
H-mordenite	Yes	-3	9	40	43	11	0
Binomial		*3.1*	*15.6*	*31.2*	*31.2*	*15.6*	*3.1*

5.3.2 Product formation rates and isotope distributions from conversion of a purified feed

Product formation rates and selectivities on H-mordenite from conversion of purified 1,4-$^{13}C_2$-*n*-butane differed considerably from those measured when a non-purified feed was used. With purification of the feed, lower product formation rates and a higher selectivity to isobutane were observed. For example, with a purified feed the rate of isobutane formation on H-mordenite was 765 μmol g^{-1} h^{-1}, whereas with a non-purified feed the rate was 1770 μmol g^{-1} h^{-1} (Table 5.4). The rates of propane and pentane formation were also lower. The selectivity to isobutane increased to 78% from 60% with a non-purified feed. The concentration of *n*-butenes in the reactor effluent was 16 ppm.

The decrease in product formation rates and changes in selectivity coincided with a change in isotope distributions (Fig. 5.2 and Table 5.7). With a purified feed, 70% of isobutane species retained two carbon-13 atoms. The fraction of propane species with one and two carbon-13 labels was 45.3 and 38.5%, respectively, whereas 37.5% is expected in a binomial distribution. Both *n*-pentane and 2-methylpentane had a slightly larger composition of species with 2 and 3 carbon-13 isotopes than expected in a binomial distribution. We note that the concentration of the disproportionation products propane and pentanes was low (115 ppm for propane, < 80 ppm for pentanes), and an accurate measurement of their mass distribution relied on data near or below the detection limits of the GC-MS.

In contrast to what was observed on H-mordenite, product formation rates and selectivities on Pt/H-mordenite using purified and non-purified 1,4-$^{13}C_2$-*n*-butane were similar (Table 5.4 and Table 5.5). The selectivity to isobutane of 83% on Pt/H-mordenite when using an olefin trap was the highest measured under any set of conditions, but was not significantly higher than the 78% selectivity observed when using a non-purified feed. It should again be noted that the partial pressure of H_2 was different in both experiments, but a large excess relative to *n*-butane was used in both cases.

Purification of the feed also resulted in 81% of isobutane species retaining two carbon-13 isotopes. This was the largest percentage of isobutane species with two carbon-13 isotopes produced under any set of conditions, and coincides with the highest selectivity to isobutane under any set of conditions. The percentage of isobutane species containing other amounts of carbon-13 atoms did not seem to follow a statistical

pattern. The low concentration of propane and pentanes again prohibited an accurate measurement of their isotope distributions.

5.4 Discussion

5.4.1 Isotope distribution in products formed from 1,4-$^{13}C_2$-*n*-butane

Carbon-13 labeled butane is a tool that can potentially be used to distinguish between competing intramolecular and intermolecular skeletal isomerization pathways. The ability to distinguish the two pathways relies heavily on the assumption that a statistical distribution of isotopes is achieved in C8 intermediates, meaning that any product produced by cracking of a C8 intermediate would also have a statistical distribution of isotopes. Once adsorbed, the extent of scrambling in C8 intermediates depends on the relative activation energies for isomerization, beta-scission, and desorption. Intuitively, one might expect the activation energy for isomerization to be much lower than for beta-scission, in which case the carbon-13 atoms should scramble significantly. If isobutane were produced only through an intramolecular pathway, no carbon-13 scrambling would be observed, because no intermolecular carbon-carbon bonds have to be made or broken.

Adeeva et al. [6] questioned the assumption that carbon-13 atoms in C8 intermediates are statistically scrambled. Using 1,4-$^{13}C_2$-*n*-butane to examine the reaction pathways of *n*-butane on industrial chlorided alumina catalysts, more isobutane with two carbon-13 isotopes was detected than what is expected in a binomial distribution, and the ratio of molecules with 3 and 4 carbon-13 isotopes was not equal to 4 as required in a binomial distribution. A C8 intermediate with a non-statistical

distribution of carbon-13 atoms was hypothesized, and a specific pathway to the 2,4,4-trimethylpentyl cation was proposed. No mention was made of the isotope distributions in propane and pentane side products, which were produced at an appreciable rate and also contain information about the extent of scrambling in C8 intermediates. Additionally, the effect of internal rearrangement of carbon atoms in *n*-butane, which should occur readily, was not considered in the discussion of isotope distributions in gas phase products. Oddly, the reported internal rearrangement of carbon-13 atoms in *n*-butane (6-25%) was lower than conversion to gas phase products (10-36%) [6]. In this work, we found the internal isomerization to be 9-11% in all cases, which is much higher than the 0.5-4.5% conversion to gas phase products.

To properly determine the extent of carbon scrambling in C8 intermediates, both the test of Adeeva et al. [6] and the isotope composition in side products should be considered when possible. However, with a low concentration of products an accurate measurement of fragmentation patterns is difficult. For example, when Pt/H-mordenite was used with a purified feed in this work, the concentration of isobutane in the product stream was only 520 ppm. If a binomial distribution of isotopes had resulted, only 33 ppm of the isobutane would have contained four carbon-13 isotopes. Thus, the disadvantage of operating at differential conversions is that determining the isotope distribution in some products can be analytically challenging, but the advantage is that secondary reactions are minimized.

The isotope distributions for isobutane produced under different reaction conditions can be divided into two general categories: i) that in which there was extensive scrambling (non-purified feed on H-mordenite), and ii) those in which there

was less extensive scrambling (all others). When the arguments of Adeeva et al. [6] are applied to determine if carbon-13 atoms in C8 intermediates were statistically scrambled, in case i) the ratio between isobutane species with 3 and 4 carbon-13 isotopes was 5.9. However, the ratio between the fraction with 1 and 0 carbon-13 isotopes was 2.6. Adeeva et al. [6] made a similar observation, but explained that the data from species with three and four isotopes is more reliable because there is less of a contribution to the respective molecular ion fragments from species with a higher m/z (more carbon-13 isotopes). However, they reported that "the concentration of molecules containing three ^{13}C is equal, within experimental error, to that of molecules with one ^{13}C atom." If species with 0 and 1 carbon-13 isotopes are also considered, the test is inconclusive.

The isotope distribution in propane and pentanes can also be used to glean information about the extent of isotope scrambling in C8 species. Of use is Eqn. 19:

$$D = \frac{\sum|C_{obs} - C_{bin}|}{n} \tag{19}$$

C_{obs} is the observed percent molar composition of a species with a particular molecular mass, and C_{bin} is the percent molar composition for that molecular mass in a binomial distribution, and n is the number of carbon atoms in the species of interest. The resulting value is an indicator of either i) the extent of scrambling (or lack thereof) in C8 intermediates, ii) measurement error, or in the case of isobutane, iii) the contribution of an intramolecular pathway. The value of D in Eqn. 19 for a product containing a perfectly binomial distribution of isotopes is zero. For propane, *n*-pentane, and isopentane produced on H-mordenite with an impure feed, the value of Eqn. 19 was 3.3, 3.4, and 2.9, respectively. The value for isobutane was 6.2. It is unlikely that

measurement error can account for the deviation from the binomial distribution in isobutane, as its concentration was the highest of any product and sufficient for an accurate measurement of all masses of interest. It is possible that the deviation from a binomial distribution was due to non-statistical isotope scrambling in C8 intermediates, but the higher values of Eqn. 19 compared to the disproportionation products suggest otherwise. Thus, we conclude that a small portion of the isobutane was produced by an intramolecular pathway.

The isotope distributions in products produced by H-mordenite with a purified feed can be taken to be representative of a case in which carbon-13 scrambling in isobutane is less extensive. Applying the arguments of Adeeva et al. [6] to isobutane, the ratio between species containing 3 and 4 carbon-13 isotopes was 10.5, but the ratio between species with 1 and 0 carbon-13 isotopes was 1.4. So again, the test is inconclusive. Turning to the isotope distribution in propane and pentane as an indicator of C8 scrambling, the value of Eqn. 19 for propane, *n*-pentane, and isopentane was 5.8, 8.2, and 6.4, respectively. The values are higher than in case i) and could indicate non-statistical scrambling or additional error in the measurements, as gas phase concentrations were about 80% lower than in case i). For example, no signal was measured at m/z = 77 for either of the pentanes. The result of Eqn. 19 for isobutane in this case was 16.5, suggesting a large contribution from an intramolecular pathway.

5.4.2 The effect of olefins on reaction pathways and isotope distributions

Three principle effects of olefins can be discerned from the data: i) higher formation rates of all products, ii) decreased selectivity to isobutane and increased selectivity to propane and pentane side products, and iii) more carbon-13 scrambling in

the isobutane product. When non-purified 1,4-$^{13}C_2$-*n*-butane was converted on H-mordenite, the rates of formation for all products were the highest measured, the selectivity to isobutane was only 60%, and the isotope scrambling in isobutane was extensive. When a purified feed was used, product formation rates were more than 50% lower, the selectivity to isobutane was 78%, and isotope scrambling in isobutane was less extensive. The only difference between the two experiments was the partial pressure of 1-butene in the feed. The 1-butene concentration was not measured after passing through the olefin trap, and it is possible that some was not removed. This would explain why a higher concentration of *n*-butene was measured in the effluent from H-mordenite than from Pt/H-mordenite when a purified feed was used, and why product formation rates were higher on the platinum-free catalyst.

As discussed in Section 1.2.4.3 and reported in Chapter 4, similar observations regarding the promoting effect of olefins in the feed on product formation rates have been made previously, but an isotopically labeled feed was not used. Engelhardt [12] found that ethene, propene, and isobutene all enhanced *n*-butane conversion rates and concluded that the role of propene and isobutene was to increase the concentration of carbenium ions, while the effect of ethene was attributed to di- and oligomerization reactions. An increased selectivity to disproportionation products with addition of olefins was observed but not discussed. In the present work, the increased rate of *n*-butane conversion in the presence of 120 ppm of 1-butene can also be partially explained by an increase in the concentration of activated surface species, which are most likely alkoxides. However, an increase in the concentration of surface species should not affect the product selectivity. As olefins are necessary for the dimerization

reaction that forms a C8 intermediate, the intermolecular pathway may be particularly sensitive to the olefin concentration, as reported in Section 4.4.2.4. Thus, as the concentration of butenes increases, the contribution of non-selective intermolecular pathways should become more prominent, resulting in a higher concentration of propane and pentane side products. This effect is observed in Fig. 4.6. Narbeshuber et al. [13] found intermolecular reactions involving olefins on zeolites to be very sensitive to the olefin concentration, even suggesting that there is a "critical lower limit" for the olefin concentration at which di- and oligomerization reactions begin to occur.

Skeletal isomerization of *n*-butene is performed industrially and is also an active area of catalysis research. The literature from this area is capable of providing an explanation for the change in selectivity with varying butene concentration. In general, when butene is used as the reactant, an increase in its partial pressure causes a decrease in selectivity to skeletal isomerization products, and an increase in selectivity to disproportionation products [14-16]. The same effect is observed in the present work. If both skeletal isomerization and disproportionation products were formed through intermolecular pathways, an increase in the gas phase concentration of one of the reactants (butene, which is probably necessary for the initial dimerization reaction) should increase the rate of formation of all products but not alter the selectivity, especially when operating with differential conversions where secondary reactions should be minimal. However, selectivities are altered by the concentration of butene, suggesting that all products are not produced exclusively through intermolecular pathways. According to Houzvicka et al. [14], suppression of skeletal isomerization and promotion of disproportionation pathways is not expected from an increase in butene

partial pressure when the prevailing mechanism of isomer formation is dimerization-cracking. Instead, the effect of increasing the gas phase concentration of butene is to facilitate non-selective intermolecular pathways due to the higher concentration of a necessary reactant, butene. Thus, the effect of butene impurities in this work suggests that there are competing intramolecular and intermolecular skeletal isomerization pathways of *n*-butane on H-mordenite and Pt/H-mordenite.

The impure 1,4-$^{13}C_2$-*n*-butane feed used in this work, diluted to a partial pressure of 10 kPa, contained 120 ppm of 1-butene. H-mordenite produced propane, isobutane, and pentane in concentrations of 690, 1610, and 300 ppm, respectively. As the molar ratio of 1-butene in the feed to the amount of propane or pentane produced is smaller than 1, the cracking products of intermolecular reaction pathways must re-enter reaction cycles. This means that each olefin in the feed is able to propagate through multiple turnovers, even at "differential" conversions.

5.4.3 Implications for the skeletal isomerization mechanism

The observation that product formation rates, selectivities, and isotope distributions all depend on the partial pressure of butene forms a convincing argument that a kinetically relevant intramolecular skeletal isomerization pathway exists for *n*-butane on H-mordenite and Pt/H-mordenite. Furthermore, it affirms the conclusion in Chapter 4 that intermolecular pathways are particularly sensitive to the concentration of olefins. It appears that one of the main roles of platinum and H_2 is to control the gas phase olefin concentration, which in turn has an effect on product formation rates, selectivities, and isotope distributions.

A substantial amount of literature supports the claim that the intramolecular skeletal isomerization pathway is both possible and kinetically relevant. This includes apparent reaction orders with respect to *n*-butane equal to or close to 1 [17,18], kinetic models that failed to describe product distributions with only an intermolecular pathway [19], DFT calculations [20-23], and portions of the butene isomerization literature [14,15,24-26]. Carbon-13 labeled reactants have been pivotal in proving that an intramolecular mechanism of butene skeletal isomerization is dominant on partially deactivated 10-membered ring zeolites [24,25]. In principle, the energy barrier associated with the rearrangement step of intramolecular butane and butene skeletal isomerization is the same, with the full reaction coordinate differing only in means of activation and desorption. Thus, the mechanistic aspects of butene skeletal isomerization are also relevant to discussion of the butane rearrangement.

It is widely accepted that in mineral acids a primary carbenium ion must be formed for intramolecular *n*-butane skeletal isomerization to occur [27-29]. The relevance of this to the rearrangement mechanism on solid acids, however, is murky. As stated by Kazansky [30], an important feature of heterogeneous acid catalysts is the possibility of catalyzing concerted reaction pathways with low activations energies and complicated reaction coordinates. Boronat et al. [20] used DFT calculations to show that the intramolecular skeletal isomerization pathway of 1-butene on a zeolite cluster does not involve formation of a primary carbenium in the transition state. Referring to the transition state, they state that "unlike in superacid media, neither the optimized geometry nor the net atomic charges of this structure correspond to a primary isobutyl cation". In mineral acids, the transition state is formed upon opening of the

cyclopropane ring, at which point a primary carbenium ion is formed [29]. On a zeolite, the transition state is the methylcyclopropane species itself, where the transferring methyl group is halfway between the other two carbon atoms of the cyclopropane ring. In this state each carbon atom in the ring is covalently bonded to two other carbon atoms, although two of the bonds are longer than a normal carbon-carbon single bond. It follows that because each carbon atom is bonded to two other carbon atoms, there is no cation in a primary position. Opening the ring results in formation of a primary alkoxide, which is lower in energy. The calculated energy requirement to move from a *sec*-butyl alkoxide to the transition state was 226-247 kJ mol^{-1} on a T3 zeolite cluster [20], but only 108 kJ mol^{-1} when the framework of a real zeolite was taken into consideration using a model of Theta-1 [21]. Thus, it is conceivable that an intramolecular isomerization pathway of butane could follow a similar reaction coordinate to that predicted by Boronat et al. [20] for butene, differing only in means of activation and desorption, both of which probably occur to a large extent by hydride transfer.

5.4.4 A unified model for interpreting the results from carbon-13 labeled butane conversion

The data presented in Chapter 4 and hitherto in the current chapter implicates the butene concentration as the variable that most heavily influences the operating reaction pathways, and consequently the amount of isotope scrambling in products produced from carbon-13 labeled butane. Thus, when olefins are present, either as impurities in the feed or from dehydrogenation of *n*-butane, there will be significant

isotope scrambling. With this in mind, a unified model is proposed to help explain some of the contradictory reports found in the literature.

The first investigation of the butane skeletal isomerization mechanism on H-mordenite using carbon-13 labeled butane was performed by Bearez et al. [1], and to our knowledge is the only previous paper reporting the isotope distribution for all products produced by this catalyst. Another paper reports only minimal results [2]. Using a recirculation reactor with 1-^{13}C-isobutane as the reactant, the isotope distribution in propane, *n*-butane, isobutane, and isopentane was reported as a function of conversion. Because isotope scrambling was detected in the three main products, a disproportionation mechanism involving formation of a C8 carbenium ion as the rate-limiting step was proposed. However, the data clearly show that the isotope composition of the disproportionation products propane and isopentane did not change at all over the range of conversion (≈ 15-50%), while the isotope distribution of the skeletal isomerization product, *n*-butane, changed significantly with conversion. Much less isotope scrambling was observed at 15% conversion than was observed at 40% conversion. In fact, the isotope distribution in *n*-butane mirrored that of the reactant, and not that of the propane and isopentane disproportionation products. The non-changing binomial isotope distribution in propane and isopentane demonstrates that isotopes in C8 intermediates were statistically scrambled. Thus, if *n*-butane was formed through similar intermolecular pathways, the isotope distribution should also be binomial over the entire range of conversion. The most reasonable explanation is that the main pathway of *n*-butane formation at low conversion was probably intramolecular. The *n*-butane formed as an intramolecular product was then able to enter intermolecular

reaction cycles that cause isotope scrambling, and the isotopic evidence of an intramolecular pathway was slowly erased.

Sachtler and co-workers converted 1,4-$^{13}C_2$-*n*-butane, also from Isotec Inc. (impurities not reported), in a recirculation reactor on a variety of sulfated zirconia based catalysts [3-5] and industrial chlorided alumina catalysts [6]. In all cases, a conclusion was reached that the operating mechanism of isobutane formation was, at least predominately, intermolecular. When any form of sulfated zirconia was used, the conversion at which the isotope distribution was reported was 40-60%. In these experiments, the high conversion may have erased any evidence that existed at lower conversions for an intramolecular pathway. In the previously discussed report of Bearez et al. [1], the distribution of carbon-13 isotopes in the isomerization product became completely binomial at about 40% conversion. Another possibility is that due to olefin impurities in the feed, the isotope scrambling was even more rapid, as seen in the data reported in this chapter. In contrast to the reports of Sachtler, Garin et al. [31] found far less isotope scrambling on sulfated zirconia and Pt/sulfated zirconia. In this case, conversions were only 8-18%, and a carefully purified homemade feed was used. The carefully purified feed eliminates the possibility of olefin feed contaminants, and the low conversion limits secondary reactions, thus allowing for isotopic evidence of an intramolecular pathway to be collected.

Finally, the skeletal isomerization mechanism on sulfated zirconia, WO_3/ZrO_2, and $Cs_{2.5}H_{0.5}PW_{12}O_{40}$ heteropolyacid was found to depend on the presence of platinum and H_2 by Okuhara and co-workers [8,9]. Platinum and H_2, for unknown reasons, promoted the intramolecular pathway, as determined by isotope distribution in gas

phase products. The 1,4-$^{13}C_2$-*n*-butane in these experiments was also from Isotec, Inc. (impurities not reported), conversions were around 10%, and H_2 was used as the feed diluent only in combination with catalysts containing platinum. The results mirror those presented in this paper; extensive isotope scrambling was seen on catalysts lacking platinum, and far less scrambling was seen on platinum-containing catalysts with H_2 in the feed. However, as demonstrated in this work, the operating mechanism is not *directly* impacted by the platinum on the catalyst or H_2 in the feed, but instead is *indirectly* impacted by their ability to control the gas phase concentration of olefins.

References

[1] C. Bearez, F. Avendano, F. Chevalier, M. Guisnet, Bull. Soc. Chim. Fr. 3 (1985) 346.

[2] M. Guisnet, N.S. Gnep, Appl. Catal., A 146 (1996) 33.

[3] H. Liu, V. Adeeva, G.D. Lei, W.M.H. Sachtler, J. Mol. Catal. A: Chem. 100 (1995) 35.

[4] V. Adeeva, G.D. Lei, W.M.H. Sachtler, Catal. Lett. 33 (1995) 135.

[5] V. Adeeva, G.D. Lei, W.M.H. Sachtler, Appl. Catal., A 118 (1994) L11.

[6] V. Adeeva, W.M.H. Sachtler, Appl. Catal., A 163 (1997) 237.

[7] F. Garin, L. Seyfried, P. Girard, G. Maire, A. Abdulsamad, J. Sommer, J. Catal. 151 (1995) 26.

[8] T. Echizen, T. Suzuki, Y. Kamiya, T. Okuhara, J. Mol. Catal. A: Chem. 209 (2004) 145.

[9] T. Suzuki, T. Okuhara, Catal. Lett. 72 (2001) 111.

[10] K.B. Fogash, Z. Hong, J.M. Kobe, J.A. Dumesic, Appl. Catal., A 172 (1998) 107.

[11] K.B. Fogash, Z. Hong, J.A. Dumesic, J. Catal. 173 (1998) 519.

[12] J. Engelhardt, J. Catal. 164 (1996) 449.

[13] T.F. Narbeshuber, A. Brait, K. Seshan, J.A. Lercher, J. Catal. 172 (1997) 127.

[14] J. Houzvicka, V. Ponec, Ind. Eng. Chem. Res. 36 (1997) 1424.

[15] J. Houzvicka, O. Diefenbach, V. Ponec, J. Catal. 164 (1996) 288.

[16] M.A. Asensi, A. Corma, A. Martínez, J. Catal. 158 (1996) 561.

[17] M.T. Tran, N.S. Gnep, G. Szabo, M. Guisnet, J. Catal. 174 (1998) 185.

[18] P. Cañizares, A. de Lucas, F. Dorado, Appl. Catal., A 196 (2000) 225.

[19] V. Nieminen, M. Kangas, T. Salmi, D.Y. Murzin, Ind. Eng. Chem. Res. 44 (2005) 471.

[20] M. Boronat, P. Viruela, A. Corma, J. Phys. Chem. A 102 (1998) 982.

[21] M. Boronat, P. Viruela, A. Corma, Phys. Chem. Chem. Phys. 3 (2001) 3235.

[22] C. Wattanakit, S. Nokbin, B. Boekfa, P. Pantu, J. Limtrakul, J. Phys. Chem. C 116 (2012) 5654.

[23] D. Gleeson, J. Phys. Chem. A 115 (2011) 14629.

[24] P. Meriaudeau, R. Bacaud, L. Ngoc Hung, A.T. Vu, J. Molec. Catal. A 110 (1996) L177.

[25] K.P. de Jong, H.H. Mooiweer, J.G. Buglass, P.K. Maarsen, in: Studies in Surface Science and Catalysis – Catalyst Deactivation, Proceedings of the 7th International Symposium, vol. 111, Elsevier B.V., 1997, p. 127-137.

[26] M.A. Asensi, A. Martínez, Appl. Catal., A 183 (1999) 155.

[27] D.M. Brouwer, H. Hogeveen, in A. Streitwieser, Jr., R.W. Taft (Eds.), Progress in Physical Organic Chemistry, vol. 9, Wiley-Interscience, New York, 1972, p. 179.

[28] D.M. Brouwer, Recl. Trav. Chim. Pay.-B. 87 (1968) 1435.

[29] M. Boronat, P. Viruela, A. Corma, J. Phys. Chem. 100 (1996) 633.

[30] V.B. Kazansky, Acc. Chem. Res. 24 (1991) 379.

[31] F. Garin, L. Seyfried, P. Girard, G. Maire, A. Abdulsamad, J. Sommer, J. Catal. 151 (1995) 26.

6 Identification of Low Temperature Carbonaceous Deposits and Their Impact on Alkane Conversion

6.1 Introduction

As discussed in Section 1.2.5, catalysts used for alkane isomerization are plagued by a tendency to deactivate during use. In the case of zeolite catalysts, deactivation is caused by a buildup of unsaturated carbonaceous deposits. The combination of platinum in the catalyst and H_2 in the feed is used to prevent their formation. As platinum is expensive and H_2 availability is limited, a catalyst that could perform the skeletal isomerization at a stable rate without platinum and H_2 would be valuable. Design of such a catalyst may only be possible with a better understanding of the surface chemistry leading both to selective formation of the desired gas phase products and to formation of carbonaceous deposits.

Methods for analysis of carbonaceous deposits can be divided into two broad categories: i) ex situ (post-mortem) and ii) in situ. The main deficiencies of ex situ methods are that they may not deliver information on the deposits as they exist during catalysis and that they often require additional chemical treatments before analysis. Guisnet and co-workers [1] developed a procedure involving digestion of spent zeolites in hydrofluoric acid, liquid–liquid extraction with dichloromethane, and GC-MS or HPLC analysis of the dichloromethane extract, which can be used for speciation of some organic residues. The technique has been particularly effective at characterizing the chemical composition of the hydrocarbon pool on methanol-to-hydrocarbons catalysts, showing that single- and multi-ring aromatic species with varying degrees of methylation are present and that the composition of the pool varies with zeolite

topology [2-4]. However, post-mortem analysis does not deliver information about a possible charged state of such deposits. Indeed, in situ analysis has shown that some aromatic species exist as cations on the working catalyst [5,6]. A recent review of coke characterization techniques, including several that are performed ex situ, has been provided by Bauer and Karge [7].

In situ methods can deliver information about the deposits as they exist on the working catalyst. For example, discrimination between neutral and cationic states is possible. In situ diffuse reflectance spectroscopy can be performed, with the proper equipment, under flow conditions at elevated temperatures, allowing for the active catalyst to be monitored. UV-vis spectroscopy is particularly sensitive to the $\pi \rightarrow \pi^*$ transitions of unsaturated hydrocarbons, which often account for a significant portion of the carbonaceous deposits. Infrared spectroscopy can also be performed under working conditions, but the absorption coefficients of vibrational transitions are usually orders of magnitude smaller than those of electronic transitions [8]. Another advantage of diffuse reflectance UV-vis spectroscopy in the investigation of zeolite catalysis is the absence of strong absorptions from the catalyst in the wavelength range of interest. In contrast, the strong vibrations of the zeolite lattice and absorption by the gas phase reactant can make identification of vibrations from the carbonaceous deposits difficult in diffuse reflectance IR spectra.

In situ UV-vis spectroscopy has previously been used for the purpose of identifying organic residues formed during conversion of methanol [5,6,9,10], ethene [11], *n*-butane [12-15], and *n*-pentane [14,16]. Interpretation of the bands formed during catalysis often relies on comparison with bands formed after adsorption of reference

compounds. Infrared spectroscopy can be used to provide complementary information. A strategy involving the use of these two spectroscopies to identify surface species formed on solid acids has been used in the past [17-24]. Typical band assignments can be retrieved from the review by Bauer and Karge [7].

Deactivation and coke formation during alkane isomerization on H-mordenite have been associated with high olefin levels in the feed [25,26], and it has been demonstrated that surface reaction products from 1-butene are similar to those formed during butane conversion [12]. The role of olefins for the formation of carbonaceous deposits in general has been emphasized in various reviews [27,28].

In this chapter, in situ diffuse reflectance UV–vis–NIR and infrared spectroscopies, and extractions of spent catalysts are used to investigate the carbonaceous deposits formed during conversion of *n*-butane or *n*-pentane on H-mordenite. The corresponding olefins are also employed as reactants to elucidate their role in the surface chemistry. In addition to analyzing the carbonaceous deposits formed in this specific scenario, a strategy combining in situ and post-mortem analysis to characterize the structure, charge, and reactivity of organic deposits is demonstrated.

6.2 Experimental

6.2.1 Materials

H-mordenite (both M1 and M2) was used. Calcination was performed at a temperature of 823–873 K in a synthetic air flow rate of 100 ml min^{-1}. Other materials were: *n*-butane (Matheson, 99.99%) containing 14 ppm isobutane and < 1 ppm propene

impurities, 1-butene (Sigma, ≥ 99%), 2% ammonia in helium (Airgas), *n*-pentane (Sigma, ≥ 99%), 1-pentene (Sigma, 98%), and 1-hexene (Sigma, 99%).

6.2.2 *n*-Butane and *n*-pentane conversion with in situ spectroscopic analysis

Conversion of *n*-butane or *n*-pentane was performed using the environmental chambers described in Section 3.3.2. The gas distribution system and online gas analysis equipment is described in Section 3.2.1. Before reaction, the zeolite (M1) was pretreated by heating to a temperature of 673 K for a series of 0.5 h treatments in flowing synthetic air, N_2, and H_2. The chamber was then cooled to reaction temperature.

Conversion of both *n*-butane and *n*-pentane occurred at atmospheric pressure. For *n*-butane, the total gas flow rate was 30 ml min^{-1} (NTP) with an *n*-butane partial pressure of 10 kPa and a balance of either H_2 or helium. For *n*-pentane, the total gas flow rate was 34 ml min^{-1} with an *n*-pentane partial pressure of 13 kPa and a balance of helium. The *n*-butane and *n*-pentane weight hourly space velocities (W/F) were 0.16 h and 0.08 h, respectively. Except for *n*-pentane, gas flow rates were controlled using mass flow controllers. To add *n*-pentane to the gas stream, helium was passed through liquid *n*-pentane in a three-legged saturator. The saturator was held at 257 K by placing it in a temperature-controlled bath of ethylene glycol and water. Gas lines were heated to 353 K.

6.2.3 In situ spectroscopic analysis of adsorption and reaction of olefins

H-mordenite was dried at temperatures of 573 to 673 K in the in situ cell and then cooled to the desired adsorption temperature in inert gas. Details of the pretreatments and heat treatments following adsorption are provided in the figure captions. The olefin (in the case of 1-pentene or 1-hexene liquid or vapor as specified)

was injected with a syringe into the gas stream through a septum; liquids vaporized in the heated lines and reached the sample as a vapor. For experiments in which H_2O vapor was applied, the inlet gas stream was diverted through a water-containing saturator.

6.2.4 Adsorption of olefins with subsequent digestion and extraction

Two hundred fifty milligrams of H-mordenite (M2) powder was loaded into a 12 mm ID tubular reactor made from quartz and placed in the furnace described in Section 3.2.1. For pretreatment, the sample was heated to 673 K while flowing 50 ml min^{-1} of synthetic air, held at 673 K for 1 h also in air flow, and then cooled to 323 K in 50 ml min^{-1} of N_2.

1-Butene was then admitted to the gas stream via mass flow controller in the amount of 45 μmol. After admission, the furnace remained at 323 K for 1 h. The zeolite powder was then removed from the reactor and a diffuse reflectance UV−vis spectrum was taken. During the transfer and the acquisition of the UV−vis spectrum, the zeolite was exposed to ambient conditions.

The zeolite was then placed in a polyethylene vial and aqueous hydrofluoric acid (Mallinckrodt, 49%) was added in the ratio of 8 ml g^{-1} zeolite. After 30 minutes, 4 ml of dichloromethane (Macron, 99.5%) was added. The liquid–liquid extraction was allowed to occur overnight. The dichloromethane phase was transferred to a different polyethylene vial and neutralized with a 0.01 M calcium hydroxide (Sigma, 95+%) solution. Species in the dichloromethane extract were then analyzed with a GC-MS (Agilent 5975E) using an HP-5MS column (Agilent, 0.25 mm ID x 30 m) for separation.

6.3 Results

6.3.1 In situ investigations of H-mordenite during alkane conversion

6.3.1.1 Catalyst activation

The UV–vis spectra of H-mordenite were characterized by a number of weak bands, which changed slightly during activation and could not be unambiguously assigned. Spectra recorded before activation showed bands at 1369 nm (7305 cm^{-1}), 1409 nm (7092 cm^{-1}), 1461 nm (6845 cm^{-1}), and 1906 nm (5247 cm^{-1}) in the NIR range, as exemplified in Fig. 6.1. Fundamental vibrations of silanol groups in H-mordenite are reported at 3740 cm^{-1}, whereas vibrations of bridging OH groups are reported at 3612 and 3585 cm^{-1} [29]. Assuming perfectly harmonic behavior, overtones should be observed at 1337 nm (Si–OH, 7480 cm^{-1}) and at 1384 and 1395 nm (Si–OH–Al, 7224

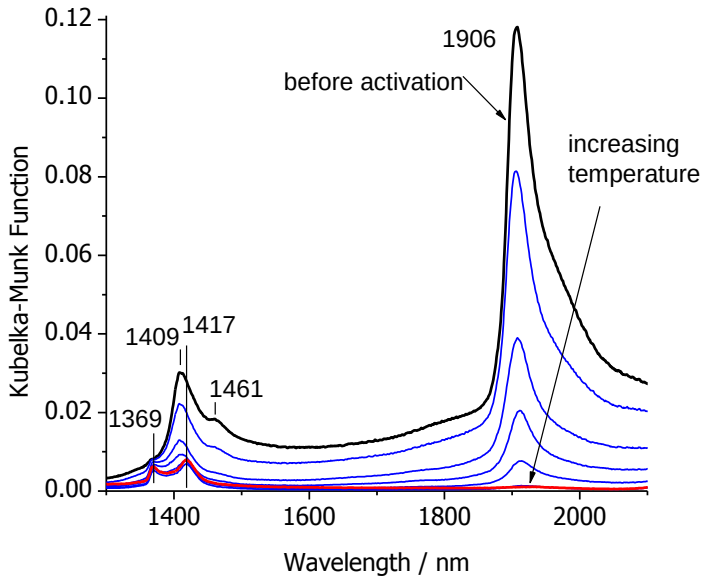


Figure 6.1: Diffuse reflectance NIR spectra of H-mordenite (M1) recorded during activation. Initial spectrum: black line, during heating to 673 K in a flow of synthetic air: blue lines, and after further treatment in N_2 and H_2 at 673 K and cooling to 623 K: red line.

and 7170 cm^{-1}). However, overtones are typically observed at slightly lower wavenumbers and thus longer wavelengths as a result of anharmonic behavior. We assign the band at 1369 nm to silanol groups and the band at 1409 nm to the two types of bridging OH groups. In IR spectra (Fig. 6.4), a band at 3650 cm^{-1} was resolved, which can be assigned to extraframework Al–OH vibrations [30].

The band at 1906 nm disappeared during heating in air flow. This band is a combination mode of the OH stretching and deformation vibrations of water (3652 cm^{-1} + 1595 cm^{-1} = 5247 cm^{-1} or 1906 nm). Thus, the spectra indicate dehydration of the catalyst surface. Consistent with this interpretation, the low frequency shoulder of the first overtone of the OH stretching vibrations (at 1461 nm, corresponding to 6845 cm^{-1} = 2 * 3423 cm^{-1}), which is assigned to OH vibrations perturbed by adsorbed water, disappears during activation. Switching of the gas flow to N_2 or H_2, respectively, and cooling to the reaction temperature had no significant effect on the OH vibrations, which were located at 1369 and 1417 nm at the end of the activation.

6.3.2 *n*-Butane conversion on H-mordenite: Catalytic performance and spectra collected in situ

When H_2 was used as the diluent, the performance was stable (Fig. 6.2, first 1.5 h), and no bands formed in the UV−vis spectra (Fig. 6.3). Isobutane, propane, and pentanes were the main products. The formation rates at 563 K in the in situ cell were somewhat lower than expected from experiments performed in an isothermal packed bed reactor (Table 4.1). This discrepancy can be explained by a temperature gradient in the catalyst bed caused by the heater placement. When H_2 was replaced with helium (Fig. 6.2, after 1.5 h), product formation rates increased by a factor of 20 and then

slowly decreased with time on stream. With H_2 as the diluent, the only olefins detected in the effluent stream were *n*-butenes at a concentration of 4 ppm. After changing the diluent to helium, the concentration of *n*-butenes immediately increased to 14 ppm and then decreased at a similar rate as the other products. Concurrent with the slow deactivation was the growth of a band at a wavelength of 286–292 nm. The absorption maximum of this band was initially at 286 nm and then slowly shifted to 292 nm with time. The Kubelka–Munk value at 292 nm is plotted versus time on stream in Fig. 6.2. Bands with less intensity relative to the 292 nm band were formed at longer wavelengths; a shoulder around 335 nm, a distinct band at 395 nm, and a broader band around 455 nm were noted.

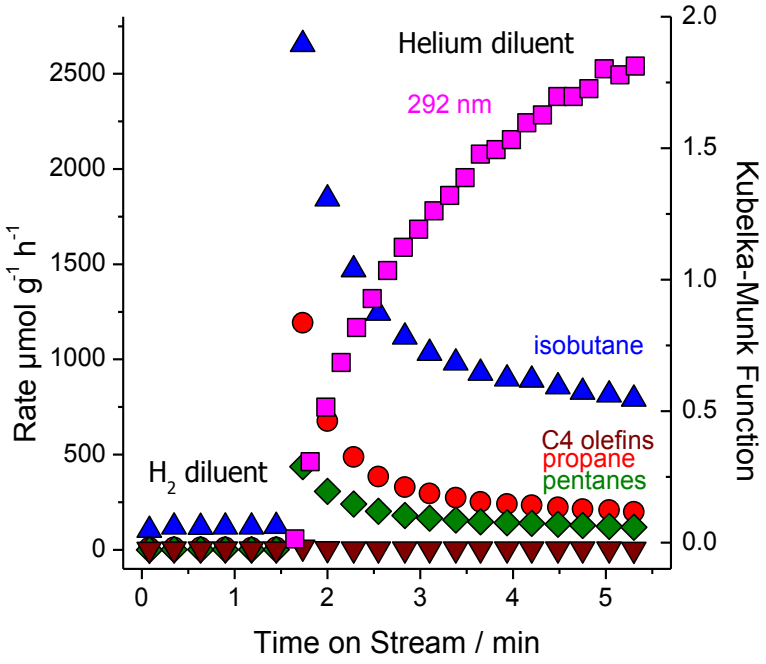


Figure 6.2: Rates of formation of gas phase products during conversion of *n*-butane (10 kPa partial pressure) on H-mordenite (M1, W/F = 0.16 h) at a reaction temperature of 563 K using either H_2 (first 1.5 h) or helium (after 1.5 h) as the diluent. The Kubelka-Munk value at 292 nm is plotted on the right axis. The corresponding UV–vis spectra are shown in Fig. 6.3.

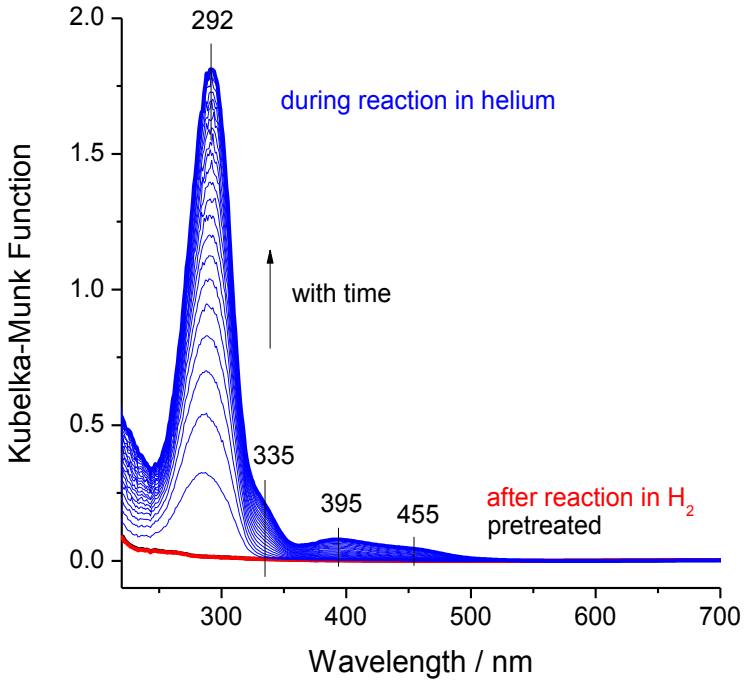


Figure 6.3: Evolution of diffuse reflectance UV–vis spectra recorded in situ during conversion of *n*-butane (10 kPa partial pressure) on H-mordenite (M1, W/F = 0.16 h) at a reaction temperature of 563 K. The corresponding gas phase products are shown in Fig. 6.2. Black line: pretreated catalyst; red line (superimposed on black line): last spectrum in *n*-butane/H_2; blue lines: in *n*-butane/helium.

During conversion of *n*-butane at 563 K using helium as a diluent, only very weak C-C and C-H stretching vibrations evolved in the IR spectra. However, the effect of butane admission on the acid sites of H-mordenite was clear, and is shown in Fig. 6.4. The OH stretching vibration of bridging hydroxyl groups was initially centered at 3601 cm [1] and after admission of *n*-butane, the center shifted to 3598 cm^{-1}. A difference spectrum showed that the perturbed hydroxyl groups absorb at 3608 cm^{-1}.

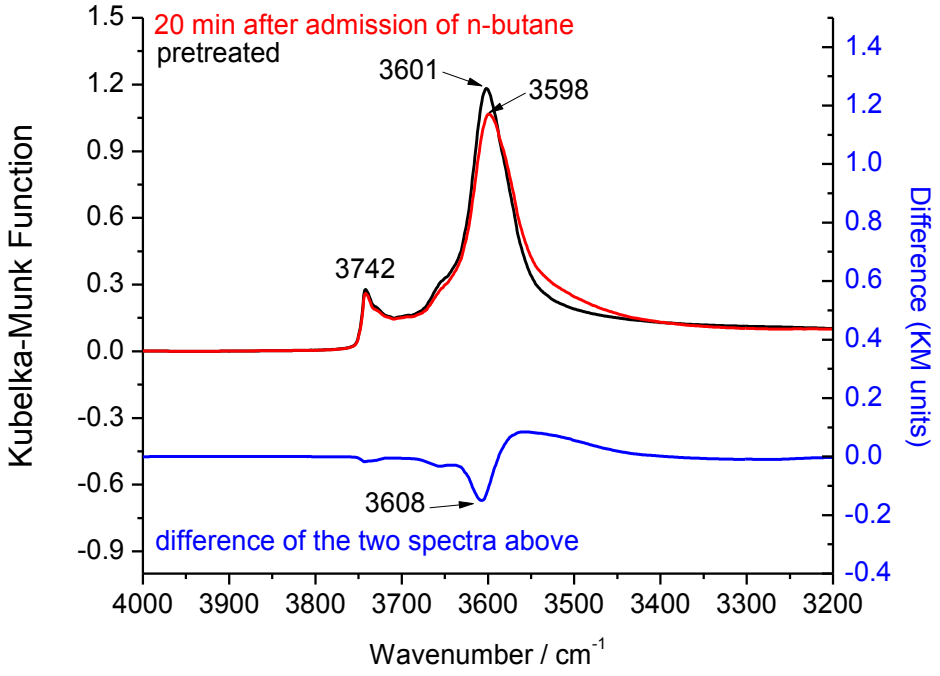


Figure 6.4: DRIFT spectra recorded during in situ conversion of *n*-butane (10 kPa partial pressure) on H-mordenite (M1) in helium (90 kPa partial pressure) at a reaction temperature of 563 K. Black line: pretreated catalyst. Red line: spectrum taken 20 min after admission of *n*-butane. Blue line: subtraction of the red line from the black line.

6.3.3 *n*-Pentane conversion on H-mordenite: Catalytic performance and spectra collected in situ

During conversion of *n*-pentane using helium as a diluent, product formation rates decreased with time on stream as shown in Fig. 6.5. Isobutane was the main product at 3 minutes on stream but 2-methylbutane was the main product at every point thereafter. Propane, *n*-butane, and hexanes (*n*-hexane, 2-methylpentane, 3-methylpentane, and 2,2-dimethylbutane) were also formed.

Concurrent with the decrease in catalytic performance was the growth of a band in the UV range at a wavelength of 293–295 nm as shown in Fig. 6.6. The absorption

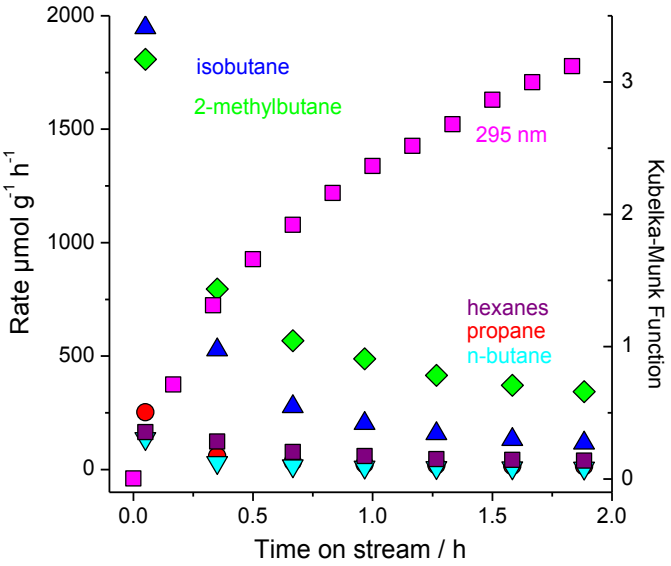


Figure 6.5: Rates of formation of the gas phase products during conversion of *n*-pentane (13 kPa partial pressure) on H-mordenite (M1, W/F = 0.08 h) at 453 K using helium as the diluent. The Kubelka-Munk value at 295 nm is plotted on the right axis. The corresponding UV–vis spectra are shown in Fig. 6.6

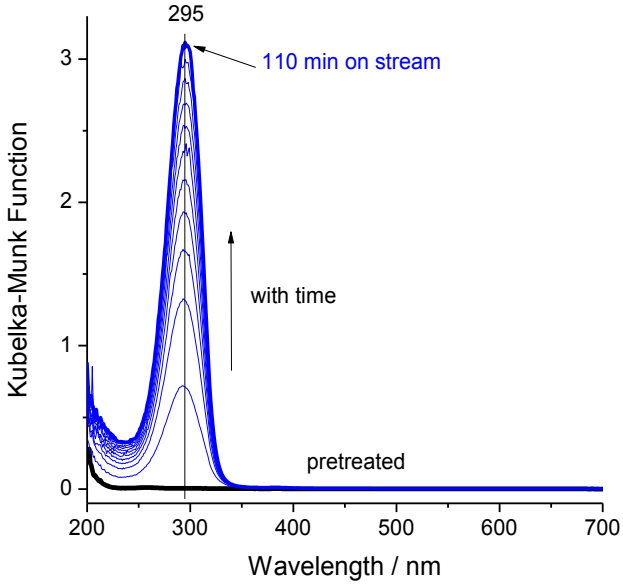


Figure 6.6: Evolution of diffuse reflectance UV–vis spectra recorded in situ during conversion of *n*-pentane (13 kPa partial pressure) on H-mordenite (M1, W/F = 0.08 h) at a reaction temperature of 453 K using helium as the diluent. Black line: pretreated catalyst; blue lines: in *n*-pentane/helium.

maximum was at 293 nm after 10 minutes on stream and shifted to 295 nm with time. The Kubelka–Munk value at 295 nm is plotted versus time on stream in Fig. 6.5.

6.3.4 Adsorption of reference compounds

6.3.4.1 Spectra collected in situ at temperatures below ≈ 550 K after adsorption of 1-butene, 1-pentene, or 1-hexene

The electronic bands that formed after adsorption of 1-butene, 1-pentene, and 1-hexene were all similar. After 1-butene was adsorbed at 303 K, an initial band at 318 nm was observed; within 5 h, a second, much more intense band at 295 nm had begun to form. During heating to 483 K, the band at 295 nm intensified, and a weak band at 382 nm emerged. The spectra are shown in Fig. 6.7.

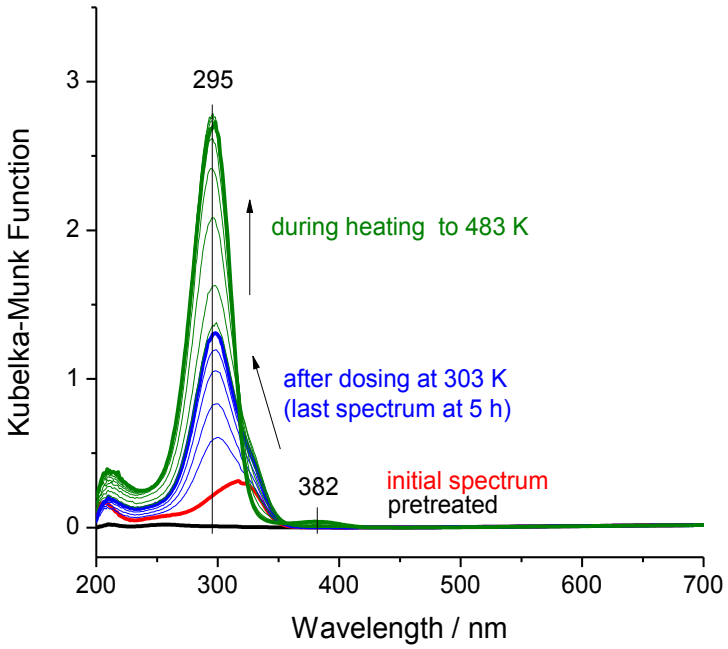


Figure 6.7: Diffuse reflectance UV-vis spectra of H-mordenite (M1) recorded in situ during exposure to a 30 µL gas pulse of 1-butene at 303 K (red line). The in situ cell was held at 303 K for 5 h (blue lines) and then heated at 2 K min^{-1} to 483 K in 30 ml min^{-1} N_2 (green lines). Pretreatment was at 673 K with subsequent treatments of synthetic air, N_2, and H_2.

After 1-pentene was adsorbed at 303 K, bands formed initially at wavelengths of 205 and 320 nm (Fig. 6.8). With time, the band at 320 nm decreased in intensity while a new band with a maximum absorption between 295 and 300 nm grew. An isosbestic point at 314 nm was evident. As the catalyst was heated, the new band became symmetric and well-defined, with a maximum absorption at 295 nm. A smaller band at 215 nm also grew. A band at 384 nm grew initially and then shrunk.

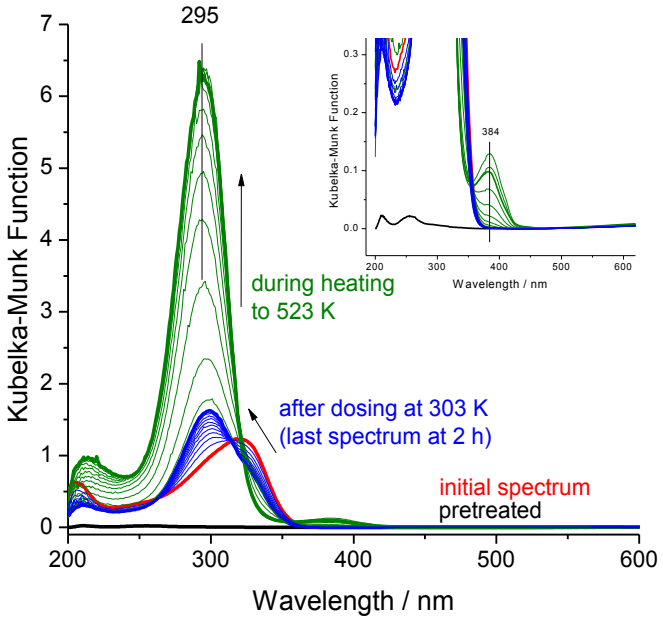


Figure 6.8: Diffuse reflectance UV–vis spectra of H-mordenite (M1) recorded in situ during exposure to 1-pentene at a temperature of 303 K. Five µL of 1-pentene vapor was taken from the headspace above 1-pentene liquid and then injected. The in situ cell was held at 303 K for 2 h (blue lines) and then heated at 2 K min^{-1} to 523 K (green lines). Spectra were collected in 10 minute intervals. Pretreatment was at 673 K in N_2.

After 1-hexene was adsorbed at 303 K, bands formed initially at 205 and 320 nm (Fig. 6.9). Although the chamber was only held isothermal for 30 minutes, the initial band at 320 min quickly underwent a hypsochromic shift. During heating, the new band again became symmetric and well-defined, with a maximum absorption at 295 nm. A smaller band at 215 nm grew and a new band at 381 nm was also observed.

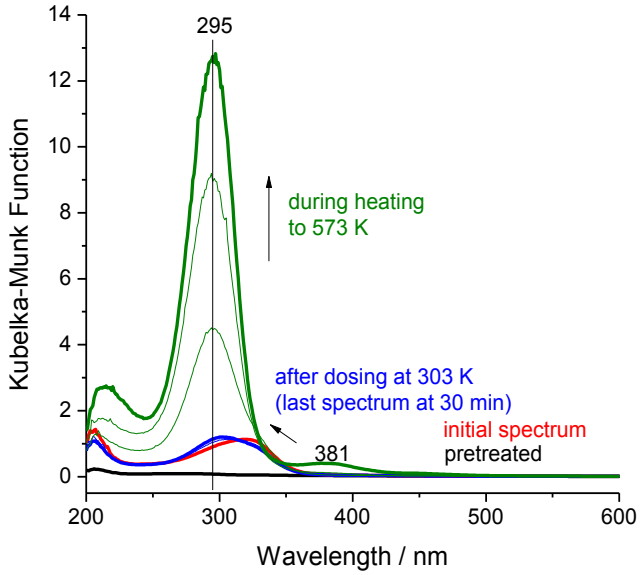


Figure 6.9: Diffuse reflectance UV–vis spectra of H-mordenite (M1) recorded in situ during exposure to 1 µL of 1-hexene liquid at a temperature of 303 K (red line). The cell was held at 303 K for 30 minutes (blue lines) and then heated at 10 K min^{-1} to 573 K (green lines). Pretreatment was performed at 673 K with sequential 30 minute treatments in synthetic air, N_2, and H_2.

6.3.5 In situ infrared spectra after adsorption of 1-pentene

Adsorption of 1-pentene at 453 K resulted in formation of bands in the infrared range at 2970, 2935, 2905, 1505 and 1400–1350 cm^{-1} (Fig. 6.10). The intensity of the band of the bridging OH groups at 3604 cm^{-1} decreased without concomitant formation of a band at lower frequency that would indicate mere perturbation of the OH groups. The intensity of the bands at 1610–1650 and 1875 cm^{-1} also decreased.

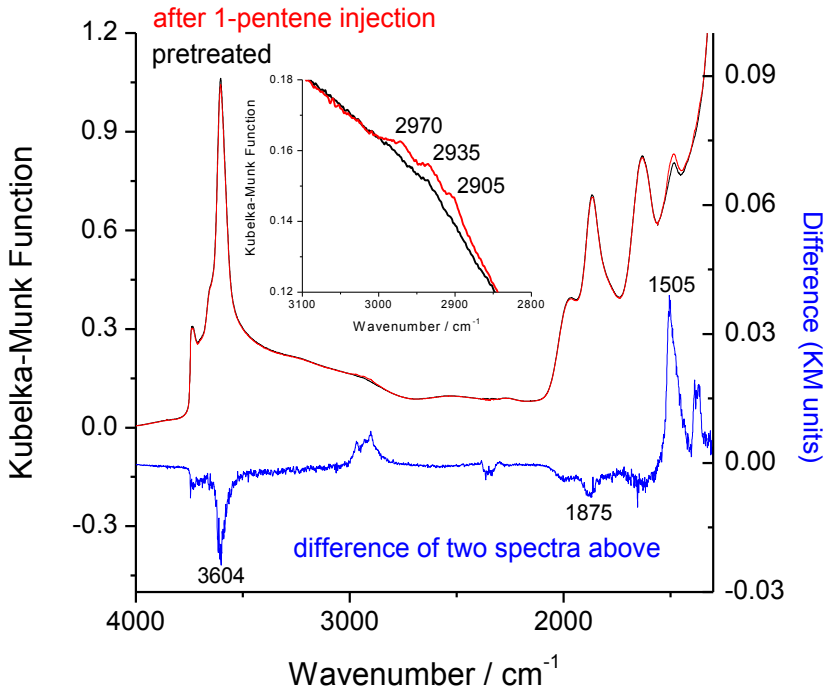


Figure 6.10: Diffuse reflectance infrared spectra of a physical mixture of H-mordenite (M1) and KBr (1:2 mass ratio) recorded in situ before (pretreated, black line) and after (red line) introduction of 0.2 µL 1-pentene (injected as liquid) with the chamber at a temperature of 453 K. The blue line is a subtraction of the black line from the red line. The resolution is 2 cm^{-1}. The zeolite was pretreated at 573 K in N_2.

6.3.6 Neutralization of cationic species

The introduction of water vapor, which is known to neutralize some cationic species on solid acids [31], had a minimal effect on the 295 nm band produced through 1-pentene adsorption. When water vapor was admitted, the band slowly decreased in intensity while new bands formed at 372 and 456 nm (Fig. 6.11). Ammonia had a much different and more immediate effect; the main band was completely eroded and a new band formed at 258 nm (Fig. 6.12).

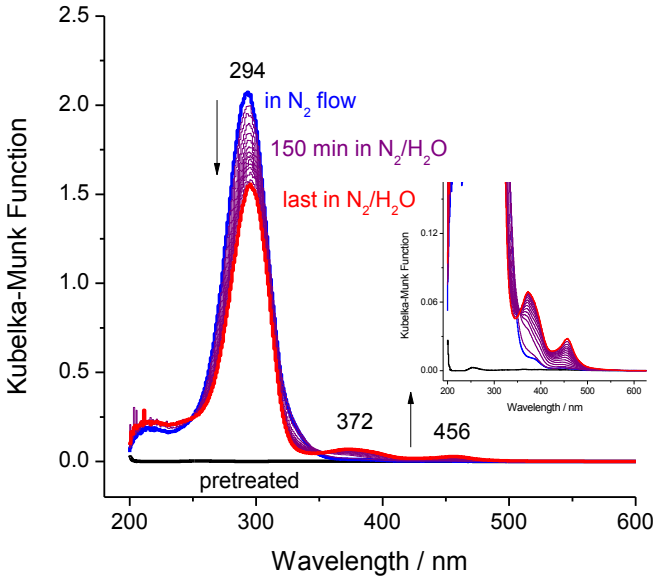


Figure 6.11: Diffuse reflectance UV–vis spectra of H-mordenite (M2) recorded in situ after exposure to 0.1 µL of 1-pentene (injected as liquid) at a temperature of 373 K (blue line) and after application of water vapor at 303 K (purple lines). Spectra were taken in 10 minute intervals. Pretreatment was performed at 673 K in 30 ml min^{-1} N_2.

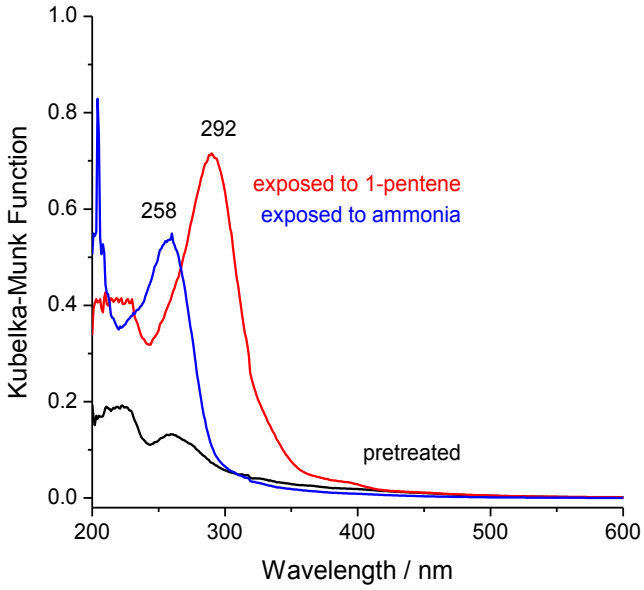


Figure 6.12: Diffuse reflectance UV–vis spectra of H-mordenite (M2) recorded in situ during exposure to 3 µL 1-pentene (injected as liquid) at a sample temperature of 373 K (red line) and subsequent application of ammonia at 303 K (blue line). Pretreatment was at 673 K in N_2.

6.3.7 Extraction of deposits formed on H-mordenite

Extraction of the solubilized H-mordenite that had been exposed to either 1-butene or 1-pentene at 323 K revealed a mixture of aliphatic hydrocarbons with a broad distribution of molecular weights. The hydrocarbons contained a number of carbon atoms not necessarily corresponding to multiples of 4 or 5 (*viz.*, the number of carbon atoms in the reactants). Alkanes and species with one double bond were detected in the mixture. A GC-MS chromatogram of the dichloromethane extract from H-mordenite exposed to 1-butene at 323 K is shown in Fig. 6.13. The extract from H-mordenite exposed to 1-pentene gave a similar chromatogram. The UV–vis spectrum of the H-mordenite before digestion showed a band at 295 nm, whereas the spectrum of the dichloromethane extract did not (Fig. 6.14). Consistently, the GC-MS analysis did not lead to identification of a structural unit in the extract that would give rise to absorption close to 295 nm.

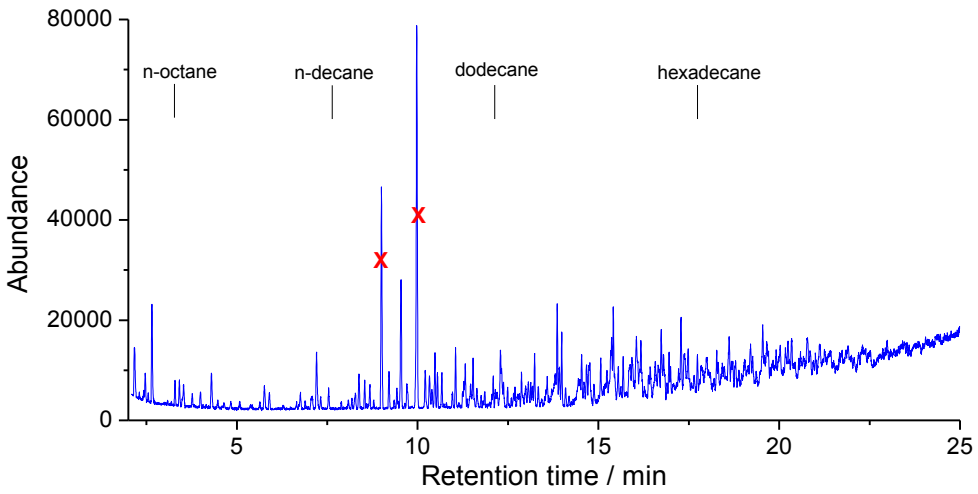


Figure 6.13: GC-MS chromatogram of the dichloromethane extract collected from H-mordenite (M2) after exposure to 1-butene at a temperature of 323 K and digestion in hydrofluoric acid. The retention times of several reference compounds are provided. The UV–vis spectrum of the dichloromethane extract is shown in Fig. 6.14. The red X indicates known *cis*- and *trans*- decalin impurities leached from the polyethylene vials.

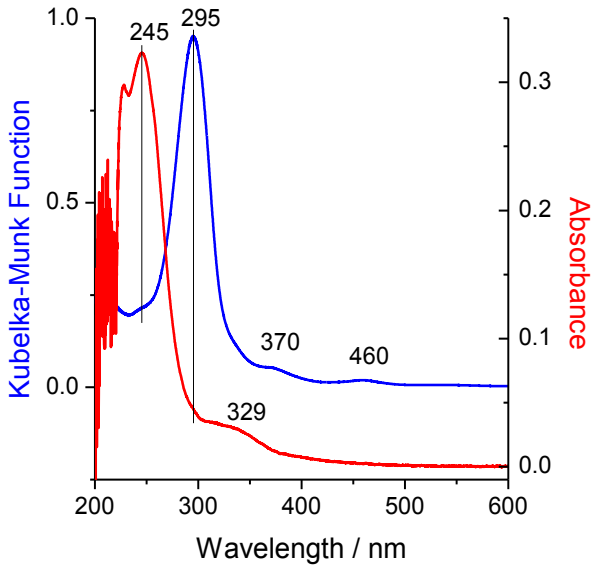


Figure 6.14: Diffuse reflectance UV–vis spectrum of H-mordenite (M2) after exposure to 1-butene at a temperature 323 K and transfer under ambient conditions (blue line) and transmission UV–vis spectrum the dichloromethane extract (red line) collected after digestion of the zeolite in hydrofluoric acid. The GC-MS chromatogram of the dichloromethane extract is shown in Fig. 6.13.

6.4 Discussion

6.4.1 Catalytic performance of H-mordenite in *n*-butane and *n*-pentane conversion

The main products formed during *n*-butane conversion are consistent with those in earlier reports [32,33]. Isobutane was the main product and propane and pentanes (*n*-pentane and 2-methylbutane) were the most abundant side products. H_2 has a stabilizing effect on the performance of H-mordenite in the conversion of *n*-butane. In the first 1.5 h using H_2 as the diluent, conversion was stable and no unsaturated deposits accumulated on the catalyst surface. When H_2 was replaced by helium, H-mordenite deactivated rapidly and a band at 292 nm concurrently formed. The deactivation is ascribed to higher concentrations of butenes in absence of H_2, which initiate the

formation of carbonaceous deposits. Higher concentrations of butenes were measured, 14 vs. 4 ppm of *n*-butenes in helium vs. in H_2, respectively. The higher rates of product formation in helium in comparison to those in H_2 are further evidence of olefins, which are known to promote conversion to alkane products [25,34]. The deactivation is in discord with observations made by Engelhardt [34], who found H-mordenite, even without H_2 in the feed, to be capable of stable operation during *n*-butane conversion. Olefin levels in the effluent stream seem comparable to those measured here, making it more likely that variations among zeolite samples are responsible for the different deactivation behavior. In any case, the role of H_2 is obviously to control the butene concentration.

The performance of H-mordenite in the conversion of *n*-pentane was also as expected. The bare zeolite is known to deactivate rapidly in the absence of a noble metal and H_2 [35]. Essayem et al. [36] operated with similar reaction conditions to those used in this work and found H-mordenite to lose 80% of its activity after 1 h. They also observed that isobutane was produced with the highest initial rate, but after 1 h 2-methylbutane became the main product. In this work, isobutane was also the main initial product, at 3 minutes on stream, and 2-methylbutane was the main product at every point thereafter. The decrease in conversion over 2 h was 75%.

6.4.2 Interpretation of spectra and identification of deactivation-causing species

A well-defined, symmetric band at 292–296 nm emerged in the spectra of H-mordenite recorded during *n*-butane or *n*-pentane conversion, and during gentle heating after adsorption of 1-butene, 1-pentene, and 1-hexene. Thus, the discussion and interpretation of this band apply to all of these scenarios. Bands formed after adsorption

of aliphatic hydrocarbons on solid acids in this region of the UV–vis spectrum are typically assigned to monoenylic cations [17,37-40], which are simple allylic cations without further conjugation that can form through protonation of a diene or hydride abstraction from a monoene. For example, Melsheimer et al. [11] assigned a band at 280–310 nm on H-ZSM-5 formed from ethene to cyclopentenyl and cyclohexenyl species. Cycloalkenyl cations were also named by Knözinger [41] as a possible assignment for a band at 292 nm that formed during *n*-butane conversion on sulfated zirconia.

The assignment of electronic bands arising from hydrocarbons adsorbed on solid acids relies strongly on comparison with the spectra of species prepared in solution, where the chemistry can be more carefully controlled. For monoenylic cations, Sorensen et al. [42] found the cation formed by protonation of 2,4-dimethyl-1,3-pentadiene in sulfuric acid to absorb at 305 nm, and Deno et al. [43] found the 2,4-dimethylpentenyl and 2,3,4-trimethylpentenyl cations to absorb at 305 nm and 307 nm, respectively. Deno et al. [43] also found the position of the monoenylic species formed by protonation of a variety of alkyl-substituted cyclopentadienes to vary with the type and position of alkyl substituents. For example, 1,3-dimethylcyclopentenyl absorbed at 275 nm, 1-ethyl-3-methylcyclopentenyl absorbed at 278 nm, and 1,2,3,4,4,5-hexamethylcyclopentenyl absorbed at 301 nm. Thus, in solution, the longest reported wavelength for a methyl-substituted cyclopentenyl species is 301 nm, implying that most of this type of cyclic species absorb below 300 nm, whereas the absorption of acyclic methyl-substituted pentenyl species is observed at wavelengths longer than 300 nm.

The assignment of the 292–296 nm band to a monoenylic cation is supported by the intense band at 1505 cm^{-1} that formed after adsorption of 1-pentene (Fig. 6.10). Bands in this region of the infrared spectrum are characteristic of carbon–carbon bonds with an intermediate bond order between 1 and 2, and are often attributed to monoenylic cations. In solution, the infrared spectrum of a symmetrically substituted allyl cation has a sharp absorption at 1530 cm^{-1} [44]. Bands at similar positions have been found after adsorption of olefins on solid acids. After adsorption of propene on H-ZSM-5, a band formed at 1510 cm^{-1} and was assigned to an allyl carbenium ion [17]. Bands at 1490–1530 cm^{-1} were formed after adsorption of numerous cyclic olefins on H-form zeolites and were assigned to alkenyl carbenium ions [23]. Pazè at al. [22] found bands at 1500 cm^{-1} and 285 nm after adsorption of 1-butene on H-ferrierite and heating to 473 K. The authors pointed out the general problem of distinguishing band shifts resulting from a charged state from those resulting from the presence of substituents. While the IR band was considered to not provide conclusive information, the UV band was assigned to neutral conjugated polyenes. However, for a neutral conjugated polyene to absorb at 285 nm, three to four double bonds are required, depending on the number of alkyl substituents [45]. The infrared band for C=C stretching vibrations in a highly conjugated acyclic species is typically around 1600 cm^{-1} [46]; for example, 1,3,5-hexatriene has a strong absorption at 1612–1623 cm^{-1} [47]. As both bands reported by Pazé et al. cannot be assigned to the same neutral polyene, they may alternatively be attributed to a monoenylic cation.

Formation of bands at 295 nm and 1505 cm^{-1} after adsorption of 1-pentene is consistent with formation of monoenylic cations. However, discriminating between the

cyclic or acyclic nature of monoenylic species is difficult with only the UV−vis and infrared spectra of the cationic form. Several nucleophiles, such as water [31] and ammonia [19,31], have been used previously to neutralize cationic species on solid acids. In this case, application of water caused bands to form at longer wavelengths at the expense of the monoenylic species (Fig. 6.11). While the exact chemistry is admittedly unknown, it is clear that the species is not neutralized. The new bands fall near the range of what is expected from dienylic and trienylic cations [17,42]. Application of ammonia produced a species absorbing at 258 nm from that absorbing at 295 nm (Fig. 6.12). Monoenylic species should be converted to dienes through application of ammonia. The UV−vis spectrum of the neutral diene provides additional information that can potentially be used to discriminate between cyclic and acyclic species. Because the ring of a cyclic entity provides an additional degree of unsaturation, cyclic dienes absorb at longer wavelengths than acyclic dienes. For example, 1,3-butadiene absorbs UV radiation at a wavelength of 217 nm [45] and cyclopentadiene absorbs UV radiation at a wavelength of 240 nm [48]. As the Woodward–Fieser rules apply to conjugated dienes, addition of alkyl groups should cause a +5 nm shift per group [45]. Thus, eight alkyl groups would be required on the neutral species to explain the absorption band at 258 nm. Only three to four alkyl groups are required on cyclopentadiene to explain the same band.

Formation of methyl-substituted cyclopentenyl species has been observed in numerous ^{13}C NMR investigations of adsorption and reaction of olefins on zeolites and the species are considered to be extremely stable. For example, Stepanov et al. [49] found 1,2,3-trimethylcyclopentenyl ions to be formed from 1-butene on H-ferrierite.

Haw and co-workers found evidence that methyl-substituted cyclopentenyl species formed from propene on HY [50] and from ethene on H-ZSM-5 [51]. Methyl-substituted cyclopentadienes have a high gas phase proton affinity, making them excellent candidates to persist in zeolites as stable cations. For example, Nicholas et al. [52] calculated the gas phase proton affinity of 1,3-dimethylcyclopentadiene to be 903 kJ mol^{-1}. Fang et al. [53] calculated the gas phase proton affinity of 1,2,3-trimethylcyclopentadiene to be 918 kJ mol^{-1} and found that the most energetically favored state for methyl-substituted cyclopentadienes adsorbed in several zeolites is the cationic state. Consumption of acidic OH groups (Fig. 6.10) indicates that proton transfer to a hydrocarbon species takes place at some point of olefin conversion. The obtained surface cations can be neutralized provided a sufficiently strong base is used. For example, the proton affinities of water, ammonia, and pyridine are 696, 853, and 930 kJ mol^{-1}, respectively [54]. These values apply for the free molecules and ions in the gas phase, and it is conceivable that the influence of the zeolitic surroundings makes possible the neutralization of alkyl-substituted cyclopentenyl species by ammonia. In light of the combined experimental evidence and information from the literature, the bands at 292–296 nm and 1505 cm^{-1} are assigned to alkyl-substituted cyclopentenyl species.

Additional confirmation of this assignment was sought through digestion and extraction of H-mordenite that had reacted with 1-butene or 1-pentene at 323 K. The extraction procedure was validated by the fact that the GC-MS data revealed a diverse mixture of paraffins and olefins of varying chain length. This result is consistent with the work of Guisnet and co-workers [1], who adsorbed propene on USHY at 393 K and

found the extract to contain polymers with the number of carbon atoms not equal to multiples of three, olefins, and naphthenes. The UV–vis spectrum of our dichloromethane extract did not have a band at 295 nm (Fig. 6.14), suggesting that the species responsible for this absorption was either transformed or was not recovered. As the alkyl-substituted cyclopentadienes have high proton affinities, it is possible that the species remained protonated and stayed in the hydrofluoric acid during the liquid–liquid extraction with dichloromethane. Sorensen [42] used a combination of neutralization with potassium hydroxide and extraction with hexane to recover protonated polyenes from sulfuric acid with less than 50% yields. It is noted that digestion and extraction of used methanol-to-hydrocarbons catalysts has not resulted in recovery of neutral forms of alkyl-substituted cyclopentenyl species [2-4], even though the ionic forms are known, or at least suspected, to be important intermediates for conversion of methanol to hydrocarbons on zeolite and zeotype catalysts [51,55,56]. While the extraction could not expressly confirm the cyclopentadiene-derived monoenylic species, the findings are explainable and do not contradict the interpretation.

For a monoenylic species to be formed from an olefin, abstraction of a hydride must occur. Thus, a Lewis acid is necessary. The Lewis acidity can be provided by either coordinatively unsaturated extraframework aluminum in the zeolite or from carbenium ions. Another pathway leading to formation of monoenylic species is protonation of a diene, however hydride abstraction is also a necessary step in the acid-catalyzed formation of a diene from a monoene. The band at 315-320 nm formed immediately after admission of 1-butene, 1-pentene, or 1-hexene (Figs. 6.7-6.9) could be representative of an initial acyclic monoenylic species formed either directly from

the olefin or after di- or oligomerization, deprotonation, and hydride abstraction. In order for a cyclic species to form, a 1,5 cyclization reaction must occur, requiring formation of an intermediate dienylic cation. Dienylic species absorb at longer wavelengths than monoenylic species; for example, Sorensen [42] reported that the dienylic species formed by protonation of 2,6-dimethyl-1,3,5-heptatriene absorbs at 396 nm. On zeolites, dienylic species have been reported to absorb between 350–380 nm [17]. In fact, a small band at 380-385 nm grew during heating and then shrunk (Figs. 6.7-6.9). Thus, the band at 380-385 nm is assigned to an acyclic dienylic cation.

We conclude that a major fraction of what may be referred to as "soft coke" formed during *n*-butane and *n*-pentane conversion on H-mordenite consists of alkyl-substituted cyclopentenyl cations. The first step in their formation is dehydrogenation of the alkane to form the corresponding alkene, which is the ultimate precursor to the deactivation-causing species.

References

[1] P. Magnoux, P. Roger, C. Canaff, V. Fouche, N.S. Gnep, M. Guisnet, in: Studies in Surface Science and Catalysis – Catalyst Deactivation, Proceedings of the 4th International Symposium, vol. 34, Elsevier B.V., 1987, p. 317-330.

[2] B. Arstad, S. Kolboe, Catal. Lett. 71 (2001) 209.

[3] M. Bjørgen, S. Svelle, F. Joensen, J. Nerlov, S. Kolboe, F. Bonino, L. Palumbo, S. Bordiga, U. Olsbye, J. Catal. 249 (2007) 195.

[4] S. Svelle, U. Olsbye, F. Joensen, M. Bjørgen, J. Phys. Chem. C 111 (2007) 17981.

[5] W. Dai, M. Scheibe, N. Guan, L. Li, M. Hunger, ChemCatChem 3 (2011) 1130.

[6] L. Palumbo, F. Bonino, P. Beato, M. Bjørgen, A. Zecchina, S. Bordiga, J. Phys. Chem. C 112 (2008) 9710.

[7] F. Bauer, H.G. Karge, in: H.G. Karge, J. Weitkamp (Eds.), Characterization II, Springer-Verlag, Berlin Heidelberg, 2007, p. 249.

[8] W. Schmidt, Optical Spectroscopy in Chemistry and Life Sciences, Wiley-VCH, Weinheim (Germany), 2005.

[9] W. Dai, X. Wang, G. Wu, L. Li, N. Guan, M. Hunger, ChemCatChem 4 (2012) 1428.

[10] Y. Jiang, J. Huang, V.R. Reddy Merthala, Y.S. Ooi, J. Weitkamp, M. Hunger, Microporous Mesoporous Mater. 105 (2007) 132.

[11] J. Melsheimer, D. Ziegler, J. Chem. Soc. Faraday Trans. 88 (1992) 2101.

[12] M.J. Wulfers, G. Tzolova-Müller, J.I. Villegas, D.Y. Murzin, F.C. Jentoft, J. Catal. 296 (2012) 132.

[13] D. Spielbauer, G.A.H. Mekhemer, E. Bosch, H. Knözinger, Catal. Lett. 36 (1996) 59.

[14] R. Ahmad, J. Melsheimer, F.C. Jentoft, R. Schlögl, J. Catal. 218 (2003) 365.

[15] F.C. Jentoft, in: M. Che, J.C. Védrine (Eds.), Characterization of Solid Materials and Heterogeneous Catalysts: From Structure to Surface Reactivity, vol. 1&2, Wiley-VCH, 2012, p. 138.

[16] S. Kuba, P. Lukinskas, F.C. Jentoft, R.K. Grasselli, B.C. Gates, H. Knözinger, J. Catal. 219 (2003) 376.

[17] A.V. Demidov, A.A. Davydov, Mater. Chem. Phys. 39 (1994) 13.

[18] S. Bordiga, G. Ricchiardi, G. Spoto, D. Scarano, L. Carnelli, A. Zecchina, J. Chem. Soc. Faraday Trans. 89 (1993) 1843.

[19] M. Bjørgen, F. Bonino, S. Kolboe, K.-P. Lillerud, A. Zecchina, S. Bordiga, J. Am. Chem. Soc. 125 (2003) 15863.

[20] C. Flego, I. Kiricsi, W.O. Parker Jr., M.G. Clerici, Appl. Catal., A 124 (1995) 107.

[21] W. Adam, I. Casades, V. Fornés, H. García, O. Weichold, J. Org. Chem. 65 (2000) 3947.

[22] C. Pazè, B. Sazak, A. Zecchina, J. Dwyer, J. Phys. Chem. B 103 (1999) 9978.

[23] S. Yang, J.N. Kondo, K. Domen, Catal. Today 73 (2002) 113.

[24] S. Bertarione, F. Bonino, F. Cesano, A. Damin, D. Scarano, A. Zecchina, J. Phys. Chem. B 112 (2008) 2580.

[25] K.B. Fogash, Z. Hong, J.M. Kobe, J.A. Dumesic, Appl. Catal., A 172 (1998) 107.

[26] K.B. Fogash, Z. Hong, J.A. Dumesic, J. Catal. 173 (1998) 519.

[27] C.H. Bartholomew, Appl. Catal., A 212 (2001) 17.

[28] M. Guisnet, P. Magnoux, Appl. Catal., A 212 (2001) 83.

[29] M. Maache, A. Janin, J.C. Lavalley, E. Benazzi, Zeolites 15 (1995) 507.

[30] M.A. Makarova, A.E. Wilson, B.J. van Liemt, C.M.A.M. Mesters, A.W. de Winter, C. Williams, J. Catal. 172 (1997) 170.

[31] H.P. Leftin, M.C. Hobson, Adv. Catal. 14 (1963) 115.

[32] C. Bearez, F. Chevalier, M. Guisnet, React. Kinet. Catal. Lett. 22 (1983) 405.

[33] R.A. Asuquo, G. Eder-Mirth, J.A. Lercher, J. Catal. 155 (1995) 376.

[34] J. Engelhardt, J. Catal. 164 (1996) 449.

[35] H.W. Kouwenhoven, W.C. van Zijll Langhout, Chem. Eng. Prog. 67 (1971) 65.

[36] N. Essayem, Y. Ben Taârit, C. Feche, P.Y. Gayraud, G. Sapaly, C. Naccache, J. Catal. 219 (2003) 97.

[37] P. Fejes, H. Förster, I. Kiricsi, J. Seebode, in: Studies in Surface Science and Catalysis – Structure and Reactivity of Modified Zeolites, vol. 18, Elsevier B.V., 1985, p. 91-98.

[38] H. Förster, S. Franke, J. Seebode, J. Chem. Soc. Faraday Trans. I 79 (1983) 373.

[39] E. Garbowski, J. Chem. Soc. Faraday Trans. I 81 (1985) 497.

[40] H. Förster, J. Seebode, P. Fejes, I. Kiricsi, J. Chem. Soc. Faraday Trans. I 83 (1987) 1109.

[41] H. Knözinger, Top. Catal. 6 (1998) 107.

[42] T.S. Sorensen, J. Am. Chem. Soc. 87 (1965) 5075.

[43] N.C. Deno, J. Bollinger, N. Friedman, K. Hafer, J.D. Hodge, J.J. Houser, J. Am. Chem. Soc. 85 (1963) 2998.

[44] N.C. Deno, in G.A. Olah, P.v.R. Schleyer (Eds.), Carbonium Ions, Wiley Interscience, New York, 1968, vol. 1.

[45] L.G. Wade, Jr., Organic Chemistry, 6th Ed., Pearson Prentice-Hall, Upper Saddle River, NJ, 2006.

[46] J. Coates, in R.A. Meyers (Ed.), Encyclopedia of Analytical Chemistry, John Wiley & Sons Ltd, Chichester, 2000.

[47] E.R. Lippincott, T.E. Kenney, J. Am. Chem. Soc. 84 (1962) 3641.

[48] L.W. Pickett, E. Paddock, E. Sackter, J. Am. Chem. Soc. 63 (1941) 1073.

[49] A.G. Stepanov, M.V. Luzgin, S.S. Arzumanov, H. Ernst, D. Freude, J. Catal. 211 (2002) 165.

[50] J.F. Haw, B.R. Richardson, I.S. Oshiro, N.D. Lazo, J.A. Speed, J. Am. Chem. Soc. 111 (1989) 2052.

[51] J.F. Haw, J.B. Nicholas, W. Song, F. Deng, Z. Wang, T. Xu, C.S. Heneghan, J. Am. Chem. Soc. 122 (2000) 4763.

[52] J.B. Nicholas, J.F. Haw, J. Am. Chem. Soc. 120 (1998) 11804.

[53] H. Fang, A. Zheng, J. Xu, S. Li, Y. Chu, L. Chen, F. Deng, J. Phys. Chem. C 115 (2011) 7429.

[54] E.P.L. Hunter, S.G. Lias, J. Phys. Chem. Ref. Data 27 (1998) 413.

[55] W. Song, J.B. Nicholas, J.F. Haw, J. Phys. Chem. B 105 (2001) 4317.

[56] D.M. McCann, D. Lesthaeghe, P.W. Kletnieks, D.R. Guenther, J.J. Hayman, V. Van Speybroeck, M. Waroquier, J.F. Haw, Angew. Chem., Int. Ed. 47 (2008) 5179.

7 Identification of high temperature carbonaceous deposits formed on H-mordenite and Pt/H-mordenite and their impact on *n*-Butane Conversion

7.1 Experimental

7.1.1 Materials

H-mordenite (both M1 and M2) and Pt/H-mordenite (Pt/M-T) were used. For the catalyst used to perform *n*-butane conversion, NH_4-mordenite was calcined in air (Airgas, zero grade) flowing at 100 ml min^{-1} at a temperature of 873 K before use. The temperature was increased at 2 K min^{-1} to 423 K and held for 1 h, and then further increased at 5 K min^{-1} to 873 K and held for 2 h. The weight hourly space velocity (W/F) with respect to O_2 was 0.82 h. Other materials were: *n*-butane (Matheson, 99.99%) containing 14 ppm isobutane and < 1 ppm propene impurities, 1-butene (Sigma, ≥ 99%), 1-pentene (Sigma, 98%), 2% ammonia in helium (Airgas), and argon (Airgas, UHP 99.999%) which was passed through a dual O_2 and moisture trap (Chromres, ZPure Dual Purifier).

7.1.2 N_2 physisorption

Surface areas were calculated from adsorption isotherms measured using a Micromeritics ASAP 2010 physisorption apparatus and N_2 as probe molecule. Samples were degassed by heating at 2 K min^{-1} to a temperature of 353 K while evacuating and holding for 1 h at 353 K after a pressure of 5 x 10^{-2} torr had been reached. Heating continued at 2 K min^{-1} to 523 K and this temperature was held for 6 h, while maintaining vacuum. The Brunauer–Emmett–Teller (BET) surface area was calculated using data points at relative pressures (p/p_0) between 0.05 and 0.15. Micropore surface

areas and volumes were calculated from t-plots using thicknesses between 4.10 and 5.35 Å derived from the Harkins-Jura thickness equation.

7.1.3 CO chemisorption

Platinum dispersion was measured by performing CO chemisorption on a Micromeritics ASAP 2020 chemisorption apparatus. The sample was first heated at 2 K min^{-1} to 353 K while evacuating and then held at this temperature for 1 h after a pressure of 10^{-2} torr had been reached. The temperature was then raised at 5 K min^{-1} to 423 K in flowing H_2 and held for 2 h. Finally, the temperature was raised at 5 K min^{-1} to 623 K in flowing H_2 and held for 2 h. The sample chamber was then evacuated at 308 K before CO dosing began.

7.1.4 Temperature-programmed oxidation (TPO)

TPO was performed in a thermogravimetric apparatus (Netzsch, STA 449 F1 Jupiter) with an online mass spectrometer (Netzsch, QMS 403 C Aëolos). The sample was first dried for 4 h at 473 K in 60 ml min^{-1} of argon flow and then cooled. To oxidize the deposits, the sample was heated at 10 K min^{-1} from 313 K to 1073 K in a mixed flow of 20 ml min^{-1} argon and 40 ml min^{-1} synthetic air. The reported percentage of carbonaceous deposits was determined from the mass loss that occurred during CO_2 evolution.

7.1.5 *n*-Butane conversion with in situ spectroscopic analysis: switching experiments

In situ diffuse reflectance UV–vis–NIR spectroscopy was performed using the equipment described in Section 3.3. Before reaction of *n*-butane, H-mordenite was heated at 5 K min^{-1} to 673 K in 30 ml min^{-1} (NTP) synthetic air and held at this

temperature for treatments of 0.5 h duration each in synthetic air, N_2, and H_2. The sample was then cooled in H_2 to the reaction temperature. Pt/H-mordenite was heated at 5 K min^{-1} to 423 K in 30 ml min^{-1} N_2; after 2 h at this temperature, the gas flow was switched to H_2 and the temperature was increased at 5 K min^{-1} to 623 K and held for 2 h.

Conversion of *n*-butane was performed at 623 K, atmospheric pressure, and a W/F of 0.16 using a feed composed of 10 % *n*-butane in H_2 or helium at a total flow of 30 ml min^{-1}. The diluent gas was changed from H_2 to helium and back after certain intervals. Conversions in H_2 were less than 1% and thus differential. The conversion in helium reached as much as 6.3%; steady state conversions were lower and can also be considered differential. Rates observed in the Harrick reaction chamber were lower than anticipated from measurements in an isothermal tubular plug flow reactor; to a large extent, this difference can be ascribed to the actual bed temperature being lower than the nominal (display) temperature.

7.1.6 In situ spectroscopic analysis of adsorption and reaction of olefins

Adsorption and heating of 1-butene and 1-pentene was performed as described in Section 6.2.3.

7.1.7 Adsorption of olefins with subsequent digestion and extraction

Adsorption of 1-butene was performed as described in Section 6.2.4. However, after adsorption, the reactor remained at 323 K for 5 min and was then heated to 573 K and held for 1 h. Extraction of carbonaceous deposits was then performed as described in Section 6.2.4.

7.2 Results

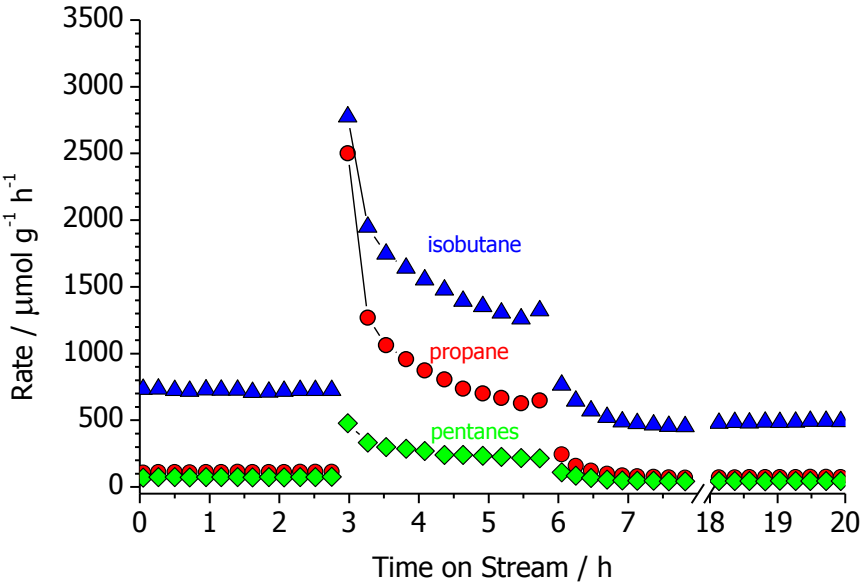
7.2.1 Catalytic performance and spectra collected with H_2 in the feed

The main product of *n*-butane conversion on H-mordenite and Pt/H-mordenite in the presence of H_2 was isobutane (Figs. 7.1a and 7.2a, first 3 h on stream). Substantial amounts of propane and pentanes (*n*-pentane and 2-methylbutane) were also formed on both catalysts. Minor products (Figs. 7.1b and 7.2b) were methane, ethane, and butenes (1-butene, *cis*-2-butene, *trans*-2-butene, and isobutene).

The rates of isobutane formation were comparable within a 10% margin on Pt/H-mordenite (675 µmol g^{-1} h^{-1}) and on H-mordenite (725 µmol g^{-1} h^{-1}) under the conditions initially applied. The product formation rates were stable on H-mordenite except for that of methane, which decreased slightly with time on stream. On Pt/H-mordenite, isobutane and pentanes were formed with constant rates, whereas the conversion to methane, ethane and propane declined slightly with time on stream.

Spectra of H-mordenite in the UV−vis range showed a very small increase of the bands at 208 and 257 nm with time in the feed stream (Fig. 7.3a). The UV−vis spectra of Pt/H-mordenite varied slightly in overall intensity, and specific changes were hard to discern (Fig. 7.3b). There were no intense bands characteristic of platinum, and no bands characteristic of carbonaceous deposits. According to the literature [1], surface-PtO_2 species exhibit broad asymmetric bands with a maximum at 340 nm, whereas platinum-Mohr (platinum black) and platinum dispersed on silica should show broad absorptions in the range of 250–650 nm. After pretreatment, the platinum on Pt/H-mordenite is expected to be reduced [2]; presumably, the corresponding features are too broad and, as a result of the low platinum content, too weak to be discerned.

(a)



(b)

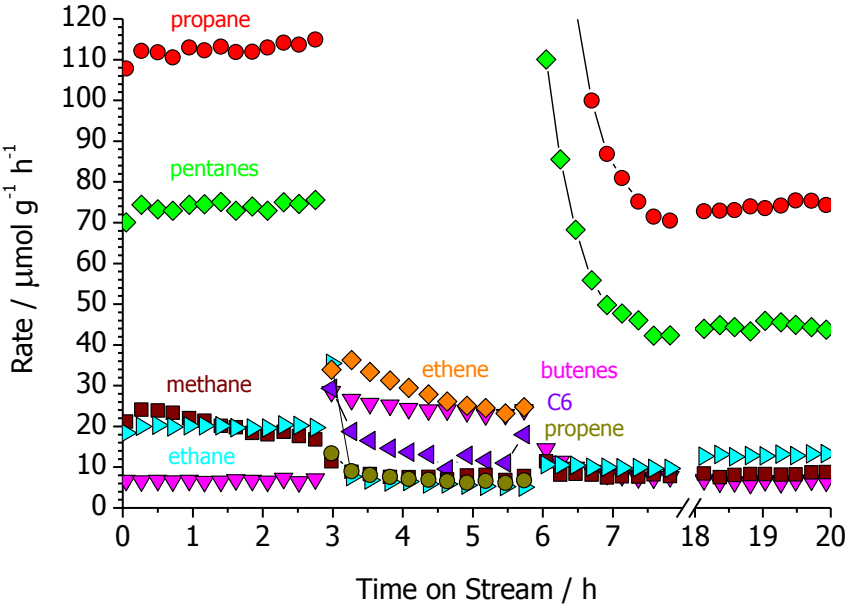
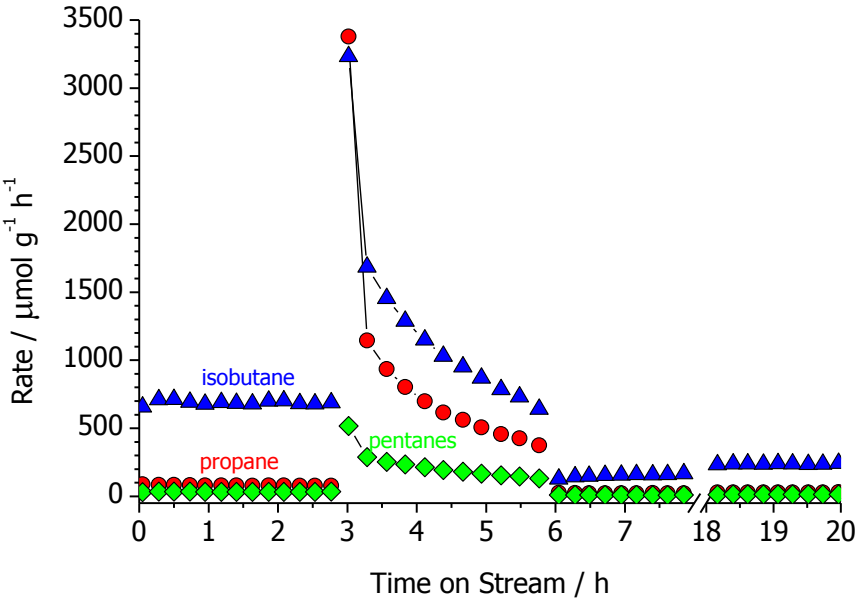


Figure 7.1: Rates of formation of various products of *n*-butane conversion on H-mordenite, (a) major products and (b) minor products. Pressure 101 kPa; total feed flow 30 ml min^{-1}; 10% *n*-butane mixed with 90% H_2 or helium (from 3 to 6 h on stream); temperature of in situ cell ≈623 K.

(a)



(b)

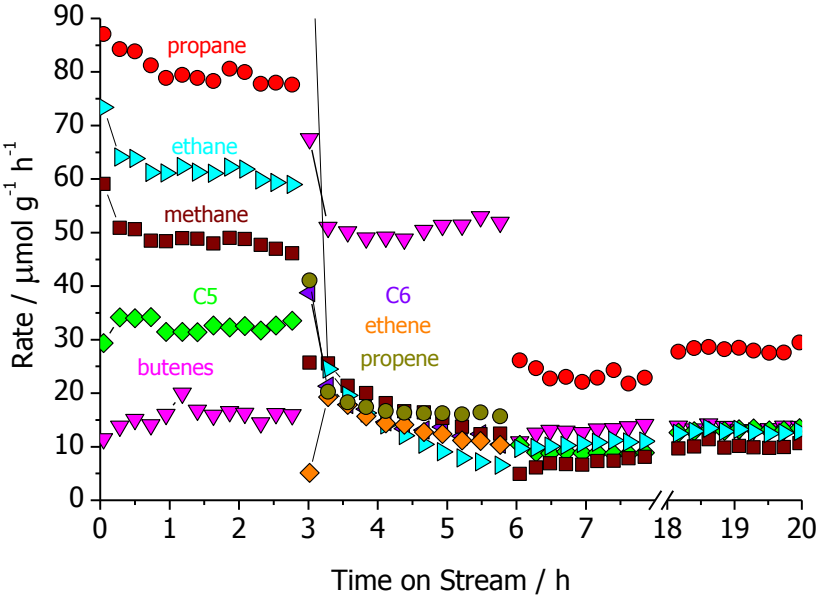
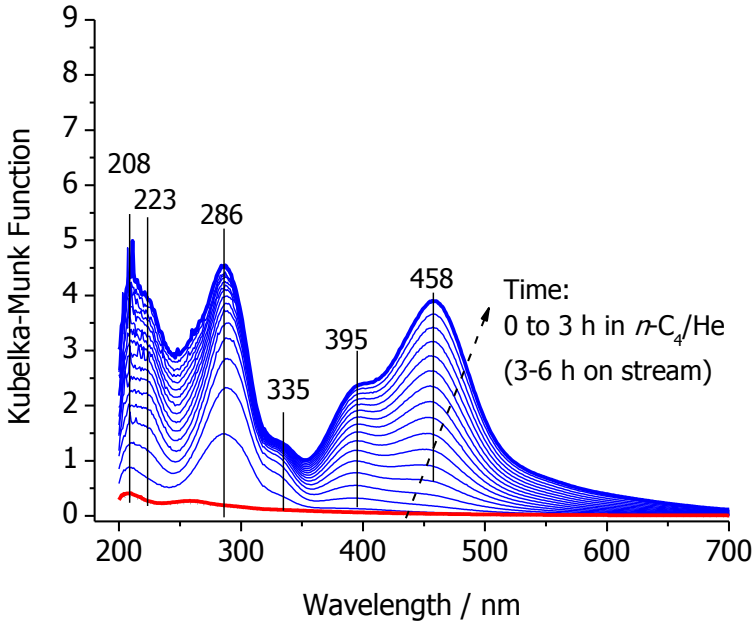


Figure 7.2: Rates of formation of various products of *n*-butane conversion on Pt/H-mordenite, (a) major products and (b) minor products. Pressure 101 kPa; total feed flow 30 ml min^{-1}; 10% *n*-butane mixed with 90% H_2 or helium (from 3 to 6 h on stream); temperature of in situ cell ≈623 K.

(a)



(b)

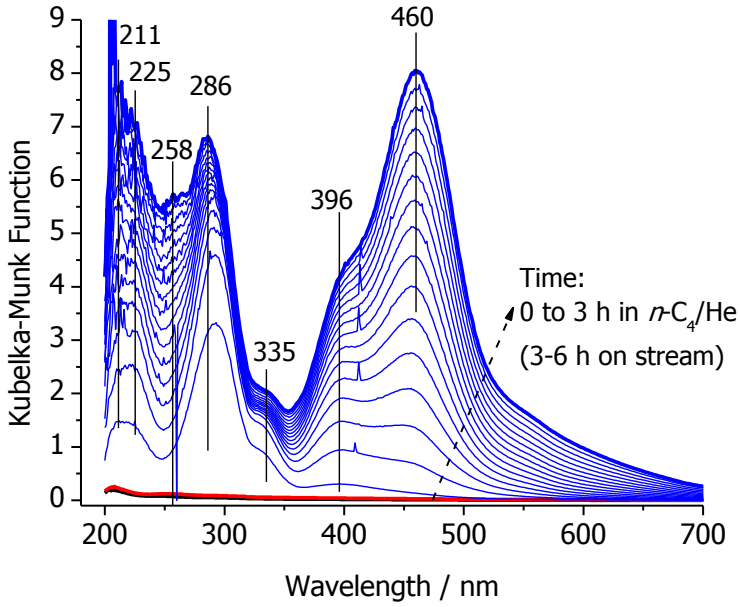


Figure 7.3: Diffuse reflectance UV–vis spectra of (a) H-mordenite and (b) Pt/H-mordenite recorded during *n*-butane conversion. Pressure 101 kPa; total feed flow 30 ml min^{-1}; 10% *n*-butane mixed with 90% H_2 or helium; temperature of in situ cell ≈623 K. Spectra originate from the same experiments as catalytic data in Figs. 7.1 and 7.2. Black line: activated catalyst; red line: last spectrum in *n*-butane/H_2 (3 h on stream); blue lines: in *n*-butane/He. Numbers indicate wavelength positions of vertical lines.

7.2.2 Catalytic performance and spectra collected when H_2 in the feed is replaced with helium

When the H_2 in the feed was exchanged with helium, the rates of formation of the major products increased abruptly (Figs. 7.1a and 7.2a, 3–6 h on stream). Isobutane remained the main product, while the selectivity towards propane and pentanes increased in comparison to the H_2-containing feed. The ratio of propane to pentanes in the effluent grew to more than two. On both catalysts, the formation rates of methane and ethane dropped, the rate of butene production increased, and ethene and propene appeared as new minor products (Figs. 7.1b and 7.2b). After a quick burst in activity, the conversion dropped rapidly. On H-mordenite, the rates of formation of all products approached a steady state after about 2.5 h, with most rates higher than those measured in presence of H_2. On Pt/H-mordenite, the rates declined continuously except for those of propene and butenes formation.

The UV–vis spectra of both catalysts (Fig. 7.3) showed rapidly growing bands following the switch from H_2 to helium. The band intensities, especially at wavelengths longer than 350 nm, were far different than those reported in Chapter 6 for reactions performed at lower temperature (623 K vs. 563 K). In the spectra of H-mordenite (Fig. 7.3a), distinct bands evolved at 286, 335, 395, and 458 nm, and the intensity of the bands below 250 nm also increased. In the spectra of Pt/H-mordenite (Fig. 7.3b), distinct bands at 293, 335, 396 and 460 nm grew rapidly after the switch, with the maximum of the band at 293 nm shifting towards 286 nm with time. The intensity below 250 nm increased, and a band at 258 nm emerged. Spectra of both catalysts showed additional weak bands at 724, 874, 984, and 1107 nm. Whereas the evolving

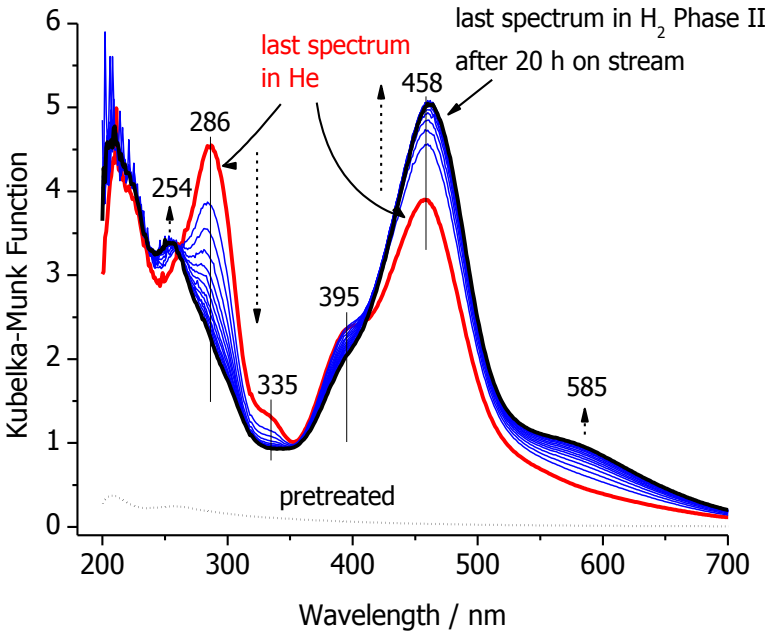
spectral patterns were similar for both catalysts, the intensity of all bands was much higher for Pt/H-mordenite (cf. Figs. 7.3a and 7.3b).

7.2.3 Catalytic performance and spectra collected after reintroducing H_2 to the feed

After replacing helium with H_2, the activity of H-mordenite dropped, and all rates decreased to levels lower than those measured during the first period in H_2-containing feed (Fig. 7.1). Within 14 h, there was no significant recovery of catalytic activity. The performance of Pt/H-mordenite also dropped after re-introduction of H_2 into the feed. This catalyst suffered a more severe deactivation during the period in the helium/*n*-butane mixture than H-mordenite, as evident from the sharp decline in rates during the helium period and the very low rates of formation of isobutane, propane, and pentanes after switching back to H_2-containing feed (Fig. 7.2). However, there was some recovery in the presence of H_2, and the rate of isobutane formation doubled within 14 h.

UV–vis spectra of H-mordenite (Fig. 7.4a) show that after re-adding H_2 to the feed, the intensity of the bands at 286, 335, and 395 nm decreased gradually. Of the three bands, the one at 286 nm experienced a strong reduction in intensity and continued to shrink with time, whereas the band at 395 nm soon stopped decreasing. Because the band at 335 nm is weak, the variations are subtle and the behavior is not easily classified but perhaps is closer to that of the 286 nm band. These trends are illustrated in Fig. 7.5a. The band at 458 nm continued to grow until about 14 h on stream and then leveled off. Two new bands formed at 254 and 585 nm.

(a)



(b)

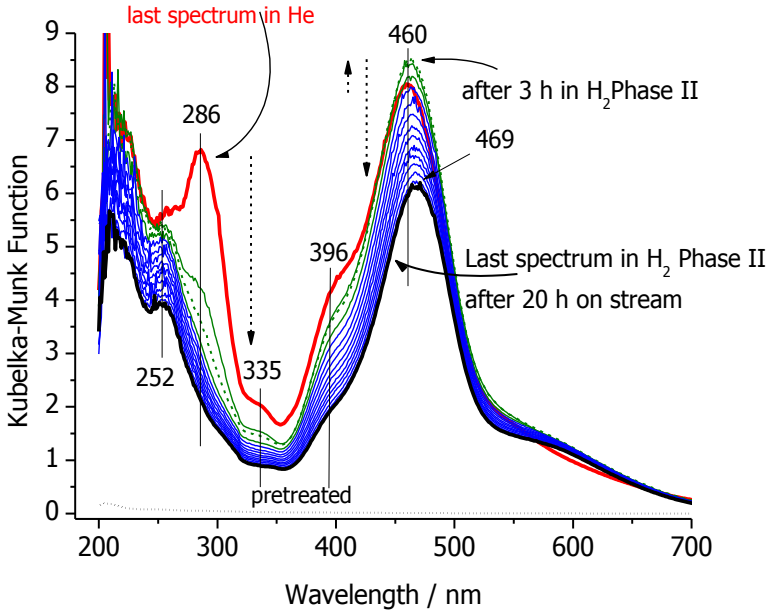
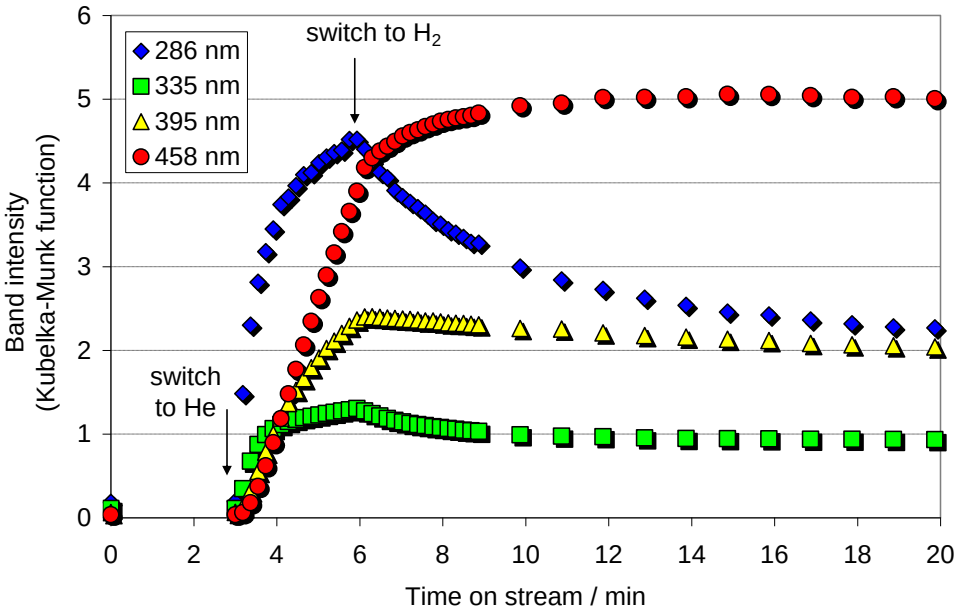


Figure 7.4: Diffuse reflectance UV–vis spectra of (a) H-mordenite and (b) Pt/H-mordenite recorded during *n*-butane conversion. Pressure 0.1 MPa; total feed flow 30 ml/min; 10% *n*-butane mixed with 90% H_2 or helium; temperature of in situ cell ≈623 K. Spectra originate from the same experiments as catalytic data in Figs. 7.1 and 7.2. Black dashed line: activated catalyst; red line: last spectrum in *n*-butane/He (3 h on stream); blue lines: in *n*-butane/H_2. Numbers indicate wavelength positions of vertical lines.

(a)



(b)

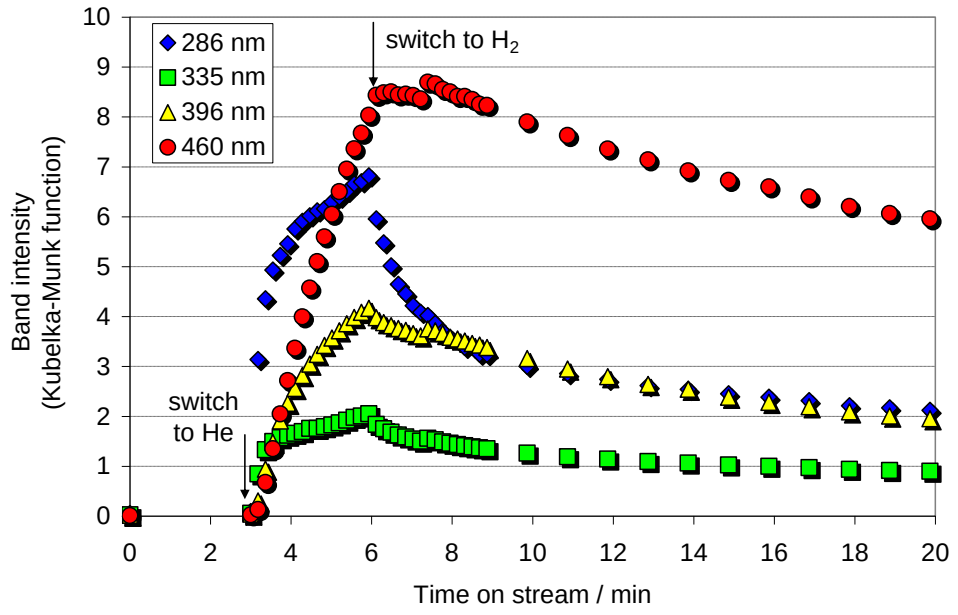


Figure 7.5: Evolution of various bands in the UV–vis spectra shown in Figs. 7.3 and 7.4 with time on stream. (a) H-mordenite and (b) Pt/H-mordenite.

Spectra of the Pt/H-mordenite catalyst recorded after the switch to the H_2-containing feed showed a decrease in intensity of the bands at 286, 335, and 396 nm; the band at 460 nm increased slightly before it also started decreasing (Figs. 7.4b and 7.5b). In contrast to H-mordenite, the band at 286 nm decreased much more rapidly.

7.2.4 Diffuse reflectance infrared spectra recorded in situ during conversion of *n*-butane

During conversion of *n*-butane at 633 K, a well resolved band between wavenumbers of 1580–1620 cm^{-1} grew with time on stream (Fig. 7.6). The band was initially centered at 1605 cm^{-1}; with time the position of maximum absorbance shifted to 1596 cm^{-1}.

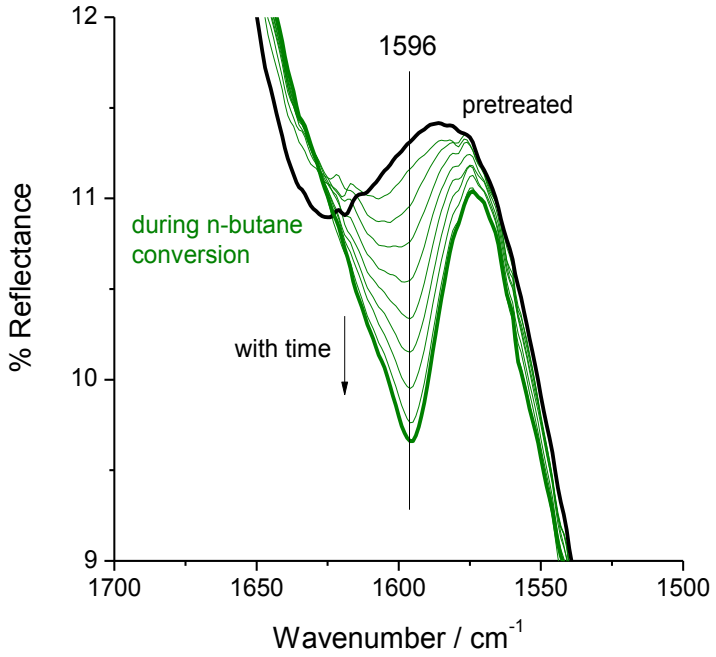


Figure 7.6: Evolution of diffuse reflectance infrared spectra recorded in situ during conversion of *n*-butane (10 kPa partial pressure) on H-mordenite (M1, W/F = 0.13 h) at a reaction temperature of 633 K using helium as the diluent. Black line: pretreated catalyst; green lines: during conversion of *n*-butane. The time interval between spectra is 20 minutes. The resolution is 4 cm^{-1}.

7.2.5 Adsorption of reference compounds: 1-Butene and 1-pentene

To identify the reactions of alkenes on the surface H-mordenite, the activated zeolite was exposed to single pulses of 1-butene or 1-pentene at 303 K while UV–vis spectra were recorded. The spectra shown in Figs. 7.7 and 7.8 differ from those in Chapter 6 (Figs. 6.7 and 6.8) only in the range of temperature that is reached during heating. Spectra in Figs. 7.7 and 7.8 include the evolution of bands at longer wavelengths, which form only at a temperature setting above 563 K. Further heating resulted in a decrease of the 295-296 nm band and a hypsochromic shift to 280-285 nm while bands around 400 and 450 nm and grew.

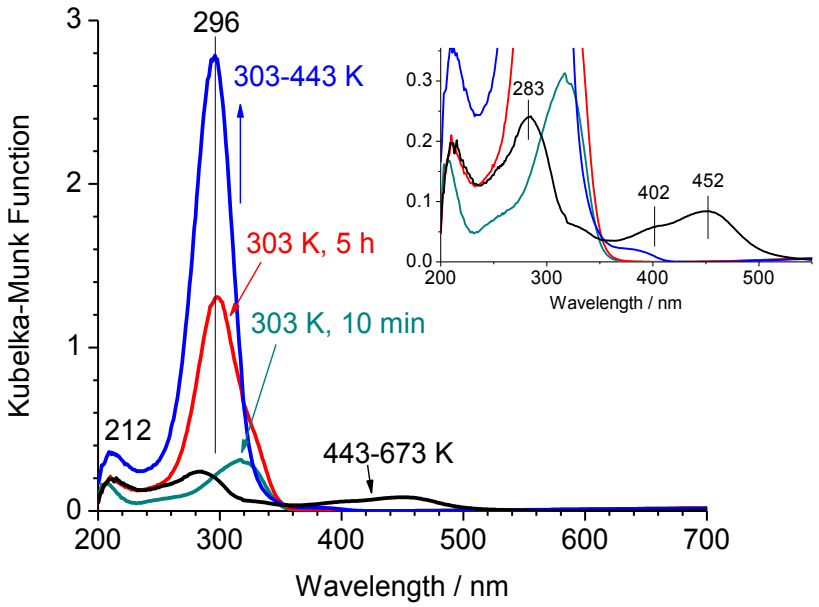


Figure 7.7: Diffuse reflectance UV–vis spectra of H-mordenite after exposure to a pulse of 1-butene at 303 K and subsequent heating to 673 K. The spectra below a temperature of 483 K are the same as those reported in Fig. 6.7. Numbers indicate wavelength positions of vertical lines. Inset shows a zoom.

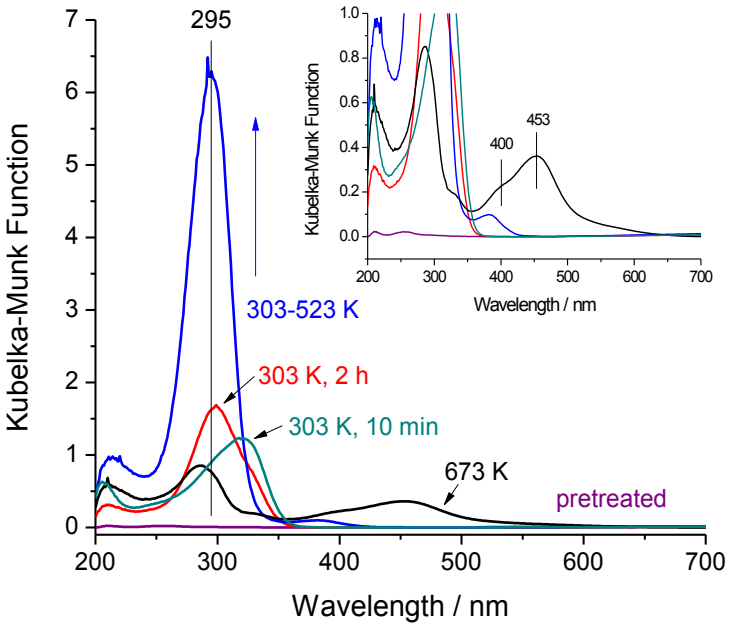


Figure 7.8: Diffuse reflectance UV–vis spectra of H-mordenite after exposure to a pulse of 1-pentene at 303 K and subsequent heating to 673 K. The spectra at and below a temperature of 523 K are the same as those reported in Fig. 6.8. Numbers indicate wavelength positions of vertical lines. Inset shows a zoom.

7.2.6 Evolution of UV-vis spectra upon exposure to water vapor or ammonia

The bands at wavelengths longer than 350 nm were eroded when the sample was exposed to water vapor, as shown in Fig. 7.9. In this experiment, *n*-butane conversion was performed on H-mordenite at 636 K for 2 h using helium as the diluent and the reaction chamber was cooled to room temperature while flowing helium through the catalyst bed. When water vapor was then added to the gas stream, the intense bands at 395 and 460 nm were replaced by many new, less intense bands between 350 and 500 nm, and two new bands with Lorentzian shape appeared below 300 nm. The effect of water was largely reversible; that is, the broad bands at 395 and 460 nm were almost completely recovered when the humidified zeolite was reheated.

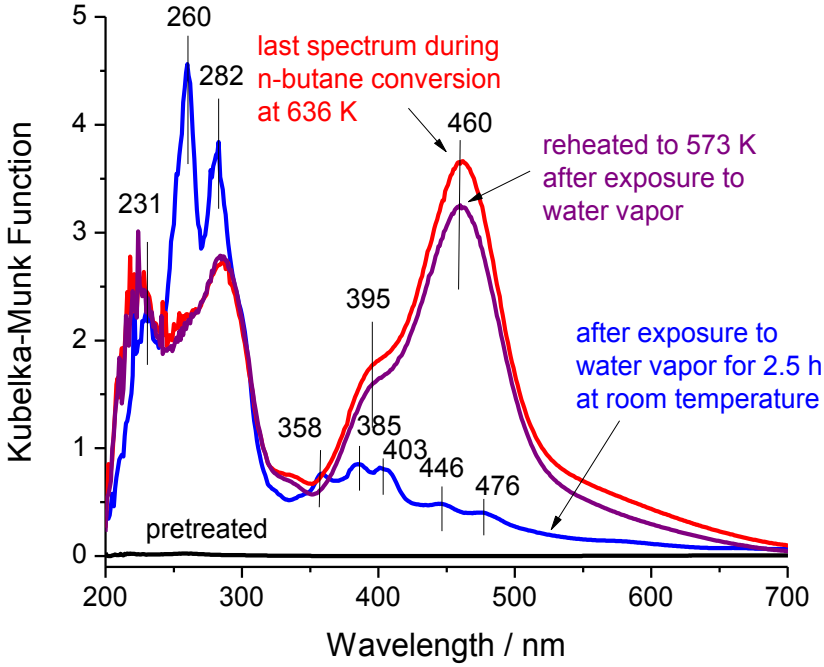


Figure 7.9: Diffuse reflectance UV–vis spectra of pretreated, spent, humidified, and re-heated catalyst. *n*-Butane (10 kPa partial pressure) conversion was performed on H-mordenite (M1) for 2 h at a reaction temperature of 636 K using helium as the diluent. The *n*-butane was then removed from the gas stream and the chamber was cooled to 303 K. The gas flow was then switched to 5 ml min^{-1} N_2 saturated with water vapor. After exposure to water vapor for 2.5 h, the catalyst was re-heated to 573 K in a stream of pure N_2. Black line: pretreated catalyst; red line: last spectrum during conversion of *n*-butane; blue line: after 2.5 h exposure to water vapor; purple line: re-heated after exposure to water vapor.

Exposure to ammonia produced a similar change in the spectra as exposure to water vapor. After 1-pentene was adsorbed on H-mordenite and heated to 673 K (shown in Fig. 7.8), the cell was cooled to 303 K and the catalyst was exposed to ammonia (Fig. 7.10). The bands at wavelengths longer than 350 nm were immediately eroded and many smaller, less intense bands appeared. Bands with a Lorentzian shape appeared at 256, 277, and 300 nm, while many smaller, less intense bands appeared at longer wavelengths (Fig. 7.10, inset).

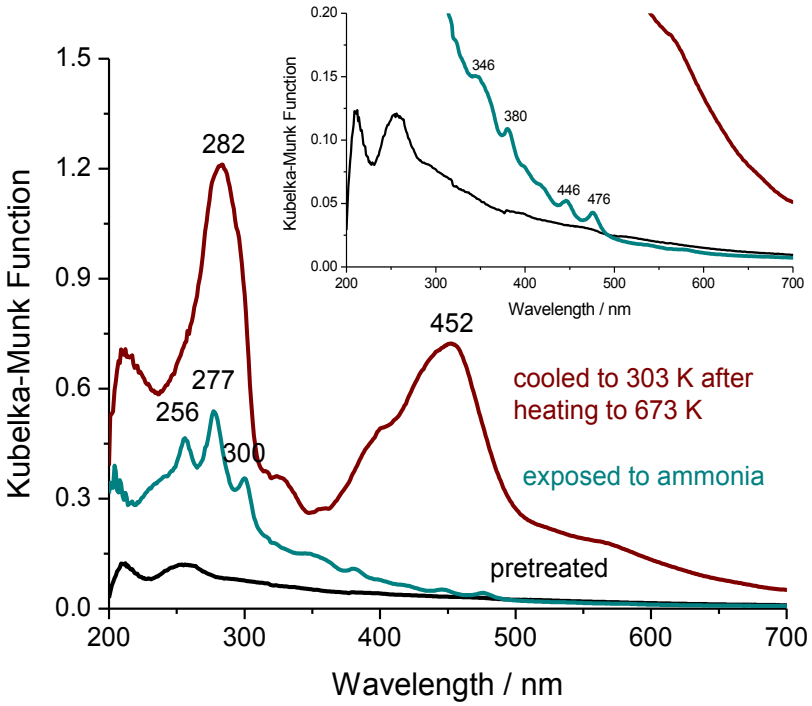


Figure 7.10: Diffuse reflectance UV–vis spectra of H-mordenite (M1) after exposure to a pulse of 1-pentene at 303 K and subsequent heating to 673 K. After heating to 673 K, the cell was cooled to 303 K and ammonia was admitted. The spectra have been normalized to account for reflectance values higher than the reflectance standard. Black line: pretreated zeolite; maroon line: cooled to 303 K after heating to 673 K; turquoise line: exposed to ammonia.

7.2.7 Extraction of carbonaceous deposits formed from 1-butene and 1-pentene

To be able to assign the bands observed at wavelengths > 350 nm at reaction temperatures above ≈ 550 K, additional information was gathered. 1-Butene was adsorbed on H-mordenite, heated to 573 K, and the zeolite was then digested and extracted. The extract contained alkyl-substituted naphthalene and anthracene species (Fig. 7.11). The naphthalenes contained up to four methyl groups and the anthracenes contained up to three methyl groups. The concentration of naphthalenes was in the order of methylnaphthalene > dimethylnaphthalene > trimethylnaphthalene >

tetramethylnaphthalene > naphthalene. The concentration of anthracenes was in the order of dimethylanthracene > trimethylanthracene > methylanthracene.

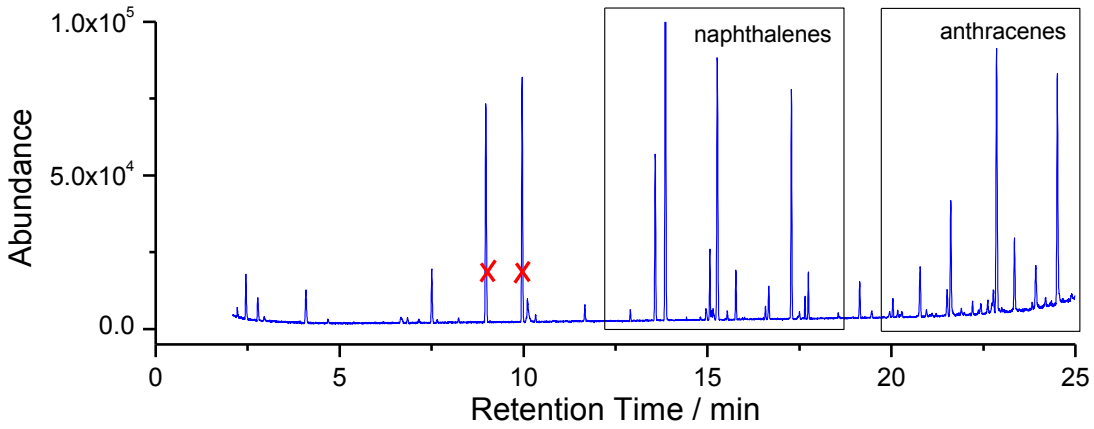


Figure 7.11: GC-MS chromatogram of the dichloromethane extract collected from H-mordenite (M2) after exposure to 1-butene at a temperature of 573 K and digestion in hydrofluoric acid. The UV-vis spectrum of the dichloromethane extract is shown in Fig. 7.12. The red X indicate known *cis*- and *trans*- decalin impurities leached from the polyethylene vials.

The UV–vis spectrum of the H-mordenite that was reacted with 1-butene and then exposed to ambient air (Fig. 7.12) was similar to the spectrum of the catalyst that was used for conversion of *n*-butane at 636 K and then exposed to water vapor in the in situ cell (Fig. 7.9). The spectrum of the dichloromethane extract contained many of the same bands seen in the zeolite spectrum before digestion (Fig. 7.12). Both on the solid catalyst and in the dichloromethane extract, bands with Lorentzian character were present at 228 nm and 257 nm. The band positions at wavelengths >320 nm were similar, and the bands were less intense than the shorter wavelength bands. However, the intensity of the bands >320 nm, relative to the intensity of bands at shorter wavelength, was greater on the zeolite than in the dichloromethane. A band with Lorentzian character at 278 nm and a shoulder at 300 nm existed on the zeolite but were not distinctly resolved in the dichloromethane.

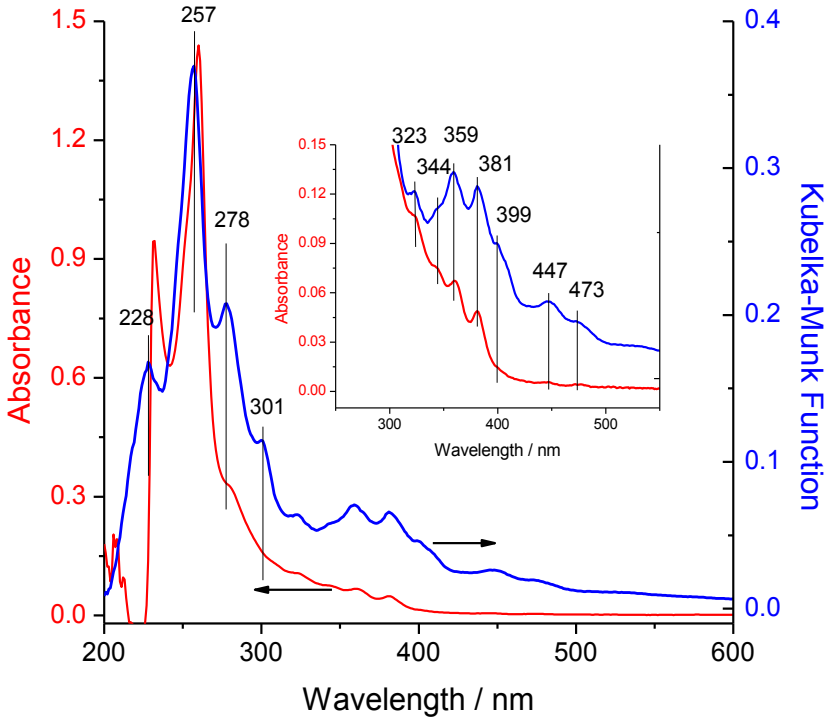


Figure 7.12: UV–vis spectra of spent catalyst and extract. H-mordenite (M2) was activated in an isothermal reactor, exposed to 1-butene at a temperature of 323 K, heated to 573 K, and held for 1 h. The two spectra represent the solid, ambient-exposed H-mordenite before digestion (blue line, Kubelka–Munk scale) and the dichloromethane extract obtained after digestion (red line, absorbance scale).

7.3 Discussion

7.3.1 H-mordenite: Impact of deposits on reaction pathways

Butane isomerization was the predominant pathway on H-mordenite, as indicated by an isobutane selectivity of 76% during the initial period in H_2. Propane and pentanes were always observed as side products. Disproportionation of C8 species into C3 and C5 alkanes is a likely side reaction; however, the ratio of propane to pentanes was about 1.6. One possibility for formation of excess propane is protolytic cracking of *n*-butane and subsequent hydrogenation. Methane and ethane were always detected, and

the corresponding olefinic cracking products propene and ethene were observed when H_2 was not present (Fig. 7.1).

Except for the so far unexplainable ethene excess, these selectivities are consistent with protolytic cracking. One must however infer that the alkenes are immediately hydrogenated when H_2 is present, which is conceivable given the hydrogenation ability of H-mordenite in excess of H_2, as recently demonstrated by Gounder et al. [3]. The equilibrium constants for gas phase alkene hydrogenations decrease with increasing temperatures (Fig. 7.13), and are about two orders of magnitude larger at the temperature used here (623 K) than at those used by Gounder et al. (718–778 K). The large value of the constant and the H_2 excess drive ethene and propene equilibrium concentrations below our detection limit and equilibration cannot

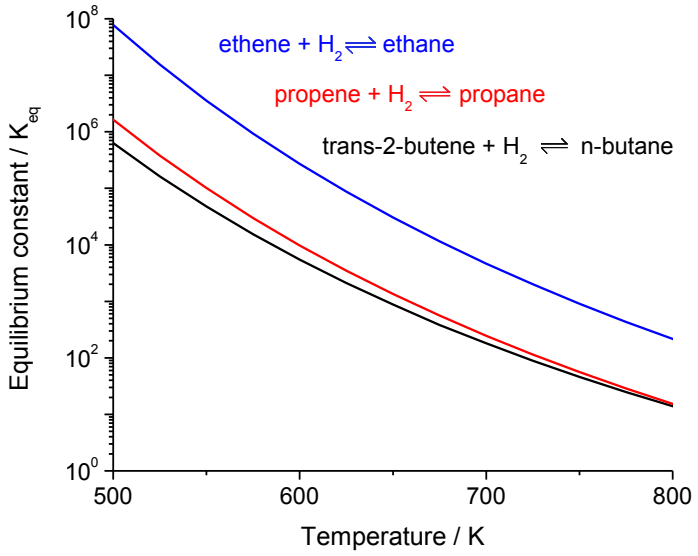


Figure 7.13: Gas phase equilibrium constants for the hydrogenation of ethene, propene and trans-2-butene, to their respective alkanes, as calculated by the software package Thermosolver v. 1.0.

be ascertained. The absence of gas phase ethene and propene during operation in H_2 indicates that acid-catalyzed hydrogenation is faster than protolytic cracking at 623 K.

Not all of the propane produced in excess of pentanes can be accounted for by cracking, as the ratio of excess propane to methane is about two. Thus, additional routes to propane exist besides disproportionation of C8 species and cracking of *n*-butane. Some authors have explained a ratio of 1.6 by secondary reactions of pentanes with C4 species to give C9 entities, which cleave with high selectivity to propane [4-6].

After replacing H_2 by helium, the rate of formation of the main products on H-mordenite increased significantly. This trend is consistent with the literature, and also Chapter 4, which report that H_2 lowers the *n*-butane isomerization activity [7] and more so with increasing H_2/butane ratio [8,9]. In Chapter 4, the butene concentration was linked both to product formation rates and selectivities. Asuquo et al. [10] postulated that the formation of alkenes is depressed through H_2 but did not show any data that would directly prove this point. Our data reveal a measurable variation in alkene concentration. Fig. 7.1b shows that when the diluent is switched from H_2 to helium, the concentration of butenes in the effluent stream increases, and ethene and propene are also produced. Butenes may be formed through dehydrogenation of *n*-butane, as described by Gounder and Iglesia [11] for the H-forms of various zeolites, while ethene and propene are probably primary cracking products of *n*-butane. We attribute the increase in rates to the availability of olefins throughout the bed.

The increase in selectivity to propane (from 12 to 42 %) upon removing H_2 from the feed also corresponds to reported observations. Yori et al. [12] found less propane in the presence of H_2 and concluded that H_2 blocks the “stronger” acid sites, which

preferentially catalyze disproportionation, polymerization and cracking, in turn leading to improved selectivity to isobutane. Whereas our data are consistent with those of Yori et al., we do not find the evidence sufficient to attribute the effect to blocking of acid sites by H_2. Instead, the higher selectivity to disproportionation products is probably due to the higher concentration of butenes, which were shown in Chapter 4 to favor disproportionation pathways because they have a near second order dependence on the butene partial pressure.

After re-introducing H_2 into the feed, the steady state rate of isobutane formation was only about 60–65% of the rate achieved with the fresh catalyst. The rate of butene formation was almost the same. That the butene concentration was the same but the rate was lower indicates that fewer active sites were available. The propane to isobutane ratios at steady state during each of the phases of the experiment were 0.16 (fresh catalyst in H_2-containing feed), 0.50 (during the period in helium), and 0.15 (after reintroducing H_2 to the feed). This result suggests that, provided the slight drop in conversion from the initial phase in H_2 to the final phase in H_2 has no significant effect on selectivity, isomerization and disproportionation products are formed on the same sites, or the various involved sites disappear at comparable rates, through individual site or pore blocking.

7.3.2 Pt/H-mordenite: Impact of deposits on reaction pathways

Isobutane was also the main product formed on Pt/H-mordenite, and propane and pentanes were again the main side products. In the presence of H_2, the propane to pentanes ratio was about 2.5, which is higher than on H-mordenite and thus indicative of further routes to propane. Considerable amounts of methane and ethane were also

produced, much more than can be accounted for by acid-catalyzed cracking (cf. Figs. 7.1b and 7.2b). Hydrogenolysis on platinum is a possible pathway, and the fact that only traces of methane and ethane were produced when H_2 was not supplied supports hydrogenolysis as a major pathway to these products. Assuming that propane is formed through disproportionation in about equal amounts to pentanes, the data indicate that all remaining propane is formed through hydrogenolysis because the sum of the pentanes and methane formation rates equals that of the propane formation rate.

The selectivity of the hydrogenolysis reaction varies with the support [13,14] and with the nature of the platinum particles. According to some literature, ethane is favored over propane on small platinum particles [15], but it has also been reported that large, flat ensembles of platinum promote ethane formation [16]. CO adsorption measurements indicate a low platinum dispersion of less than 10% in our catalyst (Table 7.1), implying that the majority of particles are large. Consistent with the size, the observed relative hydrogenolysis rates (more ethane than propane or methane) match best those reported by Campbell et al. [16] for large planar ensembles of platinum. The slightly declining rates to methane, ethane and propane during the first period in H_2 indicate slow deactivation of the hydrogenolysis function of platinum, which is also consistent with literature reports [17].

Table 7.1: Properties of Pt/H-mordenite measured before and after 20 h reaction with *n*-butane

		BET Surface Area (m^2/g)	Micropore Surface Area (m^2/g)	Micropore Volume (cm^3/g)	Pt dispersion %	Carbon deposit, mass %[a]
Pt/H-mordenite	Fresh	534	463	0.201	<10%	
	Used	419	342	0.148		3.1

[a] on a dry basis

On Pt/H-mordenite, propane briefly became the main product after replacing H_2 by helium in the feed. A steep but short-lived increase in olefin concentration was observed after the switch to helium (Fig. 7.2b), and oligomerization and consequently disproportionation could be promoted. As reported in Chapter 4, the olefin concentration has a great impact on product selectivity, and the observation is again consistent with literature reports [18]. That propane was produced in large excess to pentanes suggests that desorption is incomplete, consistent with the accumulation of surface species (see following sections). Our result differs somewhat from a report by Asuquo et al. [8], who did not see a large effect of platinum on selectivity and always observed isobutane as the main product. However, the reaction temperature used by Asuquo et al. was only 523 K, and, at least on pure H-mordenite, it has been reported that propane becomes the main product at temperatures higher than about 575 K [10]. However, the relative selectivities depend on the ability of the catalyst to produce olefins, which may vary from sample to sample. While the main reaction pathways suffered from deactivation, the production of butenes remained at a constant level. Hence, the dehydrogenation functions were not impaired during the period in helium.

After re-introducing H_2 into the feed, the isobutane formation rate in the first two hours was only about 20% of the rate achieved with the fresh catalyst. However, the butene formation rate was unaffected. This is consistent with a significant loss of active sites. The very low levels of hydrogenolysis products after return to H_2-containing feed indicate that the platinum particles were no longer active for this reaction, most likely because carbonaceous deposits accumulated on the platinum in the absence of H_2 [17]. Ensemble sites, on which carbon-containing fragments are formed,

could be permanently disabled through stripping of hydrogen from these fragments to give carbon, which is difficult to rehydrogenate and remove. The propane to isobutane ratio immediately after the switch was 0.16, which is typical of pure H-mordenite. The rate of methane and pentanes formation did not account for the production of propane as on the fresh catalyst, indicating that the additional route to propane observed on pure H-mordenite becomes operative on deactivated Pt/H-mordenite. One possible explanation for a behavior reminiscent to that of pure mordenite is that active hydrogen produced on the platinum is consumed by hydrogenation of carbonaceous species on the zeolite, which occurs predominantly in the first few hours after reintroducing H_2 (Fig. 7.5b). Consistent with this scenario, the ratio of propane to isobutane was 0.12 at 19 h on stream and thus close to the ratio of 0.11 observed for the fresh Pt/H-mordenite, and less additional propane was formed.

7.3.3 Interpretation of UV-vis absorption bands

The evolution of the spectra for both catalysts is similar. Pronounced are absorption features below 250 nm and discrete bands at 286 nm, 335 nm, 395 (Pt/H-mordenite 396) nm and 458 (460) nm. The evolution of the four well defined bands with time on stream is presented in Figs. 7.3a and 7.3b. Bands at almost the same positions indicate that species on H-mordenite and Pt/H-mordenite are similar in nature. Spectroscopically detected species on Pt/H-mordenite are thus located on the zeolite and not on the platinum. The low metal content and a dispersion of less than 10 % (Table 7.1) imply a low platinum surface area, which may be one reason why species on the platinum cannot be discerned. Because the bands do not behave in parallel, they must characterize different species. An unambiguous assignment on the basis of a single

band is difficult, and, particularly for the bands at longer wavelengths, multiple assignments are possible. In general, higher wavelengths are indicative of larger π-systems with extended conjugation. The absorption coefficient increases with increasing conjugation, and the intensity distribution does not properly reflect the relative concentrations.

Bands also formed at 350–500 nm after heating a zeolite containing species absorbing at 292–296 nm, assigned to alkyl-substituted cyclopentenyl species in Chapter 6, to temperatures greater than ≈ 550 K . It is important to note that 550 K is an estimate of the actual temperature at which the formation of bands at wavelengths longer than 350 nm begins to take place, because of uncertainty in the temperature measurement and low time resolution (about 10 min per spectrum).

There are four pieces of information regarding the identity of the deposits formed above ≈ 550 K. GC-MS and UV–vis analysis of the dichloromethane extract after digestion of the zeolite in hydrofluoric acid (Figs. 7.11 and 7.12) and the UV–vis spectra of the catalyst after exposure to either water vapor (Figs. 7.9 and 7.12) or ammonia (Fig. 7.10) provide information on the identity of the neutral species. The in situ UV–vis and infrared spectra provide information on the species as they exist on the zeolite, probably as cations (Figs. 7.3, 7.4, and 7.6-7.10). The discussion of results will proceed in this order.

The GC-MS chromatogram of the extracted deposits revealed mostly naphthalenes and anthracenes, and a few non-chromophoric impurities leached from the polyethylene vials. The transition away from “low temperature coke” is said to occur around 473 K, with polyaromatic coke dominating at 623 K [19]. On H-mordenite,

phenanthrene was identified at 613 K [20]. Polynuclear aromatics formed on H-mordenite from ethylene at and above 550 K [21]. Stepanov et al. [22] found polycyclic aromatics to form from methyl-substituted cyclopentenyl cations on H-ferrierite already at 523 K. Thus, the formation of polycyclic aromatics at ≈ 550 K is in agreement with previous reports.

The UV–vis spectra of the catalyst taken in situ after exposure to ammonia or water vapor, or ex situ (after exposure to atmospheric water vapor) are representative of the deposits in their neutral state. The neutralizing effect of water vapor has been reported previously by Leftin and Hobson [23] who used it to neutralize the trityl cation on silica–alumina. Subsequent analysis showed that water did not cause hydrolysis of the cationic species with formation of triphenylmethanol, but instead triphenylmethane was recovered. Likewise, no hydroxylated aromatics were found in the dichloromethane extract, confirming that neutralization occurs and not hydrolysis. According to the GC-MS analysis, the most prevalent naphthalene was 2-methylnaphthalene, which has a band with partial Lorentzian shape at 224 nm and a broader benzenoid band characterized by fine structure at 266, 275, and 286 nm [24]. The most prevalent anthracenes had two methyl groups but the location of these groups could not be determined exactly. A representative example would be 1,3-dimethylanthracene which has an intense band at 257 nm and a benzenoid band with vibrational fine structure at 343, 360, and 380 nm [25]. Thus, the band at 228 nm in Fig. 7.10 is assigned to methyl-substituted naphthalenes and the band at 257 nm is assigned to methyl-substituted anthracenes. In the UV−vis spectrum of the extract (Fig. 7.12), the band at 228 nm is partially cut off through the absorption of the dichloromethane solvent in the UV range.

The bands at 344, 359, and 381 nm are part of the fine structure of the anthracene benzenoid band. The bands at 447 and 473 nm in the spectrum of the solid zeolite are consistent with a methyl-substituted tetracene; tetracene has an intense band at 278 nm and the most intense components of the benzenoid band are at 443 and 473 nm [26]. Tetracenes could not be detected in the extract but they are known to have limited solubility in dichloromethane [27]. Bands at similar positions were found on the zeolite after exposure to water and ammonia (Fig. 7.10), although the overall intensity of the bands after exposure to ammonia was lower. An additional band at 300 nm was also noted, which would be consistent with formation of a pentacene [28]. It is notable that the aromatic deposits are all members of the acene family, which suggests that the one-dimensional pore structure of H-mordenite plays a prominent role in determining the type of species that can form.

During conversion of alkanes, or after heating the initial surface products of olefin adsorption in the presence of inert gas, the polycyclic aromatic species exist in the zeolite as cations. That the species were largely cationic is in agreement with DFT calculations, which predict the cations of some aromatic species to persist in the zeolite in their cationic state. The probability of forming an ion pair versus a π complex is related to the proton affinity of the corresponding neutral hydrocarbons [29]. The bands in the UV–vis spectra at wavelengths between 350 and 500 nm are central to the interpretation, because these bands can only be explained by either neutral chromophores of a size and type that are unlikely to form under these conditions and for which no other evidence exists, or by the cationic forms of the aromatic species detected in the extract. The assignment of these bands to the cations of acenes is

consistent with the observation of the "coke band" in the IR spectra at 1580–1620 cm^{-1}, which is generally attributed to polycyclic aromatic species. Thus, on the working catalyst, the deposits exist as cations, indicating that they reside in the micropores of the zeolite.

Specific band assignments become possible through comparison of the spectra of the surface cations with the reported spectra of cations in mineral acids, specifically cations of the species identified in the extract by GC-MS. This comparison is straightforward because the band positions of aromatic cations have been shown to not vary significantly (≈ 5 nm) with the environment. For example, the UV–vis spectra of hexamethylbenzene [19] and anthracene [30] cations on a solid acid are very similar to the spectra of the same cations in a mineral acid [31,32]. In the series of naphthalene, anthracene, and tetracene cations, the wavelength of maximum absorption increases with the number of aromatic rings. The cations have been reported to absorb at 391, 408, and 447 nm, respectively [32]. Addition of methyl groups causes a modest shift in the wavelength of maximum absorption. For example, the strongest absorption bands of 1,4-dimethylnaphthalene and 2,3-dimethylnaphthalene cations undergo a 5–10 nm hypsochromic shift and that of the 2-methylanthracene [33] cation undergoes an even smaller bathochromic shift. Thus, the assignment of the electronic absorption bands at wavelengths larger than 380 nm to the cations of methyl-substituted naphthalene, anthracene, and tetracene is supported by the positions of the maximum absorptions of these cations in mineral acids.

7.3.4 Surface species evolution and catalyst performance

In H_2-containing feed, changes observed in the UV-vis spectra of both catalysts were minute. The data imply that no significant amounts of unsaturated adsorbates accumulated on the zeolite surface, and the stable rates of isomerization, disproportionation, and dehydrogenation indicate that no other species block the active sites for these reactions on the zeolite or on the platinum. Our data do not provide an explanation for the deactivation of the hydrogenolysis pathway. Bond and Cunningham [17] observed that deactivation during hydrogenolysis was faster when the H_2:*n*-butane ratio was lower (investigated range 17:1 to 5:1) and reported that carbonaceous deposits formed on Pt/Al_2O_3 at temperatures above 575–600 K. The concentrations of these deposits may not be high enough for us to detect, or their nature may preclude detection by UV–vis spectroscopy.

Evidence for olefins being the precursors of the carbonaceous deposits formed on the zeolite includes the fact that surface species similar to those observed during catalysis can be generated by reacting 1-butene (Fig. 7.7) on H-mordenite. The observed band positions are comparable; moreover, the opposite trends in the bands at 296 nm and at longer wavelengths during heating suggest that the alkyl-substituted cyclopentenyl species absorbing at 296 nm is a precursor to species absorbing at longer wavelengths. This is consistent with the fact that the bands at 286 nm grew more rapidly than those at longer wavelengths (Fig. 7.5) during conversion of *n*-butane immediately after the switch in feed, but then the intensity seems to level off, whereas the other species grow almost linearly with time. This behavior is explainable if it is assumed that the species absorbing at 286 are precursors for the larger, more highly unsaturated

species. The evolution of bands after adsorption of the corresponding olefins supports this hypothesis; in this experiment, no gas phase hydrocarbons were present that could contribute to oligomer formation. The two bands at 395 and 460 nm grow at the expense of the bands of the presumed precursors.

After replacement of helium by H_2, the rates measured for H-mordenite immediately dropped to a lower level; then slow deactivation occurred for about 2 h before the rates stabilized (Fig. 7.1). During this time, the intensity of the band at 458 nm kept increasing, while those of the other bands decreased (Fig. 7.4a). These trends indicate that transformation of the alkyl-substituted cyclopentenyl species to methyl-substituted acenes progresses further on the surface although H_2 is present in the feed. The bands at 335 and 395 nm stop changing when that at 458 nm does, whereas the band at 286 nm continues to decrease. The species absorbing at 286 nm may be able to be hydrogenated; however, the band continues to decrease without significant recovery of the activity. This behavior implies that the hydrogenated species do not desorb, the number or liberated sites is negligible, or that the liberated sites are irrelevant for the catalysis.

The rates observed for Pt/H-mordenite also dropped when helium was replaced by H_2. In contrast to H-mordenite though, rates did not decline further; rather, a slight recovery of the catalyst from 25 to about 35% of its original activity was observed, which was evident in the rate of formation of isobutane (Fig. 7.2a). Simultaneously, the intensities of the four bands at 286, 335, 396 and 460 nm decreased. Through the presence of platinum, significant amounts of activated hydrogen may become available on the surface and cause hydrogenation of unsaturated species. Alternatively, neutral

species in equilibrium with the cations may slowly diffuse to the platinum surface where they may be hydrogenated. Given that the decline of the first three bands is not associated with a recovery of the activity of H-mordenite, it is tempting to associate the recovery of activity with the reduction of the band at 460 nm (Fig. 7.4b and Fig. 7.5b); in this case, one would have to explain why hydrogenation of these species should liberate active sites while hydrogenation of other species does not.

The relevance of the amount of carbon deposited (Table 7.1) for the catalysis is difficult to assess, because it is unclear what fraction of the internal surface is accessible to the reacting species. On the basis of IR spectroscopic data, it has been inferred that *n*-hexane [34], *n*-pentane [35], and even *n*-butane [36] do not enter the side pockets of mordenite, and that at saturation only 25% of the Brønsted acid sites interact with *n*-butane [36]. However, other groups have attributed the catalytic conversion of *n*-butane to Brønsted acid sites residing in the side pockets of mordenite [37]. The carbon content of 3.1 mass % (Table 7.1) roughly corresponds to one carbon atom per aluminum atom in the sample. Because the spectra indicate the presence of molecules with several carbon atoms this amount would not suffice to individually block 65% of all existing bridging OH groups, but might suffice to block a significant fraction of the actually participating sites. The sorption data have to be interpreted with caution because N_2, for its smaller kinetic diameter in comparison to *n*-butane (3.64 Å vs. 4.3 Å), could still access internal surface in the deactivated catalyst that is no longer available for reaction. This scenario could explain the decrease of micropore surface area by only 26% with a concomitant loss of 65% activity. Alternatively, this data could imply that only about

40% of micropore surface area participated in the first place and that this volume was reduced.

We conclude that at temperatures above ≈550 K, the alkyl-substituted cyclopentenyl species formed at low temperature react to form methyl-substituted naphthalenes, anthracenes, and tetracenes. Methyl-substituted naphthalenes and anthracenes were identified on the surface as well as by GC-MS and UV–vis spectroscopic analysis after digestion and extraction, whereas methyl-substituted tetracene was identified only on the surface and only by UV–vis spectroscopy. The aromatic species reside in the micropores of the zeolite and exist in their cationic form during catalysis.

References

[1] G. Lietz, H. Lieske, H. Spindler, W. Kanke, J. Völter, J. Catal. 81 (1983) 17.

[2] S. Yuvaraj, T.-H. Chang, C.-T. Yeh, J. Catal. 221 (2004) 466.

[3] R. Gounder, E. Iglesia, J. Catal. 277 (2011) 36.

[4] J.I. Villegas, N. Kumar, T. Heikkilä, A. Smiešková, P. Hudec, T. Salmi, D.Yu. Murzin, Appl. Catal., A 284 (2005) 223.

[5] V. Nieminen, M. Kangas, T. Salmi, D.Yu. Murzin, Ind. Eng. Chem. Res. 44 (2005) 471.

[6] J.A. Dumesic, D.F. Rudd, L.M. Aparicio, J.E. Rekoske, A.A. Treviño, The Microkinetics of Heterogeneous Catalysis, American Chemical Society, Washington, D.C.,1993.

[7] J.C. Yori, M.A. D'Amato, G. Costa, J.M. Parera, React. Kinet. Catal. Lett. 56 (1995) 129.

[8] R.A. Asuquo, G. Eder-Mirth, K. Seshan, J.A.Z. Pieterse, J.A. Lercher, J. Catal. 168 (1997) 292.

[9] M.-Trung Tran, N.S. Gnep, G. Szabo, M. Guisnet, J. Catal. 174 (1998) 185.

[10] R.A. Asuquo, G. Eder-Mirth, J.A. Lercher, J. Catal. 155 (1995) 376.

[11] R. Gounder, E. Iglesia, J. Am. Chem. Soc. 131 (2009) 1958.

[12] N.N. Krupina, A.L. Proskurnin, A.Z. Dorogochinskii, React. Kinet. Catal. Lett. 32 (1986) 135.

[13] K. Ebitani, T.M. Salama, H. Hattori, J. Catal. 134 (1992) 751.

[14] S.D. Jackson, G.J. Kelly, G. Webb, J. Catal. 176 (1998) 225.

[15] D. Nazimek, J. Ryczkowski, React. Kinet. Catal. Lett. 40 (1989) 137.

[16] R.A. Campbell, J. Guan, T.E. Madey, Catal. Lett. 27 (1994) 273.

[17] G.C. Bond, R.H. Cunningham, J. Catal. 163 (1996) 328.

[18] K.B. Fogash, Z. Hong, J.A. Dumesic, J. Catal. 173 (1998) 519.

[19] M. Guisnet, P. Magnoux, Appl. Catal., A 212 (2001) 83.

[20] M. Guisnet, P. Magnoux, Appl. Catal. 54 (1989) 1.

[21] J.-P. Lange, A. Gutsze, J. Allgeier, H.G. Karge, Appl. Catal. 45 (1988) 345.

[22] A.G. Stepanov, M.V. Luzgin, S.S. Arzumanov, H. Ernst, D. Freude, J. Catal. 211 (2002) 165.

[23] H.P. Leftin, M.C. Hobson, Adv. Catal. 14 (1963) 115.

[24] R.A. Friedel, M. Orchin, Ultraviolet Spectra of Aromatic Compounds, Wiley, New York, 1951.

[25] R.N. Jones, Chem. Rev. 41 (1947) 353.

[26] R.A. Friedel, M.A. Orchin, Ultraviolet spectra of aromatic compounds, John Wiley & Sons, New York, 1951, p. 532.

[27] S.M. Leschev, A.V. Sin'kevich, Russ. J. Appl. Chem. 76 (2003) 1483.

[28] National Institute of Standards and Technology, <http://webbook.nist.gov/cgi/cbook.cgi?ID=C135488&Units=SI&Mask=400#UV-Vis-Spec>, accessed February 19, 2013.

[29] H. Fang, A. Zheng, J. Xu, S. Li, Y. Chu, L. Chen, F. Deng, J. Phys. Chem. C 115 (2011) 7429.

[30] W.K. Hall, J. Catal. 1 (1962) 53.

[31] L.S. Singer, I.C. Lewis, J. Am. Chem. Soc. 87 (1965) 4695.

[32] H.-H. Perkampus, E. Baumgarten, Angew. Chem., Int. Ed. 3 (1964) 776.

[33] G. Dallinga, E.L. Mackor, A.A.V. Stuart, Mol. Phys. 1 (1958) 123.

[34] M. Bevilacqua, A.G. Alejandre, C. Resini, M. Casagrande, J. Ramirez, G. Busca, Phys. Chem. Chem. Phys. 4 (2002) 4575.

[35] V.I. Bogdan, A.E. Koklin, V.B. Kazanskii, Kinet. Catal. 51 (2010) 736.

[36] J.A. van Bokhoven, M. Tromp, D.C. Koningsberger, J.T. Miller, J.A.Z. Pieterse, J.A. Lercher, B.A. Williams, H.H. Kung, J. Catal. 202 (2001) 129.

[37] R. Gounder, E. Iglesia, J. Am. Chem. Soc. 131 (2009) 1958.

8 Connecting gas phase product formation with growth of the hydrocarbon pool on H-ZSM-5 and H-beta during methanol conversion

8.1 Introduction

Eventually, nontraditional carbon sources will have to be used out of necessity in production of fuels and chemicals. It is within this context that we approach the subject of converting methanol to hydrocarbons. Carbon sources such as natural gas [1], coal [2], and biomass [3] can be used to produce methanol via well-established methanol synthesis technology. The end products of methanol-to-hydrocarbon (MTH) conversion can vary greatly, as indicated by the already commercialized methanol-to-gasoline (MTG) [4], methanol-to-olefins (MTO) [5], and methanol-to-propylene (MTP) [6] technologies. Although early efforts by Mobil in the 1980s to implement their MTG technology in New Zealand were technologically successful, the plant was an economic failure and the MTH portion was shut-down after a decade of operation [7]. Several MTH plants, including MTG [4], MTO [8] and MTP [9] are either being constructed or have opened recently in China, however, and a recent abundance of cheap natural gas has revived interest in other parts of the world as well.

Although several MTH processes have already been commercialized, the underlying chemistry is not completely understood. Product distributions are, to a large extent, related to the structure of the zeolite or zeotype that is used as a catalyst. For example, H-SAPO-34 is silicon-aluminum phosphate zeotype based on the chabazite framework structure which has 8-membered ring pores through which only linear structures can pass. The steric constraints help direct product formation towards olefins;

hence, H-SAPO-34 is used commercially for MTO. H-ZSM-5 is a three-dimensional, 10-membered ring zeolite. The larger pores allow single ring aromatics with up to four methyl groups to pass, but steric constraints prohibit larger polycyclic aromatic structures from exiting the pores; hence, H-ZSM-5 is used commercially for MTG. Beyond the impact of the catalyst framework on product distribution, a better understanding of the surface chemistry occurring on MTH catalysts could aid in development of more selective and more efficient processes. To appreciate the novelty of the work described in this chapter, one must have an up-to-date understanding of the current perspectives on MTH chemistry. This information is, perhaps, best delivered in a historical context.

Researchers at Mobil were trying to make high octane gasoline by reacting methanol and isobutane on a recently discovered zeolite, H-ZSM-5, when they accidentally discovered that methanol could be converted to hydrocarbons [10]. The first patent was filed in 1974 [11], the discovery was made public in 1976 [12], and the first technical report in the peer-reviewed literature appeared in 1977 [13]. For the next 15 years, the main research focus was on the mechanism that led to formation of the first C-C bond. More than 20 possible mechanisms were proposed, with the most relevant being i) an oxonium ylide mechanism, ii) a carbene mechanism, iii) a carbocationic mechanism, iv) a free radical mechanism, v) a consecutive type mechanism, vi) and a ‘rake’ mechanism [14]. All of the mechanisms failed to describe important aspects of the reaction chemistry, such as certain aspects of the product distribution and the kinetic induction period.

A giant intellectual leap forward occurred in 1993 when a "hydrocarbon pool" mechanism was proposed by Dahl and Kolboe [15]. Although unspecific about the exact chemical composition of the hydrocarbon pool, they showed impressive foresight by suggesting that it "may have many characteristics in common with ordinary coke", and that it corresponds to "a very dynamic situation where one has 'big' carbonaceous species inside the cages of SAPO-34 that is all the time adding and splitting off reactants/products." In the year 2000, Haw and co-workers reported evidence gathered using in situ ^{13}C NMR that cyclopentenyl cations are important hydrocarbon pool components on H-ZSM-5 [16] and that methylbenzenes are important hydrocarbon pool components on H-SAPO-34 [17]. In work independent to that of Haw, White and Xu [18] at ExxonMobil also reported in the year 2000 that the kinetic induction period could be eliminated if methylbenzene species are synthesized in the cages of H-SAPO-34 before admission of methanol. Together, this work defined a working MTH catalyst as an inorganic/organic hybrid structure.

Although the kinetic induction period could be explained by the time necessary to form a hydrocarbon pool, the chemical reactions leading to its formation were still unknown. The mystery was finally solved in 2002 when Song et al. [19] showed that trace impurities, either in the methanol (such as ethanol or acetone), on the catalyst (caused by incomplete template removal during calcination), or in the carrier gas, were responsible for building the hydrocarbon pool scaffolds through well-known chemistry leading to formation of cyclic cations and aromatics. The claim that impurities are necessary to form the hydrocarbon pool has been challenged by Hunger and co-workers [20-22], but it is generally accepted that any direct route from methanol or dimethyl

ether to larger hydrocarbons has a high activation energy and proceeds at a rate that is insignificant compared to the hydrocarbon pool route.

Most recent work (2004-present) has focused on determining the "active components" of the hydrocarbon pool and determining the selectivity of each to gas phase products. A defining study was that of Svelle et al. [23] who reported that the activity of the methylbenzene components of the hydrocarbon pool increases with additional methyl groups on the methylbenzene species on the three dimensional, 12-membered zeolite H-beta, and decreases with additional methyl groups on the methylbenzene species on H-ZSM-5. In other words, hexamethylbenzene is the most active hydrocarbon pool component on H-beta, whereas xylenes are the most active components on H-ZSM-5. This conclusion was reached from an experiment in which ^{12}C-methanol was reacted on each zeolite for 18 min and followed by 2 min of ^{13}C-methanol conversion. The total ^{13}C content of the methylbenzenes extracted from the zeolite was used as an indicator of activity. Because the H-ZSM-5 yielded seven times more ethene relative to propene than H-beta, it was concluded that methylbenzene species with fewer methyl groups are more selective to ethene, whereas methylbenzene species with more methyl groups are more selective to larger olefins.

Finally, the mechanisms by which hydrocarbon pool species are methylated, and by which alkyl branches are cleaved, have also been a topic of debate. Recent calculations suggest that methylation occurs on methylbenzene hydrocarbon pool components that are subject to transition state selectivity imposed by different zeolite frameworks [24]. There have been two notable proposals about the mechanism by which cleavage of alkyl side chains occurs, those being the side-chain alkylation

mechanism, and the paring mechanism (Fig. 8.1). The side-chain mechanism is unable to account for the fact that carbon-13 from ^{13}C-methanol is incorporated into the aromatic rings of hydrocarbon pool species, and thus variations of the traditional paring mechanism have been the recent focus. Proposed by Sullivan et al. [25] in 1961 to account for light isoparaffins produced by hydrocracking hexamethylbenzene, the traditional paring mechanism involves expansion and contraction of five- and six-membered ring species to grow alkyl side chains. A modified paring mechanism has recently been proposed by Haw and co-workers [26], and is claimed to be consistent with both experimental and theoretical observations.

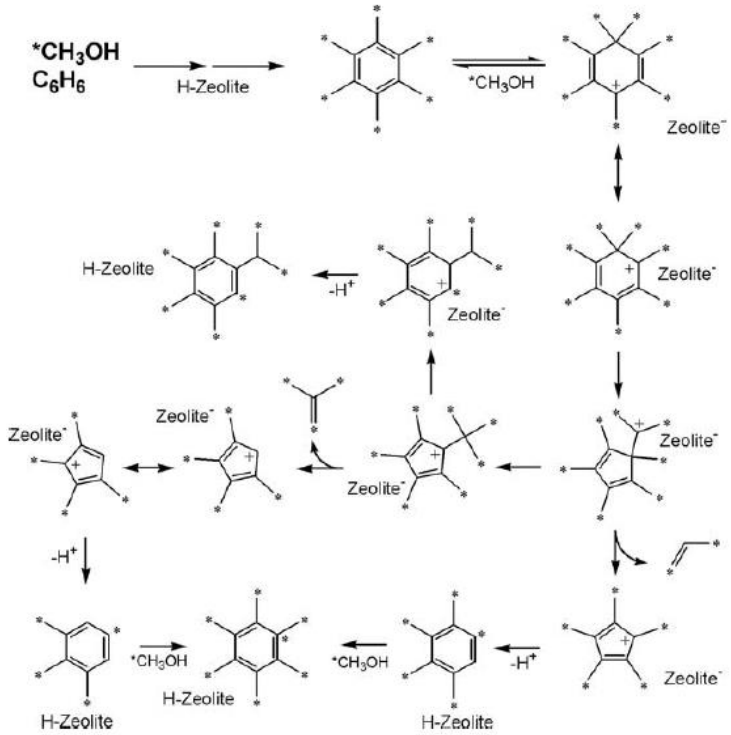


Figure 8.1: A proposed reaction pathway in methanol-to-hydrocarbons catalysis involving cleavage of alkyl side-chains by the paring mechanism. Stars (*) denote carbon-13 labels. Reprinted from Journal of Catalysis, 221, M. Bjørgen, U. Olsbye, D. Petersen, S. Kolboe, The methanol-to-hydrocarbons reaction: insight into the reaction mechanism from [^{12}C]benzene and [^{13}C]methanol coreactions over zeolite H-beta, 1-10, Copyright (2004), with permission from Elsevier [27].

As outlined separately by Haw and White, research opportunities in MTH include i) increasing catalyst lifetimes [27], ii) tailoring catalyst selectivities [27], iii) tailoring the organic component of an active MTH catalyst [28], and iv) adding additional inorganic material to the cages of active MTH catalysts [28]. Central to these goals is an understanding of the surface chemistry that occurs on a working MTH catalyst. UV-vis spectroscopy has been used previously to investigate the hydrocarbon pool formed from methanol on H-ZSM-5 [29-32], H-SAPO-34 [33-36], HY [35], and AlPO-34 [36], but has never been utilized in its fullest capacity. It has been known for many years that the wavelength of absorption of protonated methylbenzenes in mineral acid increases (between 320-395 nm) with increasing methylation [37], and that the same absorption position is observed on a solid acid [38,39]. Thus, the technique should deliver information about the extent of methylation for protonated methylbenzene species that exist on the working catalyst. This is especially true on H-ZSM-5 where steric constraints prevent polycyclic aromatic species that may have overlapping electronic bands from forming [40]. H-beta is of interest because its 12-membered ring pores accept larger aromatic species, and thus conversion of individual hydrocarbon pool components is possible. Additionally, the spectroscopic features of the growing hydrocarbon pool during the induction period have never been correlated with formation of gas phase products. Such a correlation may also provide information about the active hydrocarbon pool species.

8.2 Experimental

8.2.1 Materials

H-ZSM-5 was used as received from Süd-Chemie and had a specified Si/Al ratio of 45. NH_4-beta was received from Zeolyst and had a specified Si/Al ratio of 19. Calcination was performed by heating at 10 K min^{-1} to 823 K in a 100 ml min^{-1} flow of air (Airgas, zero grade) and holding at 823 K for 4 h to obtain H-beta. Gases used were the same as those reported in Section 3.1. Methanol used in all experiments was from Alfa-Aesar (Ultrapure, HPLC Grade, 99.8+%).

8.2.2 Equipment

The diffuse reflectance spectroscopic equipment was almost the same as described in Section 3.3. The only difference is that in experiments performed using continuous flow of methanol, the catalyst powder rested on a stainless steel frit (Mott Corp., thickness 0.16 cm, Media Grade 2) placed in the bottom of the sample cup.

For experiments using continuous flow of methanol, the outlet stream from the environmental chamber was directed to a gas chromatograph (GC, Varian 3800) using a flame-ionization detector (FID). Separation was performed with a PoraPLOT Q column (Chrompack, 0.32 mm ID x 25 m). A mass spectrometer (MS, Pfeiffer OmniStar GSD 320) using electron impact ionization at 70 eV was placed online for analysis of the effluent stream in all experiments. Gas transfer lines were heated to 343 K.

8.2.3 Reaction conditions for switching experiments using continuous flow of methanol

Before reaction, the catalyst was heated at 5 K min^{-1} to the specified reaction temperature in a flow of 30 ml min^{-1} (NTP) N_2 and held for 1 h. Conversion of

methanol was then performed at a temperature of 573 K on H-ZSM-5 or 548 K on H-beta, using a W/F of 0.14 h in both cases. Methanol was added to the gas stream by passing helium flowing at 30 ml min^{-1} through a three-legged saturator containing methanol held at 289 K in an isothermal water bath. After an initial period of methanol conversion (3 h on H-ZSM-5, 2 h on H-beta), the gas flow was switched to 30 ml min^{-1} of pure N_2 while maintaining the same temperature of the reaction chamber. After flushing with N_2 for a period of time (3 h for H-ZSM-5, 2 h for H-beta), the gas flow was switched back to helium/methanol. The time interval between spectra was 7 min.

8.2.4 Reaction conditions for a methanol pulse

Before a pulse of methanol was administered, the H-ZSM-5 catalyst was heated at a rate of 5 K min^{-1} to 623 K and held for 1 h in a flow of 30 ml min^{-1} N_2. A 1 µl pulse of methanol was then administered through a septum in the gas line upstream of the reaction chamber.

8.2.5 Adsorption and spectroscopic analysis of hexamethylbenzene and 1,2,3,4,5-pentamethylcyclopentadiene

A box oven was used to dry 205 mg of H-beta on a watchglass at 448 K for 4 h. The watchglass was then quickly transferred to a desiccator containing 10 mg of hexamethylbenzene (Sigma, 99%) on a separate watchglass. The desiccator was subsequently evacuated, and remained closed for 4 days. The H-beta was then loaded into the spectroscopic chamber, placed under a flow of 30 ml min^{-1} N_2, and heated at 2 K min^{-1} to 473 K.

Before adsorption of 1,2,3,4,5-pentamethylcyclopentadiene (Sigma, 94%), H-mordenite (M2) was dried in the environmental chamber at a temperature of 673 K for 1

h in a flow of 30 ml min^{-1} N_2 and then cooled to 323 K. A syringe was then used to inject 0.5 µl of 1,2,3,4,5-pentamethylcyclopentadiene into the gas stream. Liquid phase spectra of either hexamethylbenzene or 1,2,3,4,5-pentamethylcyclopentadiene were taken using either cyclohexane (Alfa Aesar, 99% min) or sulfuric acid (Fisher, Certified ACS Plus, 95.0-98.0% w/w) as a solvent.

8.3 Results

8.3.1 Products formed on H-ZSM-5 in continuous methanol flow

Dimethyl ether was the main product formed on H-ZSM-5. Hydrocarbon products were predominately C2-C7 aliphatic species and appeared after the induction period seen in Fig. 8.2. Ethene and propene were the main products and were produced at almost equal rates during the beginning of the induction period. After a short time ethene was produced in excess of propene. Other products were: methane, propane, C4 hydrocarbons (*n*-butane, isobutane, 1-butene, *trans*-2-butene, *cis*-2-butene, isobutene), C5 alkanes (*n*-pentane, 2-methylpentane), C6 alkanes, C7 alkanes, and a small amount of aromatic species (benzene, toluene, xylenes, trimethylbenzene (triMB), and tetraMB).

After 2.5 h on stream, the dramatic increase in gas phase product formation rates had nearly stopped, and at 3 h the chamber was purged with N_2. After the purge, conversion of methanol began again and another induction period was observed. The second induction period was shorter than the first one, and formation rates of gas phase products stopped increasing after about 2 h.

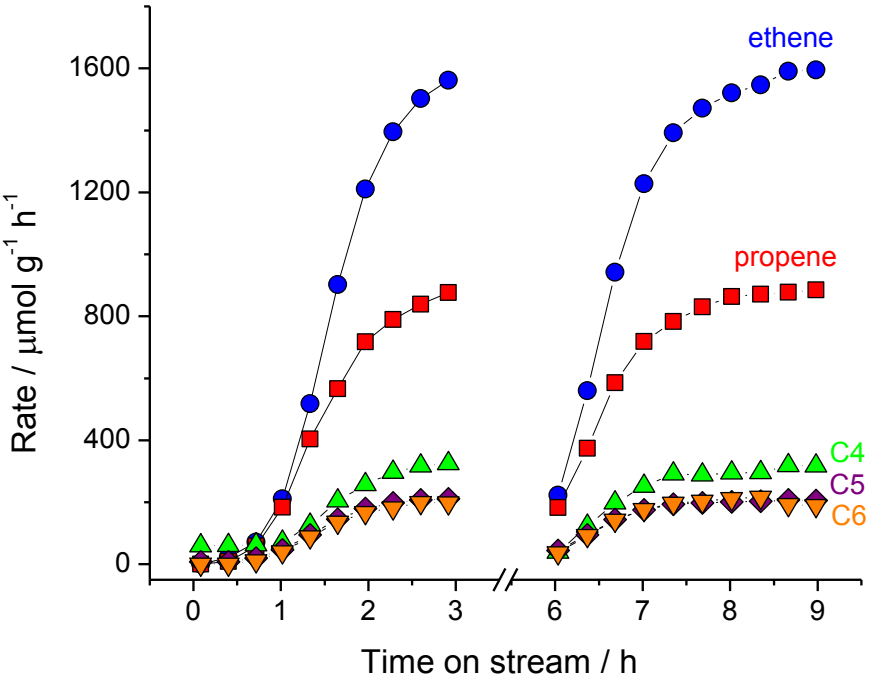


Figure 8.2: Rates of formation of the main gas phase products formed during conversion of methanol (10 kPa partial pressure) on H-ZSM-5 (W/F = 0.14 h) at a reaction temperature 573 K. The corresponding UV-vis spectra during the first 3 h are shown in Fig. 8.3.

8.3.2 Diffuse reflectance UV-vis spectra recorded in situ during continuous flow of methanol on H-ZSM-5

The diffuse reflectance UV-vis spectra recorded in situ during conversion of methanol on H-ZSM-5 are shown in Fig. 8.3. The absorptions can be broken in to four general regions: wavelengths shorter than 240 nm, between 250-310 nm, between 320-420 nm, and > 420 nm. The most intense absorptions were below 240 nm and the least intense absorptions were > 420 nm. Immediately following the initial introduction of methanol, bands formed below 220 nm, at 264 nm, and at 353 nm (Fig. 8.3, inset). With time, the bands broadened and the wavelength of maximum absorption shifted. After 3

h in methanol flow there were clear maxima at 274 and 360 nm. The peak below 240 nm was asymmetric, and a shoulder was visible at about 212 nm. A shoulder at approximately 295 nm was visible on the band centered at 274 nm. The band at 360 nm was relatively symmetric. A few small bands at longer wavelengths of 440, 490, and 560 nm also grew with time on stream. The bridging OH groups, visible in the near infrared at 1420 nm, were consumed immediately after introduction of methanol (not shown).

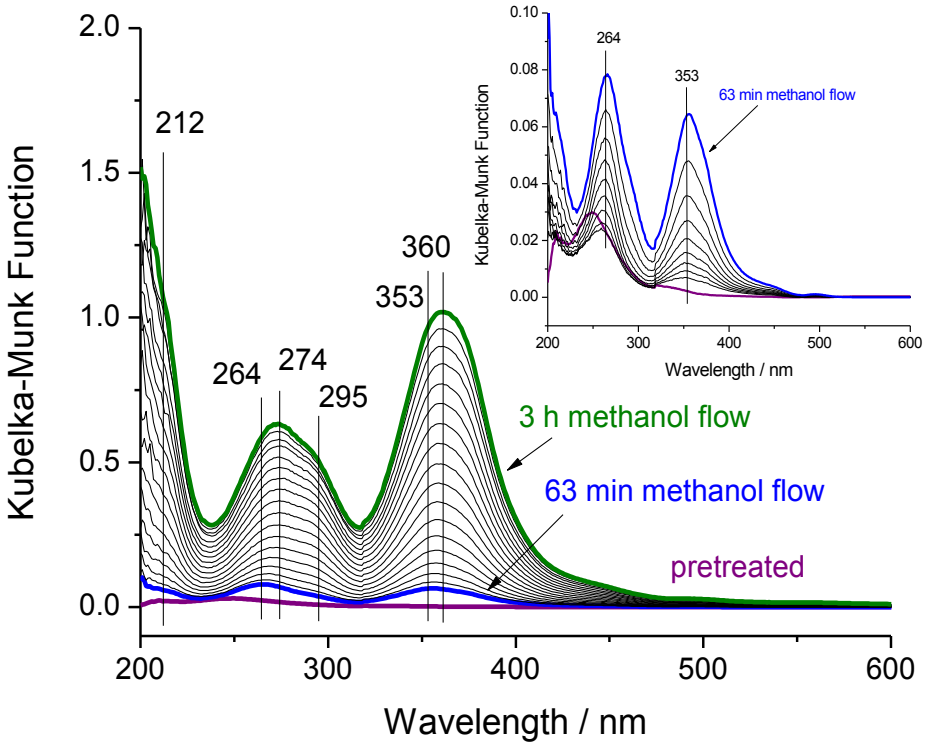


Figure 8.3: Evolution of diffuse reflectance UV-vis spectra recorded in situ during conversion of methanol (10 kPa partial pressure) on H-ZSM-5 (W/F = 0.14 h) at a reaction temperature of 573 K. The corresponding gas phase products are shown in Fig. 8.2. Purple line: pretreated catalyst; black lines: in methanol flow; blue line: after 63 min in methanol flow; green line: after 3 h in methanol flow.

8.3.3 Spectra collected and hydrocarbons detected while flushing H-ZSM-5 with inert gas after methanol conversion

After 3 h of methanol conversion at 573 K, the gas flow was switched to 30 ml min^{-1} of pure N_2. Immediate changes were seen in the UV-vis-NIR spectra (Fig. 8.4). After only 7 minutes, the broad band at 320-420 nm had lost about a quarter of its intensity. The intensity of the absorption continued to decrease exponentially, with a final absorption maximum at 350 nm and a less distinct shoulder at 375 nm. The absorption below 240 nm decreased in intensity at a similar exponential rate as the band at 320-410 nm. The intensity of the overtone of bridging OH groups at 1420 nm was partially restored after 1 h and almost fully restored after 3 h (Fig. 8.4, inset). The small bands at 440, 490, and 560 nm were relatively unaffected.

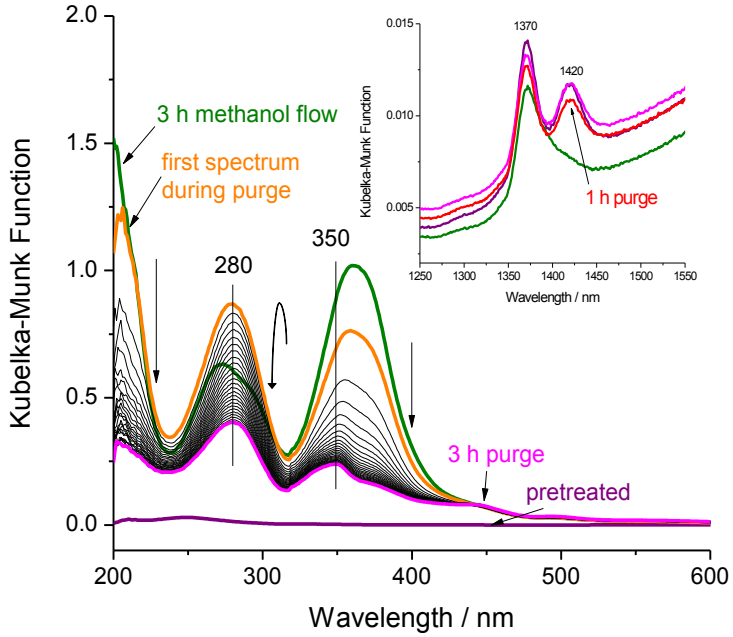


Figure 8.4: Evolution of diffuse reflectance UV-vis spectra recorded in situ after conversion of methanol on H-ZSM-5. The temperature remained at 573 K and the flow rate of N_2 was 30 ml min^{-1}. The spectra correspond to the period of 3-6 h on stream in Figs. 8.2 and 8.15. Purple line: pretreated catalyst; green line: last spectrum in methanol flow (same as in Fig. 8.3); orange line: first spectrum during flush; black lines: during flush; red line: after 1 h of flushing; pink line: after 3 h of flushing.

The broad band at 250-310 nm behaved differently. Immediately after the switch to N_2, the band lost its asymmetric features and grew, becoming a larger, symmetric band with a maximum absorption at 280 nm. After the initially rapid growth, the band decreased in intensity at an almost linear rate.

The online MS revealed that a surge of hydrocarbons eluted from the reaction chamber after the initial switch to N_2 (Fig. 8.5). The signal for dimethyl ether (m/z = 46) immediately doubled in intensity, but decreased by 90% over the next 1.5 minutes. Propene, butenes, and aromatics were also detected in the effluent. The signal at m/z =42, marked as representing propene but also containing contributions from fragments of larger hydrocarbons (confirmed by online GC analysis), quadrupled in intensity over the first 45 seconds and then lost 90% of its intensity over the next 3.5 minutes.

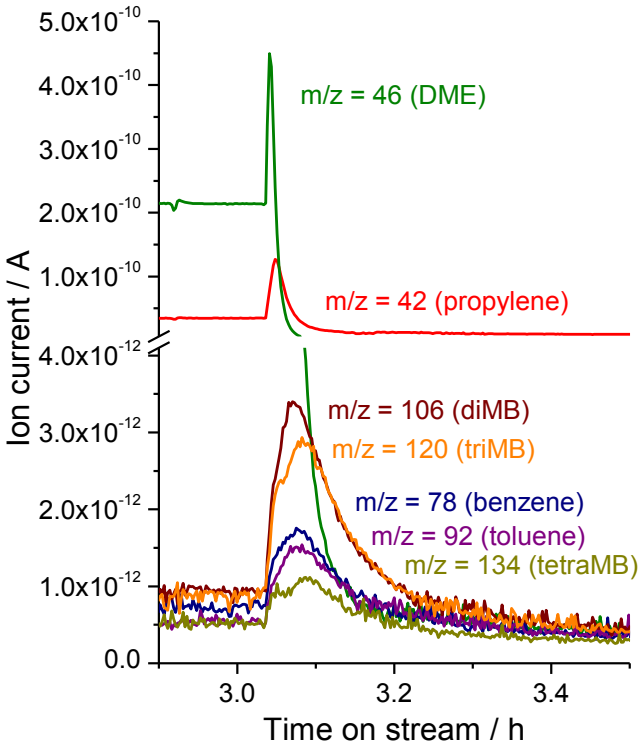


Figure 8.5: Evolution of selected products (determined by the m/z ratio) while flushing H-ZSM-5 with N_2 after conversion of methanol (10 kPa partial pressure) at 573 K.

Aromatic species took longer to elute from the reaction chamber; for example, dimethylbenzene took 18 min to lose 90% of its signal. Other aromatic species were benzene, toluene, trimethylbenzene, and tetramethylbenzene.

8.3.4 Spectra collected and products formed while administering methanol pulses

A pulse of methanol administered at a temperature of 623 K resulted in significant conversion to gas phase products. Apparently, the higher temperature allows for hydrocarbon pool species to form, and thus for gas phase products to be produced. The MS signals at m/z = 42 and 56, containing large contributions from propene and butenes, are shown in Fig. 8.6. Methylbenzenes with 1-4 methyl groups were also detected.

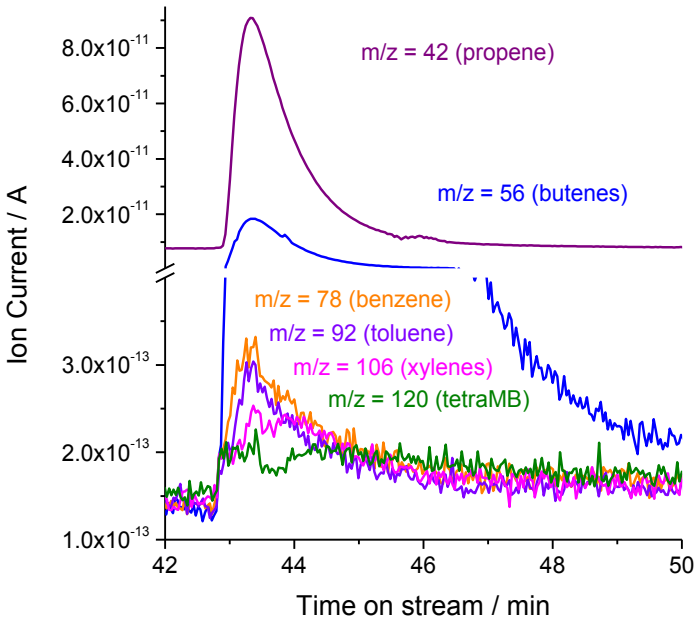


Figure 8.6: Evolution of gas phase products produced on H-ZSM-5 after a 0.5 µl pulse of methanol was administered at a temperature of 623 K. The corresponding UV-vis spectra are shown in Fig. 8.7.

The only significant band seen in the UV-vis spectra after administering the methanol pulse was at 283 nm (Fig. 8.7). Smaller bands were observed at 220, 335, 355, and 445 nm. The band at 283 nm decreased in intensity as the reaction chamber was purged with inert gas after the methanol pulse.

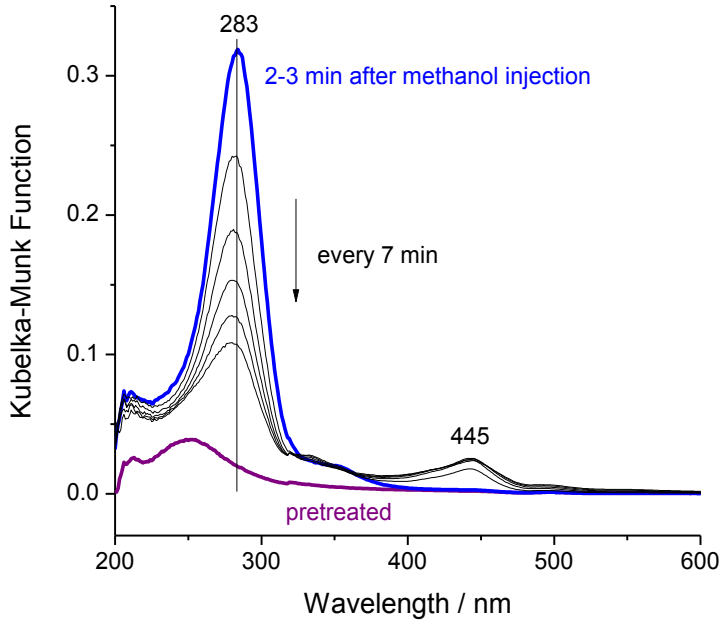


Figure 8.7: Diffuse reflectance UV-vis spectra of H-ZSM-5 taken after administering a 1 µl pulse of methanol at a temperature of 623 K. Gas phase products produced from the pulse are shown in Fig. 8.6.

8.3.5 Products formed during methanol conversion on H-beta

Dimethyl ether was also the main product formed on H-beta. Other products were the same as those produced on H-ZSM-5, but they were formed at different rates and with different selectivities. Isobutane was the main product, and after the short induction period the rate of formation declined steadily with time on stream. Reaction pathways leading to isobutane appeared to deactivate more rapidly than those leading to other products. The formation rates of aliphatic products are shown in Fig. 8.8.

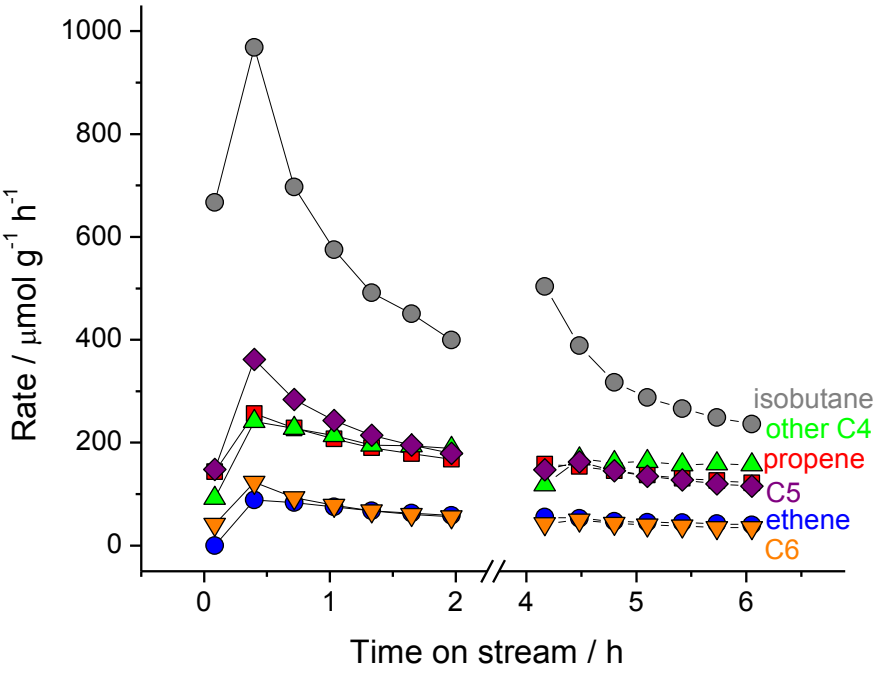


Figure 8.8: Rates of formation of the main gas phase products formed during conversion of methanol (10 kPa partial pressure) on H-beta (W/F = 0.14 h) at a reaction temperature of 548 K. The corresponding UV-vis spectra during the first 2 h are shown in Fig. 8.9.

After 2 h of methanol conversion the reaction chamber was purged with N_2. At 4 h on stream (after a 2 h purge) methanol conversion began again. No induction period was observed at the beginning of the second reaction, and the formation rate of isobutane was slightly higher than just before the purge began. The formation rate of all products decreased with time on stream, with pathways to isobutane again being most affected.

8.3.6 Diffuse reflectance UV-vis spectra recorded in situ during conversion of methanol on H-beta

The diffuse reflectance UV-vis spectra recorded in situ during conversion of methanol on H-beta are shown in Fig. 8.9. The spectra, again, can be broken into four general regions of absorption: wavelengths shorter than 250 nm, between 260-340 nm, between 340-420 nm, and > 420 nm. The first spectrum, taken during the first 7 minutes of methanol flow, showed initial bands below 220 nm, at 291 nm, and at 395 nm. A small band at 250 nm on the pretreated catalyst decreased in intensity. With time on stream, the band at 291 nm underwent a bathochromic shift while the band at 395 nm underwent a hypsochromic shift. After 2 h, specific maxima were visible at 305, 378, and 455 nm. The band at 305 nm grew quickly and growth was finished after about 1 h in methanol flow. All other bands continued to grow over the 2 h duration of the reaction. The large band below 250 nm was not well resolved, and a specific maximum or a shift in position was hard to discern. Both the 305 and 378 nm bands appeared to have shoulders, absorbing at approximately 290 and 355 nm. The overtone of bridging OH groups in the near infrared was not well resolved, but the intensity of the overtone of silanol OH groups, absorbing at 1372 nm, gradually decreased in intensity during the reaction (not shown).

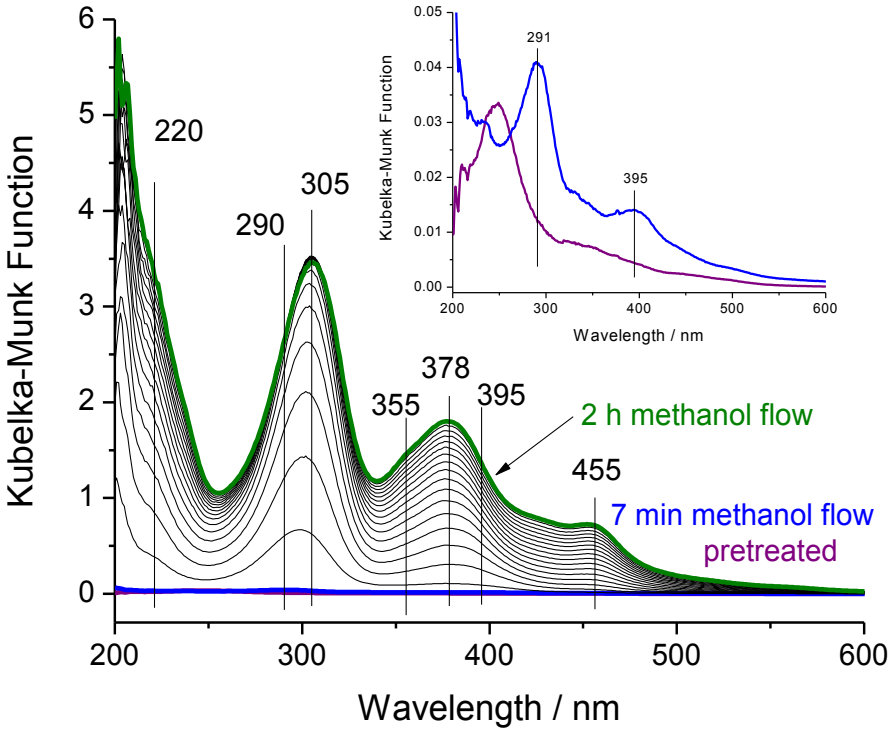


Figure 8.9: Evolution of diffuse reflectance UV-vis spectra recorded in situ during conversion of methanol (10 kPa partial pressure) on H-beta (W/F = 0.14 h) at a reaction temperature of 548 K. The corresponding gas phase products are shown in Fig. 8.8. Purple line: pretreated catalyst; blue line: after 7 min in methanol flow; black lines: in methanol flow; green line: after 2 h in methanol flow.

8.3.7 Spectra collected and hydrocarbon products detected while flushing H-beta with inert gas after methanol conversion

After converting methanol at 548 K for 2 h, the reaction chamber was purged with N_2. Compared to the rapidly changing spectra observed while purging H-ZSM-5, changes in the spectra evolved slowly (Fig. 8.1). The broad band below 250 nm decreased in intensity while a new, distinct band grew at 230 nm. The band originally centered at 305 nm displayed a quick initial growth and hypsochromic shift to 303 nm but then decreased in intensity with time. Bands grew at 345, 421, and 450 nm and a band at 387 nm became better defined. The band originally centered at 378 nm

decreased in intensity. True isosbestic points were observed at 267 and 352 nm. The overtone of external silanol groups, absorbing at 1372 nm, slowly regained intensity (Fig. 8.10, inset).

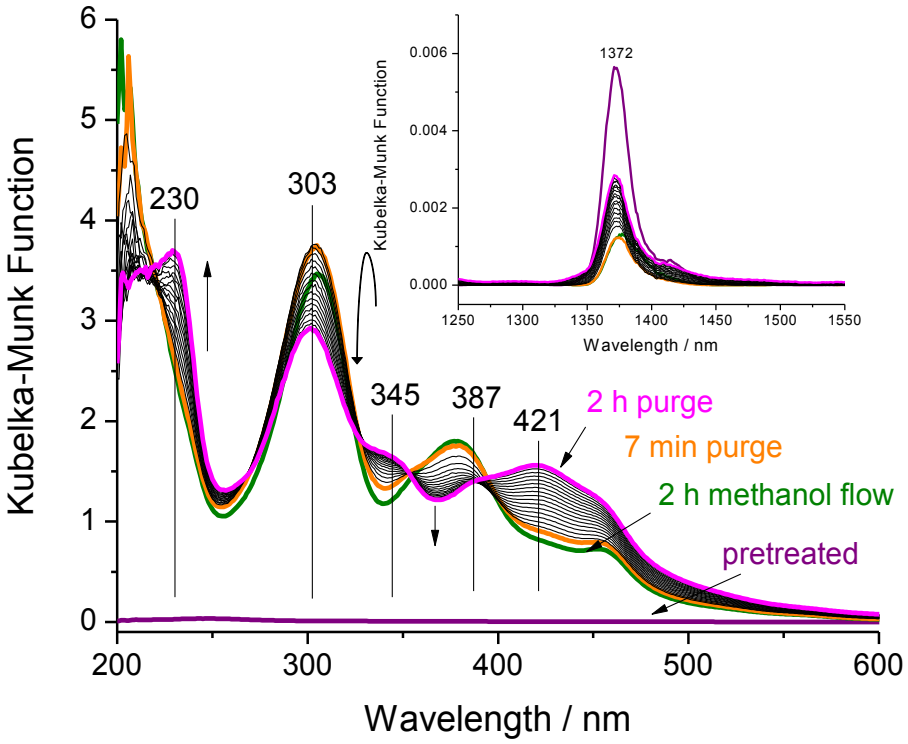


Figure 8.10: Evolution of diffuse reflectance UV-vis spectra recorded in situ after conversion of methanol on H-beta. The temperature remained at 548 K and the flow rate of N_2 was 30 ml min^{-1}. The spectra correspond to the period of 2-4 h on stream in Figs. 8.8 and 8.16. Purple line: pretreated catalyst; green line: last spectrum in methanol flow (same as in Fig. 8.9); orange line: first spectrum during purge; black lines: during purge; pink line: after 2 h purge.

The online MS revealed that hydrocarbons again eluted from the reactor after the switch to N_2 (Fig. 8.11). The signal for dimethyl ether (m/z = 46) more than doubled in the first 30 seconds, but decreased by 90% over the next 1.5 minutes. Propene, butenes, isobutane, and aromatics were also detected in the effluent. The signal at m/z = 43 contains contributions from both propene, isobutane and some larger hydrocarbons

(confirmed by online GC analysis). The signal increased by 3.5 times in the first minute and then lost 90% of its intensity over the next 45 minutes. The concentration of aromatic species in the effluent was miniscule compared to the concentration that eluted while purging H-ZSM-5. Detected species include benzene, toluene, and dimethylbenzene.

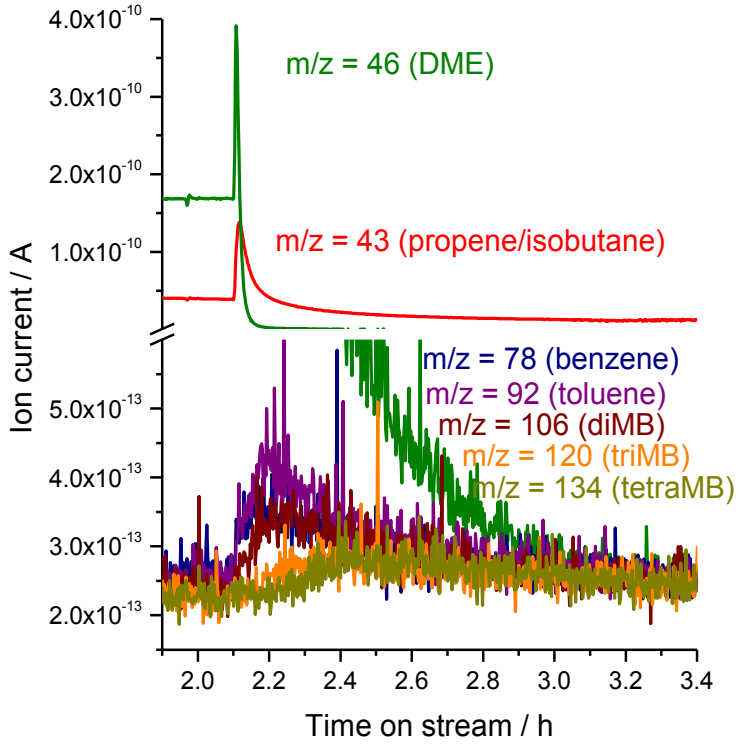


Figure 8.11: Evolution of selected products (determined by the m/z ratio) while flushing H-beta with N_2 after conversion of methanol (10 kPa partial pressure) at a temperature of 548 K.

8.3.8 Adsorption of hexamethylbenzene and 1,2,3,4,5-pentamethylcyclopentadiene

Before heating, the wavelengths at which hexamethylbenzene absorbed UV-vis radiation were similar to the wavelengths at which it absorbs in a non-polar solvent. In

cyclohexane, hexamethylbenzene displayed a weak absorption at 271 nm, and on the H-beta a small absorption was visible at 272 nm. A larger band was present below 210 nm, which was intense but poorly resolved on H-beta. As the chamber containing the H-beta was heated to 473 K, new absorptions were seen at 278 and 391 nm. In sulfuric acid, hexamethylbenzene displayed absorptions at 280 and 393 nm.

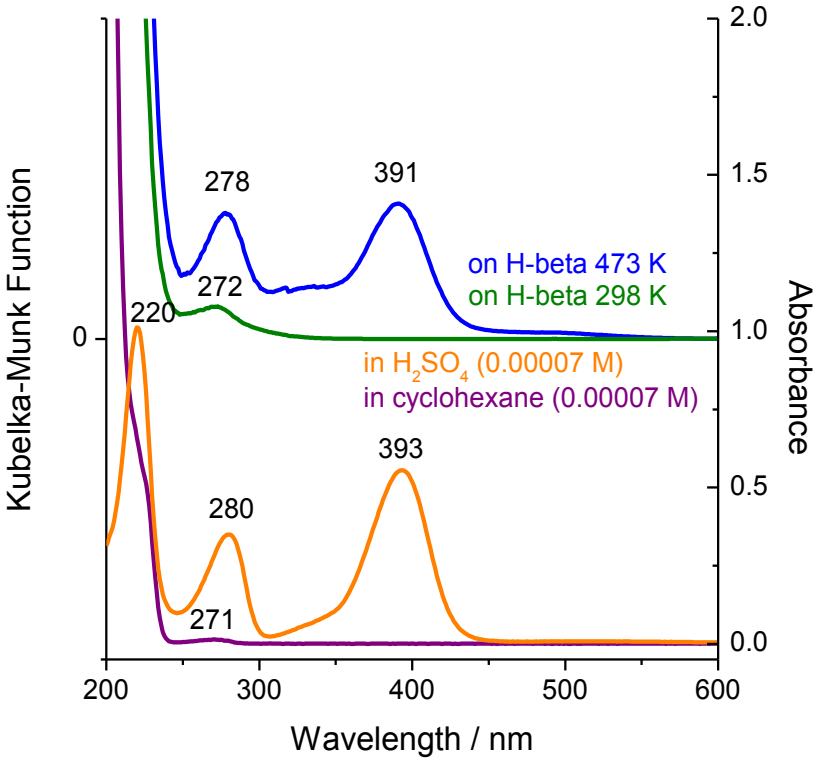


Figure 8.12: UV-vis spectra of hexamethylbenzene adsorbed on H-beta (top) and in sulfuric acid (bottom). Green line: on H-beta at room temperature; blue line: on H-beta at 473 K; purple line: in cyclohexane; orange line: in sulfuric acid.

Adsorption of 1,2,3,4,5-pentamethylcyclopentadiene on H-mordenite at 323 K immediately caused a band to form that was similar to that seen in sulfuric acid (Fig. 8.13). In sulfuric acid, the strongest band was at 297 nm, and on the zeolite the strongest band was at 299 nm.

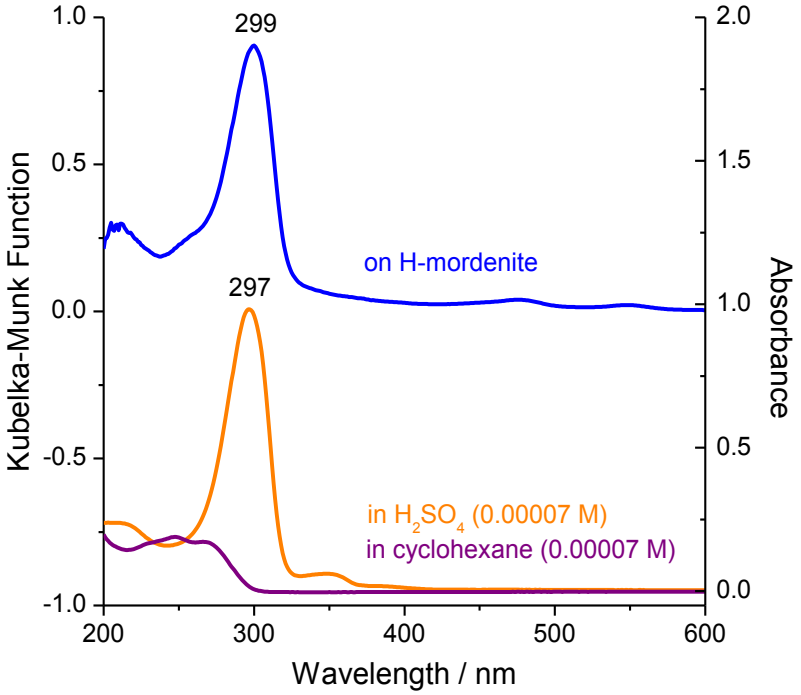


Figure 8.13: UV-vis spectra of 1,2,3,4,5-pentamethylcyclopentadiene on H-mordenite at 323 K (blue line) or in cyclohexane (purple line) or sulfuric acid (orange line).

8.4 Discussion

8.4.1 Gas phase product formation

H-ZSM-5 is used commercially in both methanol-to-gasoline (MTG) and methanol-to-propylene (MTP) processes. As suggested by the process names, there is some variability in possible product distributions. Typically, reaction conditions for MTG involve "lower" temperatures (623-683 K) and a pressure of around 20 bar [7]. MTP is performed at "higher" temperatures (733-753 K) and close to atmospheric pressure [7]. Because the goal of this work was to correlate spectroscopic analysis of the growing hydrocarbon pool with product formation rates, reaction conditions were selected that forced the chemical events of interest to occur on a time scale compatible

with UV-vis spectroscopy, hence the lower temperatures and methanol partial pressure of only 10 kPa.

It has already been established that a kinetic induction period occurs when converting methanol on a zeolite or zeotype catalyst. The induction period is typically cited as the time in which a hydrocarbon pool forms on the catalyst, which then allows for gas phase products to be produced [10]. While an induction period is known to occur, a spectroscopic characterization of the evolving hydrocarbon pool with simultaneous analysis of gas phase products in flow has never been reported. Our data will unequivocally show that a hydrocarbon pool is indeed necessary to form gas phase products.

The results of methanol conversion on H-ZSM-5 at comparable conditions were reported by Ono et al. [41]. Using H-ZSM-5 with a Si/Al ratio of 42, a reaction temperature of 573 K, and a space time of 0.17 h, the total conversion to hydrocarbon products was about 15 mol%. About 65% of the carbon in methanol went to ethane, ethene, and propene, and about 35% went to larger aliphatic hydrocarbons and propane. In this work, using a catalyst with a similar Si/Al ratio (Si/Al = 45), the same temperature setting, and a slightly shorter space time (0.14 h), the total conversion to hydrocarbon products was about 4.5 mol% when the catalyst reached a pseudo-steady state. About 55% of the carbon in converted methanol went to ethene and propene. The lower conversion compared to Ono et al. is probably a result of the actual temperature (in this work) being lower than the reported temperature of 573 K. It is well known that in situ spectroscopic reaction chambers such as the one used in this work suffer from temperature gradients in the catalyst bed caused by uneven heating, which can result in

lower than expected conversions [42]. Methanol conversion is known to be extremely sensitive to temperature [41]. The high selectivity to ethene may be caused by a hydrocarbon pool that is mostly aromatic in nature; aromatics are suspected as being the primary source of ethene, whereas on H-ZSM-5, larger products are largely produced in secondary methylation reactions [7].

Isobutane is known to be produced in copious amounts from conversion of methanol on large pore zeolites, including H-beta. Salehirad et al. [43] found the selectivity to C4 products, consisting largely of isobutane, to be 53% on H-beta at a temperature of 573 K. C5 products were formed with a selectivity of 30%. Mikkelsen et al. [44] also found isobutane to be the C4 species produced with the highest selectivity on H-beta. Isobutane is believed to be produced by larger methylbenzene species. To prove the point, Bjørgen et al. [45] converted hexamethylbenzene and 1,2,3,3,4,5-hexamethyl-6-methylene-1,4-cyclohexadiene on H-beta and found isobutane to be the main non-aromatic product. Lighter aliphatics such as ethene and propene were also produced, but with lower selectivity.

The stability of zeolites used for methanol-to-hydrocarbons catalysis is believed to be closely related to the type of surface species that are able to form. On H-ZSM-5, deactivation is slower because formation of polycyclic aromatic species is sterically hindered. For example, Bjørgen et al. [40] observed a decrease in conversion from 85% to 82.5% over 20 h of methanol conversion. The stability of our H-ZSM-5 after the initial induction period is reasonable given the short reaction time, low temperature, and low methanol partial pressure. The slow but inevitable deactivation of H-ZSM-5 was

recently reported to be caused by the buildup of graphitic deposits on the external surface of the zeolite crystals [32].

Large pore zeolites such as H-beta are known to deactivate rapidly during methanol conversion. Mikkelsen et al. [44] found H-beta to deactivate completely after 6 h on stream at a temperature of 673 K. Formation of polycyclic aromatic species is believed to be responsible. Species much larger than hexamethylbenzene, for example hexamethylnaphthalene (hexaMN), have been extracted from H-beta after less than 5 minutes of co-feeding benzene and methanol [**Error! Bookmark not defined.**,46]. Even larger species, such as phenanthrene and pyrene, have been extracted from H-SAPO-34 [40], a framework with spacious channel intersections. We note that the reported reasons for deactivation of H-ZSM-5 and zeolites with larger pores and channel intersections are believed to be significantly different; polycyclic aromatics may clog pores and block sites on H-beta, whereas transport to the internal surface is hindered by external, graphitic coke on H-ZSM-5. Overall, the stability of our H-ZSM-5, and the rapid deactivation of our H-beta, are both consistent with previous reports.

8.4.2 Background information for identification of electronic bands

The hydrocarbon pool on catalysts used for conversion of methanol has been characterized in numerous ways. Thus, information about the general composition of the pool that forms on several zeolite frameworks is already available. Extractions of spent catalysts have shown that very few aromatic species larger than the methylbenzenes are formed on H-ZSM-5 [40]. Larger polycyclic aromatic species such as methylated naphthalenes are able to form on H-beta in addition to the methylbenzenes [**Error! Bookmark not defined.**,46]. ^{13}C NMR has identified methyl-

substituted cyclopentenyl species as very stable species that can also form, for example 1,3-dimethylcyclopentenyl [16] and 1,2,3-trimethylcyclopentenyl [16,47] on H-ZSM-5, and even heptamethylcyclopentenyl [48] on H-SAPO-34. It has been observed that some methylbenzenes are also stable as protonated species [49,50]. The UV-vis band assignments in the sections that follow will draw from these, and other reports, which have already identified many hydrocarbon pool components.

It is well known that some of the methylbenzene species expected to be active hydrocarbon pool components can exist on a zeolite as stable cations. For example, Bjørgen et al. [38] found protonated hexamethylbenzene to be formed in H-beta from neutral hexamethylbenzene upon heating, as determined by both UV-vis and infrared spectroscopy. The lowered symmetry activated a vibrational mode in the infrared at 1600 cm^{-1} and a new band was seen at a wavelength of 391 nm in the UV (confirmed in our lab, Fig. 8.12). One reason for the new band in the UV is that protonated aromatic species are cyclohexadienyl cations [37]. Dienylic species typically have new bands absorbing at longer wavelengths in comparison to their neutral counterparts. DFT calculations on the electronic spectrum of protonated benzene have confirmed that a new band should appear at longer wavelengths [51]. That a new band appears at longer wavelengths is not unique to protonated aromatic species; Sorensen et al. [52] found the dienylic species formed by protonation of 2,4-dimethyl-1,3,5-heptatriene to absorb at 396 nm in 96% H_2SO_4, and Deno et al. [53] found that protonation of methyl-substituted cyclopentadienes with 2-6 methyl groups shifted the absorption to between 275 and 301 nm. We found 1,2,3,4,5-pentamethylbenzene to absorb at 297 nm in

sulfuric acid and 299 nm on H-mordenite, both being consistent with formation of a cationic species.

The similarity of UV-vis spectra of species on solid acids and in mineral acids is additional evidence of the ionic character of such species. In 98% H_2SO_4, hexamethylbenzene was found to have absorptions at wavelengths below 250 nm, at 280 nm, and at 393 nm [54], which is very close to the absorptions below 250 nm, at 277 nm, and at 391 nm observed on H-beta [38]. (The spectrum of hexamethylbenzene in 96% H_2SO_4 reported by Bjørgen et al. [38] appears to also contain contributions from radical species, as shown by Singer et al. [54]). The similarity between spectra of species taken in mineral acid and on a solid acid has been observed in other cases as well, for example with the trityl cation [39]. The stability of cationic species in a zeolite is somewhat surprising, however the behavior was recently also predicted by DFT calculations. Fang et al. [55] found that the zeolite framework facilitates formation of ion pairs for species with larger π systems, and that the preferential formation of an ion pair over a π complex is related to the proton affinity of the neutral species.

The protonated species also has an absorption at a similar wavelength as the neutral species, although this is probably coincidental. Neutral benzene absorbs at 254 nm (referred to as the α band with the notation of Clar) in non-polar solvents, and the protonated species has an absorption at 245 nm [56]. In the neutral species, the absorption at 254 nm is a LUMO ← HOMO transition with $^1B_{2u} \leftarrow {}^1A_{1g}$ symmetry [57]. According to Rode et al. [51], the transition at 245 nm in the protonated species is also a π* ← π transition but not a LUMO ← HOMO transition. Thus, protonation alters the electronic structure of the species, but the protonated species retains an absorption at

a similar position as the α band in the neutral species. In the case of hexamethylbenzene, the α band of the neutral species absorbs at 271 nm [38], whereas the protonated species in H_2SO_4 absorbs at 280 nm [54].

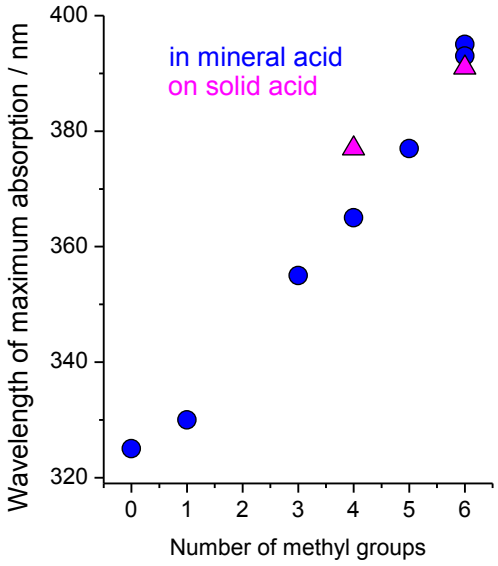


Figure 8.14: Reported wavelengths of absorption for protonated single ring methylated aromatic species in mineral acids [37,54,58-60] or on solid acids [38,61].

The new band appearing at wavelengths > 300 nm upon protonation of methylbenzenes undergoes a bathochromic shift with increasing methylation of the aromatic ring. This is similar to the bathochromic shift of the α band with increasing methylation in neutral methylbenzenes. The increase in absorption wavelength parallels the increase in base strength and has been attributed to a hyperconjugation interaction [37]. The absorption positions of protonated methylbenzene cations with 0, 1, and 3-6 methyl groups in mineral acid have been reported [37,54,58-60] and are shown in Fig. 8.14. It should be noted that there may be a slight variance in the absorption positions of di-, tri-, and tetra- methyl benzene species, even in their neutral state, based on the

position of methyl groups. Also included in Fig. 8.14 are the reported absorption positions of the protonated species on solid acids. These include: 1,2,4,5-tetramethylbenzene on H-beta [61], and hexamethylbenzene on H-beta [38]. Two important features of Fig. 8.14 are the linearity of the plot and the proximity of absorption position between liquid and solid acids. When the mineral acid data is fit with a straight line, the slope is 11.6, meaning that for every added methyl group an increase of approximately 11.6 nm is expected in the position of maximum absorption.

8.4.3 Interpretation of UV-vis-NIR spectra taken during conversion of methanol on H-ZSM-5

Absorption over the entire range of the UV-vis spectrum grew with time on stream. The first bands that formed, seen in the inset of Fig. 8.3, were below 230 nm and at 264 and 353 nm. All three bands are consistent with formation of protonated methylbenzene species. The absorption at 353 nm, according to Fig. 8.14, suggests that the majority of species contained 3 methyl groups. While it may seem peculiar to somewhat selectively form species with only three methyl groups, the behavior is consistent with the predicted transition state shape selectivity of the MFI framework. The activation energy for the methylation reaction usually goes down with an increasing number of methyl groups on the benzene ring, however the calculated barrier goes up for addition of a fourth methyl group when catalyzed by H-MFI [24].

Between 1 h and 3 h on stream, the absorption maximum at 264 nm shifted to 274 nm and the absorption maximum at 353 nm shifted to 360 nm. Both shifts indicate an increase in the average number of methyl groups on methylbenzene species in the hydrocarbon pool. Also visible is the growth of a shoulder around 295 nm that cannot

be assigned to any methylbenzene species. A more likely candidate is an alkyl-substituted cyclopentenyl species, considering that i) there is ^{13}C NMR evidence that methyl-substituted cyclopentenyl species can be formed and are quite stable on H-ZSM-5 [16], ii) alkyl-substituted cyclopentenyl species are a necessary intermediate in a "paring" type mechanism [62], and iii) alkyl-substituted cyclopentenyl species absorb in this range of the UV. In H_2SO_4, Deno et al. [53] found 1,3,4,4,5-pentamethylcyclopentenyl, 1,3,4,4,5,5-hexamethylcyclopentenyl, 1,2,3,4,4-penta-methylcyclopentenyl, and 1,2,3,4,4,5-hexamethylcyclopentenyl to absorb at 288, 291, 299, and 301 nm, respectively. The species absorbing at 295 nm on H-ZSM-5 could also have fewer, but larger, alkyl substituents. For example, 1,3-dimethylcyclopentenyl absorbs at 275 nm, but 1-ethyl-3-methylcyclopentenyl and 1-propyl-3-methylcyclopentenyl absorb at 278 and 280 nm, respectively. Cyclohexenyl and acyclic monoenylic cations were also considered as a possible assignment, but both absorb at wavelengths longer than 295 nm [53]. Thus, we assign the shoulder at 295 nm to an alkyl-substituted cyclopentenyl species.

The aromatic species detected in the effluent from the reactor during the post-reaction flush are consistent with assignment of the band at 320-420 nm to protonated methylbenzenes. At the beginning of the flush, the concentration of aromatic species in the effluent increased suddenly, with xylenes and trimethylbenzenes being the most prevalent species (Fig. 8.5). Concurrently, the intensity of the overtone of Brønsted acid sites at 1420 nm was restored. It has previously been reported that aromatic species with four or fewer methyl groups can be flushed from H-ZSM-5. Bjørgen et al. [40] extracted H-ZSM-5 catalysts used for methanol conversion either without a post-

reaction flush or after 8 minutes of post-reaction flush and observed that most methylbenzenes with 5-6 methyl groups remained in the zeolite, whereas methylbenzene species with fewer methyl groups were able to be flushed. It is clear from Fig. 8.4 that many of the flushed species were initially present in the zeolite as cations. Thus, as the long wavelength band at 330-410 nm lost intensity, the intensity of the overtone of bridging OH groups at 1420 nm was restored. It is important to note that our data does not discount that pentamethylbenzene and hexamethylbenzene species are present on H-ZSM-5. However, it does suggest that they are not present in large concentrations as protonated species, as evidenced by the lack of absorption intensity at wavelengths longer than 375 nm. Once formed, they either decompose rapidly to species with fewer methyl groups or are present mostly as neutral species. Bjørgen et al. [38] estimated the absorption coefficient of the longest wavelength band of the protonated hexamethylbenzene species to be about 50 times larger than the absorption coefficient of the longest wavelength band of the neutral species. This is consistent with the spectra we took of hexamethylbenzene and 1,2,3,4,5-pentamethylcyclopentadiene in cyclohexane or sulfuric acid. Thus, the bands of neutral species may be masked by the intense absorptions of the cationic species.

The other major feature of the spectra taken during the flush is the immediate growth of a band at 280 nm and its almost linear decrease in intensity with time. The rate at which the band must have formed after methanol was eliminated from the gas stream correlates well with the length of time that aliphatic hydrocarbon products, represented by propene in Fig. 8.5, were produced. A band at 283 nm was the only band formed from a methanol pulse at 623 K (Fig. 8.7). Thus, the species responsible for the

absorption at 280-283 nm is quite stable and may be an organic residue that remains after alkyl groups are lost as gas phase products.

Using ^{13}C NMR to investigate formation of the hydrocarbon pool, Song et al. [16] found 1,3-dimethylcyclopentenyl and 1,2,3-trimethylcyclopentenyl to be formed on H-ZSM-5 from ethene. In the presence of carrier gas flow, the half-life of 1,3-dimethylcyclopentenyl was 10 minutes at 548 K. Thus, the species are also quite stable. The wavelength of the absorption of the 1,3-dimethylcyclopentenyl species in H_2SO_4 reported by Deno et al. was 275 nm [53], which is consistent with assigning the absorption at 280-283 nm to cyclopentenyl species with 2 or 3 methyl groups. Thus, we conclude that a cyclopentenyl species, potentially with 2 or 3 methyl groups, is responsible for the absorption.

8.4.4 Interpretation of UV-vis-NIR spectra taken during conversion of methanol on H-beta

Because a greater variety of species make up the hydrocarbon pool on large pore zeolites such as H-beta, the UV-vis spectra are more complex and the interpretation is more difficult. Again, the absorption over the entire range of the UV-vis spectrum increased with time on stream during methanol flow. The first bands formed below 250 nm and at 291 and 395 nm, as shown in the inset of Fig. 8.9. The band positions are in excellent agreement with those expected of protonated 1,2,3,3,4,5-hexamethyl-6-methylene-1,4-cyclohexadiene (HMMC), which has been reported to absorb at 287 and 397 nm in H_2SO_4 [63]. Thus, as evidence of aromatic species with fewer methyl groups are absent in the first spectrum, complete methylation of the aromatic ring must occur

very rapidly. It appears that there is no, or at lease less, transition state selectivity directing which methylbenzene species form on H-beta.

With time on stream, the absorption at 287 nm shifted to 305 nm and the absorption at 397 nm shifted to 378 nm. The band at 305 nm was more intense than the band at 378 nm, which is the opposite of what was seen on H-ZSM-5. If all species contained a single aromatic ring, the shift to 378 nm could be interpreted as indicating that protonated methylbenzene species with approximately 5 methyl groups were accumulating. However, larger polycyclic aromatic species such as methylnaphthalenes are known to also form, and can also absorb in this region. For example, the 1,4-dimethylnaphthalene and 2,3-dimethylnaphthalene cations absorb at 381 nm [59]. Thus while protonated methylbenzene species with fewer methyl groups probably do accumulate, their absorption can not be separated from the absorption of some of the larger protonated species.

The band at 305 nm is the most intense band formed above 250 nm, suggesting that the responsible species constitutes a large portion of the hydrocarbon pool on the working catalyst. Neither protonated methylbenzene nor protonated methylnaphthalene species can be responsible for the absorption. Song et al. [48], using ^{13}C NMR to investigate the hydrocarbon pool on H-SAPO-34, found evidence that a heptamethylcyclopentenyl species was formed from acetone. Such a heavily methylated cyclopentenyl species may also form on H-beta, as the larger pores would be able to accommodate it. From the mineral acid literature, it is known that 1,2,3,4,4,5-hexamethylcyclopentenyl absorbs at 301 nm [53], so either addition of one methyl group or substitution of a methyl group with an ethyl, propyl, isopropyl, or *t*-butyl

substituent may extend the absorption to 305 nm. It is interesting to note the fantastic agreement between the species we propose and the hydrocarbon pool species that have been suggested as being responsible for isobutene/isobutane formation, such as the one shown in Fig. 8.1.

Changes in the spectra that occurred during the post-reaction flush are quite complex. Bands that grew at wavelengths longer than 400 nm are consistent with the build-up of larger protonated polycyclic aromatic species, in particular alkyl-substituted anthracenes, phenanthrenes, and possibly naphthalenes with a larger number of methyl-substituents. The MS signal from methylbenzenes in the effluent stream was an order of magnitude smaller than on H-ZSM-5 (Fig. 8.11). Thus, changes in the spectra resulting from desorption of single ring aromatic species should be miniscule. The intensity of the overtone of external silanol groups, seen in the inset of Fig. 8.10, was slowly restored during the purge, suggesting that the groups are not merely innocent bystanders, and are instead adsorption sites for some hydrocarbon pool species.

8.4.5 Connecting spectroscopic and catalytic data

Over a limited range of reflectance values, the Kubelka-Munk function is proportional to the absorption coefficient of the absorbing species, and thus the concentration. While the range of proportionality may vary from sample to sample, the preferred working range is 20% to 60% reflectance (corresponding to Kubelka-Munk values of 0.13 and 1.6) [64]. Thus, Kubelka-Munk values can lend insight into changes in the concentration of species with time. For this reason, the Kubelka-Munk values at certain wavelengths are plotted versus time, along with the MS signal for selected gas phase products, in Fig. 8.15 for H-ZSM-5 and in Fig. 8.16 for H-beta.

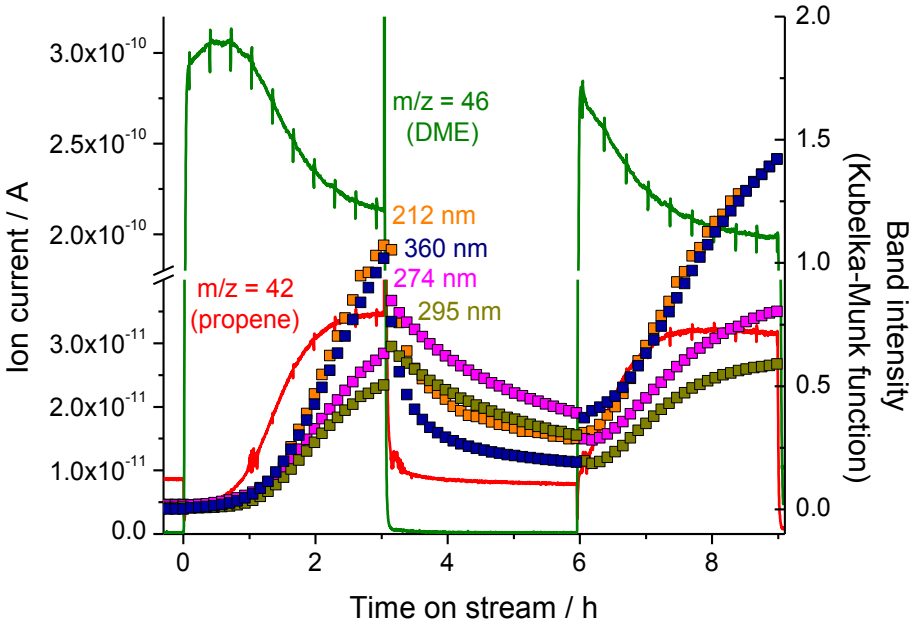


Figure 8.15: Evolution of various bands in the UV-vis spectra of H-ZSM-5 shown in Figs. 8.3 and 8.4, and the ion current at selected m/z ratios monitored with an online MS.

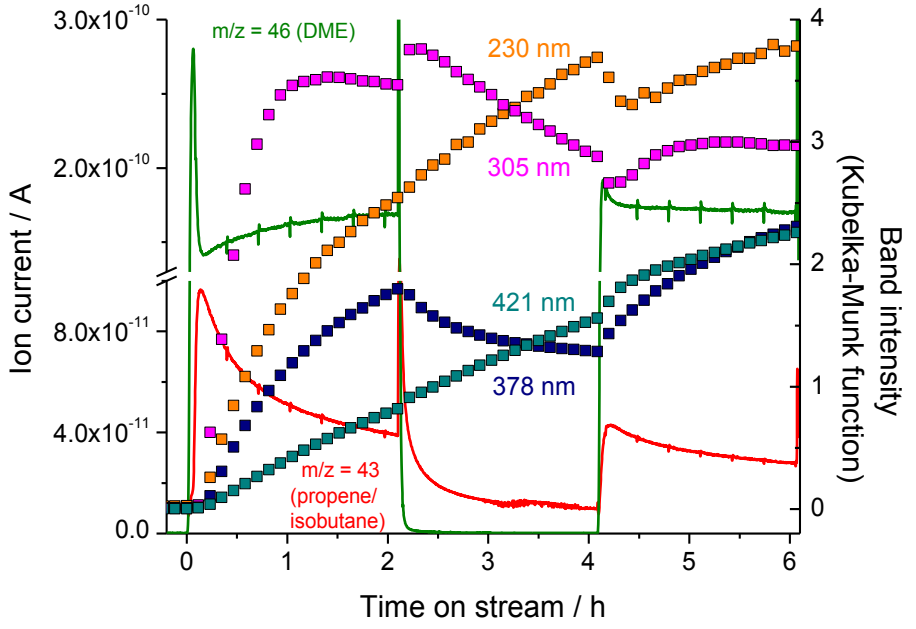


Figure 8.16: Evolution of various bands in the UV-vis spectra of H-beta shown in Figs. 8.9 and 8.10, and the ion current at selected m/z ratios monitored with an online MS.

On H-ZSM-5, the growth of the band at 295 nm (which has been assigned to alkyl-substituted cyclopentenyl species) correlates most closely with the formation of gas phase products during the kinetic induction period (Figs. 8.2 or 8.15, first 3 h). The bands at 212 and 360 nm exhibit almost linear growth after the initial exponential growth. Thus, even after gas phase product formation leveled off after 2.5 h, the bands at 212 and 360 nm were still growing at an almost linear rate, suggesting that the gas-phase products are not cleaved directly from these species. The absorption at 274 nm contains overlapping contributions from multiple species, namely neutral methylbenzenes, protonated methylbenzenes, and alkyl-substituted cyclopentenyl species, with the largest absorption coefficients belonging to the cationic species. The absorption at 295 nm probably contains contributions from the latter two. Thus, plotting the Kubelka-Munk value at 274 or 295 nm does not perfectly capture the change in concentration of any one species. If the 274 or 295 nm bands were only representative of protonated methylbenzene species they should increase at the same rate as the 360 nm band.

After the purge, when methanol was re-admitted to the reaction chamber, the rate of propene formation was the same as that measured after 1 h on stream in the first period of methanol conversion. The reason that the rate was not zero, as it was at the beginning of the first period of methanol conversion, is that there were still some hydrocarbon pool components remaining on the zeolite. The 360 nm band continued its near linear rate of growth while the growth of cyclopentenyl species at 295 nm again leveled off as gas phase product formation reached a pseudo steady-state.

The changes in the spectra that occur during gas switching provide information about the rate of individual chemical transformations. That a stable alkyl-substituted cyclopentenyl species absorbing at 280 nm is formed immediately after switching to inert gas indicates that formation of the species does not require methanol and occurs rapidly. If the species is formed after cleavage of an alkyl group, then bond breaking may not be rate-limiting. Upon switching back to methanol flow, the band at 280 nm was immediately transformed to species absorbing at longer wavelengths (see Fig. 8.15 at 6 h on stream). Thus, ring expansion back to a protonated methylbenzene requires methanol and is not rate-limiting. Finally, that bands representative of protonated aromatic species continued to increase as gas phase hydrocarbon formation reached a pseudo-steady state indicates that formation of the protonated methylbenzene species is also not rate-limiting. However, the band at 295 nm did level out, suggesting that formation of the species responsible for the absorption may be rate-limiting, or that the number of sites on which it can form is limited, or that its formation is limited by diffusion. If our band assignment is correct, it could mean that the ring contraction to form the alkyl-substituted cyclopentenyl species (which eventually cleaves an alkyl group) is rate-limiting. This also implies dominance of a paring-type mechanism.

The story is, again, more complex on H-beta. As discussed previously, the hydrocarbon pool is more diverse, and deactivation must also be considered. The band that grows most rapidly after the initial introduction of methanol is the one at 305 nm, and the band does not grow further after about 1 h on stream. During the purge after 2 h of methanol conversion, the band at 305 nm decreased in intensity at a linear rate, and the band at 421 nm increased at an almost linear rate. It is tempting to suggest that the

species absorbing at 305 nm is transformed into the one absorbing at 421 nm, but one would then have to explain why the rate of hydrocarbon formation at 4 h on stream after methanol was reintroduced was not lower than before the purge. Additionally, the presence of isosbestic points suggests the transformation of species with overlapping absorptions, which is not true of the bands at 305 and 421 nm. That external silanol groups are restored during the purge may hint that deposits on the external surface of the zeolite crystal moved inward. This would explain why the zeolite was not less active after the purge, even though the hydrocarbon pool contained more polycyclic aromatic species. Apparently, the sites at the external parts of the zeolite crystal were more accessible.

We conclude that a paring mechanism is dominant on both catalysts, as indicated by the distinct absorptions of alkyl-substituted cyclopentenyl species in the UV range. The hydrocarbon pool species on H-beta are larger, in general, and contain more alkyl groups. The cyclopentenyl species responsible for cleaving isobutene is highly methylated, and may contain four methyl substituents and one *t*-butyl substituent. The cyclopentenyl species on H-ZSM-5 have fewer alkyl substituents, and probably cleave to produce ethene as the primary product. UV-vis spectroscopy proved to be an extremely useful technique for monitoring the active species in the hydrocarbon pool.

References

[1] D.A. Hickman, L.D. Schmidt, Science 259 (1993) 343.

[2] W.Y. Wen, Catal. Rev. Sci. Eng. 22 (1980) 1.

[3] D. Sutton, B. Kelleher, J.R.H. Ross, Fuel Process. Technol. 73 (2001) 155.

[4] ExxonMobil, Methanol to Gasoline (MTG), Production of Clean Gasoline from Coal <http://www.exxonmobil.com/Apps/RefiningTechnologies/files/sellsheet_09_mtg_brochure.pdf >, accessed March 1, 2013.

[5] R. Kempf, Advances In Commercialization of the UOP Advanced MTO Technology, 2011 Middle East Chemical Week Conference, Abu Dhabi, October 16-19, 2011, <http://core.theenergyexchange.co.uk/agile_assets/1547/1120H_Rick_Kempf_UOP.pdf>, accessed March 1, 2013.

[6] H. Koempel, W. Liebner, Stud. Surf. Sci. Catal. 167 (2007) 261.

[7] U. Olsbye, S. Svelle, M. Bjørgen, P. Beato, T.V.W. Janssens, F. Joensen, S. Bordiga, K.P. Lillerud, Angew. Chem. Intl. Ed. 51 (2012) 5810.

[8] UOP LLC, Honeywell UOP's Advanced Methanol-to-Olefins Technology Selected in China to Produce Chemical Products, <http://www.uop.com/honeywell-uops-advanced-methanoltoolefins-technology-selected-china-produce-chemical-products/>, accessed March 1, 2013.

[9] Process Worldwide, Lurgi to Build Methanol to Propylene Facility in China, <http://www.process-worldwide.com/engineering_construction/plant_design/basic_detail_engineering/articles/328824/>, accessed March 1, 2013.

[10] J.F. Haw, W. Song, D.M. Marcus, J.B. Nicholas, Acc. Chem. Res. 36 (2003) 317.

[11] J.C.W. Kuo, US Patent 3 931 349 (1976), to Mobil Oil Corporation.

[12] S.L. Meisel, J.P. McCullough, C.H. Lechthaler, P.B. Weisz, Chemtech, 6 (1976) 86.

[13] C.D. Chang, A.J. Silvestri, J. Catal. 47 (1977) 249.

[14] M. Stöcker, Microporous Mesoporous Mater. 29 (1999) 3.

[15] I.M. Dahl, S. Kolboe, Catal. Lett. 20 (1993) 329.

[16] J.F. Haw, J.B. Nicholas, W. Song, F. Deng, Z. Wang, T. Xu, C.S. Heneghan, J. Am. Chem. Soc. 122 (2000) 4763.

[17] W. Song, J.F. Haw, J.B. Nicholas, C.S. Heneghan, J. Am. Chem. Soc. 122 (2000) 10726.

[18] T. Xu, J.L. White, US Patent 6 734 330 (2004), to ExxonMobil Chemical Patents Inc.

[19] W. Song, D.M. Marcus, H. Fu, J.O. Ehresmann, J.F. Haw, J. Am. Chem. Soc. 124 (2002) 3844.

[20] Y. Jiang, W. Wang, V.R. Reddy Marthala, J. Huang, B. Sulikowski, M. Hunger, J. Catal. 238 (2006) 21.

[21] J.F. Haw, D.M. Marcus, P.W. Kletnieks, J. Catal. 244 (2006) 130.

[22] Y. Jiang, W. Wang, V.R. Reddy Marthala, J. Huang, B. Sulikowski, M. Hunger, J. Catal. 244 (2006) 134.

[23] S. Svelle, U. Olsbye, F. Joensen, M. Bjørgen, J. Phys. Chem. C 111 (2007) 17981.

[24] D. Lestaeghe, B. DeSterck, V. Van Speybroeck, G.B. Marin, M. Waroquier, Angew. Chem. Intl. Ed. 46 (2007) 1311.

[25] R.F. Sullivan, C.J. Egan, G.E. Langlois, R.P. Sieg, J. Am. Chem. Soc. 83 (1961) 1156.

[26] D.M. McCann, D. Lesthaeghe, P.W. Kletnieks, D.R. Guenther, M.J. Hapman, V. Van Speybroeck, M. Waroquier, J.F. Haw, Angew. Chem. Intl. Ed. 47 (2008) 5179.

[27] J.L. White, Catal. Sci. Technol. 1 (2011) 1630.

[28] J.F. Haw, D.M. Marcus, Top. Catal. 34 (2005) 41.

[29] M. Hunger, W. Wang, Chem. Commun. (2004) 584.

[30] H.G. Karge, M. Laniecki, M. Ziolek, G. Onyestyak, A. Kiss, P. Kleinschmit, M. Siray, Stud. Surf. Sci. Catal. 49 (1989) 1327.

[31] L. Palumbo, F. Bonino, P. Beato, M. Bjørgen, A. Zecchina, S. Bordiga, J. Phys. Chem. C 112 (2008) 9710.

[32] D. Mores, E. Stavitski, M.H.F. Kox, J. Kornatowski, U. Olsbye, B.M. Weckhuysen, Chem. Eur. J. 14 (2008) 11320.

[33] Y. Jiang, J. Huang, V.R. Reddy Marthala, Y.S. Ooi, J. Weitkamp, M. Hunger, Microporous Mesoporous Mater. 105 (2007) 132.

[34] W. Dai, M. Scheibe, N. Guan, L. Li, M. Hunger, ChemCatChem 3 (2011) 1130.

[35] Y. Jiang, W. Wang, V.R. Reddy Marthala, J. Huang, B. Sulikowski, M. Hunger, J. Catal. 238 (2006) 21.

[36] W. Dai, X. Wang, G. Wu, L. Li, N. Guan, M. Hunger, ChemCatChem 4 (2012) 1428.

[37] G.A. Olah, C.U. Pittman, M.C.R. Symons, in G.A. Olah, R.v.R. Schleyer (Eds.), Carbonium Ions, vol. 1, Interscience, New York, 1968, p. 153-222.

[38] M. Bjørgen, F. Bonino, S. Kolboe, K.-P. Lillerud, A. Zecchina, S. Bordiga, J. Am. Chem. Soc. 125 (2003) 15863.

[39] H.P. Leftin, M.C. Hobson, Adv. Catal. 14 (1963) 115.

[40] M. Bjørgen, S. Svelle, F. Joensen. J. Nerlov, S. Kolboe, F. Bonino, L. Palumbo, S. Bordiga, U. Olsbye, J. Catal. 249 (2007) 195.

[41] Y. Ono, E. Imai, T. Mori, Z. Phys. Chem. Neue Fol. 115 (1979) 99.

[42] X. Gao, J.-M. Jehng, I.E. Wachs, J. Catal. 209 (2002) 43.

[43] F. Salehirad, M.W. Anderson, J. Chem. Soc., Faraday Trans. 94 (1998) 1911.

[44] Ø. Mikkelsen, S. Kolboe, Microporous Mesoporous Mater. 29 (1999) 173.

[45] M. Bjørgen, U. Olsbye, S. Svelle, S. Kolboe, Catal. Lett. 93 (2004) 37.

[46] M. Bjørgen, S. Akyalcin, U. Olsbye, S. Benard, S. Kolboe, S. Svelle, J. Catal. 275 (2010) 170.

[47] J.F. Haw, B.R. Richardson, I.S. Oshiro, N.D. Lazo, J.A. Speed, J. Am. Chem. Soc. 111 (1989) 2052.

[48] W. Song, J.B. Nicholas, J.F. Haw, J. Phys. Chem. B 105 (2001) 4317.

[49] W. Song, J.B. Nicholas, A. Sassi, J.F. Haw, Catal. Lett. 81 (2002) 49.

[50] T. Xu, D.H. Barich, P.W. Goguen, W. Song, Z. Wang, J.B. Nicholas, J.F. Haw, J. Am. Chem. Soc. 120 (1998) 4025.

[51] M.F. Rode, A.L. Sobolewski, C. Dedonder, C. Jouvet, O. Dopfer, J. Phys. Chem. A 113 (2009) 5865.

[52] T.S. Sorensen, J. Am. Chem. Soc. 87 (1965) 5075.

[53] N.C. Deno, J. Bollinger, N. Friedman, K. Hafer, J.D. Hodge, J.J. Houser, J. Am. Chem. Soc. 85 (1963) 2998.

[54] L.S. Singer, I.C. Lewis, J. Am. Chem. Soc. 87 (1965) 4695.

[55] H. Fang, A. Zheng, J. Xu, S. Li, Y. Chu, L. Chen, F. Deng, J. Phys. Chem. C 115 (2011) 7429.

[56] B.S. Freiser, J.L. Beauchamp, J. Am. Chem. Soc. 99 (1977) 3214.

[57] D.C. Harris, M.D. Bertolucci, Symmetry and Spectroscopy – an Introduction to Vibrational and Electronic Spectroscopy, Dover, New York, 1989.

[58] H. Luther, G. Pockels, Z. Electrochem. 59 (1955) 159.

[59] G. Dallinga, E.L. Mackor, A.A. Verrijn Stuart, Mol. Phys. 1 (1958) 123.

[60] H.-H. Perkampus, E. Baumgarten, Angew. Chem. Intl. Ed. 3 (1964) 776.

[61] M. Bjørgen, F. Bonino, B. Arstad, S. Kolboe, K.-P. Lillerud, A. Zecchina, S. Bordiga, ChemPhysChem 6 (2005) 232.

[62] R.F. Sullivan, C.J. Egan, G.E. Langlois, R.P. Sieg, J. Am. Chem. Soc. 83 (1961) 1156.

[63] W.v.E. Doering, M. Saunders, H.G. Boyton, H.W. Earhart, E.F. Wadley, W.R. Edwards, Tetrahedron 4 (1958) 178.

[64] F.C. Jentoft, Adv. Catal. 52 (2009) 129.

9 Recommendations

The fundamental investigation of the *n*-butane skeletal isomerization mechanism on H-mordenite, presented in Chapters 4 and 5, revealed that intramolecular skeletal isomerization of *n*-butane on a zeolite is possible, as has previously been shown to be true for *n*-butene isomerization. However, intermolecular isomerization pathways on H-mordenite are extremely sensitive to the butene concentration, making it unlikely to be a good industrial catalyst. An intriguing possibility is to use the zeolite currently used for commercial butene isomerization, H-ferrierite. Several survey experiments performed in our lab indicated that bimolecular reactions, including both hydride transfer and oligomerization, are severely depressed on this zeolite. The narrow two-dimensional pore structure of interconnecting 10-membered ring and 8-membered ring channels is probably responsible. Thus, to make alkanes, a noble metal and H_2 would be required. This would facilitate a classical dual-functional isomerization mechanism. It may also be worth investigating other medium pore zeolites such as H-ZSM-22 and Theta-1. The most obvious hiccup is that high temperatures will probably be necessary, which is undesirable because of thermodynamic limits on potential single-pass yields.

An observation that was not able to be satisfactorily explained was the enhanced rate of *n*-butane conversion after injections of nitrobenzene or 1,3-bis(trifluoromethyl)benzene. Work directed towards explaining the effect of these, and other co-adsorbates, is currently underway. If the observations truly do reflect a lower energy barrier, as proposed by Haw, then one can begin to think about constructing a Brønsted acidic material with “promoters” grafted in close proximity to the acid sites, so that continuous application of the promoter is not necessary.

Our work has, for the first time, unified in situ spectroscopic analysis of species adsorbed on solid acids with species extracted ex situ from the solid acid. The ultimate goal was to develop a better understanding of the chemical identity of surface species identified with in situ spectroscopy. Previous studies have only focused on one technique or the other, and the two have never been used in a complementary way. In many spectroscopic papers, the unsaturated adsorbates are so reactive that only general band assignments can be made because so many different surface species form. These band assignments (for example, to monoenylic, dienylic, or trienylic species) would become much more convincing if the neutral species could be extracted. That being said, we were not able to extract what we claim is an alkyl-substituted cyclopentenyl cation. It may be that the species either needs to be neutralized on the zeolite before extraction, or that the species could be recovered if the hydrofluoric acid containing the digested zeolite was neutralized and then extracted. This also deserves further investigation.

10 Appendix A: Diffuse reflectance UV-vis spectra of additional adsorbed reference compounds

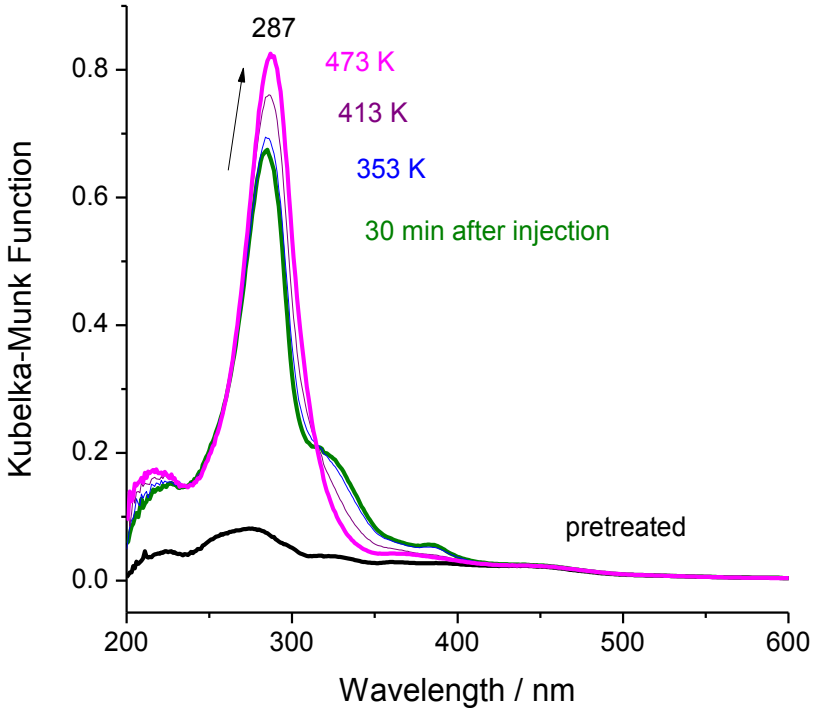


Figure 10.1: Adsorption of 1,4-pentadiene (Aldrich, 99%) on H-mordenite (M2). Pretreatment was at 673 K in 40 ml min^{-1} N_2. The cell was cooled to 303 K and 5 µL of headspace above 1,4-pentadiene liquid was injected. After 30 min, the cell was heated at 5 K min^{-1}.

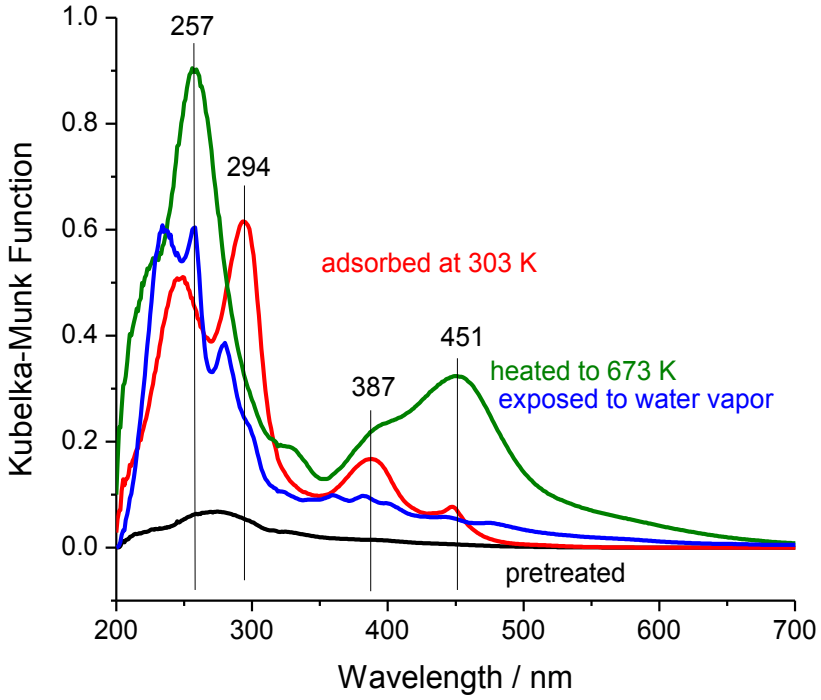


Figure 10.2: Adsorption of 1-methylcyclopentene on H-mordenite (M2). Pretreatment was at a temperature of 573 K in a flow of 30 ml min^{-1} N_2 (black line). Initial adsorption of 0.2 µl 1-methylcyclopentene occurred at 303 K (red line). After 80 min, the chamber was heated at 2 K min^{-1} to 673 K (green line). The chamber was then cooled to 303 K and water vapor was admitted (blue line).

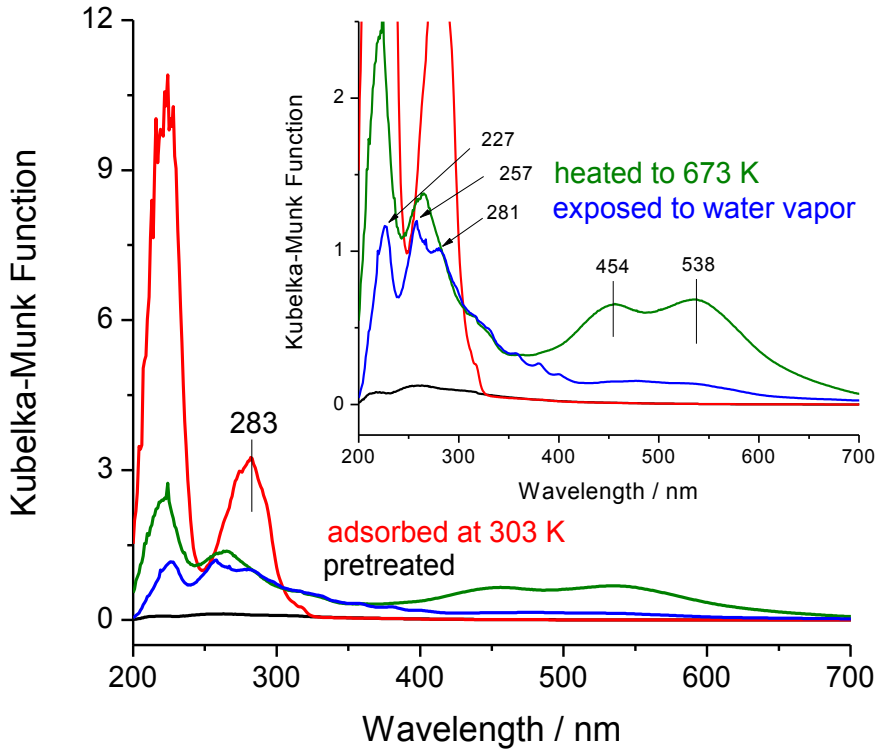


Figure 10.3: Adsorption of 1-methylnaphthalene on H-mordenite (M2). Pretreatment was at a temperature of 673 K in synthetic air. The chamber was then cooled to 303 K in N_2 (black line) and 1 µl of 1-methylnaphthalene was admitted to the chamber (red line). The chamber was then heated at 5 K min^{-1} to 673 K (green line).

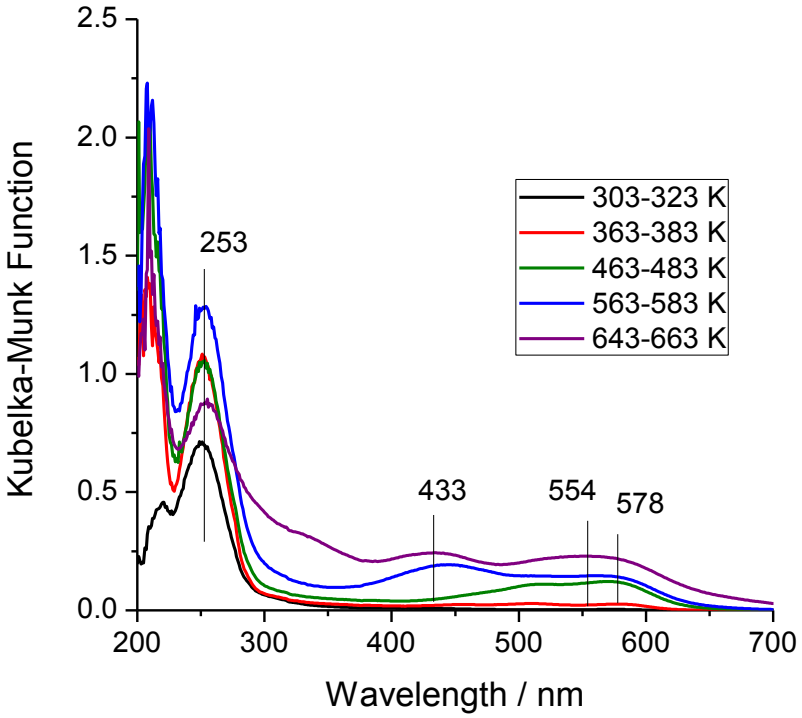


Figure 10.4: Adsorption of biphenyl on H-mordenite (M1) was performed by placing both on separate watchglasses in an evacuated desiccator. The biphenyl-containing H-mordenite was then placed in the chamber and heated at 5 K min^{-1} in a 30 ml min^{-1} flow of N_2. The temperature range over which a scan was taken during heating is given in the legend.

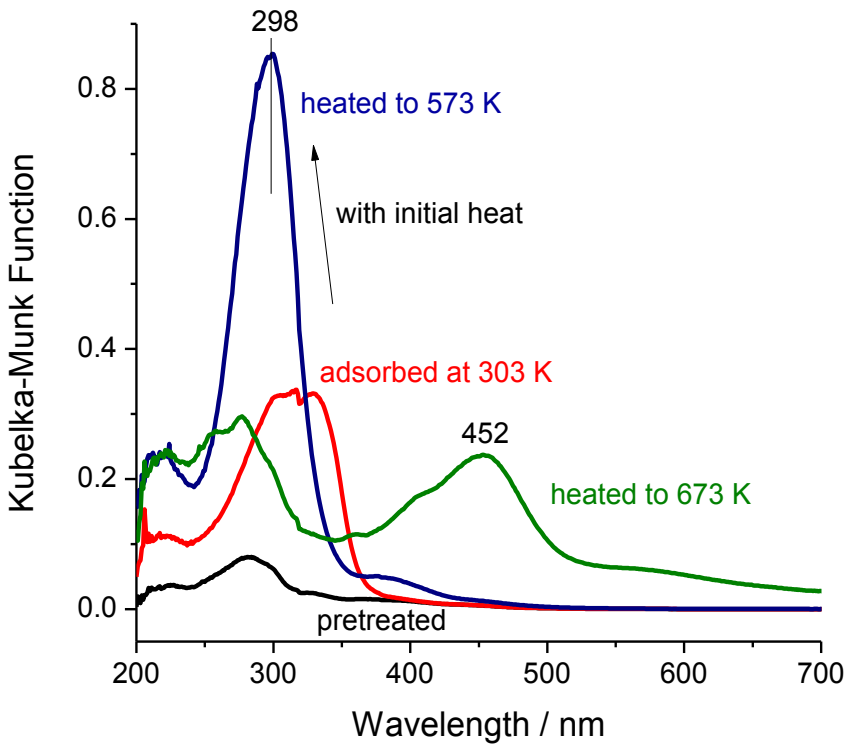


Figure 10.5: Adsorption of cyclohexene on H-mordenite (M2). Pretreatment was at 673 K in 30 ml min^{-1} N_2. The cell was then cooled to 303 K (black line) and 1 µl of cyclohexene liquid was injected. After 60 min at 303 K (red line), the chamber was heated at 5 K min^{-1} to 673 K. Blue line: taken between 250 K and 300 K; green line: taken after 2 h at 673 K.